Rare-Earth-Free Manganese Bismuth Permanent Magnet Synchronous Motor Design for Electric Vehicle Applications

by

Ryan M. Brody

Bachelor of Science in Electrical Engineering, University of Pittsburgh, 2018

Master of Science in Electrical and Computer Engineering, University of Pittsburgh, 2020

Submitted to the Graduate Faculty of the

Swanson School of Engineering in partial fulfillment

of the requirements for the degree of

Doctor of Philosophy

University of Pittsburgh

2024

UNIVERSITY OF PITTSBURGH

SWANSON SCHOOL OF ENGINEERING

This dissertation was presented

by

Ryan M. Brody

It was defended on

March 12, 2024

and approved by

Paul Ohodnicki, PhD., Associate Professor,
Department of Mechanical Engineering and Materials Science, University of Pittsburgh

Robert Kerestes, PhD., Associate Professor,
Department of Electrical and Computer Engineering, University of Pittsburgh

Zhi-Hong Mao, PhD., Professor,
Department of Electrical and Computer Engineering, University of Pittsburgh

Michael McIntyre, PhD., Associate Professor,
Department of Electrical and Computer Engineering, University of Louisville

Troy Beechner, PhD., VP Engineering,
Power Systems Division, RCT Systems

Dissertation Director: Brandon M. Grainger, PhD., Associate Professor,
Department of Electrical and Computer Engineering

Copyright © by Ryan M. Brody

2024

Rare-Earth-Free Manganese Bismuth Permanent Magnet Synchronous Motor Design for Electric Vehicle Applications

Ryan M. Brody, Ph.D.

University of Pittsburgh, 2024

This dissertation examines using Manganese Bismuth (MnBi) permanent magnets (PMs) in permanent magnet synchronous motors (PMSMs) for electric vehicle (EV) applications compared to popular commercially available alternatives, namely Neodymium Iron Boron (NdFeB) and ferrite PMs. MnBi has recently emerged as a promising rare-earth-free (RE-free) PM material, but until now, no group has designed a MnBi PMSM suitable for EV applications, which typically require large quantities of rare-earth PMs with high, volatile cost. Three research Objectives explore this topic, serving as foundational work for MnBi PMSMs at the power, torque, speed, and current ratings required for EV drivetrains.

Objective 1 presents a trade study for MnBi interior permanent magnet synchronous motors (IPMSMs) using a topology commonly found in EVs today. The study is based on an exemplary design from industry that is well documented in literature: the motor design first used in the 2011 Nissan Leaf, also used in the 2012 Nissan Leaf. Objective 1 confirms trends in literature for other PM materials which suggested that MnBi IPMSMs will suffer from low power factor and low constant power speed ratio (CPSR) compared to a similar NdFeB IPMSM because MnBi has a lower remanent flux density (B_r) than NdFeB.

Therefore, Objective 2 presents a trade study for a MnBi permanent magnet assisted synchronous reluctance motor (PMASynRM) topology that is better suited for RE-free PMSMs in some applications than the IPMSM topology. Comparing the MnBi IPMSM and MnBi

PMASynRM reveals tradeoffs between torque density, temperature-dependent irreversible demagnetization, mechanical rotor stress, power factor, and CPSR.

These tradeoffs occur because MnBi PMs are significantly more susceptible to irreversible demagnetization at low temperatures, since coercivity (H_c) significantly increases with increasing temperature. To enable competitive MnBi PMSM designs despite demagnetization risk, Objective 3 presents an observer capable of estimating magnet temperature with fast convergence and a control scheme tolerant of temperature-dependent demagnetization risk. Only normal operating conditions (i.e., without faults) are considered here because other groups have demonstrated current sourced inverters (CSIs) with wide bandgap (WBG) semiconductors can limit fault current while achieving comparable power densities as voltage sourced inverters (VSIs) with Silicon (Si) semiconductors.

Table of Contents

List of Tables

List of Figures

Nomenclature

λ	Split Ratio, Ratio of Stator Inner and Outer Diameters
λ_{pm}, ψ_m	PM flux linkage
ψ_{mn}	Normalized PM Flux Linkage
σ_{MAX}	Maximum Rotor Lamination Stress at 1.2x Maximum Motor Speed
ξ	Saliency Ratio, L_q/L_d
ALS	Adaptive Least-Squares
B_{g1}	Magnetic Loading
B_k	Flux Density at Permanent Magnet Knee Point
B_r	Remanent Flux Desnity
BH_{max}	Maximum Energy Product
B-H	Flux Density vs. External Magnetic Field
COP	Coefficient of Optimal Prognosis
$cos(\theta_{gap})$	Power Factor Measured at Motor Terminals
CPSR	Constant Power Speed Ratio
CSI	Current Sourced Inverter
DR	Demagnetization Ratio
DR_1	Demagnetization Ratio at High Temperature Demagnetization Check
DR_2	Demagnetization Ratio at Low Temperature Demagnetization Check
$\frac{d\dot{x}}{dt}, \dot{x}$	First Derivative with Respect to Time
$\frac{d^2\ddot{x}}{dt^2}, \ddot{x}$	Second Derivative with Respect to Time

Dy	Dysprosium
EV	Electric Vehicle
$f(t)$	Unknown System Dynamics
$\hat{f}(t)$	Estimate of Unknown System Dynamics
FEA	Finite Element Analysis
FN	False Negative
FP	False Positive
FW	Flux Weakening
GA	Genetic Algorithm
H_c	Coercivity
H_k	External Magnetic Field at Permanent Magnet Knee Point
HIL	Hardware-in-the-Loop
HWFET	EPA Highway Fuel Economy Test Cycle
I_d, i_d	d-Axis Stator Current
I_{pk}	Peak Current
I_q, i_q	q-Axis Stator Current
I_{rt}	Rated Current
I_s, i_s	Stator Current
I_{SC}	Short Circuit Current
ID	Inner Diameter
IM	Induction Motor
IPMSM	Interior Permanent Magnet Synchronous Motor
IPMSM1	MnBi IPMSM without Magnet Posts

IPMSM2	MnBi IPMSM with Magnet Posts
J_{pk}	Slot Current Desnity at Peak Current
J_{rt}	Slot Current Density at Rated Current
J_s	Slot Current Density
K_{pk}	Electric Loading at Peak Current
K_{rt}	Electric Loading at Rated Current
K_s	Electric Loading
L_d	d-Axis Inductance
L_q	q-Axis Inductance
LPTN	Lumped Parameter Thermal Network
LUT	Lookup Table
MA	Current-Limit Circles
MnBi	Manganese Bismuth
MTPA	Maximum Torque Per Ampere
MTPV	Maximum Torque Per Volt
MTWD	Maximum Torque Without Demagnetization
MV	Voltage-Limit Ellipses
NdFeB	Neodymium Iron Boron
Ny	Neodymium
OD	Outer Diameter
P_e	Motor Electromagnetic Power
P_{MAX}	Peak Power at Maximum Speed
P-HIL	Power Hardware-in-the-Loop

PI	Proportional Integral
PM	Permanent Magnet
PMASynRM	Permanent Magnet Assisted Synchronous Reluctance Motor
PMASynRM2	MnBi PMASynRM with Lower Maximum Speed
PMASynRM3	MnBi PMASynRM with 10,000 RPM Maximum Speed
PMFSM	Permanent Magnet Flux Switching Motor
PMSM	Permanent Magnet Synchronous Motor
RE	Rare-earth
RE-free	Rare-earth-free
RISE	Robust Integral of Sign of Error
RMS	Root mean square
ROM	Reduced Order Model
Si	Silicon
SPMSM	Surface Permanent Magnet Synchronous Motor
SynRM	Synchronous Reluctance Motor
T_{D2L}	Torque Electromagnetic of D2L Sizing Equation
T_{D3L}	Torque Electromagnetic of D3L Sizing Equation
$T_{D2.5L}$	Torque Electromagnetic of D2.5L Sizing Equation
T_e	Motor Electromagnetic Torque
T_{pm}	Permanent Magnet Temperaure
T_{PM1}	Permanent Magnet Temperature for High Temperature Demagnetization Check
T_{PM2}	Permanent Magnet Temperature for Low Temperature Demagnetization Check
UDDS	EPA Urban Dynamometer Drive Schedule

US06	EPA Supplemental Federal Test Procedure US06
v_d	d-Axis Stator Voltage
V_{DC}	DC-Link Voltage
v_q	q-Axis Stator Voltage
VSI	Voltage Sourced Inverter
VSM	Vibrating-Sample Magnetometer
WBG	Wide Bandgap
WLTP3	World Light Vehicle Test Procedure Class 3
WRSM	Wound Rotor Synchronous Motor
ZOH	Zero-Order Hold

Preface

I would like to acknowledge many individuals who have provided guidance, support, and motivation throughout my studies at the University of Pittsburgh, starting with those on my committee. First, thank you Dr. Brandon Grainger, who has supported me financially and academically throughout the entirety of my graduate education. He has been responsible much of my development as a researcher and engineer. I would also like to thank Dr. Paul Ohodnicki and Dr. Michael McIntyre, two collaborators in this research who offered foundational perspective, advice, and support throughout this research. I would also like to thank Dr. Robert Kerestes and Dr. Zhi-Hong Mao who shaped my underlying knowledge of electrical engineering and inspired me to pursue a graduate education while I was an undergraduate student. Finally, I would like to thank Dr. Troy Beechner from RCT Systems for providing useful feedback on motor design through the Advanced Magnetics for Power and Energy Development (AMPED) research consortium. And to all committee members, thank you for volunteering your time.

I would also like to thank all my friends and family who have supported me in an innumerable number of ways throughout this journey. First and foremost, I would like to thank my parents, Michael and Debra Brody. Their unconditional, selfless love and their support emotionally, financially, and otherwise have been life-giving for as long as I can remember, and their incredible work ethic has inspired me to always work hard and do what I think is right even when circumstances seem most difficult. Additionally, I would like to thank my older brother, Zachary Brody, who I have always looked up to and who has always inspired me to be the best person I can. Finally, I would like to thank all other friends, family, and lab mates who have helped me enjoy life through the good times and supported me through the difficult times.

1.0 Introduction

Due to many factors [1], [2], [3], demand for electric vehicles (EVs) has rapidly increased over the past decade, and this trend will likely continue throughout the next decade [4]. These factors include environmental, economic, and geopolitical concerns related to oil production and consumption; superior EV performance compared to internal combustion engine vehicles; and technological advancements like the proliferation of renewable energy sources, high energy density batteries, and wide bandgap (WBG) semiconductors. Figure 1 shows a block diagram of the powertrain in a typical EV on the road today [5]. It consists of battery energy storage, power electronics to enable bidirectional power flow for traction and regenerative braking, a high-speed electric motor that converts electrical energy to mechanical energy, a gearbox to increase output torque while decreasing output speed [6], [7], [8], a controller that regulates the system, and sensors that provide information to the controller [8]. The power electronics include common-mode filters, differential-mode filters, and an optional DC/DC converter [5]. The motor is usually an interior permanent magnet synchronous motor (IPMSM) [6], which is one possible configuration of a permanent magnet synchronous motor (PMSM).

Competitive EV powertrains must deliver constant power over a large range of speeds while finding a system-wide, optimal tradeoff between volume, weight, efficiency, and cost [2], [3], [6]. These performance metrics all impact each other and are constrained by the requirements of the overall vehicle (e.g. top speed, milage, etc.). Power and torque requirements are dictated by the mechanical dynamics of the wheel related to desired vehicle speed, acceleration, weight (e.g. curb weight, passenger weight, payload, etc.), and driving conditions

(e.g. grade) [1], [2], [3], [4]. Furthermore, the vehicle must meet these requirements while guaranteeing passenger safety in the event of motor faults and other system failures [3].

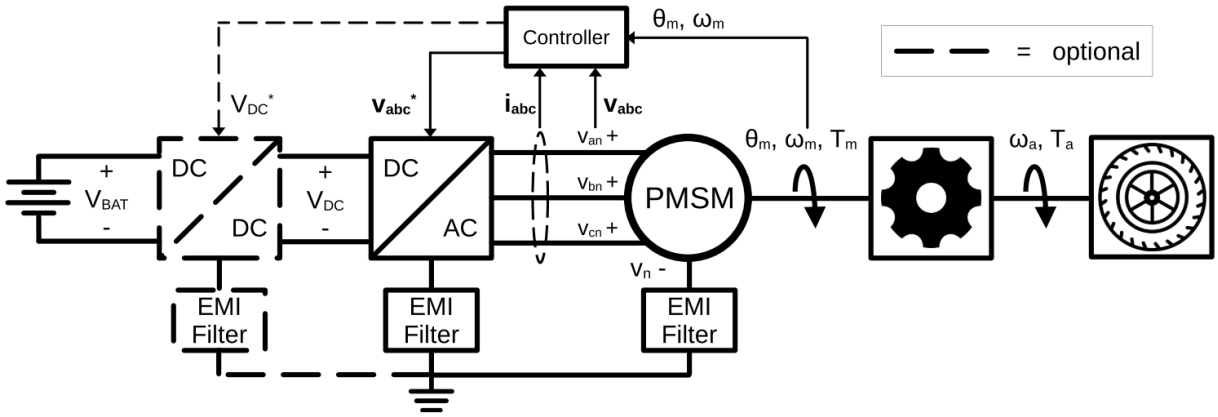

Figure 1: Typical Electric Vehicle Powertrain

Volume and weight are closely related and generally must both be minimized. Volume is primarily constrained by the space and form factors that fit onboard the vehicle [4], and the power output per unit volume of a component is referred to here as power density. Weight is primarily constrained by the desired mileage of the vehicle because approximately 10 lb of additional mass increases power consumption by about 10 W/mi [1]. Cost and efficiency relate to each other, volume, and weight in ways that are difficult to generalize across the entire powertrain. For the motor specifically, larger motors are generally more efficient for a given torque output because larger motors can have lower flux density and current density, both of which relate to the motor losses [9], [10], [11]. However, larger motors also generally cost more because they use more material. Hence, a tradeoff exists between cost and efficiency in EV motors, where cost generally is minimized to limit sticker price while efficiency is generally maximized to maximize the energy available for propulsion.

As subsequent sections will explain in more detail, it is well-known that increasing the maximum speed of a motor for a given output power will increase power density because the required torque decreases, so the motor size can decrease without overly saturating the motor

core [3], [6], [7], [10], [11]. A gearbox can then increase torque and decrease speed as needed, where a high-speed motor with a gearbox tends to be more power dense and less expensive at a system level than a low-speed motor without a gear box [6], [7], [8]. Based their analysis of the trends for motor, battery, inverter, and gearbox technology, the US DRIVE partnership [4] and others [6] expect EV motors must have a large constant power speed ratio (CPSR) with a high maximum speed to reach the power, volume, and weight requirements needed to achieve widespread EV adoption.

With the design goals of high torque/power density, high efficiency, and reasonable cost/manufacturability, electric vehicle engineers typically choose to use IPMSMs with Neodymium Iron Boron (NdFeB) permanent magnets (PMs) for these applications because of superior torque density and efficiency [6], [9]. One reason for such performance of NdFeB based PMSMs is due to the high coercivity (H_c) and remanent flux density (B_r) of NdFeB, leading to a high maximum energy product (BH_{max}) overall [6], [9]. However, because NdFeB PMs use rare-earth (RE) elements, namely Neodymium (Nd) and Dysprosium (Dy), the cost is high (accounting for 20-30% of motor costs in electric transportation applications [4]) and volatile (with prices of Nd and Dy increasing by more than 20:1 in 2011 as an example [9]) due to rapidly increasing demand amid relatively stagnant supply. Producing competitive motor designs that use less or no RE elements requires significant research effort [6].

Traditionally, ferrite PMs are the next best option after NdFeB, and ferrite PMs do not use expensive RE elements. As a result, the cost of ferrite PMs is significantly lower than that of NdFeB PMs, but so are their B_r and H_c performance, preventing widespread use in tractions motors [1]. For example, the US DRIVE partnership has established cost and power density goals to accelerate EV adoption, aiming for a 25% reduction in cost and 88% reduction in

volume by 2025 compared to the state-of-the-art in 2017 [4]. While RE-free ferrite PMs can certainly help achieve cost reduction, inferior B_r and H_c prevents such a drastic decrease in volume. In essence, this is because H_c impacts the maximum achievable current density and speed, while B_r impacts the air gap flux density. As Section 2.0 will show, current density and flux density both directly impact the torque and power density of the motor. Therefore, researchers have been searching for alternative RE-free PM materials that outperform ferrite PMs, and Manganese Bismuth (MnBi) is one such material.

1.1 Contributions

This work serves as foundational benchmarking for using MnBi PMs in electric motors designed for EV applications, as no others have designed a MnBi PMSM suitable for EVs. Only one other group has published a MnBi motor design [12], [13], [14], [15]. In these studies, the rated speed, power, and torque are not suitable for EV applications, and neither is the surface permanent magnet motor topology that is examined. Furthermore, the previous studies do not rigorously analyze how irreversible demagnetization risk changes with temperature due to the significant decrease in H_c as temperature decreases. This effect is particularly important in traction motors because vehicles are often exposed to below-freezing temperatures.

Therefore, Objective 1 evaluates MnBi PMs in a typical IPMSM topology used in EV drivetrains today, shown in Figure 2. When using NdFeB PMs, this motor topology can achieve high torque density, efficiency, and CPSR with minimal amounts of PM material volume [3], [6], [9], [16], [17], [18], which is crucial for minimizing motor cost when using NdFeB PMs due to the cost of RE elements. However, the opposite can be true when using RE-free PMs with lower

H_c, B_r, and cost: topologies which use more RE-free PM material per unit length can achieve higher torque densities than the RE-free IPMSM while remaining cost effective due to the drastic price difference between RE and RE-free PM materials. These designs use more PM material per unit length of motor but also use less copper and steel because the motor is smaller overall.

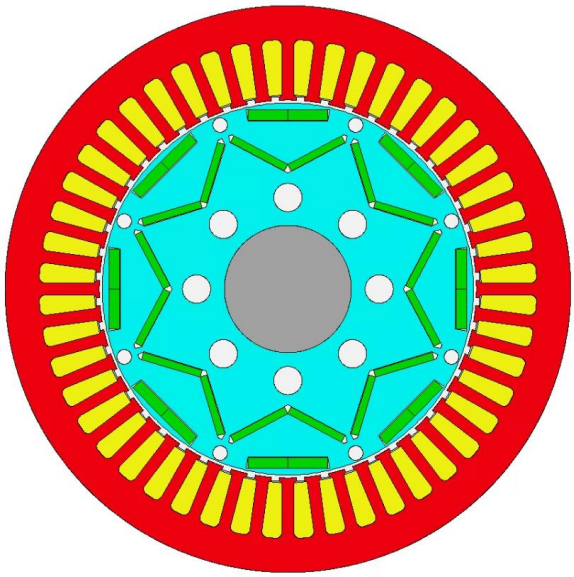

Figure 2: Radial Cross Section of the IPMSM Topology Based on the Reference NdFeB Motor in the 2011 and 2012 Nissan Leaf

Therefore, Objective 2 tests this claim when using MnBi PMs by considering the permanent magnet assisted synchronous reluctance motor (PMASynRM) topology in Figure 3. This topology is a more common choice for RE-free motors [3], [9], [17], [18]. Objective #2 also compares the resultant MnBi IPMSM and MnBi PMASynRM designs, revealing that irreversible demagnetization at low temperatures significantly limits MnBi PMSM torque density. The comparison considers how low temperature demagnetization impacts EV drive cycle performance at low temperatures.

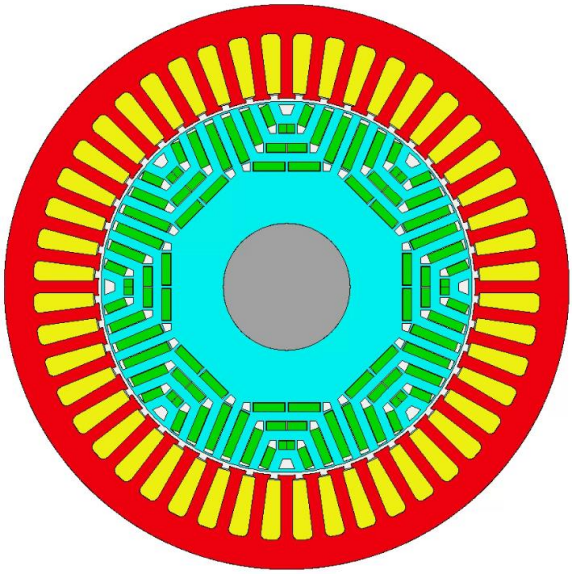

Figure 3: Radial Cross Section of the PMASynRM Topology

To maximize MnBi PMSM torque density in applications that can tolerate risk of irreversible demagnetization at low temperatures, Objective 3 designs an observer which estimates PM temperature and a control scheme which derates motor current at low temperatures to prevent irreversible demagnetization under fault-free conditions. Future work considers how faults in the motor and power electronics impact MnBi PMSM design, where the current sourced inverter (CSI) has been shown to control fault current in PMSM for the most common types of power electronics faults in motor drives [19] and control schemes have been shown to prevent irreversible demagnetization during motor faults [20], [21], [22].

Section 2.0 reviews important concepts for motor design and control as well as a comparison of MnBi, ferrite, and NdFeB material properties. Then, Section 3.0 presents the work completed for Objective 1, Section 4.0 presents the work completed for Objective 2, and Section 5.0 presents the work completed for Objective 3. Finally, Section 6.0 summarizes the contributions.

2.0 Background

This section reviews important background information referenced through this work. Section 2.1 compares the relevant motor topologies. Section 2.2 explains PM irreversible demagnetization and how this damages PMSM when it occurs. Section 2.3 shows the material properties and cost of MnBi, ferrite, and NdFeB PMs which demonstrates the potential of MnBi but also the significantly elevated risk of irreversible demagnetization at low temperatures. Section 2.4 explains various motor sizing equations which relate the fundamental physics of electric machines to torque and power density. This explanation focuses on the impact of motor topology and PM material on torque and power density. Section 2.5 shows how synchronous motor equivalent circuits alone dictate a motor's power capabilities above base speed (i.e., CPSR). This section also focuses on the impact of motor topology and PM material.

2.1 Relevant Motor Topologies

This subsection is intended to explain the choice of IPMSM and PMASynRM topology, rather than another SPMSM topology, a synchronous reluctance motor (SynRM) without PMs, a wound rotor synchronous motor (WRSM), an induction motor (IM), or more advanced topologies such as a permanent magnet flux switching motor (PMFSM). In summary, this study investigates the IPMSM and PMASynRM because these topologies have suitable performance to demand overwhelming popularity in EV applications [6] while also having a simple enough design to be compatible with advanced and robust CAD tools, like ANSYS Motor-CAD [23]

used here. In general, PMSMs have the best combination of torque density, power density and efficiency currently available for EVs [3], [6], [9], [16]. Note that although used in the Tesla Model S [6] and the Toyota Prius until 2011 [24], the IM generally cannot achieve the same efficiency for a given torque density because rotor windings generally have higher losses than rotor PMs. This also degrades power density due to cooling requirements [3], [7], [10], [11]. Similar conclusions apply to the WRSM [11]. Furthermore, the *stator* windings in IMs must carry magnetizing current in addition to excitation current, leading to higher *stator* winding losses compared to a PMSM with the same electric loading. These features of the IM and WRSM make them unsuitable for EV applications. Thus, this study does not consider them.

Other interesting topologies exist. The SynRM does not use any PM material and thus only uses reluctance torque (i.e., torque produced to minimize the reluctance of the flux paths) rather than the magnet torque (i.e., torque produced to align rotor and stator magnetic field). On the other hand, the surface permanent magnet synchronous motor (SPMSM) only uses magnet torque, and the IPMSM and PMASynRM use a combination of the two types of torque [9], [17], [18], [25]. Because reluctance torque requires only a salient pole rotor and not a rotor magnetic field, SynRMs do not use rotor windings or PMs, making them an interesting candidate for RE-free motors. However, SynRMs generally require complex rotor geometries to achieve a high enough saliency ratio to be worth considering, and even still, the SPMSM, IPMSM, and PMASynRM generally can perform better than the SynRM [3], [9]. Due to the generally inferior performance, this study also does not consider the SynRM.

Now focusing on PMSMs specifically, namely the SPMSM, IPMSM, and PMASynRM. When using NdFeB PMs, these types of motors are generally the best options available for applications that require low mass, low volume, and high efficiency [3], [6], [9], [16]. This is

because NdFeB PMs requires less stator winding losses than the IM and no rotor winding losses to produce the same magnetic field in the air gap [3], [7], [10], [11]. This allows for higher stator current density without compromising thermal performance [7]. As Section 2.4 will explain, the air gap flux density and stator currently density are proportional to the motor torque and power density, as determined by the fundamental physics dictating electric motor sizing [9], [10], [26].

Table 1 at the end of this subsection compares qualities of the IPMSM, SPMSM, PMASynRM, and a more advanced machine topology, the permanent magnet flux-switching motor (PMFSM). A comparison of the SPMSM and IPMSM topologies for speeds used in EV applications show similar torque density, specific torque, losses, and cost per unit torque between the two topologies [9]. Here, torque density refers to torque per unit volume (e.g., Nm/L), while specific torque refers to torque per unit mass (e.g., Nm/kg), but generally, these metrics are correlated. Based on the designs surveyed in [27], [28], [29], [30], [31], these metrics seem to vary within designs of the same topology as much they do between designs of different topologies. Still, [6] notes that the IPMSM dominates the electric vehicle market today, despite a slightly more difficult design and manufacturing process compared to the SPMSM, because the reluctance torque present due to IPMSM rotor saliency yields “unparalleled” torque density compared to the SPMSM. Other unstated factors undoubtedly impact this conclusion, such as overloading capabilities, susceptibility to irreversible demagnetization (“demag” in Table 1), and CPSR explained subsequently.

Despite the similarities in Table 1, the SPMSM can achieve maximum speeds an order of magnitude higher than those of IPMSMs because SPMSMs can include mechanical sleaves to secure the PMs to the rotor. These sleeves have higher mechanical strength than the silicon steel rotor bridges that attach PMs to the rotor in IPMSMs. As a result, higher speed SPMSMs can

achieve significantly higher power densities unmatched by the IPMSM in [31]. However, the mechanical sleeves increase the air-gap length thereby decreasing the inductances of the windings. Ultimately, achieving such high speeds likely requires other system-level changes (e.g., to the inverter, gearbox, etc.), so such high speeds are not considered in this work.

While ranking the SPMSM and IPMSM by torque density, specific torque, losses, and normalized cost depends on the exact designs in comparison, the IPMSM tends to outperform the SPMSM regarding the risk of irreversible demagnetization as well as overload and CPSR capabilities [27]. In general, burying the PMs in the rotor in an IPMSM compared to directly exposing them to the air gap flux density in an SPMSM is thought to somewhat protects the PMs from the irreversible demagnetization [10], [11], [22], [32]. A survey of results in literature confirm this general trend with a few exceptions. The IPMSM is shown to have more resistance to demagnetization than the SPMSM in [28], [33], [34], [35], [36], less than the SPMSM in [37], and about the same as the SPMSM in [27]. However, the IPMSM will certainly have better overloading and CPSR capabilities than the SPMSM because of the presence of saliency and, therefore, reluctance torque. The following two paragraphs explain these points in more detail.

First, consider the CPSR. Large CPSR is desirable to facilitate the use of single-gear transmissions thereby simplifying transmission control and improving transmission power density. However, a large CPSR will come at the expense of PMSM power density [6]. The shape of the power and torque vs speed curves for the SPMSM and IPMSM depend on the normalized permanent magnet flux linkage (ψ_{mn}) and the saliency ratio (L_q/L_d) of the machine (the latter of which is always equal to 1 for the SPMSM) [17], [18], [38], [39], [40]. Section 2.5 will explain the CPSR and shape of the power capability curve for PMSMs in more detail, so the key insights will only be introduced here.

A theoretically infinite CPSR occurs when the permanent magnet flux linkage and the maximum d-axis flux linkage at rated current are equal. This is equivalent to saying the rated current is equal to the short circuit current ($I_{SC} = \psi_m / L_d$). While only ideal, lossless motors can achieve an infinite CPSR, both the IPMSM and SPMSM can approach this limit [9], [17], [18]. However, the SPMSM has fewer degrees of freedom in the design, so these machines can only achieve a high CPSR with low normalized magnet flux-linkages (i.e. either a low magnet flux linkage or high rated current) [17], [18]. This limits power and torque production at the expense of inverter utilization due to low power factor [17]. On the other hand, the IPMSM can achieve a high CPSR over a wide range of normalized flux linkages if also designing for the appropriate saliency ratio [17]. Note that as the saliency ratio increases while the normalized PM flux linkage decreases, the distinction between the IPMSM and PMASynRM becomes less meaningful.

Now considering the overload capabilities of each machine, again the IPMSM tends to outperform the SPMSM because of the presence of reluctance torque [18]. With an SPMSM, increasing the stator current above the rated current does not increase peak power. It increases peak torque, but it also increases the back EMF at each speed, so the motor enters the constant power region at lower than base speed without increasing peak power due to voltage limitations. However, this is not the case in the IPMSM because the relationship between stator current and maximum torque is nonlinear. As a result, increasing the stator current above the rated current increases peak power production in the IPMSM, and machines with a higher saliency ratio will have larger increases in peak power. Section 2.5 will also explain this in more detail. However, this peak power is only available over a finite range of speeds above base speed. Above this range of speeds, the power capability converges either to the rated power capability or to zero as

speed increases [18]. Furthermore, the presence of saturation will limit the peak power, especially for high saliency ratio [18].

The PMASynRM performs similarly to the IPMSM because they use a combination of magnet and reluctance torque by including PMs and flux barriers in the rotor to add PM flux linkage and saliency, respectively. In fact, some sources refer to the two topologies interchangeably [9], but here, the ratio of magnet and reluctance torque distinguishes the two topologies [8], [25]. In general, magnet torque dominates torque production in an IPMSM, but reluctance torque dominates in an PMASynRM. Throughout the rest of this work, the terms IPMSM and PMASynRM will be used to refer specifically to the topologies in Figure 2 and Figure 3, respectively, but other possible topologies exist for both motor types. Due to the higher reluctance torque and lower PM flux linkage, the PMASynRM can achieve high power densities, high torque densities, high efficiencies, and a large CPSR [8], [9], [17], [18], [38], [39], [40] without using RE elements. On the other hand, achieving such a high saliency ratio requires carefully optimizing the shape, size, and location of the rotor flux barriers [8], complicating design and manufacturing. Furthermore, efficiency will generally decrease as saliency increases [9], and high saliencies are generally required to achieve high CPSR when using RE-free PMSMs [17], [18].

Finally, the PMFSM was introduced relatively recently in 1955 [41]. It has been shown in [37], [42] and elsewhere that the PMFSM can achieve similar power densities, torque densities, and efficiencies as a PMSM. The PM utilization (i.e., the amount of torque produced per kg of PM used) is 2-5 times those of the PMSMs studied in [37], [42] if using NdFeB PMs, but if using ferrites, the PM utilization of the PMFSM and PMSM are similar in [37]. Furthermore, the PMFSM can be designed such that the winding and PM flux paths are in series or parallel. If

they are in parallel, there is very little risk of irreversible demagnetization [43]. Additionally, the PMFSM has superior CPSR, always able to provide constant power above base speed, because the rotor does not contain PMs [37]. Low demagnetization risk and high CPSR are significant advantages in RE-free PMFSMs compared to PMSMs.

Despite these advantages, the research regarding the design, manufacturing, and validation of the PMFSM topologies lags the research for PMSM topologies because of the complicated structure [8]. This study ignores this topologies for this reason. Still, the PMFSM has become an attractive topology for EV applications, especially in-wheel motors [44], because they naturally facilitate double-stator [8], doubly-salient rotor [43], and axial flux topologies [44]. While further complicating the design process, all of these types of topologies have potential to significantly increase power density, torque density, and efficiency compared to single-stator, singly-salient rotor, radial flux PMSMs.

Table 1: Comparison of Candidate Motor Topologies

<table>
<tr><th></th><th>Torque Density</th><th>Specific Torque</th><th>Losses</th><th>Material Cost</th><th>Overload</th><th>Demag</th><th>CPSR</th><th>Design and Manufacturing</th></tr>
<tr><td>SPMSM</td><td rowspan="3">SPMSM, IPMSM, and PMSynRM motors can achieve similar torque densities. The SPMSM has slightly worse torque density than IPMSM in some sources. The PMSynRM is not as well studied as the other two topologies.

Generally, all will have better torque desnity that induction motors.</td><td rowspan="3">The SPMSM, IPMSM, and PMSynRM have similar masses for similar torque, power, and speed outputs.

Generally, all will have better specific torque than induction motors.</td><td rowspan="3">Similar peak efficiency for IPMSM and SPMSM, but SPMSM has higher losses at high speeds and/or low toruqe while IPMSM has higher losses at low speed.

The PMSynRM will also have high efficiency, but it will degrade as the saliency increases.</td><td rowspan="3">Cost for SPMSM, IPMSM, and PMSynRM is highly dependent on the specific design used.

Cost is highly dependent on PM mass and type. PMSynRMs require the least PM material and are most suitable for REE-lean PMSM.

Cost will likely be higher than induction machines because of PMs.</td><td>Smaller constant torque region, larger constant power region, no change in peak power</td><td>Generally worse than the IPMSM</td><td>Mechanical sleeve for magnets increases airgap hence decreasing inductance thereby limiting FW capabilities</td><td>Simplest, most common rotor geometry to design and manufacture.</td></tr>
<tr><td>IPMSM</td><td rowspan="2">Existance of constant torque or constant power regions depends on design, but higher peak power than SPMSM</td><td rowspan="2">Generally better than the SPMSM</td><td rowspan="2">Higher inductance so higher CPSR than SPM, and lossless designs have infinite CPSR where losses/torque limit speed maximum</td><td>More challenging to design and manufacture than the SPMSM, but much simpler than PMSynRM and FSPMM.</td></tr>
<tr><td>PMASynRM</td><td rowspan="2">Most complicated to design and manufacture due to complex and/or rare geometries.</td></tr>
<tr><td>PMFSM</td><td colspan="3">Possible significant reduction in volume, mass, and losses with same rated torque, power, current and voltage, especially if considering dual stators, doubly-salient rotors, and/or axial flux topologies</td><td>Typically better PM utilization for motors with similar torque outputs</td><td>Always can achieve constant power even at higher than rate current</td><td>Magnetic field from stator windings never demagnetizes the permanent magnets.</td><td>Infinite CPSR (ideally) even when overloading</td></tr>
</table>

2.2 Irreversible Demagnetization in Permanent Magnets

PM demagnetization occurs when a magnetic field intensity, H, is applied in the opposite direction as the PM remanence. This decreases PM flux density, B, hence "demagnetizing" the PM [10], [45], [46]. Figure 4 represents a typical second quadrant B-H curve for RE-free PMs, referred to as the "demagnetization curve". When $H = 0$ in Figure 4, no external field is applied to the magnet, so B_r (the remanent flux density, or the B-intercept of the demagnetization curve) represents flux density produced by the aligned magnetic domains in the PM material. The "knee" of the demagnetization curve, $(-H_k, B_k)$, is the boundary between reversible and irreversible demagnetization, and its position is temperature dependent. In NdFeB PMs, B_k increase with temperature, whereas it decreases with temperature in MnBi and ferrite PMs. Section 2.3 will show that some grades of NdFeB PMs have B_k in the third quadrant at all temperatures, and MnBi PMs have B_k in the third quadrant only at high temperatures. Ferrite PMs have B_k in the second quadrant at all temperatures.

In the linear, reversible region ($H > -H_k$), irreversible demagnetization processes are limited and the magnetic domain structure changes in a predominantly reversible fashion. As a result, μ and B_r do not change after removing the external field. The nonlinear, irreversible region of the demagnetization curve exists beyond the B-H knee ($H < -H_k$). Here, the magnetic domain structures are modified irreversibly in the presence of a strong external field [10]. Therefore, B_k lowers to approximately the minimum B in the PM while demagnetizing (e.g., to B_d in Figure 4). The permeability above the knee point typically still approximately equals the

original value prior to irreversible demagnetization [10], [47], so B_r decreases by the same amount as B_k (e.g., to B_r' in Figure 4). Irreversible demagnetization in PMSMs degrades performance by lowering PM flux linkage while increasing back EMF harmonics [47], [48]. It also leads to costly downtimes and repairs [22], [47].

Reversible demagnetization is useful for PMSM performance, directly leveraged in flux weakening control and indirectly enabling reluctance torque. Therefore, high speed, power dense, and torque dense PMSM design must consider irreversible demagnetization and how demagnetization risk changes with temperatures. High temperatures increase demagnetization risk in conventional NdFeB PMSMs, but coercivity (H_c) is still relatively high even at high temperatures, and high temperatures must be avoided anyways for the sake of other components (e.g., winding insulation, bearings, etc.). However, the low coercivity at low temperatures compared to NdFeB complicates the design with MnBi PMs, requiring careful design and mitigation strategies to avoid demagnetization at low temperatures.

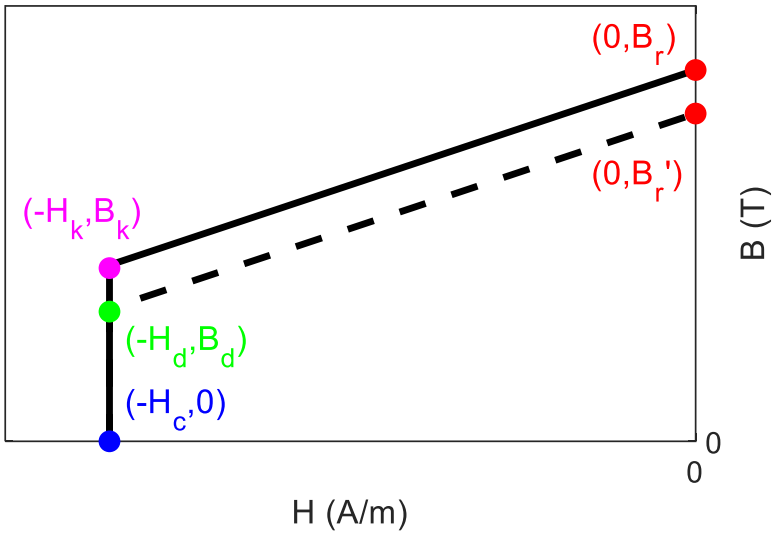

Figure 4: Example RE-Free PM demagnetization curve before (solid line) and after (dashed line) irreversible demagnetization

2.3 MnBi, NdFeB, and Ferrite Permanent Magnet Material Properties

Recently, MnBi has emerged as a promising alternative to NdFeB and ferrite PMs [49]. Figure 5 and Table 2 compares the demagnetization B-H curves at various temperatures for MnBi, N30UH NdFeB [23], Y32 ferrite [23] PMs. The MnBi B-H data used here and throughout this paper was collected by collaborators at Iowa State University and Ames Laboratory led by Dr. Jun Cui [14], [15], [50], [51]. MnBi B-H data was collected using a vibrating-sample magnetometer (VSM) at temperatures as low as 27°C. This data is extrapolated down to 0°C using the curve fitting technique from [23], also used to calculate the B-H data for NdFeB and ferrite PMs in Figure 5 and Table 2. Relatively small MnBi samples were used compared to PM sizes required in PMSMs, so the B-H characteristics of bulk MnBi magnets may differ.

Because RE PMs generally have much larger H_c than RE-free PMs, Figure 5(a) shows all three PM materials while Figure 5(b) focuses on only the RE-free PMs. All PM materials have B_r that decreases as temperature increases. For the ferrite PM in Figure 5, decreasing H_c with decreasing temperature causes an increase in B_k with decreasing temperature, despite a slight increase in B_r. On the other hand, MnBi has the unique property of significantly decreasing H_c with decreasing temperature, which causes B_k to increase significantly with decreasing temperature. This leads to a much greater risk of irreversible demagnetization near and below room temperature [6]. In fact, the degree to which H_c changes with temperature is similar in MnBi and NdFeB magnets. However, H_c in NdFeB decreases with increasing temperature, rather than increasing with increasing temperature like in MnBi. Furthermore, the MnBi PM has H_c similar to the NdFeB PM at 100°C yet similar to the ferrite PM at 27°C. This leads to a significant change in demagnetization risk throughout typical motor operating temperatures.

More specifically, B_r and H_c of MnBi at 300K are about 1.52 and 2.83 times greater than the value for ferrites, respectively. Although not yet commercially available, the cost of MnBi (estimated $11-26/kg [15], [51]) is projected closer to the cost of ferrites ($10/kg [52]), which also do not require RE elements. The cost of NdFeB PMs can be around 25 times that of ferrites [9], and also can be highly volatile, but are estimated to be about $70/kg [53] in this work. The NdFeB grade used in Figure 5, N30UH, has a maximum operating temperature of about 180°C, making it a practical choice for electric transportation, where PM temperature is usually limited to about 100°C [10]. N30UH B_r is about 1.83 times that of MnBi at 300K, and the H_c at 300K is about 3.76 times that of MnBi.

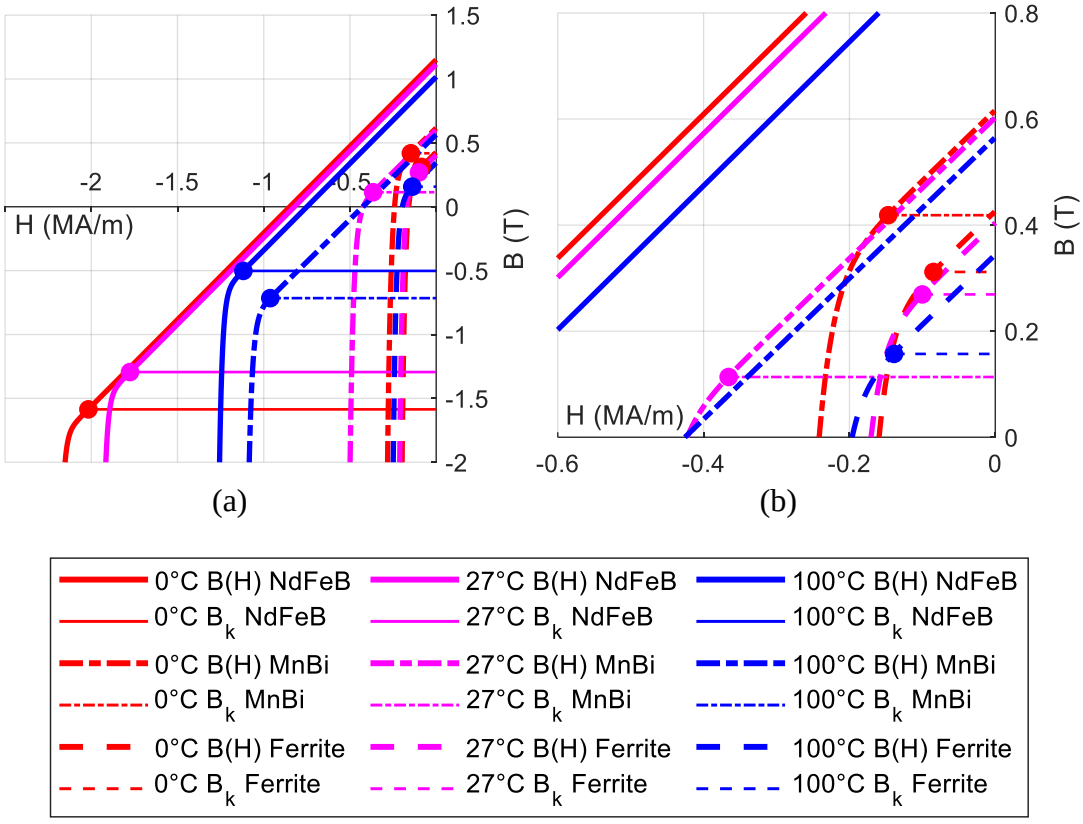

Figure 5: Comparing Demagnetization Curves of MnBi to Those of Typical RE (NdFeB N30UH) and RE-free (Y32 Ferrite) PMs at Low and High Temperatures

While the NdFeB PM outperforms the MnBi PM at low temperatures, the same is not true at higher temperatures, as shown in Table 2. At 450K, for example, the B_r of NdFeB is still slightly higher than that of MnBi by a factor of about 1.72, but now the H_c of MnBi is higher by a factor of about 3.07. In fact, at 450K, the H_c of MnBi is only lower than the H_c of NdFeB at 300K by about 0.86 times. MnBi also has a higher maximum operating temperature than that of NdFeB, similar to that of Samarium Cobalt (SmCo) instead. SmCo is another RE PM material with similar B-H characteristics as NdFeB but a higher maximum operating temperature. Because of the significant increase in H_c at high temperatures, BH_{max} of MnBi remains relatively constant as temperature increases, whereas those of NdFeB and ferrite PMs decreases. Furthermore, higher H_c means a PMSM using MnBi can withstand more current before demagnetizing, although certain power factor and thermal limitations also constrain the maximum current [10], [11]. As Section 2.4 will explain, using more current within the same volume of a machine will increase the available torque. Moreover, since demagnetizing current is used to limit the back EMF of the machine at high speeds using flux weakening control [9], [25], [54], a higher H_c can facilitate higher speeds for a given DC link voltage, but once again, other power factor, thermal and mechanical limitations also constrain the maximum speed [10], [11], [50], [54], [55].

Table 2: Coercivity (H_c) and Remanent Flux Density (B_r) of NdFeB [23], MnBi [50], and Ferrites [23] at Different Temperatures

Temperature	NdFeB (N30UH)		MnBi		Ferrite (Y32)	
	H_c (MA/m)	B_r (T)	H_c (MA/m)	B_r (T)	H_c (MA/m)	B_r (T)
27°C (300 K)	1.92	1.12	0.51	0.61	0.18	0.40
102°C (375 K)	1.23	1.01	1.11	0.55	0.22	0.34
177°C (450 K)	0.54	0.91	1.66	0.53	0.26	0.28

Additionally, the electrical resistivity of MnBi (6.85 $\mu\Omega$-m at 20°C, 7.27 $\mu\Omega$-m at 200°C [49]) is about 4.5 times higher than that of NdFeB (1.55 $\mu\Omega$-m [49]) but still several orders of magnitude lower than that of ferrites (100 Ω-m [23]). A higher electrical resistivity will lead to lower eddy current losses in PMSM designs, which will increase as speed increases. In NdFeB PMs, the increase in PM temperature due to eddy current losses at high speeds can lead to irreversible demagnetization [56]. Lastly, the density of MnBi is estimated as 9000 kg/m^3 compared to 7500 kg/m^3 for N30UH grade NdFeB.

2.4 Electric Motor Sizing Equations

Equations (2-1) – (2-9) are fundamental sizing relationships for any three-phase AC or DC electric machine. Essentially, (2-1) – (2-9) relate the magnetic loading (B_{g1}, the fundamental component of the air gap flux density, in Tesla, due either to rotor PMs or windings [10]) and electric loading (K_s, the peak current density per unit length of air gap circumference, in A/m [10]) to the motor volume and electromagnetic torque output. Equation (2-1) expresses K_s in terms of peak stator current (I_s, A) and peak slot current density (J_s, A/m^2), where k_{cu} is the copper slot fill factor (ratio of copper area to slot area), A_s is the slot area, S_1 is the number of slots, k_1 is the winding factor, N_s is the number of series turns per phase, and D_{is} is the stator inner diameter (ID).

In (2-2), multiplying K_s and B_{g1} is proportional to the magnetic shear stress (σ, Pa) at the rotor outer diameter (OD). Then, (2-3) gives the effective rotor volume V_r in terms of the rotor OD (D_{ro}, m) and the effective length of the motor (l_e, m). According to [10], l_e for the designs here is the stacking factor (k_{is}) multiplied by the average of the rotor and stator lengths (l_r and

l_s, respectively). If neglecting stator resistance, (2-4) relates σ and V_r to the machine torque [9]. Here, T_{2DL} is the estimated torque, and η_{gap} is the efficiency measured at the air gap (i.e., neglecting stator losses). θ_{gap} is phase angle between the stator current and back EMF neglecting stator losses, so $\cos\theta_{gap}$ is the displacement power factor measured at the air gap, pf_{gap} (i.e., the power factor calculated neglecting stator losses).

$$K_s = \frac{k_{cu}A_sS_1}{\pi D_{is}}J_s = \frac{6k_1N_s}{\pi D_{is}}I_s \tag{2-1}$$

$$\sigma = \frac{F}{A} = \frac{1}{2}B_{g1}K_s \tag{2-2}$$

$$V_r = \frac{\pi}{4}D_{or}^2 l_e \tag{2-3}$$

$$\xi_{D2L} = \frac{\pi}{4}B_{g1}K_s\eta_{gap}\cos(\theta_{gap})$$

$$T_{D2L} = 2V_r\sigma\eta_{gap}\,cos(\theta_{gap}) = \xi_{D2L}D_{or}^2 l_e \tag{2-4}$$

$$\frac{T_{D2L}}{V_r} = B_{g1}K_s\eta_{gap}\,cos(\theta_{gap}) \tag{2-5}$$

$$\lambda = D_{is}/D_{os}$$

$$a = \left(\frac{1}{k_{is}}\frac{B_{g1}}{B_{ts}}\frac{l_e}{l_{is}} + \frac{2}{P}\frac{1}{k_{is}}\frac{B_{g1}}{B_{cs}}\frac{l_e}{l_{is}}\right)^2 - \left(1 - \frac{1}{k_{is}}\frac{B_{g1}}{B_{ts}}\frac{l_e}{l_{is}}\right)^2$$

$$b = \left(\frac{1}{k_{is}}\frac{B_{g1}}{B_{ts}} + \frac{2}{P}\frac{1}{k_{is}}\frac{B_{g1}}{B_{cs}}\right)\frac{l_e}{l_{is}}$$

$$f_0(\lambda) = a\lambda^3 - 2b\lambda^2 + \lambda \tag{2-6}$$

$$\xi_{D3L} = \frac{\pi}{16}(k_1k_{cu})\left(\eta_{gap}\cos(\theta_{gap})\right)\left(f_0(\lambda)\right)\left(B_{g1}J_s\right)$$

$$T_{D3L} = \xi_{D3L}(D_{os}^3 l_e) \tag{2-7}$$

$$\xi_{D2.5L} = \frac{\pi}{8} k_1 \eta_{gap} \cos(\theta_{gap}) \lambda \sqrt{f_0(\lambda)} \left(B_{g1} \sqrt{k_{cu} K_s J_s}\right)$$

$$T_{D2.5L} = \xi_{D2.5L}(D_{os}^{2.5} l_e) \tag{2-8}$$

$$P_w = (K_s J_s \rho \,/\, 2) \cdot A_g \tag{2-9}$$

Equation (2-4) is often referred to as the D2L sizing equation (or D_{ro}2L sizing equation, or Essen's Rule) [10], attractive due to its simplicity. The expression for torque density with respect to rotor volume in (2-5) easily follows from (2-4). Rotor volume is often correlated with stator volume, but stator volume is not explicitly considered in the D2L sizing equations.

While more complex, the D3L sizing equation [10] in (2-7) offer additional insight, where T_{D3L} is the approximate torque production for the D3L sizing equation. This sizing equation considers the impact of the stator geometry, not just the rotor geometry, by depending on k_{cu}, the winding factor for the fundamental frequency (k_1), and the "split ratio" (λ, or the ratio of stator ID, D_{is}, to stator OD, D_{os}). In particular, the split ratio, λ, significantly impacts power production for a given motor diameter, quantified by $f_o(\lambda)$ in (2-6). This nontrivial function uses an approximate magnetic circuit analysis presented in [26] to relate the maximum tooth flux density (B_{ts}), maximum core flux density (B_{cs}), and λ to torque and power. However, the D3L sizing equation is still only approximates performance by neglecting, for example, the effect of slot openings, slot wedges and slot liners.

Finally, to obtain the D2.5L sizing equation in (2-7), take the square root of the product of T_{D2L} and T_{D3L}, resulting in a predicted electromagnetic torque of $T_{D2.5L}$ [10]. Doing so in (2-8) reveals $T_{D2.5L}$ is approximately proportional to $\sqrt{K_s J_s}$, the square of which is proportional

to the DC winding loss (P_w) in (2-9). Here, A_g is the air gap surface area and ρ is the conductor conductivity. Winding loss often dominates losses and winding insulation temperature often limit machine performance, so it can be argued by [10] that the D2.5L sizing equation relates torque to steady-state temperature rise according to $\sqrt{K_s J_s}$ in (2-9).

The goal of this study is to fairly compare PMSMs with different PM materials by limiting modifications to power supply, thermal management, winding design, mechanical housing, and gearbox as much as possible. In the D2L, D3L, and D2.5L sizing equations, maximizing B_{g1} and K_s (and hence J_s) increases torque density. While important to consider the effect of the other variables (λ, η_{gap}, θ_{gap}, k_1, k_{cu}, B_{ts}, B_{cs}, etc.), physical and geometric constraints generally limit the ranges.

PM material and rotor geometry primarily determine B_{g1}, while winding design, thermal management, and power supply primarily determine K_s (and J_s). Even so, a tradeoff exists between B_{g1} and K_s due to stator slotting. Most air gap flux will travel through the teeth and back iron (i.e., the magnetizing paths) rather than leaking though the slots (i.e., the leakage paths). Thus, B_{ts} will always be higher than B_{g1}. Since core saturation limits B_{ts}, thicker teeth allow for higher B_{g1} for the same B_{ts}. However, increasing tooth width also decreases the A_s. According (2-1), this either decreases K_s for a given J_s, degrading torque density, or increases J_s for a given K_s, exacerbating thermal issues according to the D2.5L sizing equation. Therefore, there exist an optimal slot width that maximizes $B_{g1} \cdot K_s$ (and T_{D2L}, T_{D3L}, $T_{D2.5L}$, etc.). Because B_{g1} is expected to decrease when using RE-free PMs due to lower B_r compared to RE PMs, it may seem desirable to increase I_s to increase K_s, thus compensating for lower B_{g1} if ignoring winding temperature rise. However, Section 2.5 explains that increasing I_s also degrades CPSR due to stator flux and voltage limitations, regardless of thermal management design.

2.5 Power Capabilities in Permanent Magnet Synchronous Motors and Synchronous Reluctance Motors

This subsection explains why RE-free PMSMs often struggle to achieve high CPSR and power factor comparable to those of RE PMSMs. To understand why this occurs, Section 2.5.1 first explains the three typical operating regions of a PMSM based on the type of control used in each operating region. These types of control are maximum torque per ampere (MTPA) control at low speeds, flux weakening (FW) control at intermediate speeds, and maximum torque per volt (MTPV) control at high speeds. Depending on the equivalent circuit parameters, some designs will not have either a FW or MTPV region, or these operating regions will be very small, but all designs will at least have either a FW or MTPV region. Though again, the speed range for using these types of control may be very small compared to the speed range for MTPA control. Section 2.5.2 then explains how these operating regions affect the shape of the power vs. speed capability curves as determined by the equivalent circuit parameters.

Some sources refer to MTPV control as a type of flux weakening control, but in this work, FW specifically refers to the type of control used when the available current and voltage from the motor drive both limits motor torque and speed, while MTPV refers to the type of control used when only the available voltage from the motor drive constrains motor torque and speed. Similarly, MTPA control is used when only the motor drive current constrains motor torque and speed.

2.5.1 Motor Power Capabilities in Different Operating Regions

Various operating regions exist for the PMSM based on how the voltage and current available to the motor limit the motor torque and speed according to the electrical equivalent circuit model, shown in (2-10) – (2-17). A subscript d denotes a variable on the d-axis, and a subscript q denotes a variable on the q-axis according to reference frame transformation theory [25], [57], depicted in Figure 6. In this reference frame, the d-axis aligns with the PM flux linkage space vector such that the d-axis aligns with the a-axis for an electrical angle equal to 0. Furthermore, v_d and v_q are voltages, i_d and i_q are currents, L_d and L_q are inductances, λ_d and λ_q are flux linkages, R_s is the stator resistance, ω_e and ω_m are respectively the electrical and mechanical frequency in rad/s, θ_e and θ_m are respectively the electrical and mechanical angle in radians, λ_{pm} is the PM flux linkage, T_e is electromagnetic output torque, T_l is the load torque, P is the number of poles, B is the friction coefficient, and J is the rotor moment of inertia.

In summary, (2-10) and (2-11) represent Kirchhoff's Voltage Law (KVL) for the d- and q-axis equivalent circuit, (2-12) and (2-13) define the flux linkages on each axis when the d-axis is aligned with the PM flux linkage, (2-14) quantifies torque production in terms of the magnet torque ($\lambda_{pm} i_q$) and reluctance torque ($\left[L_d - L_q\right] i_q i_d$), (2-15) relates electrical and mechanical frequency by the rotor pole count, and (2-16) and (2-17) uses Newton's Second Law of Rotation and the definition of angular velocity, respectively, to define the rotor mechanical dynamics.

$$v_d = R_s i_d + \frac{d\lambda_d}{dt} - \omega_e \lambda_q \tag{2-10}$$

$$v_q = R_s i_q + \frac{d\lambda_q}{dt} + \omega_e \lambda_d \tag{2-11}$$

$$\lambda_d = L_d i_d + \lambda_{pm} \tag{2-12}$$

$$\lambda_q = L_q i_q \tag{2-13}$$

$$T_e = \frac{3}{2}\frac{P}{2}\left(i_q\lambda_d - i_d\lambda_q\right) = \frac{3}{2}\frac{P}{2}\left(\lambda_{pm}i_q + \left(L_d - L_q\right)i_q i_d\right) \tag{2-14}$$

$$\omega_e = \frac{P}{2}\omega_m \tag{2-15}$$

$$J\frac{d\omega_m}{dt} = T_e - T_l + B\omega_m \tag{2-16}$$

$$\frac{d\theta_m}{dt} = \omega_m \leftrightarrow \frac{d\theta_e}{dt} = \omega_e \tag{2-17}$$

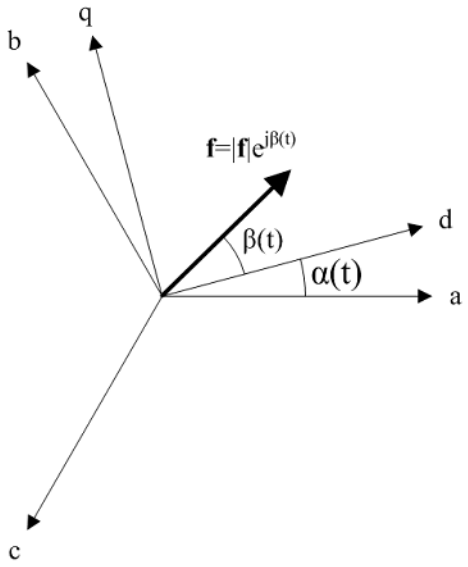

Figure 6: Space Vector in Rotating Reference Frame

Many well-established methods exist for stable, convergent control of the stator voltage and current [8], [25], [57], so the analysis presented here assumes balanced (i.e., no common mode 0-axis component), steady state (neglecting the time derivatives in (2-10) – (2-16)) behavior. Also, friction and saturation are ignored for simplicity. Finally, it is assumed that the motor drive uses a VSI topology because this type of motor drive is most common in industry today, including in EV applications.

To understand the various operating regions, first consider how power supply limitations constrain the available combinations of motor torque and speed. Equations (2-18) – (2-20) show how to calculate the magnitude of the sinusoidal voltages (v_s), currents (i_s), and flux linkages (λ_s) in the stationary, abc reference frame based on the their components in the dq reference frame from (2-10) – (2-14). Essentially, the space vector magnitude in the rotating dq-frame corresponds to the peak value of the sinusoid in the stationary abc-frame [25], [58], as depicted in Figure 6. The maximum voltage and current available from the motor power supply ultimately limit the maximum v_s and i_s a motor can achieve based on the conservation of power between the power electronics and motor.

$$i_s = \sqrt{i_d^2 + i_q^2} \tag{2-18}$$

$$v_s = \sqrt{v_d^2 + v_q^2} \tag{2-19}$$

$$\lambda_s = \sqrt{\lambda_d^2 + \lambda_q^2} \tag{2-20}$$

The motor drive can control i_d and i_d independently, so (2-18) suggests that the current limit can be represented by a circle in the i_d-i_q plane, shown in Figure 7, where $T_{e,max}$ is the maximum motor torque, and I_{rt} is the maximum continuous current, referred to as the rated current. These circles are known as the "current-limit circles" [25], [57] and sometimes abbreviated as "MA" (i.e., "maximum amps") [57]. For any desired i_s, there exist a certain combination of i_d and i_q (and hence, λ_d and λ_q) that maximizes torque production according to (2-14). The dotted black lines, representing combinations of the i_d and i_q that produce equal torque according (2-14) (i.e., "lines of constant torque"). MTPA control is achieved by minimizing i_s for a given amount of torque, which occurs when a certain line of constant torque

is tangential to a certain MA. MA corresponding to lower i_s that this critical value will not intersect the line of constant torque (i.e., the current is too low to achieve that amount of torque), and MA corresponding to higher i_s than this critical value will intersect the line of constant torque twice. The trajectory of i_d and i_q which achieve maximum torque for every possible i_s is known as the MTPA trajectory, and MTPA control simply controls the motor current such that the motor only operates along the MTPA trajectory [25], [57].

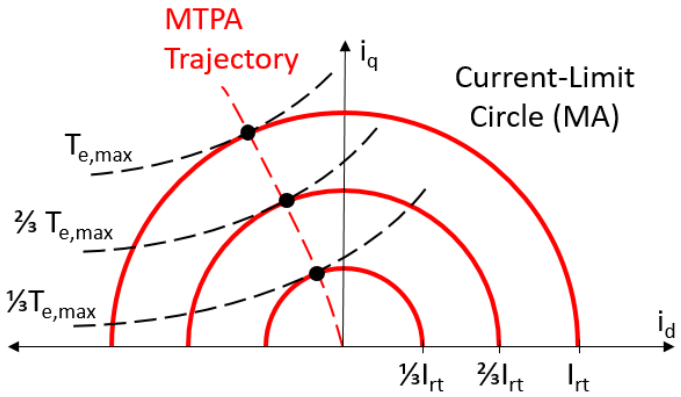

Figure 7: Sketch of the current-limit circle and the MTPA trajectory

At low speeds, the motor drive can always supply enough voltage to follow the MTPA trajectory according to (2-10) and (2-11). At some speed (referred to as base speed, Ω_{base}), the voltage required to stay on the MTPA trajectory exceeds the maximum available stator voltage. This maximum voltage limitation can also be represented graphically. Above base speed, the voltage drop across the stator resistance will be significantly smaller than the back EMF, so the resistive voltage drop in (2-10) and (2-11) is neglected when considering the voltage limit [25], [57], as shown in (2-21) – (2-22). Equation (2-23) shows the stator voltage magnitude is approximately proportional to speeds. As a result, voltage limitations imposed by the motor drive (i.e., available DC link voltages) limit the motor speed if using a VSI topology. Furthermore, the

voltage limit forms an ellipse if $L_d \neq L_q$ and a circle if $L_d = L_q$. Hence, (2-23) is referred to as the "voltage-limit ellipses" [25], [57] abbreviated as "MV" (i.e., "maximum voltage") [57].

$$v_d \cong -\omega_e \lambda_q = -\omega_e L_q i_q \tag{2-21}$$

$$v_q \cong \omega_e \lambda_d = \omega_e (L_d i_d + \psi_m) \tag{2-22}$$

$$v_s \cong \omega_e \sqrt{\lambda_d^2 + \lambda_q^2} \cong \omega_e \sqrt{(L_d i_d + \psi_m)^2 + \left(L_q i_q\right)^2} \tag{2-23}$$

Additional insight can be gained from (2-21) – (2-23). As Section 2.5.2 will show, the short circuit current, I_{SC}, for a motor is an important parameter for understanding the peak power capabilities of the motor. Modeling the short circuit as $v_{s,SC} = v_{d,SC} = v_{q,SC} = 0$, solving (2-21) and (2-22) for short circuit current components $i_{d,SC}$ and $i_{q,SC}$, and then taking the magnitude as done in (2-18) yields (2-24). In other words, I_{SC} in (2-24) is the magnitude of stator current induced in the windings by the PM flux if the motor spins during a short circuit a three-phase short circuit at the motor terminals (neglecting stator resistance, saturation, etc.). Substituting (2-24) into (2-23) then yields (2-25), showing MV is centered at $(0, -I_{SC})$ for all speeds.

$$0 = v_{d,SC} \cong -\omega_e L_q i_{q,SC} \rightarrow i_{q,SC} = 0$$

$$0 = v_{q,SC} \cong \omega_e \left(L_d i_{d,SC} + \psi_m\right) \rightarrow i_{d,SC} = -\frac{\psi_m}{L_d}$$

$$I_{SC} = \sqrt{i_{d,SC}^2 + i_{q,SC}^2}$$

$$\rightarrow I_{SC} = \frac{\psi_m}{L_d} \tag{2-24}$$

$$\rightarrow v_s \cong \omega_e \sqrt{L_d^2 (i_d + I_{SC})^2 + L_q^2 i_q^2} \tag{2-25}$$

Figure 8 shows the voltage-limit ellipses, MV, for various speeds. Here, the speeds are expressed as per-unit (pu) values for generality, where 1 pu corresponds to base speed. The

normalization procedure used to obtain per-unit values will be explained in Section 2.5.2. Similar to the MTPA trajectory, the combination of i_d and i_q that produces the maximum torque for the desired v_s at a desired speed is referred to as the maximum torque per volt (MTPV) trajectory. Controlling the motor to maintain this trajectory is known as MTPV control. This is equivalent to maximum torque per flux (MTPF) control in [57].

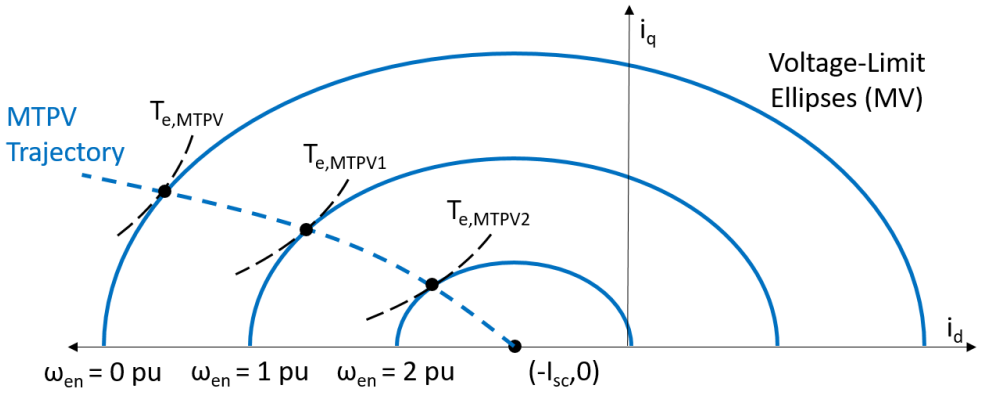

Figure 8: Sketch of the voltage-limit ellipses at various speeds and the corresponding MTPV trajectory

When plotting MA and MV on the same axes (shown in Figure 9 – Figure 11), the area enclosed by both MA and MV represents all controllable operating points [25], [57]. In general, MV below base speed will entirely enclose the MTPA trajectory, so MTPA control can always be used below base speed. Thus, maximum torque is produced at Point A in Figure 9 – Figure 11. Note that these plots are just sketches only intended to show general relationships between MA, MV, the MTPA trajectory, and the MTPV trajectory. The underlying mathematical models in (2-10) – (2-25) were not used to generate these plots.

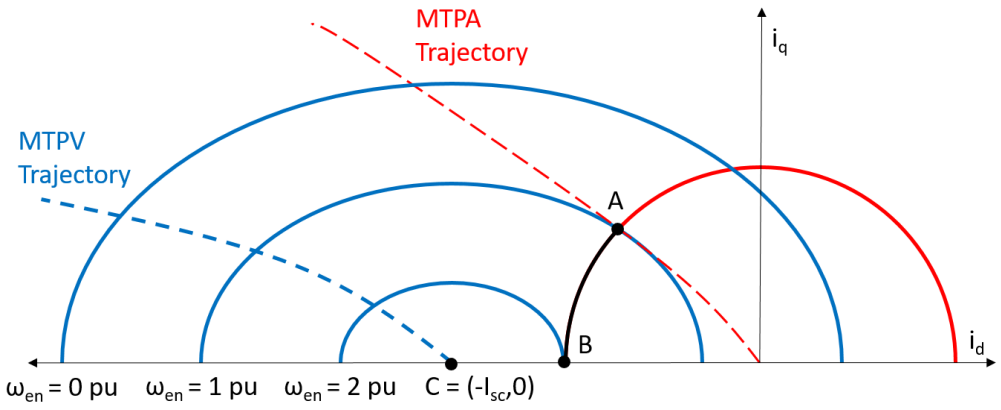

Figure 9: High Speed PMSM Operation – Case #1: $I_{SC} > I_{rt}$

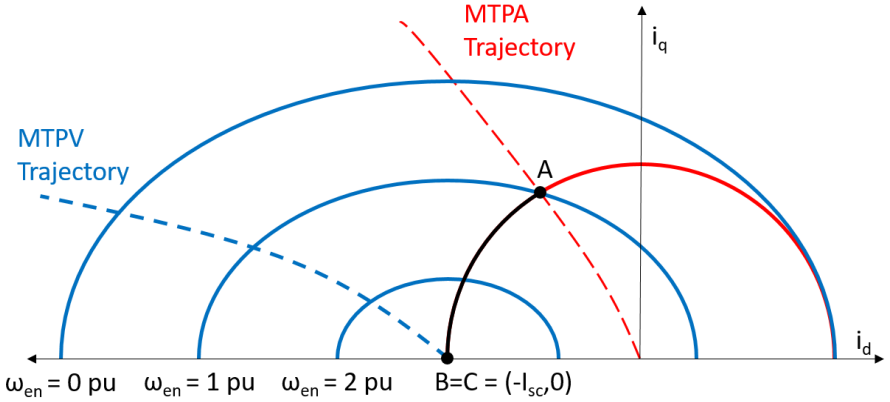

Figure 10: High Speed PMSM Operation – Case #2: $I_{SC} = I_{rt}$

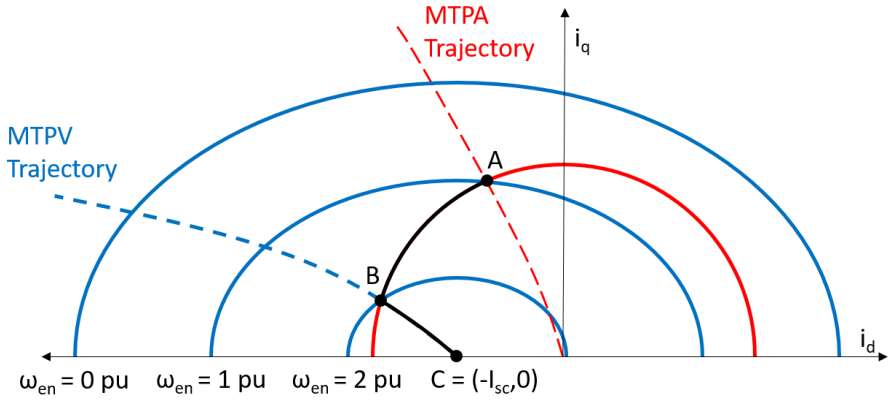

Figure 11: High Speed PMSM Operation – Case #3: $I_{SC} < I_{rt}$

Above base speed (i.e. 1 pu), MV no longer encloses the MTPA operating point. At this point, three possible maximum torque capabilities exist depending on the relationship between I_{SC} and I_{rt} (i.e., where the center of MV, denoted by Point C in Figure 9 – Figure 11, falls on the i_d-axis compared to where MA intersects the i_d-axis) [17]. The first possibility, Case 1 shown in Figure 9, is $I_{SC} > I_{rt}$. In this case, the MTPV trajectory is always outside of MA, so MTPV control cannot be used. Instead, flux weakening (FW) control will be used [25], [57], where the operating point shifts along MA, following the intersection of MA and MV towards the d-axis (i.e., the black arc between Points A and B in Figure 9 – Figure 11). This additional negative d-axis current produces flux that cancels out some of the PM flux, reversibly demagnetizing the PMs, such that the stator voltage according to (2-23) equals its maximum possible value. As a brief point of clarity, MTPV control is sometimes referred to as a specific type of FW weakening control [25] because MTPV control also uses d-axis flux to weaken the PM flux. However, here they are referred to as different types of control to concisely distinguish between the two distinct operating regions as in [57].

In Case 1 ($I_{SC} > I_{rt}$), there will exist some speed (i.e., 2 pu in Figure 9) where MA and MV are tangential to each other, intersecting at only one point on the i_d-axis (i.e., Point B in Figure 9). Because MA and MV do not intersect above this speed, there are no controllable operating points above this speed, so this represents the maximum motor speed. From another perspective, all stator current flows on the d-axis at Point B, so $T_e = 0$ Nm according to (2-14), and hence the motor cannot produce torque to increase speed beyond this point without violating the voltage constraint. From yet another perspective, FW control maximizes torque subject to voltage and current limitations at all speeds above base speed, and MTPV control is never possible due to limitations on the stator current.

Now for the second possibility (Case 2) where $I_{SC} = I_{rt}$, shown in Figure 10. In this case, Point B equals Point C, so as speed increases towards infinity, MV converges towards a point on MA. Thus, there will be at least one controllable operating point at all speeds, so for the ideal motor (i.e., neglecting losses, saturation, etc.), the maximum speed is infinite. As in Case 1, the MTPV trajectory again remains outside of MA, so it cannot be used. FW control is represented by a similar arc as in Case 1 where now Point B equals Point C, and torque production is limited by the maximum stator voltage and current. However, the shape of the torque capability curve in Case 2 does not match that of Case 1, where in Case 2, maximum torque above base speed decreases in a manner inversely proportional to speed, always greater than 0. As a result, maximum power in Case 2 converges with ideal constant maximum power behavior as speed increases towards infinity. Section 2.5.2 will demonstrate this difference between the power capability curves.

Finally, $I_{SC} < I_{rt}$ in Case 3, so now Point C is within MA rather than on the boundary of or outside of MA. As a result, there exists a certain speed above base speed (i.e., 2 pu in Figure 11) where the MTPV trajectory is within the controllable operating region. At this speed, FW and MPTV control produce the same operating point, but above this speed, MTPV control produces more torque than FW control, so torque production is only limited by the available voltage, not the current. In fact, the stator current magnitude decreases along the MTPV trajectory as speed increases because the MTPV trajectory is now within MA. Like in Case 1 and Case 2, FW control is still used along the black arc between Point A and Point B in Case 3, but unlike in Case 1 and Case 2, Point B moves away from the d-axis and is equal to the intersection of the MTPV and FW trajectories at current decreases (i.e., the diameter of MA decreases). MTPV control is therefore used from Point B to Point C.

The exact speed at which Point B is reached depends on the motor parameters, but again, the maximum speed of an ideal machine is infinite for Case 3 because Point C is within MA. Therefore, not all armature current needs to be used to fully weaken the PM flux, so some current is available for torque production at all speeds (ignoring losses, saturation, friction, etc.), and the stator current magnitude is proportional to the inverse of speed. Due to the decrease in stator current, power production is no longer constant and will be less than its maximum value for most speeds. Section 2.5.2 will compare the shape of the power curves for all three cases in more detail.

As a concluding remark for the sake of comparison, WRSMs can achieve similar torque and power capabilities of a Case 2 PMSM. However, instead of using negative d-axis flux to cancel some of the PM flux at high speeds, the rotor winding current can decrease to reduce the field flux above base speed as needed to limit the stator voltage to the maximum allowable voltage without needing to change i_d and i_q. This is known as "field weakening" control and would be equivalent to reducing λ_{pm} in (2-10) – (2-17) for a PMSM if that were possible.

2.5.2 Power Capabilities Based the Electrical Equivalent Circuit Model

Equations (2-26) – (2-29) show the normalized electrical equivalent model neglecting losses and saturation. A subscript n denotes a normalized, per-unit (pu) value, a subscript d denotes a variable on the d-axis, and a subscript q denotes a variable on the q-axis, where v_{dn} and v_{qn} are normalized voltages, i_{dn} and i_{qn} are normalized currents, L_{dn} and L_{qn} are normalized inductances, ω_{en} is the normalized electrical frequency in rad/s, ψ_{mn} is the

normalized PM flux linkage, T_{en} is normalized electromagnetic torque, and P_{en} is normalized electromagnetic power.

$$v_{dn} = -\omega_{en} L_{qn} i_{qn} \tag{2-26}$$

$$v_{qn} = \omega_{en}(L_{dn} i_{dn} + \psi_{mn}) \tag{2-27}$$

$$T_{en} = \psi_{mn} i_{qn} + \left(L_{dn} - L_{qn}\right) i_{dn} i_{qn} \tag{2-28}$$

$$P_{en} = T_{en} \omega_{en} \tag{2-29}$$

The system is normalized as in [59] such that the motor requires 1 pu voltage, current, and flux linkage at a speed of 1 pu when producing 1 pu of torque. The base values used are given by (2-30) – (2-36), where V_s is the maximum peak stator voltage, and I_d^* and I_q^* are the current space vector components under maximum torque per ampere (MTPA) control.

$$V_{base} = V_s \tag{2-30}$$

$$I_{base} = I_s \tag{2-31}$$

$$\Psi_{base} = \sqrt{(\psi_m + L_d I_d^*)^2 + \left(L_q I_q^*\right)^2} \tag{2-32}$$

$$\Omega_{\text{base}} = V_{base} / \Psi_{base} \tag{2-33}$$

$$L_{base} = \Psi_{base} / I_{base} \tag{2-34}$$

$$T_{base} = 3 V_{base} I_{base} / (P \Omega_{base}) \tag{2-35}$$

$$P_{base} = 3 V_{base} I_{base} \tag{2-36}$$

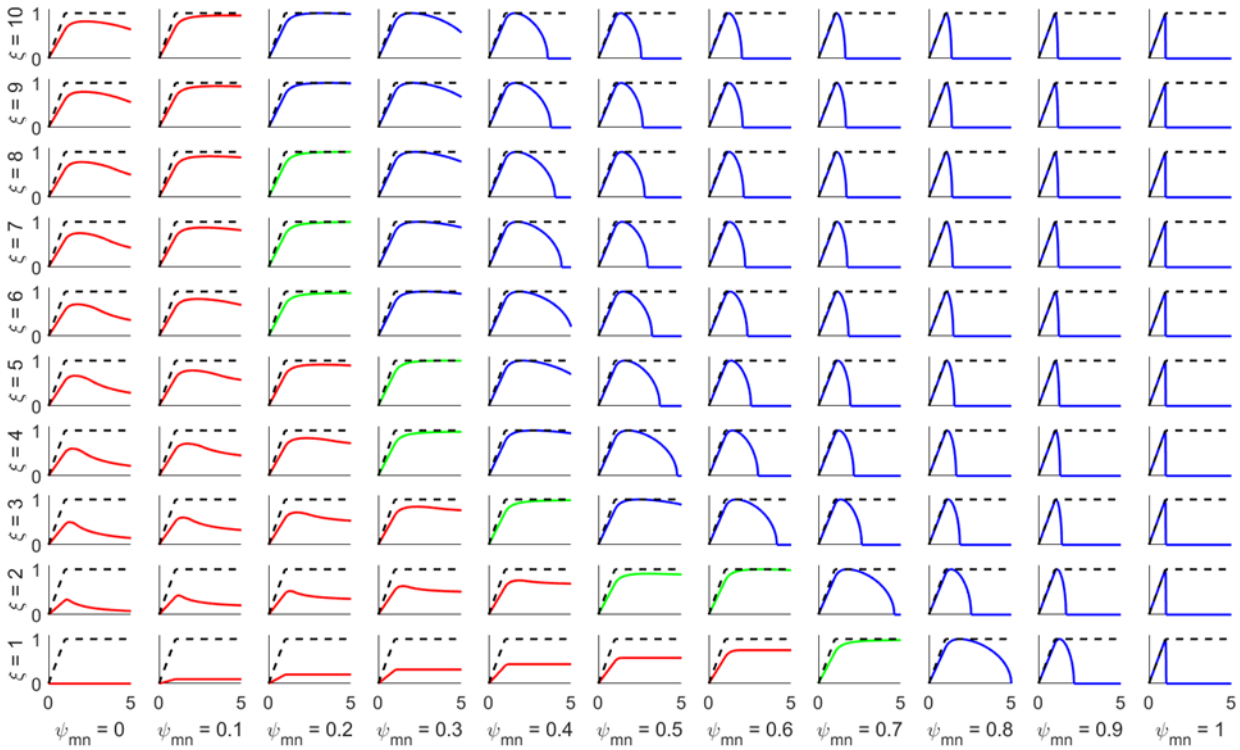

Figure 12: Effect of normalized PM flux linkage (ψ_{mn}) and saliency ratio ($\xi = L_q/L_d$) on CPSR.

It is well-known from [17], [18], [38], [40] and elsewhere that, for a given peak stator current and voltage based on power supply limitations, two parameters in the normalized electrical equivalent model conveniently determine the shape of the normalized power capability curve for the ideal model (i.e., lossless, no saturation, no frictional damping, etc.) of any PMSM. Those parameters are the normalized magnet flux linkage ($\psi_{mn} = \psi_m/\Psi_{BASE}$ where ψ_m is the magnet flux linkage) and the saliency ratio ($\xi = L_q/L_d = L_{qn}/L_{dn}$, where L_d and L_q are the d-axis and q-axis inductances). Figure 12 depicts the relationships between ξ, ψ_{mn}, and P_{en} for ω_{en} from 0 to 5 pu. SPMSMs lie on the horizontal axis where $\xi = 1$, SynRMs lie on the vertical axis where $\psi_{mn} = 0$, and IPMSMs and PMASynRMs represent all other designs.

The dotted line represents ideal constant power behavior, where $P_{en} = \omega_{en}$ using MTPA control for $\omega_{en} < 1$ pu, and $P_{en} = 1$ pu using flux weakening control for $\omega_{en} > 1$ pu. An ideal motor achieves 1 pu constant power with an infinite CPSR if $I_s = I_{SC}$ as defined in (2-24). Red

curves in Figure 12 have $I_{rt} > I_{SC} + 20\%$ and thus represent Case 1 in Section 2.5.1, green curves have $I_{rt} = I_{SC} \pm 20\%$ and thus behave similar to Case 2 in Section 2.5.1, and blue curves have $I_{rt} < I_{SC} - 20\%$ and thus represent Case 3 in Section 2.5.1.

The green and blue curves can produce approximately 1 pu peak power for a wide speed range above base speed. Such designs are easily achievable with the NdFeB IPMSM topology in Figure 2 or other similar topologies because high NdFeB B_r easily achieves high ψ_{mn} and rotor saliency yields reasonable ξ. Hence, these topologies dominate the EV market today because they can achieve both high short circuit current and reasonable saliency with relatively low amounts of NdFeB PM material. For reference, the Nissan Leaf motor in Figure 2 operates with ψ_{mn} between 0.45 and 0.5 pu and with ξ between 2.2 and 2.3 at peak current after considering non-idealities (e.g., loss, saturation, etc.) according to the FEA model used in [50]. However, the red curves experience a decrease in power factor, and hence inverter utilization [17], as shown by the difference in the maximum power of the red curves and the dotted black curves in Figure 12. Therefore, the designs that produce the red curves require a higher DC link voltage (in V) to achieve the same peak power (in kW) as the designs that produce the green or blue curves. These designs are more common when using RE-free PMs, like MnBi or ferrite PMs, because their relatively low B_r yields low ψ_{mn}. Note that it is difficult to achieve high $\xi > 10$ in PMSMs due to saturation, even when using RE-free PMSMs [17]. Additionally, examining (2-24) and (2-32) shows why solely increasing I_s in (2-1) cannot compensate for a decrease in B_{g1} when using RE-free PMs, like MnBi. Increasing I_s increases I_d^* and I_q^* , thereby increasing Ψ_{base} in (2-32). This lower ψ_{mn} after normalizing, shifting designs leftward in Figure 12.

As a result, RE-free motors commonly suffer from lower inverter utilization, power factor, and CPSR because using PMs with lower B_r can also lower ψ_{mn} [9]. Objective 1 in

Section 3.0 confirms MnBi IPMSMs follow this trend. The PMASynRM topology can potentially produce higher I_{SC} compared to the IPMSM topology by including more magnet surface area per pole, and the segmented topology used here is one popular version of the PMASynRM that is simple to design and manufacture by having rectangular barriers [9], [18]. Therefore, Objective 2 in Section 4.0 explores whether the segmented PMASynRM topology can increase I_{SC} to improve power factor and CPSR relative to the MnBi IPMSM proposed from Objective 1. Comparing the MnBi IPMSM and PMASynRM reveals that low temperature irreversible demagnetization limits torque and power density due to limitations on electric loading (K_s) and magnetic loading (B_{g1}), as described in Section 2.2 – Section 2.4, so Objective 3 in Section 5.0 presents an nonlinear observer to estimate PM temperature and a controller that derates current at low PM temperatures to increase torque and power density when operating with high PM temperatures.

3.0 Objective 1: MnBi IPMSM Design for EV Applications

Objective 1 designs a MnBi IPMSM with similar ratings and topology to an exemplary EV motor that uses NdFeB PMs: the motor in the 2011 and 2012 Nissan Leaf, shown in Figure 2. Two designs are considered here. The first exactly matches the Leaf topology in Figure 2, and the optimization procedure considers only a limited design space based on recommendations in [9], [10], [11] to avoid the need to redesign other drivetrain components (e.g., inverter, gearbox, etc.) as much as possible. Based on results from the initial design optimization, the MnBi IPMSM is improved by adding magnet posts to reduce demagnetization risk at low temperatures and rotor lamination stress at high speeds while also considering a larger design space to limit performance degradation between the initial and final MnBi IPMSM designs. Throughout this work, the initial MnBi IPMSM topology without magnet posts is referred to as MnBi IPMSM1, and the final MnBi IPMSM with magnet posts is referred to as MnBi IPMSM2.

3.1 Literature Review

MnBi PMs are not yet commercially available, so only one other group has published a MnBi motor design [12], [13], [14], [15]. However, these designs are not suitable for EV applications. First, these designs consider only a 10 kW SPMSM design. This rated power is not suitable for electric vehicle applications [4], [6]. Moreover, IPMSM dominates the market today [6]. While the IPMSMs in EVs today also use NdFeB PMs to achieve superior torque density [6], there are other inherent disadvantages of the SPMSM topology compared to the IPMSM.

First, the SPMSM has no overloading capabilities, as mentioned in Section 2.1. Electric vehicles often use carefully designed thermal management systems along with motor overloading capabilities to significantly increase power capabilities without increasing size, weight, and costs [60]. In these cases, the motor can operate up to a certain current limit (referred to here as the "rated" current) continuously without overheating. However, the motor can also operate up to a current limit greater than the rated current (referred to here as "peak" current) for thermally limited periods of time. In IPMSMs, this overloading would result in increased power production, but not in SPMSMs. Additionally, SPMSMs cannot achieve large CPSR without having a low power factor and thus a larger DC link voltage than an IPMSM with similar torque and power ratings, as mentioned in Section 2.1 and Section 2.5. Finally, the SPMSM is often more susceptible to irreversible demagnetization than the IPMSM because embedding magnets in the rotor provides some protection from demagnetizing fields, as explained in Section 2.1. Based on the material properties presented in Section 2.2 and Section 2.3, irreversible demagnetization is often an important limitation in RE-free PMSMs due to lower H_c in RE-free PMs, like MnBi, compared to RE PMs, like NdFeB.

In addition to having unsuitable power rating and topology, previous MnBi PMSM designs [12], [13], [14], [15] do not consider irreversible demagnetization at low temperatures. Instead. It only considers irreversible demagnetization at high temperatures during overcurrent conditions. Because MnBi H_c significantly lowers at lower temperatures to an exceptional degree, shown in Section 2.3, low temperature demagnetization is an important limitation to consider.

To address these weaknesses, this work bases the MnBi IPMSM design on an NdFeB IPMSM design in EVs (the 2011/2012 Nissan Leaf) currently on the road today. Section 3.1.1

now introduces the details of the reference motor design. Considering nonlinear, multi-physics phenomena, such as demagnetization at low temperatures, in IPMSM designs is difficult, so Section 3.1.2 introduces an optimization routine capable of considering such detail by using finite element analysis (FEA) and reduced order models (ROMs).

3.1.1 Reference Motor: The NdFeB IPMSM in the 2011/2012 Nissan Leaf

This work uses the design from the 2011 and 2012 Nissan Leaf because an exceptional amount of information about this design exists in literature [6], [23], [61], [62], [63], including an FEA model in [23] depicted in Figure 2. This design [23] uses N30UH NdFeB magnets and is sometimes referred to here as the reference motor. The exact design [61] uses complex rotor duct structures, rather than the circular ducts in Figure 2 [23], to reduce rotor lamination stress at high speeds without significantly impact motor performance. The exact rotor duct structure in [61] is optimized carefully to limit the rotor lamination stress to less than the rotor lamination yield stress, but [61] also suggests the yield stress can increase to almost twice the rotor lamination yield stress due only to changes in the duct shape without significantly impacting torque production if the rotor bridge thickness is kept constant.

Table 3 shows key Leaf design specifications. Here, the authors assume “rated” values represent safe values for the motor to constantly operate without overheating, whereas the motor can only achieve “peak” values for thermally limited periods of time, as suggested in [60]. Throughout this work, a variable with subscripts “rt” or “pk” corresponds to “rated” and “peak” values, respectively. Not all values in Table 3 can be found in literature (e.g., stator current magnitudes and densities), so the following logic is used to determine those specs.

The motor is rated to operate continuously at rated power $P_{rt} = 80\ kW$ [62], and Motor-CAD predicts rated current $I_{rt} = 267\ A$ is the current required to produce 80 kW of constant power in the flux weakening regime for the DC link voltage of 375 V specified in [23], [62]. This rated current, $I_{rt} = 267\ A$, also yields rated torque $T_{rt} = 160\ Nm$ in Motor-CAD. On the other hand, the motor is assumed to be able to operate at peak current $I_{pk} = 480\ A$ so long as the IGBT junctions in the inverter remain below their critical temperature, as described in [63]. Motor-CAD predicts $I_{pk} = 480\ A$ is required to produce the peak torque $T_{pk} = 280\ Nm$ specified in [61], [62], which yields peak power $P_{pk} = 120\ kW$ of constant power during flux weakening for the same DC link voltage. The rated and peak slot current densities (J_{rt} and J_{pk}, respectively) and rated and peak electric loading (K_{rt} and K_{pk}, respectively) are calculated in Motor-CAD at the selected I_{rt} and I_{pk}.

Table 3: Design Specifications for the Reference NdFeB IPMSM in the 2011 and 2012 Nissan Leaf

Input	Range
Phases, m	3
Slots, S	48
Poles, P	8
Number of Series Turns Per Phase, N_s	24 (2 paths)
Stator OD, D_{os}	198 mm
Air gap, g	1 mm
Base Speed, n_b	4000 RPM
Maximum Speed, n_{MAX}	10,000 RPM
Rated Current, I_{rt}	267 A
Peak Current, I_{pk}	480 A
Rated Power, P_{rt}	80 kW
Peak Power, P_{pk}	120 kW
Rated Torque, T_{rt}	160 Nm
Peak Torque, T_{pk}	280 Nm
Rated Slot Current Density (J_s), J_{rt}	9.39 A_{rms}/mm^2
Peak Slot Current Density (J_s), J_{pk}	16.88 A_{rms}/mm^2
Rated Electric Loading (K_s), K_{rt}	65.56 A_{rms}/mm
Peak Electric Loading (K_s), K_{pk}	117.9 A_{rms}/mm

3.1.2 Design Optimization Using Reduced Order Modeling of Finite Element Models

Interior permanent magnet synchronous motors (IPMSMs) with rare-earth (RE) PMs, like NdFeB, have attracted significant attention over the past several decades because this type of motor can achieve exceptional combinations of power density, torque density, efficiency, and manufacturability. The commercialization of RE PMs, scientific advancements in understanding PMSM reluctance torque, and the push for electrifying the transportation and industrial sectors largely fuel this trend. However, this these design goals challenge machine designers by forcing them to optimize highly saturated (for high torque density), highly salient (for high reluctance

torque that does not require PMs), and high-speed designs (for high power density) [9]. Saturation and saliency add nonlinearity to the electromagnetic analysis, and high-speed operation exacerbates electromagnetic, thermal, mechanical, and system-level (i.e. power electronics, control) trade-offs [64], [65].

To address these challenges, [9], [10], [11], [26], [50] and elsewhere provide guiding principals for machine design using a combination of analytical tools and multi-objective optimization. While closed-form calculations adequately model some machine phenomena, other important effects are difficult, possibly infeasible, to model without finite element analysis (FEA). These effects include PM irreversible demagnetization and rotor lamination stress, effects with increasing importance in modern high speed PMSMs. Although computation time usually prohibits FEA use in multi-objective optimization algorithms, ROMs of FEA models (also called surrogate models, meta-models [66], or a "model of a model") offer a compromise between the detail and accuracy of FEA and the computational ease of closed-form analytical calculations. Commercially available software, like ANSYS OptiSLang [66], [67] used here, have successfully demonstrated potential of the ROM approach. This work therefore uses ANSYS Motor-CAD [23] for FEA and ANSYS OptiSLAng [67] for building ROMs and performing multi-objective optimization.

Figure 13 shows a flow chart for machine design using multi-objective optimization of FEA ROMs. First, determine the variables, constraints, and objectives based on a variety of factors, such as application requirements, reference designs, sizing equations, scaling laws, and standards [9], [10], [11], [26], [50]. The exact definitions depend on the specific design details. From here, create a ROM by conducting a sensitivity study, and then optimize the ROM performance using typical multi-objective optimization algorithms, like the genetic algorithm

(GA) used here. Reference [9] and elsewhere show that, if applied correctly, this process can accurately produce competitive designs. Larger design spaces generally lead to lower ROM accuracy for nonlinear FEA models, so determining a design space that is large enough to contain competitive designs but small enough to have high ROM accuracy can be challenging. This is especially true for nonlinear, multi-physics phenomena that are important in MnBi PMSM design, such as low temperature irreversible demagnetization and rotor lamination stress at high speeds. Still, if done appropriately, an approach that iteratively refines the size of an initially large design space can produce accurately produce competitive design.

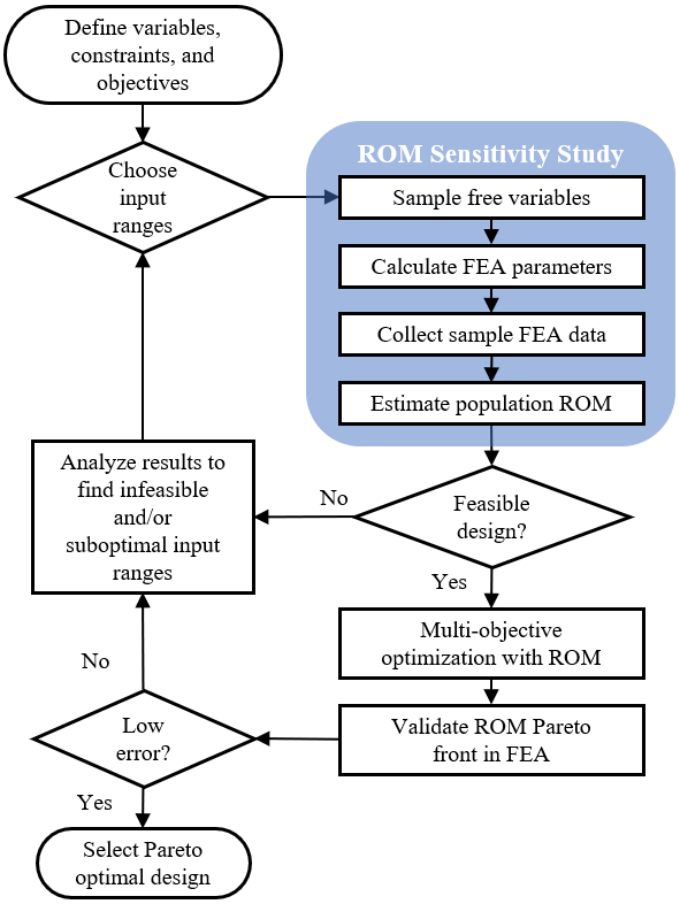

Figure 13: Flowchart for machine design using multi-objective optimization of an FEA ROM

3.2 Preliminary MnBi IPMSM Design Space, ROM, and Optimization Routine

For PMSM design, K_s is limited by factors such as current available from the power supply, the maximum temperature of stator windings according to insulation rating, and maximum demagnetization current, while B_{g1} is primarily limited by the saturation flux density of the rotor and stator laminations, the magnet geometry, and the remanent flux density (B_r) of rotor magnets [9]. After maximizing the B_{g1} and K_s based on these factors, increasing torque output requires increasing the motor volume according to the sizing equations presented in Section 2.4. Because ferrites have a much lower B_r than NdFeB, PMSMs that use ferrites with similar electric loading (K_s) must be larger to achieve the same torque output as a PMSM using NdFeB [9]. Similar logic applies to MnBi PMSMs. Using the reference design presented in Section 3.1.1 as an example, replacing the N30UH NdFeB PMs with MnBi and ferrite PMs reduces torque output from about 280 Nm to about 200 and 165 Nm, respectively. Therefore, if not altering the rotor geometry, the motor size must increase by about a factor of 280/200 = 1.4 and 280/165 ≈ 1.7 times if using MnBi or ferrites, respectively.

3.2.1 Optimization Inputs

In this initial design, the size of the design space is significantly limited by using the sizing equations presented in Section 2.4 to define the stator geometry. This is done to validate initial predictions (1.4 times size increase and the increased risk of irreversible demagnetization at low temperatures) while minimizing the need to redesign other elements of the drivetrain, such as the inverter, gearbox, and thermal management. However, results will show that power factor decreases in the MnBi IPMSM compared to the reference motor, as predicted by the equivalent

circuit analysis presented in Section 2.5, necessitating a notable increase in DC link voltage (V_{DC}) from 375 V to at least 500 V. Objective 2 will address this weakness. The rest of this section explains how the author uses sizing equations to determine the stator geometry in the optimization routine and presents the input ranges, constraints, and objectives used for this initial design.

To make a fair comparison, this MnBi design uses the same number of phases, slots, poles, turns, stator OD, air gap length, and maximum speed as the reference Leaf motor, specified in Table 3. The stator and rotor lamination stacking factors are assumed to be 0.97 based on the FEA model of the reference motor included with Motor-CAD [23] for template-based design. Similarly, the liquid cooling system for all MnBi IPMSM designed here are identical to the design in the template model of the Leaf motor [23] aside from extending the motor housing axially to accommodate the greater length of the MnBi IPMSM compared to the Leaf motor.

Additionally, the design uses the same rated and peak currents, current density, and electric loading, specified in Table 3. This limits temperature rise, as suggested by the D2.5L sizing equation in (2-8) without redesigning the thermal management system and power electronics. Together, these limitations significantly control the choice of D_{os}, so the author simply keep D_{os} constant and only vary λ. Other D_{os} were initially tried, but results did not demonstrate strong sensitivity, suggesting the reference value may be near the optimal value.

Changing the maximum speed (n_{MAX}) and the air gap length (g) could improve power density, but both variables impact the mechanical integrity of the system. 10,000 RPM from the Leaf motor is a typical n_{MAX} in EVs today [6], and increasing n_{MAX} increases bearing friction losses, which can degrade bearing lifetime [10], [11], [64]. Similarly, a 1 mm air gap matches the

reference design while also approaching the minimum recommended air gap length for this power level according to [10], so this comparison does not consider changing these values. Furthermore, the desired base speed (n_b) remains equal to 4,000 RPM to fairly compare the constant power speed ratio (CPSR, equal to n_{MAX}/n_b) of MnBi and NdFeB designs, typically an important weakness of REE-free PMSMs [9], explained in Section 2.5.

As stated in the D3L sizing equation in (2-6), the choice of split ration $\lambda = D_{os}/D_{is}$ is not arbitrary, and optimal choice of λ should maximize $f_0(\lambda)$, as described in [10], [26], where $f_0(\lambda)$ will always have a maximum between 0 and 1. However, the minimum possible λ subject to thermal constraints on K_s and J_s is often greater than the optimal value of λ that maximizes $f_0(\lambda)$ when unconstrained by thermal limitations. This happens because decreasing stator ID D_{is} increases K_s, J_s, and λ, yet temperature rise is approximately proportional to $\sqrt{K_s J_s}$ according to the D2.5L sizing equation in (2-8). Reference [10] derives the minimum λ that minimizes D_{is} subject to thermal constraints, shown in (3-1), where $J_{s(rms)}$ is simply the root mean square (RMS) value of the slot current density J_s. Although the square root yields two possible solutions, only one will be geometrically feasible (i.e., between 0 and 1).

$$\lambda = \frac{D_{is}}{D_{os}} = \frac{b}{a} + \frac{2K_s}{ak_{cu}J_{s(rms)}D_{os}} \pm \sqrt{\left(\frac{b}{a} + \frac{2K_s}{ak_{cu}J_{s(rms)}D_{os}}\right)^2 - \frac{1}{a}} \tag{3-1}$$

According to the D3L sizing equation in (2-7), maximizing the product $k_{cu}J_{s(rms)}$ maximizes torque production. Similarly, (2-1) suggests maximizing $k_{cu}J_{s(rms)}$ also maximizes K_s by definition, which then maximizes torque production according to the D2L sizing equation in (2-4). Hence, the optimization routine here adjusts the number of parallel wire strands per turn for each design to maximize the copper fill factor k_{cu}, making it approximately equal to the k_{cu} of the reference design. As a result, the only unknown parameters in (3-1) for this optimization

routine are a and b, defined in (2-6). Accordingly, the stator tooth flux density B_{ts}, stator core flux density B_{cs}, and air gap flux density B_{g1} are the only unknown variables in (2-6), where $l_e/l_{is} \cong 1$ in the reference design and in all MnBi designs presented in this work.

Furthermore, the derivation of the D3L sizing equation in (2-7) and the optimal λ in (3-1) rely on the definitions of stator tooth width t_s, stator slot depth d_s, and stator slot area A_s presented in (3-2) – (3-4) below. References [10] and [26] derive similar equations for a slightly different slot shape but are modified here according to the slot shape in the reference design, shown in Figure 14. Specifically, each slot has a rounded top with radius r, trapezoidal slot wedge with depth d_{is}, a slot opening with depth d_{os}, and slot liner with thickness d_{ls}. A_s and the desired number of turns in Table 3 can then estimate the number of wire stands per turn.

$$t_s = \frac{\pi D_{is}}{S_1 k_{is}} \left(\frac{B_{g1}}{B_{ts}}\right) \left(\frac{l_e}{l_i}\right) \tag{3-2}$$

$$b_1 = \frac{\pi}{S_1}\left[D_{is}\left(1 - \frac{B_{g1}}{k_{is}B_{ts}}\frac{l_e}{l_i}\right) + 2(d_{os} + d_{is})\right]$$

$$b_2 = \frac{\pi}{S_1}\left[D_{os} - D_{is}\left(\frac{B_{g1}}{k_{is}B_{ts}}\frac{l_e}{l_i} + \frac{2}{P}\frac{B_{g1}}{k_{is}B_{cs}}\frac{l_e}{l_i}\right) - 2r\right]$$

$$d_s = \frac{S_1}{2\pi}(b_2 - b_1) \tag{3-3}$$

$$A_s = \frac{d_s - d_{sl}}{2}[(b_1 - 2d_{sl}) + (b_2 - 2d_{sl})] \tag{3-4}$$

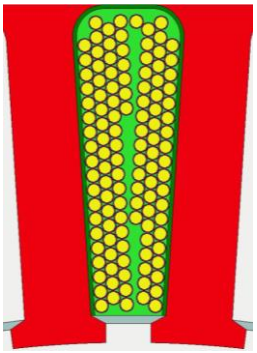

Figure 14: Slot Geometry of the Reference Nissan Leaf Motor

As in (3-1), the only unknown quantities in (3-2) – (3-4) are estimates for B_{ts}, B_{cs}, and B_{g1}, but together, (3-1) – (3-4) entirely defines the stator geometry in this limited design space. Therefore, knowledge of B_{ts}, B_{cs}, and B_{g1} can optimally define the radial cross-section of the stator geometry in this limited design space using (3-1) – (3-4). The calculated λ then dictates rotor OD D_{or} for the air gap length specified in Table 3. Hence, estimated B_{ts}, B_{cs}, and B_{g1} are used as optimization inputs. As a result, the only geometric variables left to define are the motor length and the magnet geometry.

Table 4 shows the input design space, including the values of B_{ts}, B_{cs}, and B_{g1} used in (3-1) – (3-4) above. The ranges of maximum B_{ts} and B_{cs} are selected to limit their values to 1.9 T and 1.7 T according to the recommendations in [9], [10], [11] based on the saturation point of silicon steel. Although they are within the regime of highly non-linear B-H curves for typical electrical steels, the results will show these high flux densities roughly match the reference design and do not degrade efficiency. Equations (3-1) – (3-4) explained above are only approximations, and the author observed that they tended to slightly overestimate B_{ts} and B_{cs}, so the input ranges in Table 4 for these flux densities include values greater than their respective limits. Constraints discussed later will ensure the actual values B_{ts} and B_{cs} calculated using FEA and ROMs do not exceed their limits of 1.9 T and 1.7 T.

Selecting a range for B_{g1} is not as straightforward. When using multiple magnet layers in an IPMSM, B_{g1} can often exceed the PM B_r [11], but it is difficult to analytically predict this parameter for the IPMSM in the general case [68]. Instead, the authors used the range listed in Table 4 based on trends observed while performing the sensitivity study to build the ROMs. However, I_s, J_s, K_s, and k_{cu} also constrain this input.

Table 4: Range of Input Parameters for the Initial MnBi IPMSM (MnBi IPMSM1)

Input	Color in Figure 15	Range
Stator Length Adjustment Factor, x_{ls}	N/A	0.44 – 0.46
Air gap Flux Density at I_{pk}, $B_{g1,RMS}$	N/A	0.69 – 0.71 T
Max Tooth Flux Density, B_{ts}	N/A	1.85-1.95 T
Max Core Flux Density, B_{cs}	N/A	1.65-1.75 T
Pole Arc Ratios, r_{pa1}, r_{pa2}	Orange	(L1) 0.785 – 0.959 (L2) 0.725 – 0.886
Pole Angles, θ_{p1}, θ_{p2}	Blue	(L1) 111.6 – 136.4° (L2) 162 – 180°
Magnet Thicknesses, t_{m1}, t_{m2}	Yellow	(L1) 2.34 – 3.38 mm (L2) 3.47 – 5.02 mm
Bridge Thicknesses, t_{b1}, t_{b2}	Red	(L1) 6.88 – 8.41 mm (L2) 3.47 – 5.02 mm
DC Link Voltage, V_{DC}	N/A	500 – 550 V

Next, the D3L sizing equation in (2-7) can also use the information described above to solve for the final stator geometric parameter: the stator length l_{is}. The only remaining unknown variables in this equation are η_{gap}, $\cos(\theta_{gap})$, and l_e. Winding loss and stator core loss dominate in IPMSMs, so $\eta_{gap} \cong 1$ because this efficiency is measured neglecting stator losses. However, the power factor at the air gap (i.e., neglecting stator losses), $\cos(\theta_{gap})$, is difficult to predict, like B_{g1}. Instead, this variable is estimated to be equal to the stator length adjustment factor x_{ls} in Table 4. As such, this variable can account for a changing $\cos(\theta_{gap})$ and discrepancies between B_{g1} and the rotor PM geometry for a particular design. After choosing $T_{D3L} = T_{pk}$, rearranging (2-7) can solve for effective motor length l_e. In the reference design, l_e is approximately the average of the rotor length l_r and stator length l_s, so the author assumes $l_s = l_r + 10\ mm$. Hence, $l_s = l_e + 5\ mm$ and $l_r = l_e - 5\ mm$. The same 10 mm difference between l_r and l_s is used in all MnBi PMSMs presented in Objective 1 and Objective 2.

The PM geometric variables are the only remaining geometric inputs in Table 4 to discuss. Figure 15 illustrates all possible radial geometric variables used throughout Objective 1. The colors next to each PM geometric variable in Table 4 correspond to the color-coded arrows in Figure 15 that illustrate their physical significance. Ratios are used instead of physical dimensions, when possible, to prevent geometric conflicts. This initial design only directly considers the pole arc ratios (r_{pa1}, r_{pa2}, orange arrow), pole angles (θ_{p1}, θ_{p2}, blue arrows), magnet thickness (t_{m1}, t_{m2}, yellow arrows), and bridge thickness (t_{b1}, t_{b2}, red arrows). There are two values for each PM geometric variable, one for the outer magnet layer (Layer 1, or L1), and one for the inner magnet layer (Layer 2, or L2). The number in the subscripts for these variables corresponds to the magnet layer that variable represents. The white arrow is the tooth width t_s and the grey arrow is the slot depth d_s. Similarly, the green line is the stator ID D_{is} representing the split ratio λ in this case because the stator OD D_{os} is constant. These three variables (t_s, d_s, and λ) are determined by (3-1) – (3-4).

The magnet width ratio (pink arrow) is width of the magnets (green rectangle), whereas the pole arc ratio determines the width of the white air pockets containing the magnets (sometimes referred to as flux barriers). Generally, the magnet width should be as large as possible to maximize B_{g1}, so these values are left equal to the values in the reference design, in which case the magnets are about as wide as can fit in the flux barriers. The post thicknesses (black arrows) are equal to 0 mm in this initial design to match the reference design in Figure 2 initially. The final design will consider all variables depicted in Figure 15 directly.

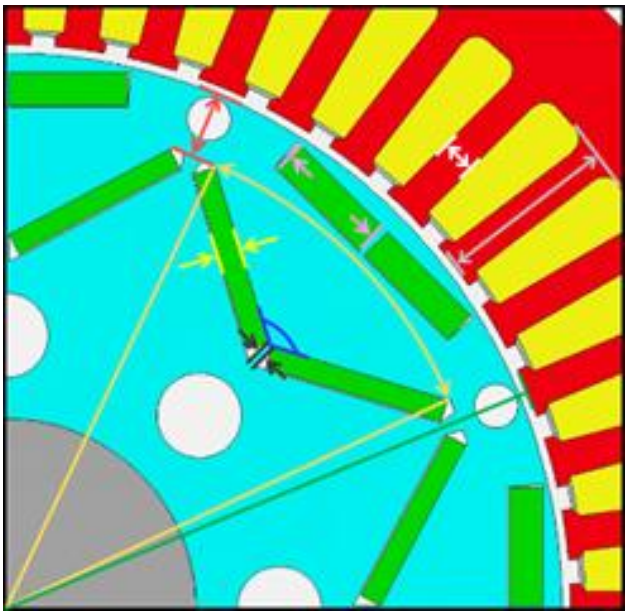

Figure 15: Radial geometric optimization inputs for MnBi IPMSM

Finally, the DC link voltage is also increased to compensate for the lower power factor of the MnBi IPMSM compared to the reference design, as described earlier in Section 2.5 and Section 3.1. This is a notable increase compared to the 375 V DC link used in the reference design, but this weakness will be addressed in Objective 2.

3.2.2 Optimization Objectives

The objectives are to minimize the weight, W, maximize the short circuit current, I_{SC}, and maximize the average efficiency over the WLTP3 drive cycle, η. The Worldwide Harmonized Light Vehicle Test Procedures (WLTP) are global, standardized drive cycles that evaluate urban, suburban, rural, and highway driving, and of the three WLTP drive cycles, WLTP3 [69] is intended for the highest power light vehicles (i.e., passenger vehicles). The short circuit current is maximized in an attempt to produce constant power above base speed, where I_{SC} is the ratio of the PM flux linkage, ψ_f, to the d-axis inductance, L_d, shown in (2-24). As explained in Section

2.5, IPMSMs must have an I_{SC} near the maximum stator current to achieve constant power behavior above base speed at the maximum current. This is well-documented in [17], [18], [38], [39]. The author observed that all MnBi designs produced by the optimization routine have $I_{SC} < I_{rt}$. Hence, maximizing I_{SC} favors designs with the best constant power behavior, as shown in [38], [39].

3.2.3 Optimization Constraints

Table 5 shows the constraints used. Those related to the motor speed, torque, or power are added in an attempt to match the capability curves of the reference motor. Constraints related to B_{ts} and B_{cs} were introduced in Section 3.2.1 and are related to the saturation point of electrical steel and machine design recommendations in [9], [10], [11]. The final two constraints relate to mechanical limitations. The "aspect ratio" is the ratio of the rotor length l_r and rotor outer radius r_{or}. While a high aspect ratio is desirable to minimize volume/weight [10], it must be limited to less than 7 to avoid the first critical rotation speed of a solid steel rotor [11] and to ensure there is adequate cooling surface area [10]. Here, the aspect ratio is therefore limited to less than 5 to ensure an adequate safety margin in absence of a more detailed mechanical and thermal analysis. All designs simulated as a part of this optimization routine have aspect ratios well below this limit. Lastly, the torque ripple is limited to below 10% to limit mechanical vibrations in the motor.

Table 5: Optimization Constraints for the Initial MnBi Design (MnBi IPMSM1)

Parameter	Constraints
Peak Torque, T_{pk} (Nm)	$280 \leq T_{pk} \leq 290$
Continuous Torque, T_{rt} (Nm)	$157 \leq T_{rt}$
Peak Power, P_{pk} (kW)	$125 \leq P_{pk}$
Continuous Power, P_{rt} (kW)	$80 \leq P_{rt} \leq 90$
Min. Speed at P_{pk}, n_{pk} (kRPM)	$4 \leq n_{pk}$
Min. Speed at P_{rt}, n_{rt} (kRPM)	$4 \leq n_{rt}$
Max Tooth Flux Density, B_{ts} (T)	$B_{ts} \leq 1.9$
Max Core Flux Density, B_{cs} (T)	$B_{cs} < 1.7$
Aspect Ratio, l_r/r_{or}	$l_r/r_{or} < 5$
Torque Ripple, T_{rip} (%)	$T_{rip} < 10$

3.2.4 Reduced Order Model Accuracy

The coefficient of prognosis (COP) matrix in Table 6 quantifies the effect of each statistically significant input on each ROM output. The COP is a measure of ROM accuracy and behaves similarly to a coefficient of determination (R^2) in statistics. A COP has a maximum value of 100% and a minimum value of 0%. Each row column represents an input, and each column represents an output, where a higher COP percentage means the input in that column has a larger impact on the output in that row. The sum in the rightmost column represents how much of the outputs' variability can be predicted by the metamodel, with a maximum sum of 100%. More details can be found in [66]. As an example, the COP matrix in Table 6 shows that x_{ls} has the greatest impact on the volume, V, and weight, W, almost entirely dictating these outputs. This makes sense because ultimately x_{ls} determines the stator length according to the sizing equation analysis in Section 3.2.1. This input also impacts torque, again in agreement with the sizing equations. However, the rotor PM geometry, represented collectively by the leftmost eight

inputs, has a greater impact. A similar conclusion applies to the power P_{pk}, except the V_{DC} input is most significant for this output.

Table 6: COP Matrix for the Reduced Order Model Used in the Initial IPMSM Optimization

	L1 Bridge Thick.	L1 Mag. Thick.	L1 Pole Arc	L1 Pole Angle	L2 Bridge Thick.	L2 Mag. Thick.	L2 Pole Arc	L2 Pole Angle	B_{g1}	x_{ls}	V_{DC}	Sum
W	0.000	0.000	0.004	0.000	0.000	0.000	0.028	0.000	0.038	0.948	0.000	0.998
η	0.337	0.028	0.190	0.032	0.012	0.011	0.456	0.000	0.000	0.016	0.000	0.980
T_{rip}	0.000	0.000	0.000	0.000	0.000	0.066	0.925	0.000	0.000	0.000	0.000	0.931
T_{rt}	0.179	0.030	0.329	0.017	0.017	0.131	0.123	0.030	0.012	0.163	0.000	0.952
n_{rt}	0.201	0.041	0.054	0.005	0.000	0.248	0.178	0.069	0.000	0.035	0.180	0.966
P_{rt}	0.192	0.038	0.129	0.010	0.007	0.216	0.060	0.017	0.000	0.000	0.337	0.962
T_{pk}	0.173	0.055	0.346	0.020	0.000	0.184	0.061	0.031	0.000	0.152	0.000	0.954
n_{pk}	0.037	0.024	0.036	0.000	0.000	0.176	0.094	0.066	0.000	0.102	0.488	0.990
P_{pk}	0.147	0.052	0.144	0.000	0.000	0.270	0.064	0.015	0.000	0.000	0.312	0.971
I_{SC}	0.241	0.054	0.072	0.008	0.019	0.522	0.044	0.077	0.000	0.000	0.000	0.964
V	0.000	0.000	0.000	0.000	0.000	0.000	0.000	0.000	0.069	0.930	0.000	1.000

3.3 Initial MnBi IPMSM Design without Magnet Posts

The author used only one iteration of the optimization routine depicted Figure 13 to produce the initial MnBi IPMSM design presented in this section to quickly assess the viability of MnBi in EV traction motors before attempting more detailed designs. In multi-objective optimization, a Pareto optimal front represents tradeoffs among the competing objectives, depicting all designs with an optimal combination of objectives according to the user-defined fitness function. All designs on the Pareto optimal front are considered optimal.

Figure 16 shows the Pareto optimal front after the single iteration determined using the ROM, and 400 designs were used to construct the ROM in Table 6. Outputs for 10,000 designs were calculated during optimization using the ROM, and the GA was the optimization algorithm used. A subset of 20 Pareto optimal designs are validated in FEA after optimization. While not all validated designs obey the constraints in Table 5, Section 3.3 will demonstrate that successive

iterations improve ROM accuracy such that all designs validated in FEA are feasible without significantly impacting the Pareto optimal front. However, this can require several time-consuming iterations depending on the considered constraints. Note that in the context of optimization routines, feasible designs are defined as designs which obey all constraints, by definition. Here, all 20 validated designs are modeled in FEA, but not all validated designs remain feasible according to FEA due to ROM inaccuracy.

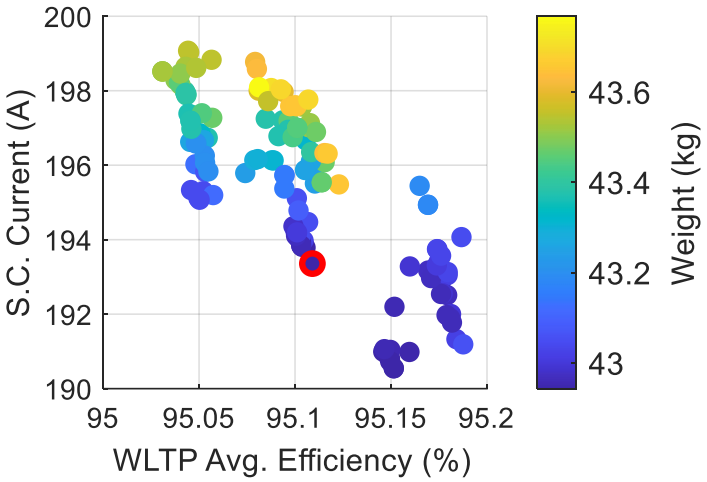

Figure 16: Pareto optimal front for the initial MnBi IPMSM1 design optimization

Of the 20 validated designs selected from Figure 13, the design circled in red (Design 9872) has the lowest weight of the feasible, validated designs. Table 7 shows relevant design metrics for the reference NdFeB Leaf motor in comparison to this optimal MnBi IPMSM design 9872. Here, IPMSM1 refers to IPMSM designs produced by this initial optimization attempt that do not have magnet posts. In later sections, IPMSM2 will refer to IPMSM designs with magnet posts. All values in Table 7 are calculated with a magnet temperature of 65°C. The author consider weight as the most important objective and thus selected MnBi design number 9872 because it was the lightest Pareto optimal design validated and feasible in FEA. Figure 17 shows radial and axial cross-sections of this MnBi design. This MnBi IPMSM1 has an active volume of

6.59, or about 1.34 times larger than the active volume of the reference motor (4.92 L). The weight increases by a similar margin.

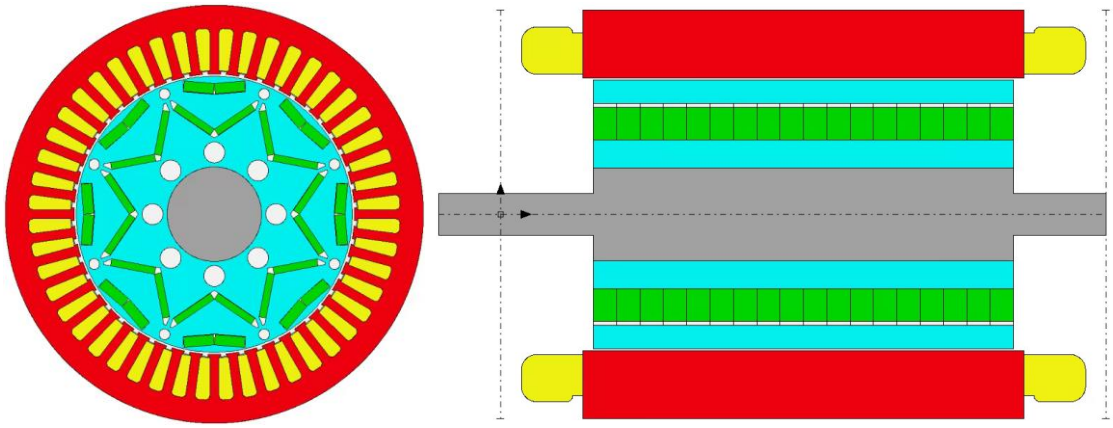

(**a**) (**b**)

Figure 17: (a) Radial and (b) Axial Cross-section of An Optimal MnBi IPMSM1 – Number 9872

While the MnBi design uses much more material by weight, the estimated magnet cost is 68% lower, so the total material cost is 25.6% lower in the MnBi IPMSM1 compared to the NdFeB reference (using $70/kg [53], $11/kg [15], $2.2/kg [52] and $9.5/kg [70] for NdFeB, MnBi, electrical steel, and copper, respectively). If using $26/kg for MnBi [51], the MnBi IPMSM1 Design #9872 $246.30, about 1.7% less than the Leaf motor. The MnBi IPMSM1 is less expensive despite being larger and heavier because MnBi is significantly less expensive per kg than NdFeB PMs, and the magnets represent most of the total material cost for the Leaf motor in Table 7. Note that the analysis in Table 7 ignores the price volatility of NdFeB, a key disadvantage compared to MnBi. For example, using a price five times higher than the current estimated cost of $70/kg [53] for NdFeB, the reference design magnet cost becomes $687 yielding a total motor cost of $800. MnBi design #9872 then reduces magnet and total cost by 93.61% and 76.73%, respectively, using $11/kg for MnBi. These values are different than the values reported by the author in [50] due to typographical errors in [50].

Table 7: Comparing initial MnBi IPMSM1 to the NdFeB Leaf Reference

	Metric			NdFeB Leaf IPMSM	MnBi IPMSM1 Design #9872 (Lightest)	
					Value	Δ
Geometry	Stator OD, mm			198	198	0.0%
	Rotor OD, mm			130	130.7	0.5%
	Active Length, mm			160	214.0	33.8%
	Active Volume, L			4.93	6.59	33.8%
	Weight (without shaft), kg			31.9	42.7	33.6%
	Magnet Weight, kg			1.97	4.00	103.3%
	Steel Weigth (without shaft), kg			23.5	30.8	31.0%
	Copper Weight, kg			6.45	7.86	21.9%
	Total Cost (whtout shaft), $			250.5	186.4	-25.6%
	Magnet Cost, $			137.6	44.0	-68.0%
	Steel Cost (without shaft), $			51.7	67.7	31.0%
	Copper Cost, $			61.3	74.7	21.9%
	Slot Copper Fill Factor			0.52	0.52	0.0%
Performance	Maximum Speed, RPM			10,000	6,250	-37.5%
	Torque, Nm (65°C)	*0 RPM*	*Rated Current*	160.1	166.7	4.1%
		0 RPM	*Peak Current*	280.5	300.6	7.1%
	Power, kW (65°C)	*Max*	*Rated Current*	83.8	93.01	11.0%
		Max	*Peak Current*	132.1	130.6	-1.2%
		10k RPM	*Rated Current*	79.4243	90.9075	14.5%
		10k RPM	*Peak Current*	124.9	92.3524	-26.0%
	Average Drive Cycle Efficiency, % (65°C)	*WLTP3*		93.7	95.6	1.9%
		UDDS		93.8	95.1	1.4%
		US06		94.2	95.5	1.4%
		HWFET		91.6	95.3	4.0%
	Losses, W (1000 RPM, 150 Nm, 65°C)	*Copper*		1161	1344.0	15.8%
		Steel		143.9	180.1	25.2%
		Magnet		0.191	0.006	-96.9%
Electrical	DC Link Voltage, V			375	500	33.3%
	Current, A	*Rated*		267	267	0.0%
		Peak		480	480	0.0%
	Power Factor at Terminals, 1000 RPM			0.788	0.682	-13.5%
	Slot Current Density, Arms/mm^2			16.88	16.88	0.0%
	Peak Electric Loading, kArms/m			117.9	117.3	-0.5%
	Saturated d-axis Inductance, mH			0.162	0.230	42.1%
	Saturated q-axis Inductance, mH			0.376	0.509	35.1%
	Saturated Saliency Ratio			2.326	2.212	-4.9%
	Saturated S.C. Current, A (65°C)			353.8	167.4	-52.7%
Magnetic	Magnetic Loading, T	*Rated Current*		0.905	0.779	-13.9%
		Peak Current		1.006	0.933	-7.3%
	Max Flux Density, T	*Rated Current*	*Tooth*	1.677	1.633	-2.6%
			Tooth Tip	1.670	1.616	-3.2%
			Core	1.383	1.359	-1.7%
		Peak Current	*Tooth*	1.898	1.863	-1.8%
			Tooth Tip	1.906	1.950	2.3%
			Core	1.681	1.644	-2.2%
Mechanical	Torque Ripple, %			6.20	6.10	-1.7%
	Rotor Aspect Ratio			2.31	3.12	35.3%
	Max Stress at 12,000 RPM, Mpa			532.5	1342	152.0%

Assuming $n_r \cong 1$ because the stator copper and iron losses dominate the losses, substituting the results from Table 7 into the D3L sizing equation in (2-7) yields predicted torques of 268.57 Nm and 292.71 Nm for the NdFeB and MnBi designs, respectively. These values are roughly in agreement with the results from Table 7, offering evidence regarding the precision of the optimization method used here. The power factor at the motor terminals as calculated in Motor-CAD is used for $\cos(\theta_{gap})$ as an estimate, although the D3L sizing equation neglects stator losses in this calculation.

Figure 18 shows the power and torque vs. speed for both the rated current and the peak current at a magnet temperature of 100°C for both designs. As shown in Table 7, the short circuit current is much lower in the MnBi IPMSM1 compared to the Leaf motor. This occurs because using MnBi decreases the magnetic loading (hence the PM flux linkage) while L_d increases (possibly because the motor steel saturates in the MnBi design than the NdFeB design, suggested by the flux density values listed in Table 7). The shape of the power curves in Figure 18 match expectations when decreasing PM flux linkage and increasing the d-axis inductance without changing saliency ratio according to the analysis in Section 2.5. Constant power behavior above base speed at peak current can be improved by increasing the short circuit current. The author achieves this using a PMASynRM topology for Objective 2 in Section 4.0. Changing winding parameters, such as the number of turns, may also decrease L_d to improve constant power behavior, but this must be done carefully as it will affect, among other things, K_s and J_s according to (2-1). The DC link voltage is increased relative to the reference design to reach desired peak power in Table 3, but this will only increase the peak of the curve without changing the general shape.

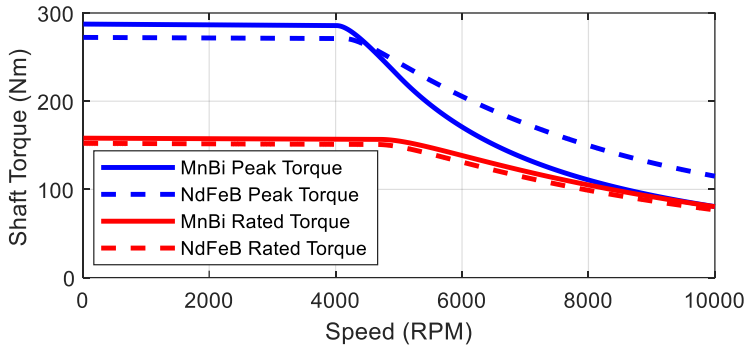

(a)

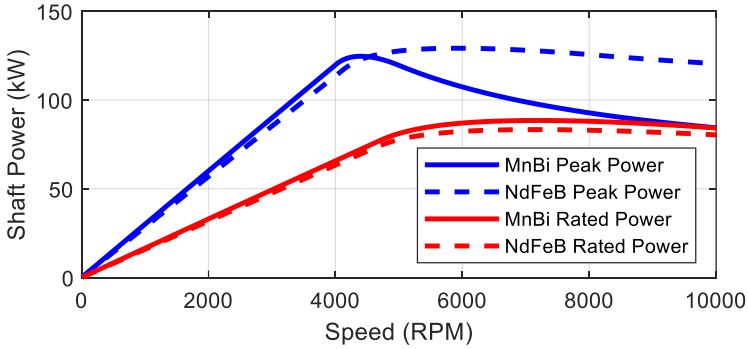

(b)

Figure 18: (a) Torque and (b) Power vs Speed for the NdFeB Leaf and MnBi IPMSM1 Designs

Figure 19 and Figure 20 show the efficiency maps for both motors with the operating points of the four drive cycles tested in Table 7. The magnet temperature is 100°C, and the mass of the modeled vehicle is equal to the curb weight of the 2011 Nissan Leaf (1521 kg). The MnBi design has a higher average efficiency over each of the drive cycles (white – WLTP3 [69], blue – UDDS [71], magenta – US06 [71], cyan – HWFET [71]). The figures suggest that average efficiency is higher for the MnBi motor because it has a higher efficiency at low-torque operating points, which make up a majority of the drive cycles. Further analysis would reveal the low-torque efficiency improvement is due to a general decrease in flux density observed in the MnBi design relative to NdFeB, thereby lowering core losses.

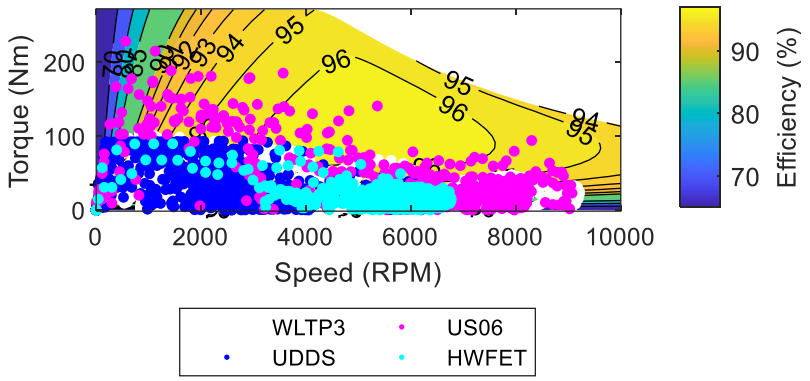

Figure 19: Efficiency map and drive cycle operating points for the NdFeB Leaf motor

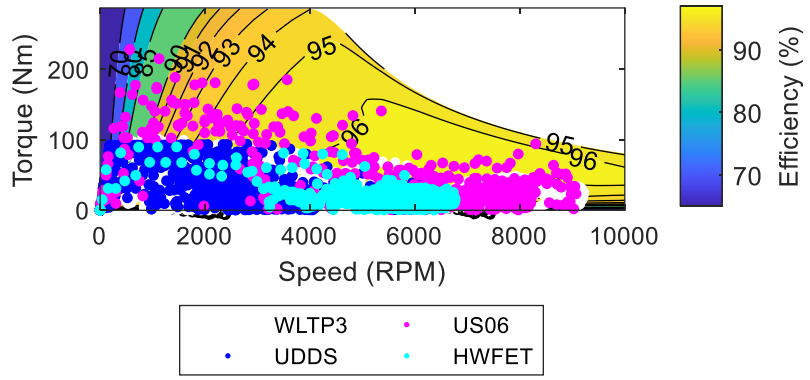

Figure 20: Efficiency map and drive cycle operating points for MnBi IPMSM1 design 9872

Next, the mechanical validation of the design. Figure 21 shows that the two designs have comparable torque ripples (6.20% and 6.10% in the NdFeB and MnBi designs, respectively). While the length of the MnBi motor is higher, the aspect ratio (2.31 and 3.12 in the NdFeB and MnBi designs, respectively) is still sufficiently low to avoid the first critical rotation speed of a solid steel rotor [11]. A higher aspect ratio decreases the rotor moment of inertia, but increasing the aspect ratio will increase K_s for a given volume, which can make cooling challenging [10]. Even so, thermal results presented in the remaining paragraphs will show satisfactory temperature rise.

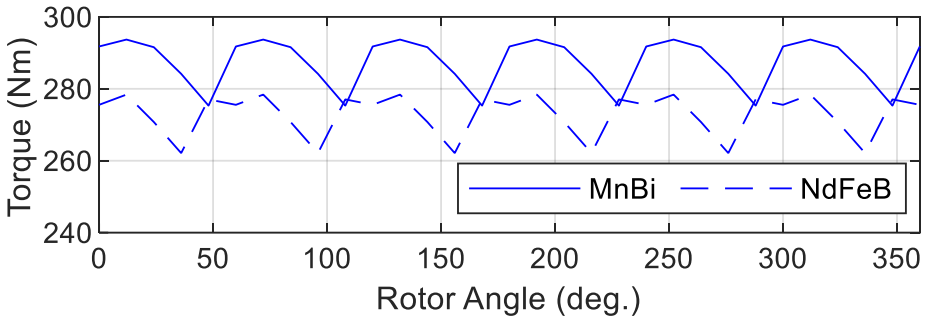

Figure 21: Torque ripple for the NdFeB Leaf (dashed line) and MnBi IPMSM1 design 9872 (solid line)

It should also be noted that the mechanical stress on the rotor bridges is significantly higher in the MnBi design than the NdFeB design, shown in Table 7. This occurs because the MnBi IPMSM1 requires more magnet mass than the Leaf motor due to the material properties of MnBi compared to NdFeB. In particular, the MnBi IPMSM1 uses wider magnets to increase magnet cross-sectional area due to the lower remanent flux density. Additionally, it uses thicker magnets to reduce demagnetization risk due to the lower coercivity. Furthermore, the density of MnBi is estimated as 9000 kg/m^3 compared to 7500 kg/m^3 for N30UH grade NdFeB. The added magnet mass with approximately the same rotor bridge thickness leads to higher mechanical stress in the MnBi IPMSM1. Section 3.3 and Section 3.4 will address the excessive rotor mechanical stress by adding magnet posts to the geometry.

To validate the design thermally, Figure 22 shows the temperature rise of the critical components in the Leaf and MnBi IPMSM1 during a step change in torque from 0 to 150 Nm at a shaft speed of 1000 RPM (e.g. near the maximum continuous torque of the motor). While the MnBi motor actually has *more* losses than the reference motor at this operating point (suggested by the larger temperature rise for the coolant outlet and confirmed in FEA), the windings and magnets have a lower temperature rise in the MnBi motor compared to the NdFeB motor, whle the bearing temperature rise only increases by 1.4°C. The lower temperature rise in the windings and magnets despite higher losses is likely because increasing stator length increases cooling

surface area. Because the winding temperatures in the MnBi design do not reach the limits of the reference design, the coolant temprature or flow rate may be altered to ease thermal management requirments if bearing temperature remains sufficiently low.

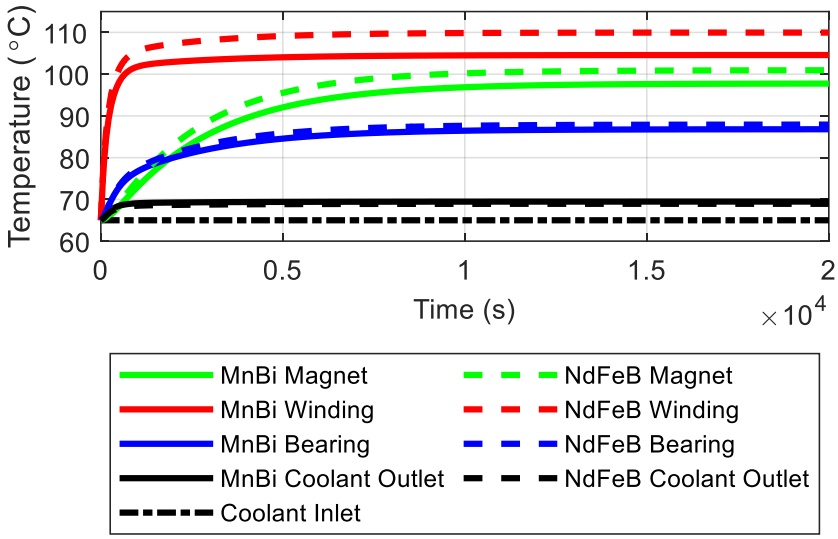

Figure 22: Temperature rise comparison for the NdFeB Leaf design and MnBi IPMSM1 design 9872

To demonstrate the advantage of high temperature operation when using MnBi, Figure 23 shows contours which enclose the current operating points that do not lead to irreversible demagnetization as temperature changes. These contours are based on the demagnetization ratio calculated by Motor-CAD, which is the ratio of PM finite elements that irreversibly demagnetizes to the total number of PM finite elements. The pink shaded region enclosed by the pink contours represents the operating points that do not lead to irreversible demagnetization at 30°C. Contours with different colors are calculated with different PM temperatures to show how PM temperature affects irreversible demagnetization risk, with the boundaries expanding leftward as temperature increases, denoted by the similarly color-coded arrows.

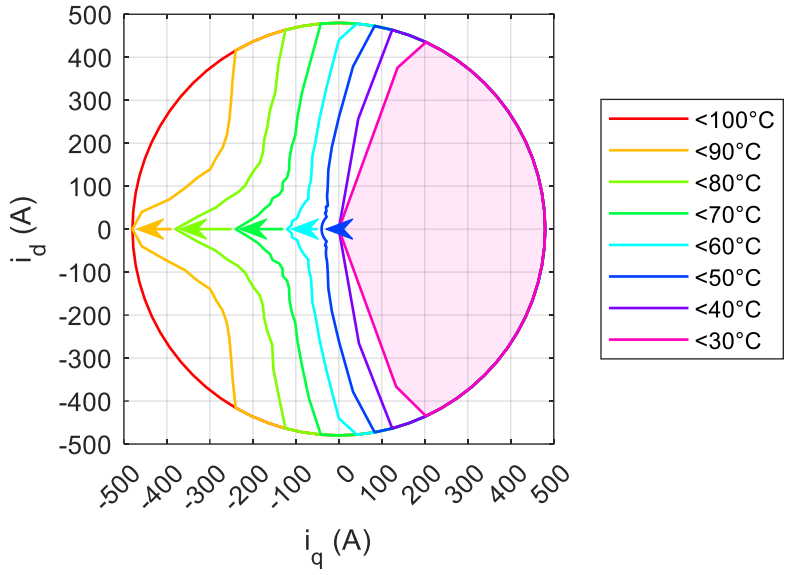

Figure 23: The safe operating regions without risk of irreversible demagnetization as temperature changes for MnBi IPMSM1 design 9872

In essence, contours that enclose larger areas in the dq current plane and areas with operating points that require higher magnitude of stator current show less irreversible demagnetization risk (i.e., less restriction on what current operating points damage PMs). Note that the second quadrant in the dq-plane below where a motor typically operates to obtain positive speed and torque as described in Section 2.5.1. The contours enclose larger and larger regions as temperature increases, so Figure 23 shows that there is less risk of demagnetizing the PMs at high temperatures when using MnBi.

For example, the pink shaded region represents all current operating points that do not lead to irreversible demagnetization at a PM temperature of 30°C. Then, as PM temperature increases, the left edge expands leftward following the color-coded arrows, leading to a larger area of safe operating points. Notably, the results in Figure 23 suggest that the MnBi IPMSM demagnetizes with *no current* (i.e., open circuit) at temperatures below 40°C. Some refer to this phenomenon as "self-demagnetization" in REE-free PMSMs [72]. Along with the excessive

rotor lamination stress, this excessive low temperature demagnetization risk makes this MnBi IPMSM design impractical. The remainder of this section now addresses these two weaknesses. For reference, the MnBi IPMSM maximum speed must be lowered to about 6,250 RPM (7,500 RPM overspeed) to lower the stress to the same value as the Leaf motor, shown in Table 7.

3.4 Improved Optimization Routine Considering Low Temperature Irreversible Demagnetization

Section 3.4 and 3.5 will now address the excessive rotor stress (i.e., shown at the bottom of Table 7) and low temperature demagnetization risk (i.e., shown in Figure 23) by including magnet posts (i.e., black arrows in Figure 15) in the design, as suggested by other sources [32], [47]. Comparing the MnBi IPMSM designs with and without magnet posts provides a unique opportunity to directly study the effect of magnet posts on electromagnetic performance, where electromagnetic performance degradation is expected because the magnet posts add leakage permeance. This tradeoff also applies to the rotor bridges (i.e., red arrows in Figure 15), where thicker bridges protect the magnets mechanically and magnetically but add leakage permeance that degrade electromagnetic performance [32], [61]. Therefore, post and bridge thickness must be optimized carefully in RE-free machines. While literature suggests these posts lower demagnetization risk and rotor lamination stress with only slight torque density degradation due to added leakage permeance, few sources, if any, demonstrate this with a one-to-one comparison between IPMSM designs with (IPMSM2 here) and without magnet posts (IPMSM1 above).

Table 8: MnBi IPMSM2 Design Specifications Based on the 2011/2012 Nissan Leaf NdFeB IPMSM

Input	Range
Phases, m	3
Slots, S	48
Poles, P	8
Number of Series Turns Per Phase, N_s	24 (2 paths)
Stator OD, D_{os}	198 mm
Air gap, g	1 mm
Base Speed, n_b	4000 RPM
Maximum Speed, n_{MAX}	10,000 RPM
Rated Current, I_{rt}	267 A
Peak Current, I_{pk}	480 A
Rated Power, P_{rt}	80 kW
Peak Power, P_{pk}	120 kW
Rated Torque, T_{rt}	160 Nm
Peak Torque, T_{pk}	280 Nm
Rated Slot Current Density (J_s), J_{rt}	9.39 A_{rms}/mm^2
Peak Slot Current Density (J_s), J_{pk}	16.88 A_{rms}/mm^2
Rated Electric Loading (K_s), K_{rt}	65.56 A_{rms}/mm
Peak Electric Loading (K_s), K_{pk}	117.9 A_{rms}/mm
First Critical PM Temperature, T_{PM1}	100 °C
Second Critical PM Temperature, T_{PM2}	0 °C
Maximum Current at T_{PM2}, I_{PM2}	267 A

Table 8 shows the design specifications for MnBi IMPSM2. All entries match those used in the initial MnBi IPMSM1 design except the last two rows. Most FEA calculations in the sensitivity study still occur at a maximum magnet temperature (T_{PM1}) of 100°C because this yields the best performance for MnBi. However, the check for irreversible demagnetization occurs at a minimum temperature (T_{PM2}) of 0°C because EV motors often cannot avoid starting at such temperatures (where losses then increase temperature over time). Testing at lower

temperatures would be better suited for EV applications, but T_{PM2} is limited by the availability of empirical MnBi B-H data, as explained in Section 2.3. To obtain competitive designs, peak current is limited to rated current (I_{rt}) at T_{PM2}, and the current phase is limited to being in-phase with the winding back EMF (i.e., entirely on the quadrature axis). The control scheme developed for Objective 3 in Section 5.0 will ensure the current is limited appropriately under normal operating conditions, and work from other groups suggests that appropriate motor drive design can ensure the current is limited under numerous different fault conditions [19], and others suggest control schemes prevent irreversible demagnetization during motor faults [20], [21], [22].

3.4.1 Input Free Variables

Table 9 lists the input free variables for the optimization and their respective initial ranges for this study. Now having a baseline MnBi IPMSM design from Section 3.3 to reference, the stator geometric variables (i.e., split ratio λ, tooth width ratio r_{tw}, and slot depth ratio r_{sd}) are used directly rather than deriving them using the sizing equation approach explained in Section 3.2. This is done to explore other combinations of tooth widths (r_{tw}) and slot widths (r_{sd}) that yield lower stator tooth and core flux densities (B_{ts} and B_{cs}, respectively) because the IPMSM1 optimization preferred lower flux densities than expected based on intuition from [9]. Specifically, [9] predicts that RE-free PMSMs will better leverage the trade-off between electric and magnetic loading by using thinner teeth and wider slots, but the IPMSM1 designs preferred wider teeth and thinner slots than the reference design. Constraints in the next subsection limit the maximum B_{ts} and B_{cs}, rather than using them as inputs, to maintain similar efficiency and temperature rise as the reference design.

Table 9: Ranges of Optimization Inputs for the Final MnBi IPMSM (MnBi IPSM2)

#	Optimization Input	Figure 15 Color	Initial Range
1, 2	Post Thickness, t_{p1}, t_{p2}	Black	0.6 – 0.8 mm
3	Tooth Width Ratio, r_{tw}	White	0.4 – 0.5
4	Slot Depth Ratio, r_{sd}	Grey	0.6413 – 0.69
5	Stator ID/OD Ratio, λ	Green	0.6667 – 0.675
6, 7	Magnet Thickness, t_{m1}, t_{m2}	Orange	(t_{m1}) 3.2 – 5 (t_{m2}) 4.8 – 6
8, 9	Magnet Width Ratio, r_{m1}, r_{m2}	Pink	(r_{m1}) 0.9 – 0.99 (r_{m2}) 0.6 – 0.75
10, 11	Bridge Thickness, t_{b1}, t_{b2}	Red	(t_{b1}) 6.9 – 8.4 (t_{b2}) 0.6 – 0.9
12, 13	Pole Arc Ratio, r_{pa1}, r_{pa2}	Orange	(r_{pa1}) 0.9 – 0.99 (r_{pa2}) 0.8 – 0.935
14, 15	Pole Angle, θ_{p1}, θ_{p2}	Blue	(θ_{p1}) 111° – 136° (θ_{p2}) 170° – 180°
16	DC Link Voltage, V_{DC}	N/A	500 – 550 V
17	Stator Length, l_{is}	N/A	180 – 260 mm

Once again, geometric ratios based on maximum values as calculated by Motor-CAD are used for some inputs, rather than physical dimensions, to avoid unnecessary geometric conflicts (e.g. tooth width greater than slot pitch, larger magnets than the space available in one rotor pole, etc.). Figure 15 shows most inputs from Table 9. Post thicknesses (t_{pL}), magnet thicknesses (t_{mL}), magnet length ratios (r_{mL}), bridge thicknesses (t_{bL}), pole arc ratios (r_{paL}), and pole angles (θ_{pL}) have different values for each layer, with the inner and outer magnet layers corresponding to $L = 1$ and $L = 2$, respectively. Because the posts serve a similar purpose as the bridges, initial ranges of t_{pL} are based on the ranges for t_{b2} (the ducts require much larger t_{b1}) in the reference design. Radial cross-sections cannot depict the DC link voltage (V_{DC}) and stator length (l_{is}) and thus are excluded from Figure 15, but their ranges are selected based on the ranges in the initial optimization, although expanded due to the added leakage paths from the magnet posts. Added

leakage permeance decreases power factor, so torque and power density are expected to decrease in the IPMSM2 compared to the IPMSM1 according to the D3L sizing equations. Increasing l_{is} and V_{DC} compensates for the decreased power and torque density.

3.4.2 Objectives

The first two objectives are to minimize weight (W) and maximize short circuit current (I_{SC}), as in the initial MnBi IMPSM1. All designs from the initial MnBi IPMSM1 optimization achieved a drive cycle efficiency η significantly greater than the value required by Constraint 12 in Table 10 due to lower B_{ts}, lower B_{cs}, and higher PM resistivity in the MnBi design. However, the initial optimization routine had difficulty obtaining adequate rated torque T_{rt}. Therefore, the authors choose to maximize T_{rt} here instead of η as the third objective to explore designs with thinner teeth and lower efficiency.

3.4.3 Constraints

Table 10 summarizes the constraints for the MnBi IPMSM2. Most of these constraints are included in the initial design (see Table 5), except Constraints 7, 8, 9, 12 13, 14 and 17 are added based on the results from the initial optimization. Constraint 7 limits the estimated material cost (USD) to be less than the cost estimated in Table 7 for the Leaf motor. Constraints 8 and 9 are added to limit temperature rise now that t_s and d_s vary independent of the sizing equation analysis in 3.2.1. Constraint 12 limits the average efficiency over the WLPT3 drive cycle (η) to greater than the drive cycle efficiency calculated for the Leaf motor because η is no

longer used as an objective. Constraints for T_{rt}, T_{pk}, P_{rt}, and P_{pk} are also relaxed to consider a larger design space.

Table 10: Optimization Constraints for the Final MnBi IPMSM (MnBi IPMSM2)

No.	Outputs	Range
1	Peak Torque, T_{pk} (Nm)	$280 \leq T_{pk} \leq 300$
2	Rated Torque, T_{rt} (Nm)	$150 \leq T_{rt}$
3	Peak Power, P_{pk} (kW)	$120 \leq P_{pk}$
4	Rated Power, P_{rt} (kW)	$80 \leq P_{rt} \leq 90$
5	Min. Speed at P_{pk}, n_{pk} (kRPM)	$4 \leq n_{pk}$
6	Min. Speed at P_{rt}, n_{rt} (kRPM)	$4 \leq n_{rt}$
7	Estimated Material Cost, USD ($)	$USD < 250.54$
8	Max Electric Loading, K_s (Arm/mm)	$K_s < 117.9$
9	Max Slot Current Density, J_s (Arms/mm^2)	$J_s < 16.88$
10	Max Tooth Flux Density, B_{ts} (T)	$B_{ts} \leq 1.9$
11	Max Core Flux Density, B_{cs} (T)	$B_{cs} < 1.7$
12	Average WLTP3 Efficiency, η (%)	$92.4 < \eta$
13	Low Temp. Demag. Ratio, DR_2 (mm^3/mm^3)	$DR_2 < 5 \cdot 10^{-5}$
14	High Temp. Demag. Ratio, DR_1 (mm^3/mm^3)	$DR_1 < 5 \cdot 10^{-5}$
15	Aspect Ratio, l_r/r_{or} (mm/mm)	$l_r/r_{or} < 7$
16	Torque Ripple, T_{rip} (%)	$T_{rip} < 10$
17	Max Rotor Stress, σ_{MAX} (MPa)	$\sigma_{MAX} < 585.475$

Constraint 13 checks for low temperatures irreversible demagnetization at T_{PM2} with current I_{PM2} in-phase with the back EMF, as described in Table 8. Constraint 14 checks for high temperature irreversible demagnetization at T_{PM1} for all operating points. The demagnetization ratios (DR_1 and DR_2) are the ratio of irreversibly demagnetized PM volume to total PM volume, so DR_1 and DR_2 are ratios of two discrete counts of finite elements. The ROM built using OptiSLang here only can consider continuous variables as inputs, so the ROM will report a very small but nonzero DR_1 and DR_2 for a significant portion of the design space. The authors

observed the minimum, nonzero demagnetization ratio reported by FEA is approximately 5e-5, so they consider it unlikely a design will demagnetize if the demagnetization ratio estimated by the ROM is less than 5e-5. Validation results will show this assumption is not ideal, but it can yield iterative Pareto front improvements when refining then design space conservatively. Due to the increased risk of irreversible demagnetization at low temperatures demonstrated in Section 3.3, current must derate at low temperatures in MnBi designs to maintain a competitive torque density. Objective 3 will therefore present a control scheme that limits the stator current at low temperatures to prevent irreversible demagnetization.

The reference FEA model for the Leaf motor provided by [23] estimates that the maximum rotor lamination stress at 1.2 times the maximum speed is about 535 MPa. This is greater than the yield stress of the rotor laminations (305 MPa) and the value calculated by Nissan [61] due to the simplified rotor duct structure in the reference FEA model from [23] compared to the actual design [17]. Exact σ_{MAX} highly depends on rotor duct geometry and varies by almost 200% in the relatively limited optimization presented by Nissan in [61]. However, while duct size and shape *can* impact electromagnetic performance, [61] also shows both the duct size and shape can vary without significantly impacting electromagnetic performance if the leakage flux in the bridges is minimized.

These mechanical details complicate the optimization routine used here and are not the focus of this trade study, so Constraint 17 limits maximum rotor stress at 1.2 times the maximum speed to 110% the value calculated in FEA for the Leaf (or 192% of the yield stress). Considering the reference FEA model also experiences excessive stress, most validated Pareto optimal designs presented here will have σ_{MAX} lower than the reference model, and the duct

shape causes σ_{MAX} to vary by almost 200% in [61], the author believe Constraint 17 is a fairer comparison of PM material than constraining σ_{MAX} to less than the lamination yield stress.

3.4.4 ROM Accuracy and Pareto Front Validation

Table 11 shows the full COP matrix for all input/output combinations in the first design iteration for a sensitivity study sample size of 400. DR_1 is not included because all designs achieved $DR_1 = 0$. Generally, larger design spaces have lower COPs, but this effect is insignificant here for all outputs but DR_2 and σ_{MAX}. All outputs but DR_2 and σ_{MAX} have COPs >95%, which is sufficient [66], [67]. From here, the COP of all outputs generally improve over each iteration, except for σ_{MAX} and DR_2. Despite these low COPs, the iterative procedure can still produce optimal designs by handling these modeling inaccuracies on a case-by-case basis.

Table 11: Coefficient of Prognosis (COP) Matrix for All Combinations of Inputs and Outputs in the First Optimization Iteration of MnBi IPMSM2 Design

	t_{b1}	t_{p1}	t_{m1}	r_{m1}	r_{pa1}	θ_{p1}	t_{b2}	t_{p1}	t_{m1}	r_{m1}	r_{pa1}	θ_{p1}	r_{sd}	λ	l_{is}	r_{tw}	V_{DC}	Sum
W	0.000	0.000	0.000	0.000	0.000	0.000	0.000	0.000	0.000	0.001	0.000	0.000	0.031	0.000	0.888	0.073	0.000	0.997
η	0.026	0.000	0.000	0.000	0.019	0.000	0.004	0.000	0.003	0.102	0.149	0.012	0.102	0.000	0.051	0.542	0.000	0.979
T_{rip}	0.511	0.000	0.000	0.000	0.032	0.000	0.143	0.000	0.000	0.098	0.282	0.000	0.000	0.000	0.000	0.076	0.000	0.951
B_{ts}	0.024	0.000	0.000	0.000	0.008	0.000	0.021	0.000	0.031	0.089	0.030	0.086	0.044	0.000	0.000	0.694	0.000	0.966
σ_{MAX}	0.006	0.075	0.075	0.000	0.061	0.019	0.052	0.022	0.063	0.061	0.013	0.012	0.000	0.000	0.000	0.004	0.000	0.461
I_{SC}	0.116	0.000	0.000	0.018	0.044	0.006	0.108	0.014	0.105	0.470	0.061	0.079	0.011	0.000	0.000	0.017	0.000	0.982
T_{rt}	0.023	0.000	0.000	0.005	0.016	0.000	0.032	0.007	0.011	0.053	0.169	0.014	0.004	0.000	0.490	0.191	0.000	0.992
n_{rt}	0.057	0.000	0.000	0.010	0.005	0.000	0.037	0.002	0.031	0.128	0.037	0.135	0.002	0.000	0.243	0.164	0.151	0.985
P_{rt}	0.069	0.000	0.000	0.012	0.021	0.000	0.074	0.005	0.028	0.213	0.161	0.065	0.003	0.000	0.000	0.014	0.356	0.992
T_{pk}	0.033	0.000	0.000	0.005	0.007	0.000	0.019	0.004	0.008	0.024	0.151	0.018	0.024	0.000	0.460	0.249	0.000	0.996
n_{pk}	0.006	0.000	0.000	0.001	0.000	0.000	0.007	0.000	0.019	0.044	0.000	0.064	0.000	0.000	0.369	0.263	0.225	0.994
P_{pk}	0.073	0.000	0.003	0.011	0.017	0.000	0.075	0.008	0.041	0.117	0.211	0.021	0.011	0.000	0.000	0.011	0.418	0.992
K_s	0.000	0.000	0.000	0.000	0.000	0.000	0.000	0.000	0.000	0.000	0.000	0.000	0.000	1.000	0.000	0.000	0.000	1.000
DR_2	0.208	0.000	0.000	0.000	0.000	0.000	0.068	0.000	0.348	0.410	0.000	0.445	0.000	0.000	0.000	0.000	0.000	0.781
USD	0.003	0.000	0.053	0.005	0.003	0.000	0.000	0.000	0.030	0.030	0.000	0.002	0.006	0.000	0.848	0.021	0.000	0.998
B_{cs}	0.000	0.000	0.000	0.000	0.002	0.000	0.003	0.000	0.005	0.000	0.002	0.122	0.561	0.000	0.000	0.297	0.000	0.992

Both DR_2 and σ_{MAX} have COPs that are lower than desired throughout this study, not just for the iteration shown in Table 11. Validation results will show that the DR_2 ROM is sufficiently accurate to approximate the Pareto front because it only needs to determine when $DR_2 < 5e-5$, not the exact value of DR_2. Undoubtably, better results could be obtained given a more accurate demagnetization ROM, an inherent limitation of this probabilistic approach. On the other hand, the σ_{MAX} COP will continue to decrease while refining the design space, suggesting the FEA model requires a finer mesh size, rounded flux barrier corners, and/or more accurate FEA solver to accurately model σ_{MAX} using a ROM [66]. However, the ROM can still be used to determine when σ_{MAX} is sufficiently low within a margin of error dictated by the variability in σ_{MAX} over the design space.

Despite the initial DR_2 inaccuracy, it is easier to start in a large design space and refine than it is to start in a small design space and expand because a ROM with a high COP can interpolate accurately but not necessarily extrapolate accurately. The sensitivity study is the most time-consuming step in Figure 13, so first start with a smaller sample size in a larger design space to find at least a few feasible designs. Then, use a larger sample size to build the ROM, and refine the design space gradually, using sensitivity study and optimization results to improve the COP near the Pareto front. In all cases, refine the design space carefully to prevent unintentionally eliminating competitive designs.

This study required 9 iterations to achieve the desired validation error (i.e., $DR = 0$, $\sigma_{MAX} < 585.475$) for the MnBi IPMSM2 (i.e., with magnet posts). Although all decisions cannot be listed here due to length, they are summarized below. Table 12 lists key results from each iteration to show that the design space refinements produced the intended effects. In Table 12, $DR = DR_2$ because all designs achieve $DR_1 = 0$. The "Passed" columns refer to the

percentage of designs that pass all constraints in either the sensitivity study or Pareto front validation, respectively. The "Failed" columns refer to the percentage of designs for which that output failed its respective constraint in Table 10.

Table 12: Model Validation Error for All Iterations of MnBi IPMSM2 Design

#	Sensitivity											Validation							
	% Passed	DR					σ_{MAX}				T_{rip}	% Passed	DR		σ_{MAX}			T_{rip}	Other
		COP	% Failed	% FN	% FP	Max	COP	% Failed	Max	Range	% Failed		% Failed	Max	% Failed	Max	Range	% Failed	% Failed
1	0.8%	78.1%	74.4%	8.5%	77.2%	0.151332	46.11%	19.3%	700.8	256.7	83.2%	10.0%	70.0%	0.003783	0.0%	576.9	96.7	35.0%	15.0%
2	2.3%	83.8%	69.2%	12.7%	96.7%	0.018042	34.76%	8.77%	662.6	215.0	75.7%	25.0%	45.0%	0.000177	55.0%	694.5	150.8	0.0%	0.0%
3	6.1%	66.7%	64.7%	12.9%	81.9%	0.008611	28.84%	2.22%	600.5	157.7	51.9%	20.0%	70.0%	0.002231	40.0%	644.6	109.6	20.0%	20.0%
4	6.3%	44.6%	52.3%	10.6%	67.2%	0.00290	22.78%	0.76%	613.0	178.3	73.2%	15.0%	55.0%	0.000195	0.0%	584.5	88.4	40.0%	20.0%
5	10.6%	42.0%	75.9%	2.5%	99.0%	0.001285	16.14%	3.28%	642.5	169.5	20.5%	55.0%	45.0%	0.000197	0.0%	581.5	77.0	0.0%	25.0%
6	17.3%	37.0%	67.8%	6.4%	69.3%	0.000603	23.2%	0.0%	577.7	108.6	10.0%	10.0%	75.0%	0.000188	0.0%	577.0	99.8	20.0%	45.0%
7	20.7%	45.2%	56.7%	36.4%	43.6%	0.000204	2.50%	0.0%	567.8	88.0	26.3%	31.6%	42.1%	0.000184	0.0%	528.9	29.5	26.3%	42.1%
8	44.6%	100.0%	0.0%	0.0%	0.0%	0.000000	4.26%	0.0%	560.6	91.5	0.0%	30.0%	65.0%	0.000179	0.0%	575.6	91.5	0.0%	20.0%
9	43.3%	100.0%	0.0%	0.0%	0.0%	0.000000	9.01%	0.0%	564.6	93.8	0.0%	14.0%	0.0%	0.000000	0.0%	552.9	80.0	15.0%	20.0%

For DR_2 specifically, Table 12 lists the percentage of designs that evaluate Constraint 13 in Table 10 as falsely positive (FP) or falsely negative (FN) during validation. In other words, when evaluating the ROM with the same designs used to build it, FP represents designs for which the ROM predicts irreversible demagnetization but FEA does not, and FN represents designs for which the ROM predicts no demagnetization but FEA does.

In the first 4 iterations, the authors aimed to limit both DR and σ_{MAX} validation error while conservatively refining design space. In Iteration 1, Constraint 13 was included in the optimization. Here, all validated designs satisfy Constraint 13, but σ_{MAX} model inaccuracy calls into question the results. Considering the simplified rotor duct geometry, the authors choose to only consider Constraint 13 in the sensitivity study and validation phases but not in the optimization phase from this point forward. No ranges for any inputs with a statistically significant COP for σ_{MAX} change between Iterations 1 and 2.

Iterations 2 – 9 demonstrate the trend, described previously, where σ_{MAX} COP decreases when refining the design space due to significant noise [66]. Iterations 2 – 4 then aim primarily to limit maximum σ_{MAX} in the sensitivity study and ROM validation. The COP matrix revealed that t_{b2}, t_{p2}, and few others impact σ_{MAX}. Therefore, the authors increase minimum t_{b2} and t_{p2} to 0.65 and 0.7 mm, respectively, after Iteration 3. As a result, Table 12 shows no validated designs after Iteration 3 fail the stress constraint. By Iteration 6, Table 12 shows σ_{MAX} range remains approximately constant while the COP is near 0%. The COP matrix in this iteration also reveals few inputs have a significant effect on σ_{MAX}.

Therefore, in Iterations 6 – 9, Constraint 17 limiting σ_{MAX} was not considered during the optimization routine because the COP is nearly 0% while all designs in the sensitivity study satisfied this constraint. Instead, the design space was aggressively refined with the focus of eliminating DR_2 validation error using the ROM in conjunction with the optimization results. DR_2 ultimately is a ratio of two integer counts of a finite number of model elements. As a result, DR_2 experiences a quantization effect, but the ROM must model DR_2 continuously due to software limitation. The DR_2 COP is high initially because most designs experience a relatively high amount of demagnetization (max of 0.15 in Iteration 1) which overshadows the quantization effect (on the order of 1e-4). As the maximum DR_2 in the sensitivity study decreases, COP also decreases because quantization becomes more significant compared to the maximum DR_2. The maximum DR_2 reported in Sensitivity for Iterations 5 – 9 and in Validation for Iterations 4 – 9 show this quantization effect, where DR_2 essentially takes on a value of 0 or 2e-4. Some designs in these iterations also then take on a value of about 1e-4. Although the DR_2 and σ_{MAX} COP behave similarly, DR_2 having a low COP is not a result of inadequate mesh sizing. Any mesh

size would exhibit this behavior. More advanced FEA solvers, such as those used in ANSYS Maxwell, would be required to improve DR_2 accuracy.

Despite the high COP initially, the ROM produces a high rate of false positives throughout all iterations (e.g. 96.7% of sensitivity study designs in Iteration 2 that do not irreversibly demagnetize evaluate as a false positive by the ROM during validation). Conversely, the rate of DR_2 false negatives is much lower throughout all iterations. This suggests that when the ROM reports no irreversible demagnetization, FEA likely will too, which is still useful despite low COP and high FP. This is corroborated by the fact that the maximum DR_2 reported in sensitivity studies generally decreases with each iteration.

The optimization also preferred designs with T_{rip} near the maximum allowable value. Despite high COP > 95% in all iterations for T_{rip}, some validated designs fail the constraint, but never by more than 2%. The authors consider this amount of validation error to be acceptable for this stage of the MnBi IPMSM trade study. Similar results occur for the T_{pk} and B_{cs}.

3.4.5 Comparing Pareto-Optimal Fronts Across Iterations

Figure 24 shows the Pareto optimal fronts for Iterations 1 (first), 5 (middle) and 9 (last), while box and whisker plots in Figure 25 show the variability among the Pareto fronts for all iterations. In Figure 25, the red lines are the medians, blue boxes span the upper and lower quartile, and the end of the blue lines span the minimums and maximums. Note that in both Figure 24 and Figure 25, W is calculated including the shaft weight, with shaft diameters equal for all designs, while results presented for IPMSM1 in Section 3.3 exclude shaft weight.

As expected, all iterations generally agree with each other, but the Pareto front becomes more precise in later iterations. The input ranges and constraints significantly limit variability in W and T_{rt}, although torque density increases slightly as iterations progress. However, I_{SC} varies more significantly (about 15% between the lowest and highest Pareto optimal I_{SC} in the first and last iterations, respectively), and I_{SC} improves over the first three design iterations. Then, when increasing minimum Layer 2 bridge thickness and Layer 2 post thickness after the Iteration 3 to limit σ_{MAX}, I_{SC} decreases, likely due to added leakage permeance, as described in [32], [61]. In fact, the iterations with the highest σ_{MAX} among validated designs in Table 12 also have the highest I_{SC}, which improves constant power behavior above base speed (a notable issue in RE-free PMSMs). This highlights the well-known trade-off between irreversible demagnetization, rotor lamination stress, and electromagnetic performance due to changing bridge and post thicknesses [32], [61].

Still, Figure 24 and Figure 25 shows that Iterations 5 – 9 outperform the Iteration 1 with respect to maximizing I_{SC} despite initial modeling inaccuracy. The best designs in Iteration 1 have similar maximum I_{SC} as those in the final iteration. On the other hand, Pareto optimal fronts for Iterations 7 – 9 do not vary significantly despite requiring so many iterations to eliminate DR_2 validation error. This suggests that an estimate of the Pareto front can be calculated without entirely eliminating DR_2 validation error. However, because irreversible demagnetization is a costly event that is difficult to model with a ROM, a significant margin of error should be included. Furthermore, based on results from Iteration 3, designs with a higher I_{SC} can be obtained with better DR_2 and σ_{MAX} ROMs.

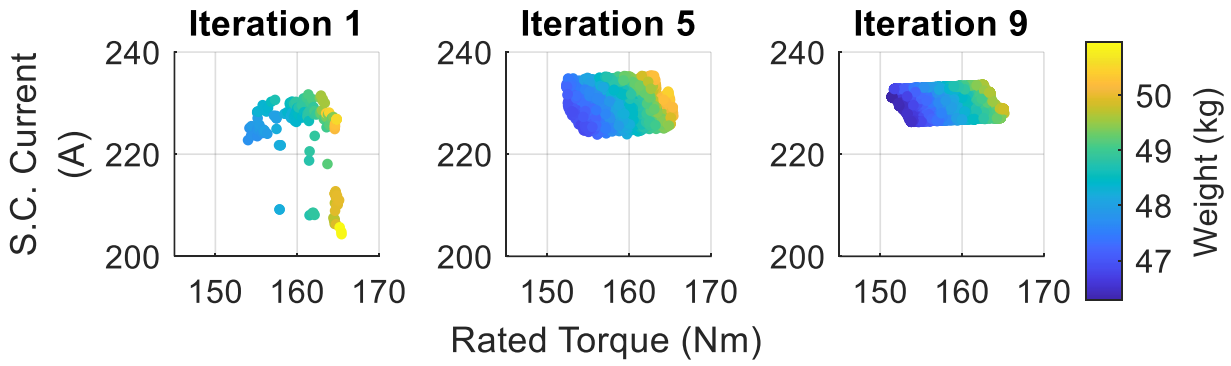

Figure 24: Pareto optinal front after first, fifth, and ninth (final) iterations of MnBi IPMSM2 optimization

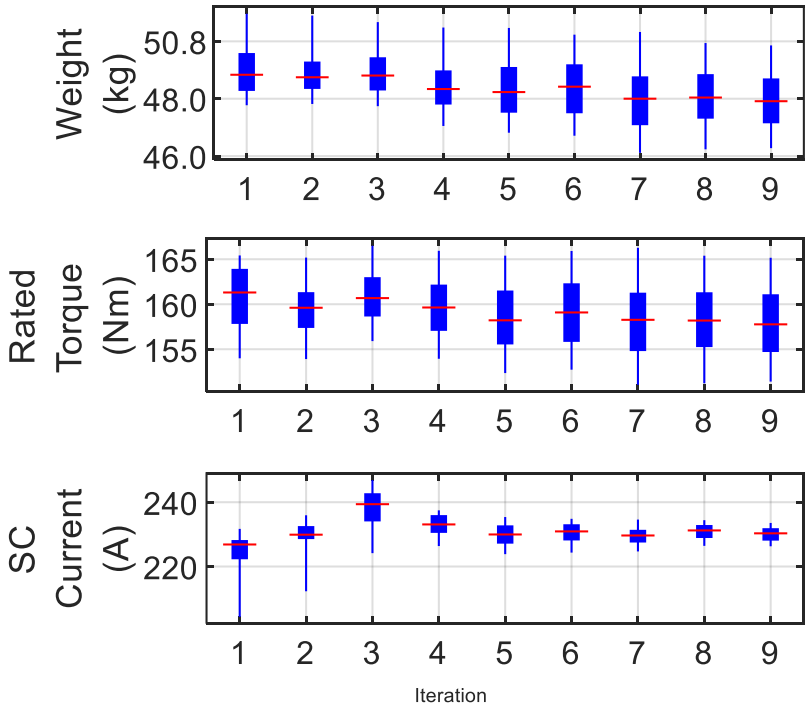

Figure 25: Box and whisker plots of Pareto optimal values for each objective across each iteration of MnBi IPMSM2 optimization

3.5 Improved MnBi IPMSM Design with Magnet Posts

Having reviewed the improved optimization routine compared to the initial approach used in Section 3.2 and Section 3.3, the following subsection details the performance of a more practical MnBi IPMSM design (MnBi IPMSM2). Comparing MnBi IPMSM1 from Section 3.3 to MnBi IPMSM2 below demonstrates the magnet posts' impact on motor performance.

Figure 26 shows the updated Pareto optimal front considering the new objectives, constraints, and inputs, most notably the added magnet posts. The Pareto front in Figure 26 has more detail than that in Figure 16 because design iterations were used to obtain Figure 26, whereas only one was used to obtain Figure 16. Comparing Figure 16 and Figure 26 to Figure 24 confirms this. Table 13 compares the feasible, validated design with the lowest weight (Design #7413) to MnBi IPMSM1 and the Leaf reference motor and to MnBi IPMSM1. All values in Table 13 are calculated at 100°C. Like in Figure 16, Figure 26 denotes with a red circle the location of Design #7413 on the Pareto front. Note that the weights in Figure 26 include shaft weight, but weights in Figure 16 do not. Therefore, Table 13 reports weights without considering the shaft to make a fair comparison.

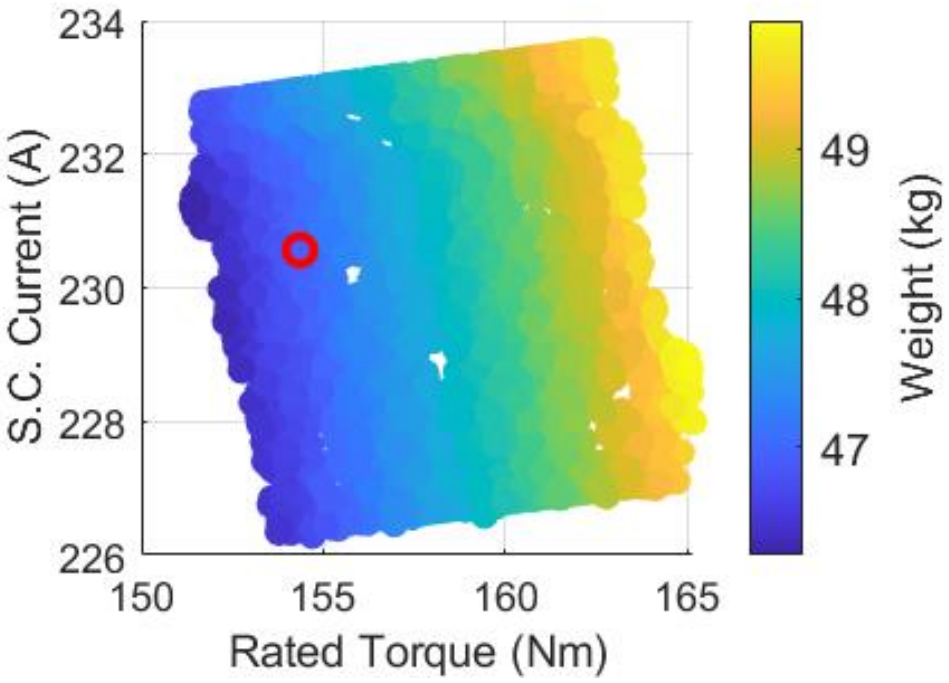

Figure 26: The pareto optimal front from the final iteration of the improved optimization for MnBi IPMSM2

Table 13: Comparing the NdFeB Leaf Reference Motor, Initial MnBi IPMSM1, and Final MnBi IPMSM2

	Metric			NdFeB Leaf IPMSM	MnBi IPMSM1 Design #9872 (Lightest)		MnBi IPMSM2 Design #7413 (Lightest)	
					Value	Δ	Value	Δ
Geometry	Stator OD, mm			198	198	0.0%	198.00	0.0%
	Rotor OD, mm			130	130.7	0.5%	131.65	1.3%
	Active Length, mm			160	214.0	33.8%	216.73	35.5%
	Active Volume, L			4.93	6.59	33.8%	6.67	35.5%
	Weight (without shaft), kg			31.9	42.7	33.6%	43.7	36.9%
	Magnet Weight, kg			1.97	4.00	103.3%	5.20	164.7%
	Steel Weigth (without shaft), kg			23.5	30.8	31.0%	30.55	30.0%
	Copper Weight, kg			6.45	7.86	21.9%	7.94	23.0%
	Total Cost (whtout shaft), $			250.5	186.4	-25.6%	199.9	-20.2%
	Magnet Cost, $			137.6	44.0	-68.0%	57.2	-58.4%
	Steel Cost (without shaft), $			51.7	67.7	31.0%	67.2	30.0%
	Copper Cost, $			61.3	74.7	21.9%	75.4	23.0%
	Slot Copper Fill Factor			0.52	0.52	0.0%	0.52	0.0%
Performance	Maximum Speed, RPM			10,000	6,250	-37.5%	10,000	0.0%
	Torque, Nm (65°C)	*0 RPM*	*Rated Current*	160.1	166.7	4.1%	158.84	-0.8%
		0 RPM	*Peak Current*	280.5	300.6	7.1%	290.52	3.6%
	Power, kW (65°C)	*Max*	*Rated Current*	83.8	93.01	11.0%	94.72	13.0%
		Max	*Peak Current*	132.1	130.6	-1.2%	132.12	0.0%
		10k RPM	*Rated Current*	79.4243	90.9075	14.5%	93.88	18.2%
		10k RPM	*Peak Current*	124.9	92.3524	-26.0%	97.58	-21.8%
	Average Drive Cycle Efficiency, % (65°C)	*WLTP3*		93.7	95.6	1.9%	95.94	2.3%
		UDDS		93.8	95.1	1.4%	95.48	1.8%
		US06		94.2	95.5	1.4%	95.76	1.7%
		HWFET		91.6	95.3	4.0%	95.70	4.4%
	Losses, W (1000 RPM, 150 Nm, 65°C)	*Copper*		1161	1344.0	15.8%	1460.00	25.8%
		Steel		143.9	180.1	25.2%	148.70	3.3%
		Magnet		0.191	0.006	-96.9%	0.001	-99.5%
Electrical	DC Link Voltage, V			375	500	33.3%	500.00	33.3%
	Current, A	*Rated*		267	267	0.0%	267.00	0.0%
		Peak		480	480	0.0%	480.00	0.0%
	Power Factor at Terminals, 1000 RPM			0.788	0.682	-13.5%	0.68	-13.5%
	Slot Current Density, Arms/mm^2			16.88	16.88	0.0%	16.88	0.0%
	Peak Electric Loading, kArms/m			117.9	117.3	-0.5%	116.40	-1.3%
	Saturated d-axis Inductance, mH			0.162	0.230	42.1%	0.24	48.8%
	Saturated q-axis Inductance, mH			0.376	0.509	35.1%	0.50	32.2%
	Saturated Saliency Ratio			2.326	2.212	-4.9%	2.067	-11.2%
	Saturated S.C. Current, A (65°C)			353.8	167.4	-52.7%	176.20	-50.2%
Magnetic	Magnetic Loading, T	*Rated Current*		0.905	0.779	-13.9%	0.71	-21.7%
		Peak Current		1.006	0.933	-7.3%	0.86	-14.7%
	Max Flux Density, T	*Rated Current*	*Tooth*	1.677	1.633	-2.6%	1.58	-5.9%
			Tooth Tip	1.670	1.616	-3.2%	1.72	3.2%
			Core	1.383	1.359	-1.7%	1.22	-11.8%
		Peak Current	*Tooth*	1.898	1.863	-1.8%	1.80	-5.4%
			Tooth Tip	1.906	1.950	2.3%	2.00	4.9%
			Core	1.681	1.644	-2.2%	1.58	-6.2%
Mechanical	Torque Ripple, %			6.20	6.10	-1.7%	8.40	35.4%
	Rotor Aspect Ratio			2.31	3.12	35.3%	3.14	36.1%
	Max Stress at 12,000 RPM, Mpa			532.5	1342	152.0%	490.40	-7.9%

The heaviest validated Pareto optimal MnBi design, MnBi IPMSM2 is about 1.43 times heavier than the Leaf design if neglecting shaft weight. On the other hand, MnBi IPMSM2 Design #7413, the lightest Pareto optimal design, is only about 1.37 times heavier, which is approximately equal to the heaviest, validated Pareto optimal design from Figure 16 for MnBi IPMSM1. Considering that MnBi IPMSM2 produces about 4.1% and 7.1% greater rated and peak torque than the Leaf motor, MnBi IPMSM2 is still approximately in agreement with the sizing equation analysis presented earlier. Still, IPMSM2 must be slightly heavier than IPMSM1 to achieve the same torque due to the added leakage permeance of the magnet posts. To support this claim, Table 13 shows that the magnetic loading (i.e., the fundamental component of the air gap flux density, B_{g1}) decreases despite using significantly more PM material in MnBi IPMSM2 compared to MnBi IPMSM1.

Figure 27 compares the capability curves calculated at 100°C for MnBi IPMSM1, MnBi IPMSM2, and the NdFeB Leaf reference motor. The IPMSM2 produces more peak torque than the IPMSM1 because the authors relax Constraint 1 as specified in Table 10. The MnBi IPMSM2 produces slightly more power than the MnBi IPMSM1 using the same voltage, which is also the minimum allowable voltage according to the range in Table 9. The DC link voltage could therefore be slightly lower for the MnBi IPMSM2 to achieve a similar P_{pk} and P_{MAX} as the MnBi IPMSM1 without changing any other parameters. In this case, the capability curves for MnBi IPMSM1 and MnBi IPMSM2 are quite similar, but MnBi IPMSM2 achieves this with a lower DC link voltage. The MnBi IPMSM2 had similar efficiency as the MnBi IPMSM1 in Section 3.3, so those results for the MnBi IPMSM2 are omitted here.

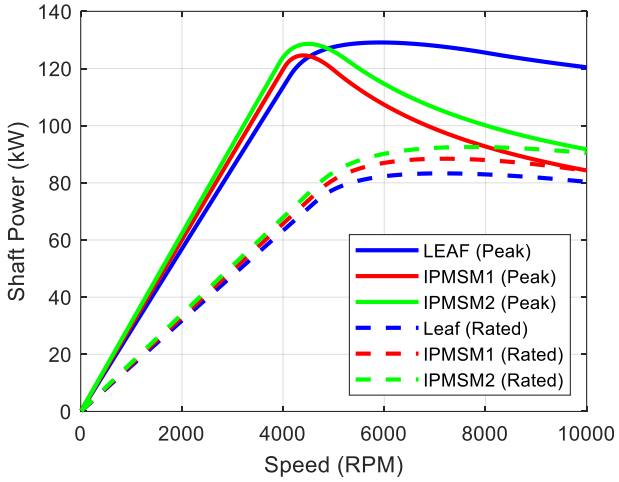

(a)

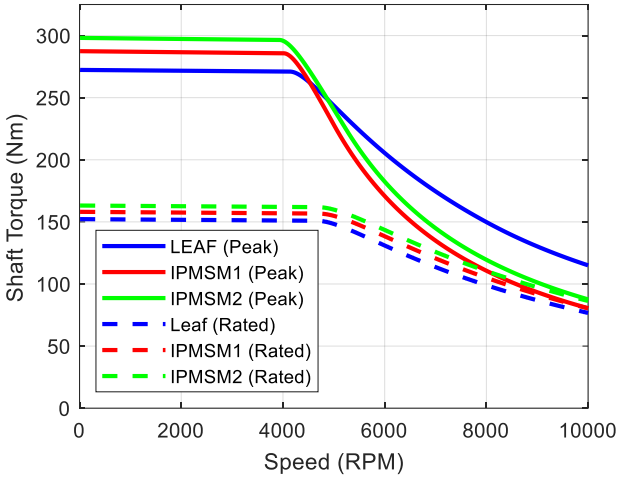

(b)

Figure 27: (a) Torque and (b) Power vs Speed for both MnBi IPMSMs and the Leaf NdFeB IPMSM

Despite the slight degradation in torque density, MnBi IPMSM2 is significantly improved compared to IPMSM1 because the magnet posts significantly lower irreversible demagnetization risk and maximum rotor stress at the maximum overspeed. Figure 28 now shows the safe operating regions without risk of irreversible demagnetization at different temperatures for MnBi IPMSM2. By including magnet posts, the pink shaded region, representing the safe operating points at ≥0°, expands substantially compared to in Figure 23, where the pink shaded region represented safe operating points at ≥30°C. Furthermore, MnBi IPMSM2 can now withstand up

to the rated current of 267 A on the quadrature axis at 0°C, whereas MnBi IPMSM1 irreversibly demagnetizes at open circuit for magnet temperatures ≤40°C (i.e., "self-demagnetization" [72]). Additionally, IPMSM2 can safely operate at peak current for most current angles when PM temperature is ≥40°C, with only one tested operating point located in the third quadrant of Figure 28 leading to irreversible demagnetization.

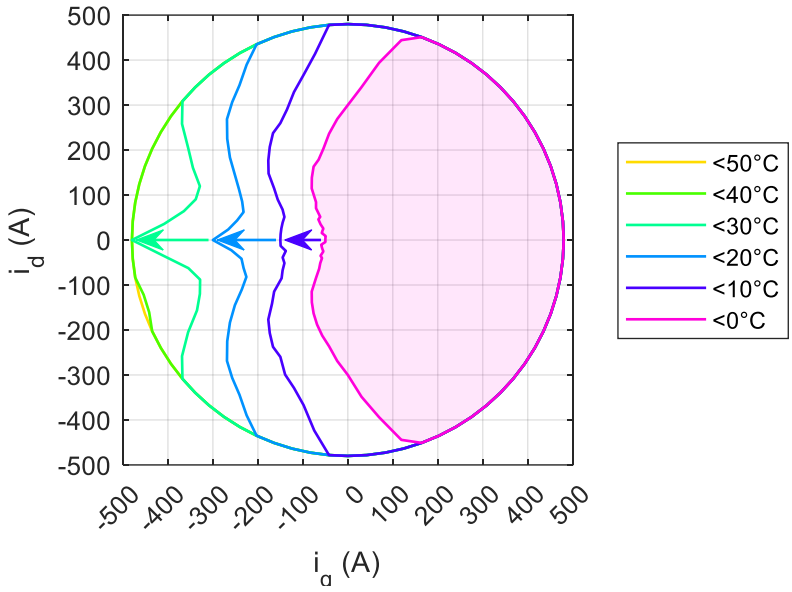

Figure 28: Safe operating regions with no risk of irreversible demagnetization at different magnet temperatures for MnBi IPMSM2.

Note that this motor can withstand over three times the peak current on the direct axis (d-axis) without irreversibly demagnetizing, while the SPMSM design presented by a previous group in [12] exhibits a small amount of demagnetization at this operating point. Despite the improvement shown in Figure 28 compared to motor in [12] designed using a more conventional approach that does not consider low temperature irreversible demagnetization, the MnBi IPMSM2 still experiences irreversible demagnetization at low temperatures. This highlights the importance of considering this unique effect with designing MnBi PMSMs.

To complete the thermal analysis, Figure 29 compares the temperature rise of MnBi IPMSM2 to that of the Leaf and MnBi IPMSM1 presented in Figure 22. This shows that the temperature rise of MnBi IPMSM2 is significantly lower than the other two designs, and bearing temperature rise is now lower than the Leaf motor. At the operating point tested, MnBi IPMSM2 has higher losses than the Leaf motor and MnBi IPMSM1, shown in Table 13.

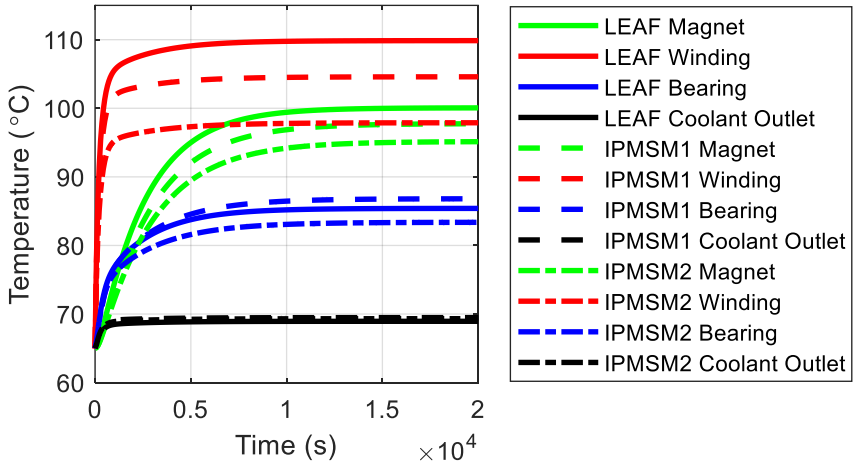

Figure 29: Temperature rise comparison for the NdFeB design, MnBi IPMSM1, and MnBi IPMSM2.

Table 13 also lists the maximum rotor stress of all three motors at 1.2 times (12,000 RPM) the maximum speed (10,000 RPM). After adding the magnet posts, MnBi IPMSM2 now experiences less stress than the reference design despite using significantly more magnetic material by weight than the other two designs. For reference, the IPMSM1 maximum speed must be lowered to about 6,250 RPM (7,500 RPM overspeed) to lower the stress to the same value as the Leaf motor, shown in Table 13. However, [61] suggests that advanced duct designs can also limit the rotor lamination stress in MnBi IPMSM2 without significantly impacting electromagnetic performance. Finally, the torque ripple in the IPMSM2 (8.4%) is relatively high compared to that of the Leaf motor (6.1%) and MnBi IPMSM1 (6.2%).

4.0 Objective 2: MnBi PMASynRM Design for EV Applications

Using the PMASynRM rotor topology, Objective 2 aims to address the final shortcoming of the MnBi IPMSMs designed for Objective 1: low short circuit current, leading to low CPSR, power factor, and higher DC link voltage. Using the exact motor topology of the NdFeB Nissan Leaf IPMSM, the MnBi IPMSM1 suffered from three main weaknesses. First, the motor suffered from excessive irreversible demagnetization at low temperatures, even experiencing self-demagnetization with no current in the stator windings at magnet temperatures of 40°C and lower. Second, rotor lamination stress at high speeds far exceeds the yield stress of the rotor laminations. Third, the motor has low CPSR and power factor, requiring a higher DC link voltage to achieve the same power capabilities as the reference motor. MnBi IPMSM2 improves upon the first two weaknesses by adding magnet posts to the topology and considering low temperature demagnetization and rotor lamination stress in the ROM and optimization routine. However, this topology still cannot improve CPSR and power factor because adding the magnet posts increases the leakage permeance, thereby degrading electromagnetic performance. Therefore, Objective 2 increases short circuit current by designing a MnBi PMASynRM, a more practical choice for RE-free PMs. In addition, this section also considers how the amount of low temperature irreversible demagnetization risk impacts EV drive cycle performance for the PMASynRM.

4.1 Literature Review

Some sources use the terms PMASynRM and IPMSM interchangeably [17], [18]. Others recognize the terms as two ends of a spectrum, where reluctance torque dominates torque production in PMASynRMs while magnet torque does so in IPMSMs [9]. This paper does not equate the two terms, and instead uses them to distinguish between different rotor topologies. The IPMSM1 is the Leaf motor topology shown in Figure 2, the IPMSM2 is similar to the Leaf motor topology but with added magnet posts, and the PMASynRM is the segmented topology [9], also called 4U [73], shown in Figure 3.

Flux barriers refer to the pockets in the rotor that contain either air or PMs, and flux guides refer to the steel ribs between each flux barrier that have high permeability. The segmented PMASynRM used here is defined by having rectangular flux barriers that fit rectangular PMs with relatively easy manufacturing requirements. Other versions of PMASynRM topologies exists, such as the circular rotor geometry, which uses circular flux barriers, and the fluid shaped rotor, which uses flux barriers shaped such that flux lines would follow a similar path to the flow of fluid through a similar shape [9]. Currently, no obvious choice exists for optimal PMASynRM rotor geometry; each topology has their own merits [9].

The most notable merits for the segmented rotor topology are relatively simple design compared to the fluid shaped rotor and the relatively simple manufacturing compared to the circular geometry due, both due to the rectangular shape of the flux barriers and hence the PMs. Additionally, compared to the circular geometry, which is also relatively simple to the design, the segmented topology typically experiences lower rotor lamination stress at high speeds compared to a similarly designed circular rotor topology [9]. This is an important advantage for

the MnBi PMASynRMs design here, which experiences high rotor lamination stress like the MnBi IPMSM. As in the MnBi IPMSM, the MnBi PMASynRMs designed here use magnet posts, and both the magnet post and the bridge thicknesses are carefully optimized to limit rotor lamination stress at high speeds and irreversible demagnetization at low temperatures.

4.1.1 Advantages of PMASynRM for RE-Free Motors: Flux Focusing and Saliency

In RE-free PMSMs, the PMASynRM topology has two fundamental advantages compared to the IPMSM. First, the PMASynRM topology typically can achieve a higher saliency ratio than the IPMSM, which would improve power factor (e.g., lowering DC link voltage, improving CPSR, etc.) compared to the MnBi IPMSM, according to Section 2.5.2. Figure 30 illustrates why by depicting the positive and negative q-axis and the positive d-axis. The negative d-axis is shifted by one pole pitch both clockwise and counterclockwise to the positive d-axis, similar to the relationship between the positive and negative q-axis in Figure 30. Furthermore, there is also a negative q-axis shifted one pole pitch clockwise to the positive q-axis in Figure 30. This pattern repeats throughout the radial cross-section of the motor [9], [74], [75].

In Figure 30, both topologies have flux barriers along the d-axis, lowering L_d because PMs have a similar permeability as air and much lower than the rotor core. The IPMSM in Figure 30(a) has a rotor duct on the d-axis with a similar effect, but it also has a rotor duct on the q-axis, lowering L_q. On the other hand, the PMASynRM in Figure 30(b) consists entirely of steel which has a substantially higher permeability than air or the PM if not saturated. This increases L_q for the PMASynRM in Figure 30(b) compared to the IPMSM in Figure 30(a) [9]. However,

saturation decreases the permeability of the steel and therefore the saliency ratio [17], and both topologies experience notable saturation for the amount of PM material depicted.

The second fundamental advantage of the PMASynRM is that it can possibly better leverage the flux focusing effect, also depicted in Figure 30. PMs act as a source of flux density based on PM B_r, illustrated by the purple arrows in Figure 30, and torque density relates to the air gap flux density B_{g1} according to the sizing equations in Section 2.4. The PMASynRM has more magnet cross-sectional area per pole than the IPMSM, yet both topologies have similar pole pitches because they have similar rotor ODs and the same number of poles. Therefore, the PMASynRM can focus more PM *flux* through a *similar air gap cross-sectional area* as the IPMSM, leading to a *higher air gap flux density* in the PMASynRM. Although, again, saturation impacts this analysis. This is known as the flux focusing effect [46], [76], [77], [78], [79], [80], [81], and is the bases for well-known magnet arrangements like the Halbach array [46].

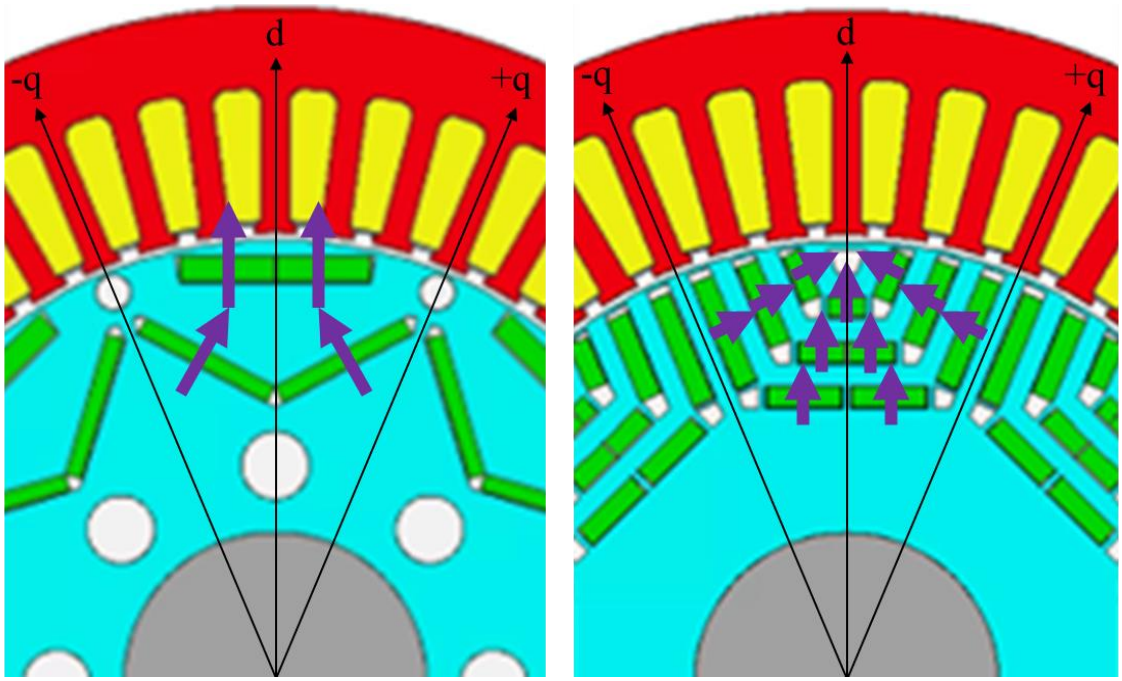

(a) **(b)**

Figure 30: Example of Flux Focusing and Saliency in the IPMSM and PMASynRM Topologies Used Here

With NdFeB and other RE PMs, the PMASynRM is undesirable due to high PM cost per unit weight because it requires more PM material per pole per unit axial length while heavily saturating the flux guides. However, when using RE-free PMs with lower cost and B_r (e.g., saturation), the PMASynRM may be more cost effective by using more magnet weight per pole per unit axial length to increase air gap flux density, thereby making a smaller motor. In other words, the PMASynRM may be cost effective for RE-free PMs by using more for PM material per unit axial length but less copper and steel overall because higher B_{g1} allows for shorter motor length compared to an RE-free IPMSMs.

4.1.2 Electric Vehicle Drive Cycle Operating Points

Using a motor with the low temperature irreversible demagnetization risk depicted in Figure 23 and Figure 28 requires decreasing the maximum available stator current at room temperature and below for the MnBi IPMSMs designed proposed in Objective 1. However, EV drivetrains rarely operate at peak power, peak torque, peak current, or peak speed [5]. To demonstrate this, Figure 31 – Figure 34 shows what percentage of EV drive cycle points fall below a given normalized power, torque, current, and speed, respectively, over the drive cycles introduced in Section 3.0. During these drive cycles, the weight was equal to the curb weight of the 2011 Nissan Leaf and 0% grade. These plots are normalized according to the ratings of the Nissan Leaf NdFeB reference motor: 120 kW peak power, 280 Nm peak torque, 480 A peak current, and 10,000 RPM maximum speed.

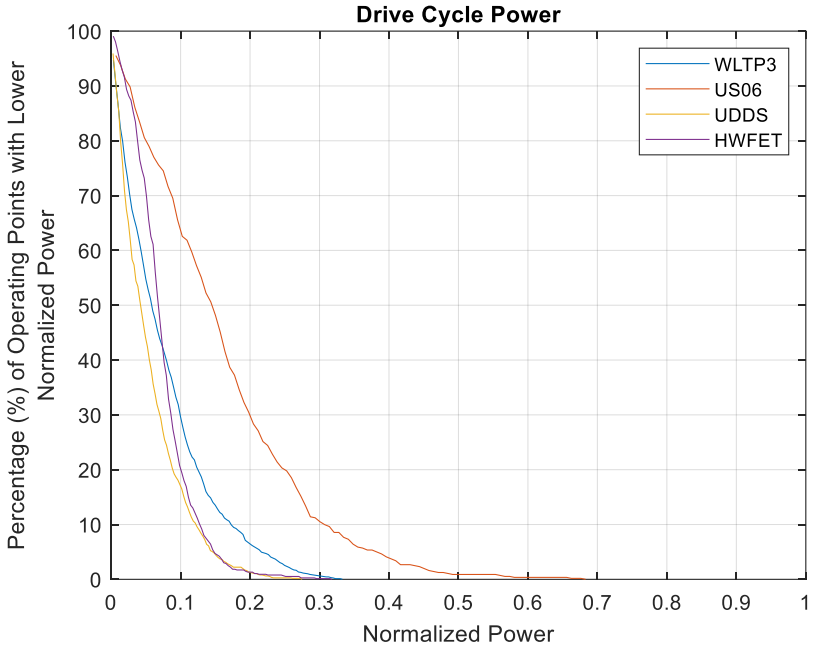

Figure 31: Comparison of Drive Cycle Powers for Various US and European Drive Cycles

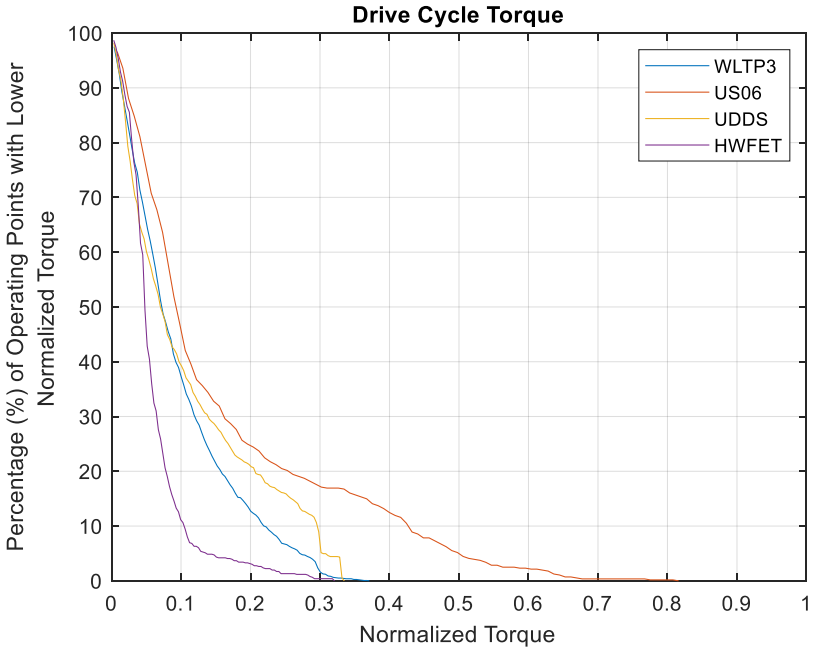

Figure 32: Comparison of Drive Cycle Torques for Various US and European Drive Cycles

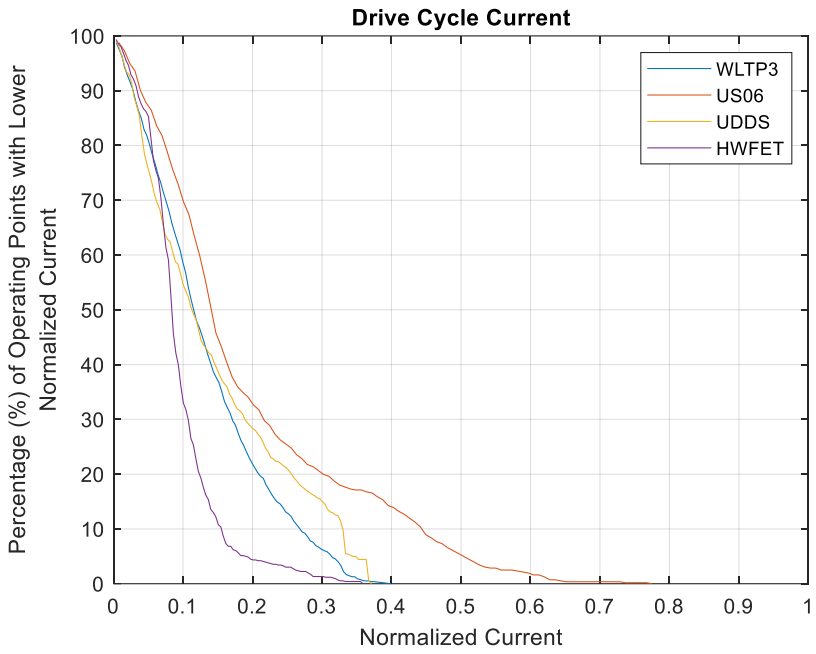

Figure 33: Comparison of Drive Cycle Stator Currents for Various US and European Drive Cycles

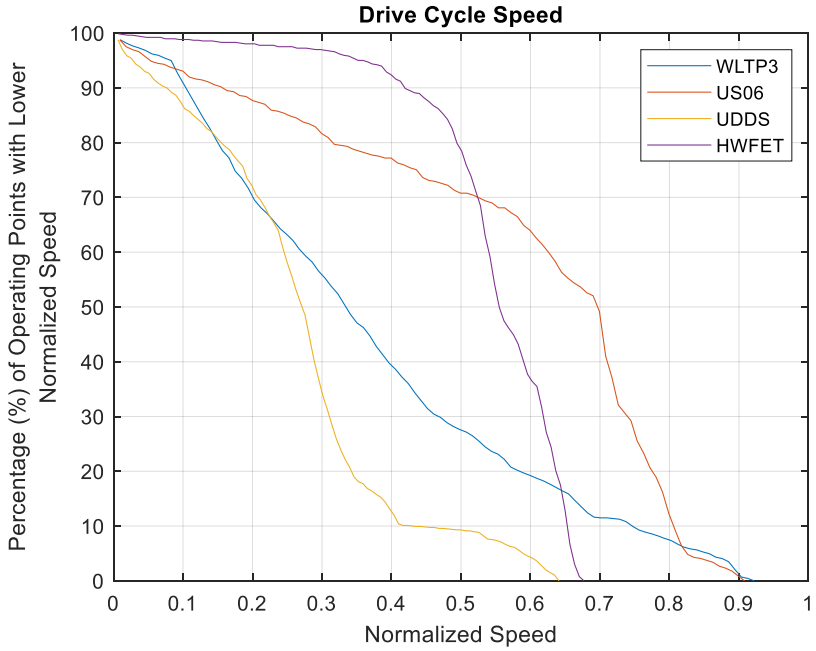

Figure 34: Comparison of Drive Cycle Speeds for Various US and European Drive Cycles

The drive cycles approach the maximum speed at times without ever reaching it. The US06 drive cycle, designed to be an aggressive, high-acceleration drive cycle, approaches maximum torque, power and current at times, but all other drive cycles always remain below

40% power, torque, and current when using the curb weight as the vehicle mass and a 0% grade. Therefore, while low temperature demagnetization risk, illustrated in Figure 23 and Figure 28, may require drastically reducing the maximum available current at low temperatures, up to a 60% reduction will not affect drive cycle performance for the WLTP3, UDDS, and HWFET drive cycles at this weight and grade. Therefore, the final key goal of Objective 2 is to analyze the relationship between irreversible demagnetization risk and drive cycle performance more rigorously to evaluate the practicality of using the MnBi PMSMs designed in this dissertation for EV applications, since EVs often cannot avoid the temperatures in Figure 23 and Figure 28 that increase demagnetization risk.

4.2 MnBi PMASynRM Design Space

The MnBi PMASynRM designed here also uses an optimization routine based on ROMs and the GA, similar to the approached used in Section 3.0 to design the MnBi IPMSMs. This subsection provides the details for said MnBi PMASynRM optimization routine. As in Section 3.0, the scope is limited to designing a MnBi PMASynRM with similar torque and power capability curves as the reference NdFeB IPMSM without redesigning the windings (e.g., use same number of poles, number of slots, number of parallel poles, insulation thickness, etc.), power electronics (e.g., use same peak stator current and as low DC link voltage as possible), thermal management (e.g., similar efficiency, slot current density, electric loading, and stator outer diameter), and mechanical components (i.e., bearings, gearbox, etc.). Due to these restrictions, the stator outer diameter (OD) and inner diameter (ID) cannot change significantly,

so the author instead only increase motor length to increase volume/weight in the MnBi designs, as described in Section 3.2.

Table 14 presents the design specifications for the MnBi PMASynRM based on the Leaf NdFeB IPMSM and the MnBi IPMSM2 designed in Section 3.0 for Objective 1. Here, peak torque (T_{pk}), rated torque (T_{rt}), peak power (P_{pk}), and rated power (P_{rt}) only represent desired targets that inform constraint selection. Actual values for these variables will depend on the exact design selected from the Pareto optimal front after multi-objective optimization. The same is true for base speed (n_b), the lowest speed at which the motor can achieve P_{rt} with I_{rt}.

The iterative design procedure used in Section 3.4 for Objective 1 is used here for the PMASynRM and reveals that low temperature irreversible demagnetization is more of a risk for PMASynRM designs with similar lamination stress the MnBi IPMSM. Therefore, to obtain competitive designs, I_{PM2} is decreased from 267 A in Table 8 to 100 A here, shown in Table 14. This is the only difference in the design specifications for the MnBi IPMSM2 and the MnBi PMASynRM. Despite the merits of the PMASynRM to be explained in Section 4.3 and Section 4.4, this increased demagnetization risk is likely the most significant disadvantage compared to the MnBi IPMSM2. As with the MnBi IPMSM2, the check for high temperature irreversible demagnetization occurs at PM temperature T_{PM1} for all operating points (i.e., current magnitude less than or equal to I_{pk}, all current phases). On the other hand, the check for low temperature irreversible demagnetization occurs at PM temperature T_{PM2} with the current magnitude equal to I_{PM2} in phase with the back EMF (i.e., entirely on the q-axis).

Table 14: MnBi PMASynRM Design Specifications Based on the 2011/2012 Nissan Leaf NdFeB IPMSM and MnBi IPMSM2 Designed in Section 3.0

Input	Range
Phases, m	3
Slots, S	48
Poles, P	8
Number of Series Turns Per Phase, N_s	24 (2 paths)
Stator OD, D_{os}	198 mm
Air gap, g	1 mm
Base Speed, n_b	4000 RPM
Maximum Speed, n_{MAX}	10,000 RPM
Rated Current, I_{rt}	267 A
Peak Current, I_{pk}	480 A
Rated Power, P_{rt}	80 kW
Peak Power, P_{pk}	120 kW
Rated Torque, T_{rt}	160 Nm
Peak Torque, T_{pk}	280 Nm
Rated Slot Current Density (J_s), J_{rt}	9.39 A_{rms}/mm^2
Peak Slot Current Density (J_s), J_{pk}	16.88 A_{rms}/mm^2
Rated Electric Loading (K_s), K_{rt}	65.56 A_{rms}/mm
Peak Electric Loading (K_s), K_{pk}	117.9 A_{rms}/mm
First Critical PM Temperature, T_{PM1}	100 °C
Second Critical PM Temperature, T_{PM2}	0 °C
Maximum Current at T_{PM2}, I_{PM2}	100 A

4.2.1 Optimization Input Variables

Table 15 lists the inputs variables used in the MnBi PMASynRM optimization, including initial ranges (which are then iteratively refined as needed) and color labels corresponding to the

dimensions called out in Figure 35. The design space is limited to flux barriers (i.e., magnets) and flux guides (i.e., rotor ribs) with constant thicknesses between layers. The input magnet thickness (t_m) dictates the thickness of the flux barriers while the input guide to barrier ratio (r_m) dictates the thickness of the flux guides relative to t_m. Some sources suggest varying t_m and r_m between layers and/or using smaller r_m can improve performance [9]. Others [74] suggest that equal flux guides and barriers produces a good combination of high saliency, low torque ripple, and low rotor stress, at least in synchronous reluctance motors without PMs. Initial sensitivity studies suggested the latter conclusions also apply to the MnBi PMASynRM, so the authors restrict $r_m \cong 1$ to improve ROM accuracy.

Table 15 also lists the bridge thickness t_b and post thicknesses of the inner magnet layer. There are three post locations, the "inner" post with thickness t_{ip} (the topmost black dimension in Figure 35), the "outer" post with thickness t_{op} (the bottommost black dimension in Figure 35), and the "center" post with thickness t_{cp} (the black dimension in between the other two posts in Figure 35). As in the MnBi IPMSM2, thicker bridges and posts primarily decrease rotor stress at high speeds and decrease risk of irreversible demagnetization, but they also degrade electromagnetic performance by increasing leakage permeance. Hence, RE-free designs that already suffer from low torque and power density require carefully selecting these post thicknesses.

Unlike t_m and r_m, the post thicknesses decrease from the inner to the outer layer. In fact, only the innermost layer (L1) has a center and outer post, where $t_{cp} = t_{op} = 0$ for the other layers. These posts are included primarily to prevent irreversible demagnetization in the first layer, which empirically was not as much of a risk in the outer layers. Still, these posts also help reduce rotor stress. On the other hand, the inner post is included in every layer to decrease stress,

but its thickness can decrease in outer layers relative to inner layers. The layer-to-layer inner post ratio (r_{ip}) specifies the difference in inner post thickness between adjacent layers. However, a certain minimum post thickness must be specified to be manufacturable [9], and a limit of 0.5 mm is used here.

The remaining rotor parameters are the magnet length (l_x) and offset (f_x) ratios. This study only considers using four layers of flux barriers, and only the first three layers have magnets, so six magnet lengths and six offsets exist. The first layer (L1) is the inner most layer with the largest magnets, followed by the second (L2) and third (L3) layers with sequentially smaller magnets. Each layer has two inner magnets (I) of equal length, one on either side of the center post, and two outer magnets (O) of equal length, one adjacent to each inner post. The abbreviations for the inner/outer magnets and each layer combine to form the subscripts for l_x and f_x in Table 15. For example, l_{OL1} is the outer magnet length ratio for the first layer, but f_{IL3} is the inner magnet offset ratio for the third layer.

For a given stator ID, all previously mentioned inputs (Inputs 1-7 in Table 15) dictate the length of the flux barriers, which also represents the maximum magnet length. The actual magnet length ratio l_x and this maximum magnet length then dictate the maximum magnet offset. The magnet lengths and offsets are normalized based on their maximums according to the convention established in Motor-CAD [23] to avoid geometric conflicts during automated design. For inner magnets, $f_x \in [0,1]$, where $f_x = 0$ and $f_x = 1$ correspond to magnets adjacent to the center and inner posts, respectively. For outer magnets, $f_x \in [-1,1]$ such that $f_x = -1$ and $f_x = 1$ correspond to magnets adjacent to the outer post and bridge, respectively, while $f_x = 0$ now corresponds to a magnet in the middle of the flux barrier, equidistant from the outer post and bridge. Magnet lengths are made as large as possible subject to optimization constraints to

maximize airgap flux density, while magnet offsets are fine tuned in later iterations of the optimization routine to control irreversible demagnetization risk.

Table 15: Optimization Inputs for the MnBi PMASynRM

#	Optimization Input	Figure 35 Color	Initial Range
1	Magnet thickness, t_m	Yellow	3.3-3.4 mm
2	Magnet/Steel Ratio, r_m	Yellow	0.99-1
3	Bridge Thickness, t_b	Red	0.6-1
4, 5, 6	Inner Layer Post Thicknesses, t_{ip}, t_{cp}, t_{op}	Black	(t_{ip}) 0.95-1.05 mm (t_{cp}) 0.95-1.05 mm (t_{op}) 0.55-0.65 mm
7	Layer-to-layer inner post ratio, r_{ip}	N/A	0.95-1
8, 9, 10, 11, 12, 13	Magnet Length Ratios, l_{IL1}, l_{IL2}, l_{IL3}, l_{OL1}, l_{OL2}, l_{OL3}	Pink	(l_{IL1}) 0.7-0.95 (l_{IL2}) 0.7-0.95 (l_{IL3}) 0.7-0.99 (l_{OL1}) 0.7-0.95 (l_{OL2}) 0.7-0.95 (l_{OL3}) 0.7-0.99
14, 16, 17, 18, 19, 19	Magnet Offset Ratios, f_{IL1}, f_{IL2}, f_{IL3}, f_{OL1}, f_{OL2}, f_{OL3}	Blue	(f_{IL1}) 0.3-0.7 (f_{IL2}) 0.3-0.7 (f_{IL3}) 0.3-0.7 (f_{OL1}) -0.7-0 (f_{OL2}) -0.7-0 (f_{OL3}) -0.7-0
20	Slot Depth Ratio, r_{sd}	Grey	0.64-0.71
21	Sator ID / OD Ratio, λ	Green	0.6667-0.68
22	Tooth Width Ratio, r_{tw}	White	0.4-0.5
23	DC Link Voltage, V_{DC}	N/A	425-525 V
24	Stator Length, l_{is}	N/A	180-250 mm

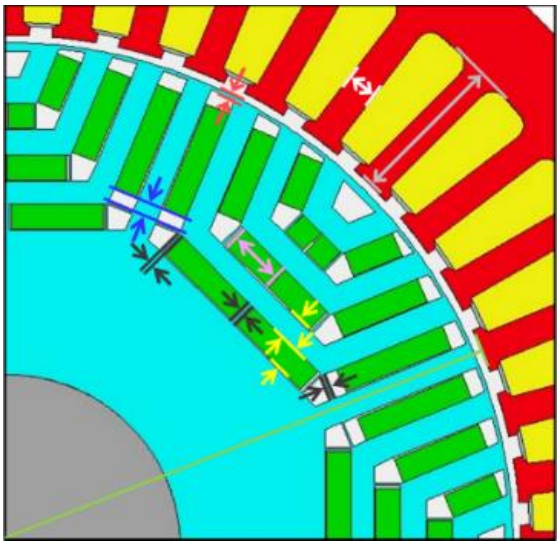

Figure 35: Location of input variables for the MnBi PMASynRM multi-objective optimization.

The remaining variables are standard machine design variables. As with the MnBi IPMSM, Stator length (l_{is}) will increase relative to the reference design to compensate for a lower airgap flux density when using RE-free PM like MnBi according to the sizing equation analysis in Section 2.4, and the DC link voltage (V_{DC}) increases to compensate for a decrease in power factor when using RE-free PMs according to the equivalent circuit analysis in Section 2.5. The "split ratio", or the ratio of stator ID to stator OD (λ), dictates the stator ID according to the stator OD specified in Table 14. An optimal λ exists based on the desired electric loading (i.e., torque production) and cooling capacity. The range of λ in Table 15 searches near that optimal value, as described in Section 3.2.1. Then, the slot depth ratio (r_{sd}) is the ratio of the slot (or tooth) depth to the total depth of the stator, which is half the difference of the stator OD and stator ID. Additionally, the stator ID and the number of slots in Table 14 dictate the slot pitch, which is equal to the theoretical maximum tooth (or slot) width. The tooth width ratio (r_{tw}) is then the ratio of the actual tooth width to the maximum tooth width (i.e., the slot pitch). The authors only consider the slot shape used in the Leaf motor and MnBi IPMSMs.

One implication of the PMASynRM design rules presented here and the parameterization in Table 15 and Figure 35 is that, collectively, Inputs 1-7 determine the number of magnet layers for a given stator ID (which is significantly constrained here by stator OD and λ). To minimize performance degradation due to excessive flux leakage, bridge and post thicknesses (dictated by Inputs 3-7) were made as small as possible while still controlling stress and irreversible demagnetization risk. With r_m (Input 2) restricted by torque/power density, stress, torque ripple, etc. as described earlier, that just leaves magnet thickness (Input 1) primarily determining what the number of layers is. Number of flux barrier layers is limited here to four, where magnets only occupy the innermost three, because initial sensitivity studies found this achieves a good combination of high torque density, high I_{SC}, low torque ripple, and low rotor stress. The maximum magnet thickness while still fitting four layers into the rotor OD specified by λ, stator OD, and gap length is approximately 3.4 mm, the upper limit for t_m. Still, not all designs with $t_m \cong$ 3.4 mm will necessarily have four layers. Designs without four magnet layers are ignored in the sensitivity studies.

4.2.2 Objectives and Constraints

The same objectives are used to design the MnBi PMASynRM as were used for the MnBi IPMSM2: minimize weight (W), maximize short circuit current (I_{SC}), and maximize rated torque (T_{rt}). This selection of objectives aims to maximize torque density, power density, power factor, and CPSR.

Likewise, Table 16 summarizes the constraints, most of which are identical to those used in Table 10 for the MnBi IPMSM2. Constraints 1–7 shape the relationships between torque,

power and speed. P_{rt} and P_{pk} in Constraints 3 and 4 are the maximum power possible with I_{rt} and I_{pk}, respectively, while n_{rt} and n_{pk} in Constraints 5 and 6 are the speed at which P_{rt} and P_{pk} occur, respectively. Although not exactly equal to n_b, the constraints for n_{rt} and n_{pk} assure $n_b \cong 4000$ RPM, as specified in Table 14, because $n_{pk} \cong n_b$ for the ranges of ψ_{mn} and ξ observed here. Results in the following subsection will verify this.

Constraint 7 limits the peak power at the maximum speed (P_{MAX}), which was not considered previously. This constraint ensures that optimal MnBi PMASynRMs achieve higher CPSR and greater power produciton at max speed. This constraint was not included for the MnBi IPMSM2 because all MnBi IPMSMs only achieved a peak power at maximum speed approximately equal to the rated power at maximum speed. This is a symptom of poor power factor due to non-optimal combinations of saliency ξ and normalized PM flux linkage ψ_{mn}, as described in Section 2.5.2.

Constrains 8-13 match their corresponding constraints used to design the MnBi IPMSM2 in Section 3.4.3. Constraint 8 limits cost of active material to less than the estimated cost of the Leaf, assuming \$70/kg for NdFeB, \$11/kg for MnBi, \$2.2/kg for steel, and \$9.5/kg for copper. In lew of redesigning thermal management or a more detailed thermal analysis in the optimaizaiton routine, Constraints 9-13 aim to restrict the losses and, therefore, temperature rise to be no greater than those of the Leaf.

To control low temperature irreversible demagnetization risk, Constraint 14 and Constraint 15 limit the FEA demagnetzation ratios at different temperatures (DR_1 at T_{PM1} and DR_2 at T_{PM2}), The demagnetization ratio is the ratio of the number of PM finite elements that irreversibly demagnetize to the total number of PM finite elements. Due difficulties approximating demagnetization ratios with a ROM as a result of quantization effects, the limits

in Constraint 14 and Constraint 15 are actually a small, nonzero value that is adjusted on a case-by-case basis in each design iteration. After ROM optimization, FEA validates that $DR_1 = 0$ and $DR_2 = 0$ for optimal designs, and this iterative design process can be repeated to reduce DR_1 and DR_2 validition error as desired. As explained previously, Constarint 14 is caclculated at T_{PM1} for all operating points, and Constraint 15 is calculated at T_{PM2} with the current magnitude I_{PM2} from Table 14 in phase with the back EMF.

The remaining constraints primarily effect the motor mechanically. To avoid the first critical rotation speed of the rotor, Constraint 16 limits the "aspect ratio" (or the ratio of rotor length, l_r, to rotor outer radius, r_{or}) to no greater than 7. To further limit vibrations, Constraint 17 restricts the torque ripple.

Finally, Constraint 18 limits the maximum rotor stress (σ_{MAX}) at 1.2 times the maximum speed. Two PMASynRM designs will be studied here. For PMASynRM2, the stress is limited to the same value used for IPMSM2, hence suffix "2" for both designs. While PMASynRM2 will achieve higher torque density, power density, and CPSR, experiencing higher σ_{MAX} than the rotor lamination yield stress (305 MPa) requires lowering the maximum speed, barring an advanced mechanical design to lower σ_{MAX} in the PMASynRM2 as in [61] for the NdFeB Leaf IPMSM. On the other hand, Constraint 18 for PMASynRM3 limits σ_{MAX} to less than the yield stress of the rotor steel (305 MPa). While the PMASynRM3 designs can safely achieve the maximum speed in Table 14 as designed, they inevitably achieve lower torque density, power density, and CPSR than the PMASynRM2 because increasing post and bridge thickness to lower rotor lamination stress degrades electromagnetic performance, as shown in Section 3.4 and Section 3.5 for the MnBi IPMSM.

Table 16: Optimization Constraints for the MnBi PMASynRM

No.	Outputs	Range
1.	Peak Torque, T_{pk} (Nm)	$280 \leq T_{pk} \leq 300$
2.	Rated Torque, T_{rt} (Nm)	$150 \leq T_{rt}$
3.	Peak Power, P_{pk} (kW)	$120 \leq P_{pk}$
4.	Rated Power, P_{rt} (kW)	$80 \leq P_{rt} \leq 100$
5.	Min. Speed at P_{pk}, n_{pk} (kRPM)	$4 \leq n_{pk}$
6.	Min. Speed at P_{rt}, n_{rt} (kRPM)	$4 \leq n_{rt}$
7.	Peak Power at Max Speed, P_{MAX} (kW)	$P_{MAX} \geq 110$
8.	Estimated Material Cost, USD ($)	$USD < 250.54$
9.	Max Electric Loading, K_s (Arm/mm)	$K_s < 117.9$
10.	Max Slot Current Density, J_s (Arms/mm^2)	$J_s < 16.88$
11.	Max Tooth Flux Density, B_{ts} (T)	$B_{ts} \leq 1.9$
12.	Max Core Flux Density, B_{cs} (T)	$B_{cs} < 1.7$
13.	Min. Average WLTP3 Efficiency, η (%)	$92.4 < \eta$
14.	Demag. Ratio at T_{PM1}, DR_1	$DR_1 \leq 0$
15.	Demag. Ratio at T_{PM2}, DR_2 (mm^3/mm^3)	$DR_2 \leq 0$
16.	Aspect Ratio, l_r/r_{or} (mm/mm)	$l_r/r_{or} < 7$
17.	Torque Ripple, T_{rip} (%)	$T_{rip} < 10$
18.	Max Rotor Stress, σ_{MAX} (MPa)	$\sigma_{MAX} < 585.475$ (PMASynRM2) $\sigma_{MAX} < 305$ (PMASynRM3)

4.3 Optimized MnBi PMASynRM Design

The results in this section primarily focus on MnBi PMASynRM3, while the next section will draw comparisons between MnBi PMASynRM2, MnBi PMASynRM3, and MnBi IPMSM2. Table 17 shows the COP matrix for first design iteration using design, input ranges, and constraints in Section 4.2. All outputs have a COP >97%, which is sufficient [4], [13], except for

DR_2 and σ_{MAX}. However, as explained in Section 3.4.4 and Section 3.4.5, these are expected to have low COPs due to quantization for the former and noise in the FEA outputs for the latter. Nevertheless, the iterative design procedure can still find Pareto-optimal designs despite these low COPs because the ROM only needs to predict when DR_2 or σ_{MAX} violates a constraint, not their exact value throughout the design space. Still, more accurate FEA solvers could likely find optimal designs with greater fitness than the design presented here. DR_1 is excluded because all designs satisfied that constraint.

Table 17: Coefficient of Prognosis (COP) Matrix for the MnBi PMASynRM Reduced Order Model

	t_m	t_b	r_m	r_{ip}	t_{cp}	t_{ip}	t_{op}	l_{IL1}	l_{IL2}	l_{IL3}	l_{OL1}	l_{OL2}	l_{OL3}	r_{sw}	λ	l_{is}	r_{tw}	V_{DC}	Sum
W	0.000	0.000	0.000	0.000	0.000	0.000	0.000	0.000	0.000	0.000	0.001	0.001	0.000	0.013	0.000	0.943	0.028	0.000	0.998
η	0.002	0.017	0.000	0.000	0.000	0.000	0.000	0.059	0.008	0.001	0.078	0.009	0.027	0.100	0.007	0.081	0.566	0.045	0.977
T_{rip}	0.112	0.027	0.002	0.003	0.000	0.000	0.003	0.083	0.000	0.011	0.400	0.061	0.078	0.122	0.001	0.000	0.076	0.000	0.981
B_{ts}	0.000	0.002	0.000	0.000	0.000	0.000	0.000	0.000	0.000	0.000	0.005	0.002	0.004	0.131	0.005	0.000	0.830	0.000	0.978
σ_{MAX}	0.048	0.090	0.000	0.028	0.021	0.034	0.000	0.000	0.028	0.016	0.000	0.021	0.054	0.000	0.163	0.000	0.007	0.000	0.483
I_{SC}	0.006	0.281	0.000	0.005	0.000	0.020	0.004	0.133	0.078	0.005	0.201	0.212	0.022	0.009	0.021	0.002	0.004	0.000	0.997
T_{rt}	0.000	0.037	0.000	0.000	0.000	0.004	0.000	0.012	0.007	0.001	0.018	0.029	0.005	0.005	0.013	0.748	0.093	0.000	0.982
n_{rt}	0.001	0.122	0.000	0.003	0.000	0.007	0.002	0.040	0.020	0.004	0.054	0.051	0.021	0.001	0.006	0.309	0.071	0.285	0.994
P_{rt}	0.000	0.078	0.000	0.002	0.000	0.006	0.000	0.026	0.011	0.003	0.042	0.042	0.016	0.001	0.008	0.000	0.010	0.762	0.995
T_{pk}	0.000	0.027	0.000	0.002	0.000	0.003	0.000	0.010	0.005	0.001	0.016	0.015	0.005	0.030	0.013	0.718	0.160	0.000	0.998
n_{pk}	0.000	0.006	0.000	0.000	0.000	0.000	0.000	0.002	0.001	0.000	0.002	0.002	0.001	0.002	0.000	0.480	0.117	0.383	0.996
P_{MAX}	0.000	0.120	0.000	0.004	0.000	0.011	0.000	0.031	0.019	0.005	0.056	0.058	0.021	0.001	0.011	0.027	0.031	0.607	0.996
P_{pk}	0.000	0.061	0.000	0.002	0.000	0.005	0.000	0.021	0.012	0.002	0.030	0.034	0.012	0.007	0.016	0.000	0.001	0.816	0.996
K_s	0.000	0.000	0.000	0.000	0.000	0.000	0.000	0.000	0.000	0.000	0.000	0.000	0.000	0.000	1.000	0.000	0.000	0.000	1.000
DR_2	0.000	0.000	0.000	0.000	0.000	0.000	0.000	0.174	0.000	0.000	0.629	0.189	0.000	0.000	0.000	0.000	0.000	0.000	0.737
USD	0.001	0.000	0.000	0.000	0.000	0.000	0.000	0.009	0.000	0.000	0.011	0.006	0.003	0.003	0.001	0.952	0.007	0.000	0.999
B_{cs}	0.000	0.000	0.000	0.000	0.000	0.000	0.000	0.000	0.000	0.000	0.000	0.000	0.001	0.669	0.051	0.000	0.274	0.000	0.986

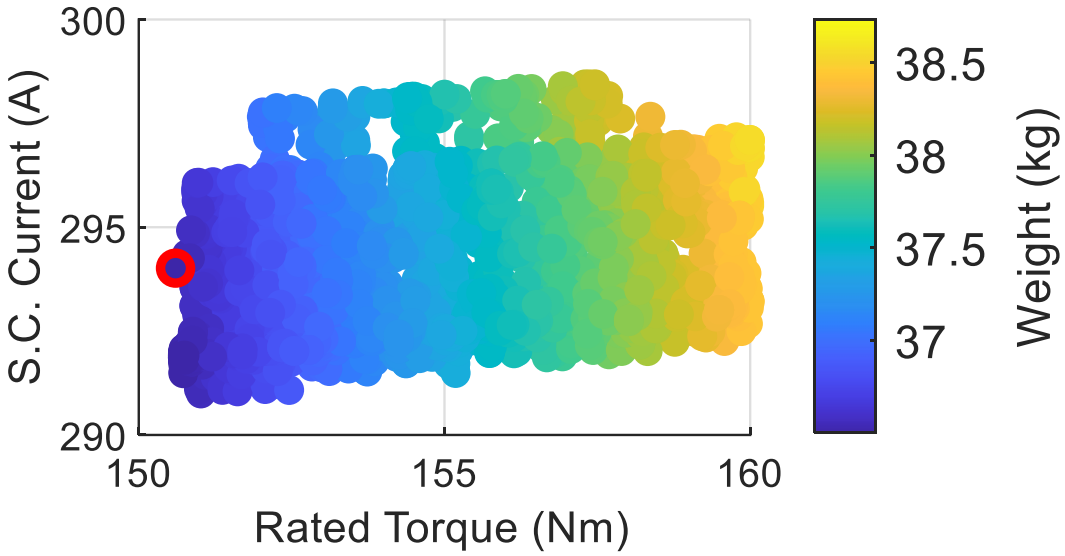

(a) MnBi PMASynRM2

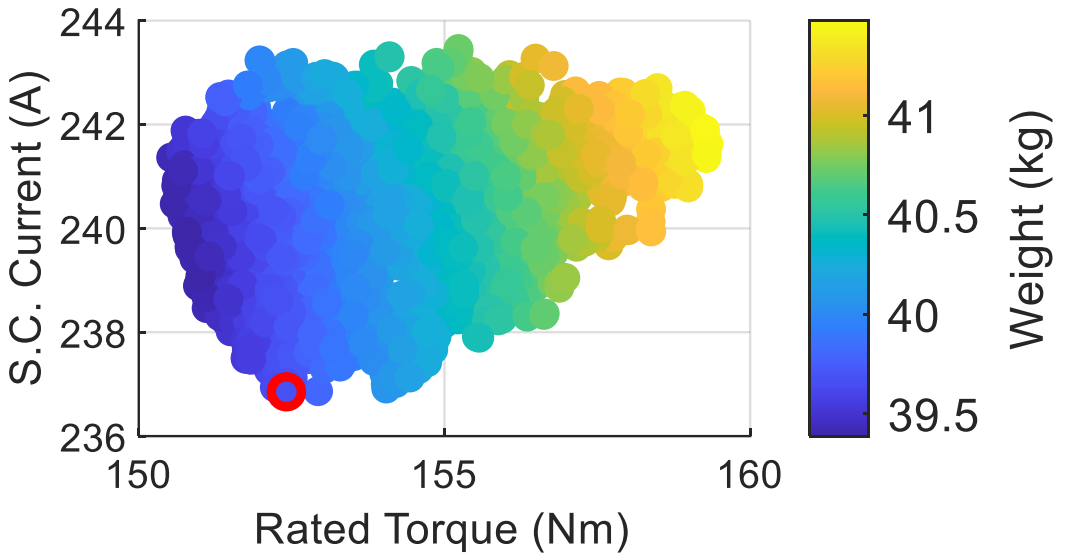

(b) MnBi PMASynRM3

Figure 36: Pareto optimal front for the final iteration of the PMASynRM multi-objective optimization using FEA reduced order modeling.

Figure 36(a) shows the Pareto optimal front for the final of five PMASynRM2 optimization iterations, and Figure 36(b) shows the Pareto optimal front for the final of seven PMASynRM3 optimization iteration. In both, weight is calculated excluding shaft weight, and

the lightest Pareto optimal design still feasible after FEA validation is circled in red. Figure 37 shows the radial and axial cross-sections of this design for PMASynRm3 (Design #9424). It has an active weight of 39.4 kg (excluding the shaft), a rated torque of 158.67 Nm, and a short circuit current of 234.3 A.

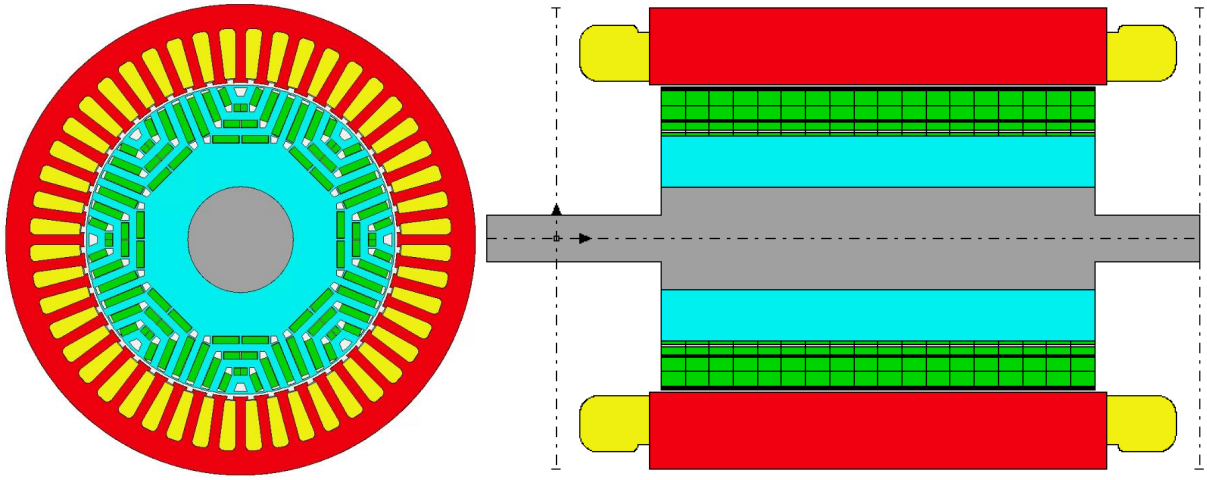

(a) **(b)**

Figure 37: (a) Radial and (b) axial cross-section of the lightest MnBi PMASynRM3 optimal design #9424

Table 18 compares MnBi PMASynRM3 Design #9424 to the NdFeB Leaf motor and the lightest Pareto optimal designs from all other topologies that remains feasible after validation. All data in the table was calculated at a motor temperature of 65°C. The table shows that the MnBi PMASynRM3 is only 1.23x heavier than the Leaf motor whereas the MnBi IPMSM2 is 1.37x heavier. In addition, the MnBi PMASynRM3 achieves 6.0% lower cost than the MnBi IPMSM2. MnBi PMASynRM2 is only 1.10x heavier than the Leaf motor with the lowest cost of all designs in Table 18, but barring a more advanced mechanical design optimization as in [61], the maximum speed of the PMASynRM2 must be decreased from 10,00 RPM to 7,500 RPM due to excessive rotor bridge stress,.

The MnBi PMASynRM3 achieves 4.0% higher magnetic loading to the MnBi IPMSM2 and essentially equal electric loading. Even so, the PMASynRM3 has about 33.0% higher short

circuit current than the MnBi IPMSM2, leading to a 5.48% increase in power factor in the MnBi PMASynRM3. This allows for the decrease in DC link voltage from 500 V in the MnBi IPMSMI to 486.2 V for the PMASynRM3. Although the MnBi IPMSM2 and PMASynRM3 have similar ξ as the Leaf motor, the MnBi PMASynR3M has 20.7% higher I_{SC} than the MnBi IPMSM2. L_d is about equal in the IPMSM2 and PMASynRM3, meaning ψ_{mn} increases in the PMASynRM3 compared to the IPMSM2. As a result, the MnBi PMASynRM3 can now achieve 110 kW of constant power above base speed with a lower V_{DC} than the MnBi IPMSM2, shown in Figure 38.

Lowering PMASynRM3 V_{DC} to about 450 V yields about the same P_{pk} as in the MnBi IPMSM2. In this case, the PMASynRM3 can produce about 100 kW of constant power above base speed, whereas the MnBi IPMSM2 can only do so up to about 7000 RPM. The maximum power at I_{rt} is 100 kW with 486 V or 90 kW with 450 V, but in both cases, the PMASynRM3 can effectively only produce 80 kW of constant power because the maximum power only occurs at the maximum speed [17]. Still, I_{SC} is much lower in both MnBi designs than in the Leaf motor, so both the MnBi IPMSM2 and PMASynRM3 designs cannot achieve 120 kW of constant power during flux weakening.

Table 18: Comparing the Leaf NdFeB IPMSM, MnBi IPMSMs, and MnBi PMASynRMs

	Metric			NdFeB Leaf IPMSM	MnBi IPMSM1 Design #9872 (Lightest)		MnBi IPMSM2 Design #7413 (Lightest)		MnBi PMASynRM2 Design #9674 (Lightest)		MnBi PMASynRM3 Design #9424 (Lightest)	
					Value	Δ	Value	Δ	Value	Δ	Value	Δ
Geometry	Stator OD, mm			198	198	0.0%	198.00	0.0%	198.00	0.0%	198	0.00%
	Rotor OD, mm			130	130.7	0.5%	131.65	1.3%	133.53	2.7%	130.1	0.05%
	Active Length, mm			160	214.0	33.8%	216.73	35.5%	173.38	8.4%	196.8	23.02%
	Active Volume, L			4.93	6.59	33.8%	6.67	35.5%	5.34	8.4%	6.06	23.02%
	Weight (without shaft), kg			31.9	42.7	33.6%	43.7	36.9%	35.2	10.3%	39.4	23.44%
	Magnet Weight, kg			1.97	4.00	103.3%	5.20	164.7%	4.32	119.9%	4.891	148.91%
	Steel Weigth (without shaft), kg			23.5	30.8	31.0%	30.55	30.0%	24.06	2.4%	27.08	15.23%
	Copper Weight, kg			6.45	7.86	21.9%	7.94	23.0%	6.84	6.0%	7.427	15.11%
	Total Cost (whtout shaft), $			250.5	186.4	-25.6%	199.9	-20.2%	165.4	-34.0%	183.93	-26.59%
	Magnet Cost, $			137.6	44.0	-68.0%	57.2	-58.4%	47.5	-65.4%	53.80	-60.89%
	Steel Cost (without shaft), $			51.7	67.7	31.0%	67.2	30.0%	52.9	2.4%	59.58	15.23%
	Copper Cost, $			61.3	74.7	21.9%	75.4	23.0%	65.0	6.0%	70.56	15.11%
	Slot Copper Fill Factor			0.52	0.52	0.0%	0.52	0.0%	0.52	0.0%	0.5198	0.02%
Performance	Maximum Speed, RPM			10,000	6,250	-37.5%	10,000	0.0%	7,500	-25.0%	10,000	0.00%
	Torque, Nm (65°C)	*0 RPM*	*Rated Current*	160.1	166.7	4.1%	158.84	-0.8%	156.44	-2.3%	158.67	-0.91%
		0 RPM	*Peak Current*	280.5	300.6	7.1%	290.52	3.6%	287.61	2.5%	289.0	3.01%
	Power, kW (65°C)	*Max*	*Rated Current*	83.8	93.01	11.0%	94.72	13.0%	89.40	6.7%	101.84	21.52%
		Max	*Peak Current*	132.1	130.6	-1.2%	132.12	0.0%	129.99	-1.6%	139.6	5.65%
		10k RPM	*Rated Current*	79.4243	90.9075	14.5%	93.88	18.2%	89.40	12.6%	101.84	28.22%
		10k RPM	*Peak Current*	124.9	92.3524	-26.0%	97.58	-21.8%	114.29	-8.5%	114.17	-8.56%
	Average Drive Cycle Efficiency, % (65°C)	*WLTP3*		93.7	95.6	1.9%	95.94	2.3%	95.16	1.5%	95.61	1.99%
		UDDS		93.8	95.1	1.4%	95.48	1.8%	94.72	1.0%	95.23	1.52%
		US06		94.2	95.5	1.4%	95.76	1.7%	95.20	1.1%	95.50	1.42%
		HWFET		91.6	95.3	4.0%	95.70	4.4%	93.54	2.1%	94.88	3.55%
	Losses, W (1000 RPM, 150 Nm, 65°C)	*Copper*		1161	1344.0	15.8%	1460.00	25.8%	1292.00	11.3%	1369	17.92%
		Steel		143.9	180.1	25.2%	148.70	3.3%	161.00	11.9%	160.9	11.81%
		Magnet		0.191	0.006	-96.9%	0.001	-99.5%	0.02	-87.9%	0.02272	-88.11%
Electrical	DC Link Voltage, V			375	500	33.3%	500.00	33.3%	400.00	6.7%	486.2	29.65%
	Current, A	*Rated*		267	267	0.0%	267.00	0.0%	267.00	0.0%	267	0.00%
		Peak		480	480	0.0%	480.00	0.0%	480.00	0.0%	480	0.00%
	Power Factor at Terminals, 1000 RPM			0.788	0.682	-13.5%	0.68	-13.5%	0.79	0.0%	0.71934	-8.71%
	Slot Current Density, $Arms/mm^2$			16.88	16.88	0.0%	16.88	0.0%	16.88	0.0%	16.88	0.00%
	Peak Electric Loading, kArms/m			117.9	117.3	-0.5%	116.40	-1.3%	114.80	-2.6%	117.8	-0.08%
	Saturated d-axis Inductance, mH			0.162	0.230	42.1%	0.24	48.8%	0.19	18.0%	0.2367	46.29%
	Saturated q-axis Inductance, mH			0.376	0.509	35.1%	0.50	32.2%	0.47	24.8%	0.5229	38.92%
	Saturated Saliency Ratio			2.326	2.212	-4.9%	2.067	-11.2%	2.460	5.8%	2.209	-5.04%
	Saturated S.C. Current, A (65°C)			353.8	167.4	-52.7%	176.20	-50.2%	303.00	-14.4%	234.3	-33.78%
Magnetic	Magnetic Loading, T	*Rated Current*		0.905	0.779	-13.9%	0.71	-21.7%	0.77	-14.5%	0.72578	-19.77%
		Peak Current		1.006	0.933	-7.3%	0.86	-14.7%	0.93	-7.4%	0.89236	-11.27%
	Max Flux Density, T	*Rated Current*	*Tooth*	1.677	1.633	-2.6%	1.58	-5.9%	1.60	-4.4%	1.562	-6.86%
			Tooth Tip	1.670	1.616	-3.2%	1.72	3.2%	1.58	-5.3%	1.498	-10.30%
			Core	1.383	1.359	-1.7%	1.22	-11.8%	1.40	1.4%	1.38	-0.22%
		Peak Current	*Tooth*	1.898	1.863	-1.8%	1.80	-5.4%	1.83	-3.4%	1.802	-5.06%
			Tooth Tip	1.906	1.950	2.3%	2.00	4.9%	1.92	0.8%	1.835	-3.73%
			Core	1.681	1.644	-2.2%	1.58	-6.2%	1.70	0.9%	1.672	-0.54%
Mechanical	Torque Ripple, %			6.20	6.10	-1.7%	8.40	35.4%	9.65	55.6%	7.4662	20.37%
	Rotor Aspect Ratio			2.31	3.12	35.3%	3.14	36.1%	2.45	6.0%	2.87279	24.49%
	Max Stress at 12,000 RPM, Mpa			532.5	1342	152.0%	490.40	-7.9%	529.50	-0.6%	284.5	-46.57%

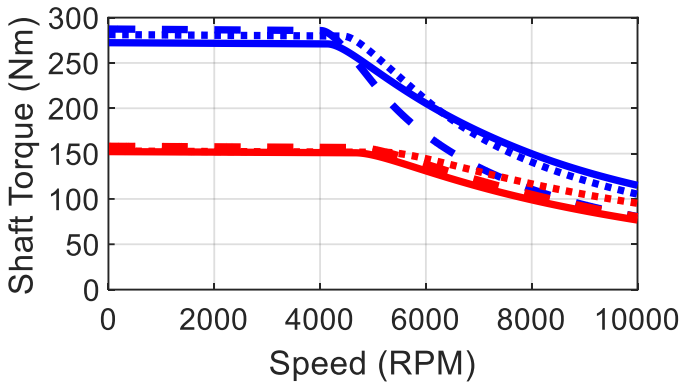

(a)

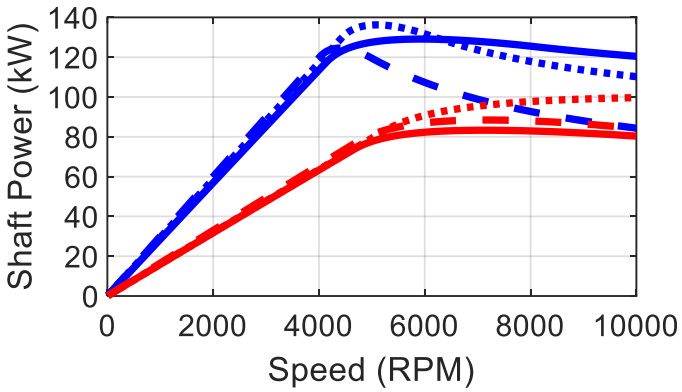

(b)

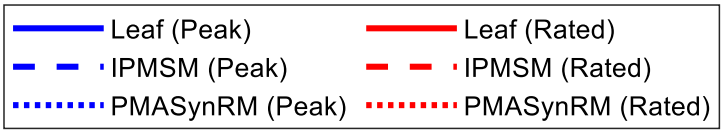

Figure 38: (a) Torque and (b) power vs speed for the Leaf NdFeB IPMSM reference, the intial MnBi IPMSM1, and MnBi PMASynRM3 Design #9424

Figure 39 maps the motors' efficiency and superimposes the drive cycle operating points used to calculate the average efficiencies in Table 18. The PMASynRM3 has greater peak efficiency and greater efficiency than the NdFeB Leaf IPMSM, the MnBi IPMSM1, and the MnBi IPMSM2 at high speed and low torque, which is the most common operating region for EV driving. Similarly, Figure 40 shows the temperature rise in key components is lowest in the

MnBi PMASynRM3 at 150 Nm and 1,000 RPM when using the same cooling system as the Leaf and IPMSM motors. Figure 41 shows a contour plot of safe operating points ($i.e. DR = 0$ according to FEA) as temperature changes. Low temperature irreversible demagnetization remains a risk in the MnBi PMASynRM3, though improved compared to the initial MnBi IPMSM1 in Section 3.2.

These performance improvements compared to the MnBi IPMSM1 and MnBi IPMSM2 come despite the significant decrease in rotor lamination stress, as shown in Table 18, due to the optimized post and bridge thicknesses. The Leaf σ_{MAX} in Table 18 exceeds the rotor yield stress because this study uses a simplified rotor duct structure (Figure 2) compared to the actual duct structure in [61] for simpler automated design. The PMASynRM2 achieves significantly higher torque density and short circuit current with lower σ_{MAX}. However, the maximum rotor speed must lower from 10,000 RPM to 7,500 RPM due to high rotor lamination stress at high speeds. Regarding the other mechanical aspects of Table 18, the torque ripple is lower in the PMASynRM3 than in the MnBi IPMSM2 but higher than in the MnBi IPMSM1 and Leaf IPMSM. The rotor aspect ratios for all designs are well below its limit to avoid the first critical rotation speed.

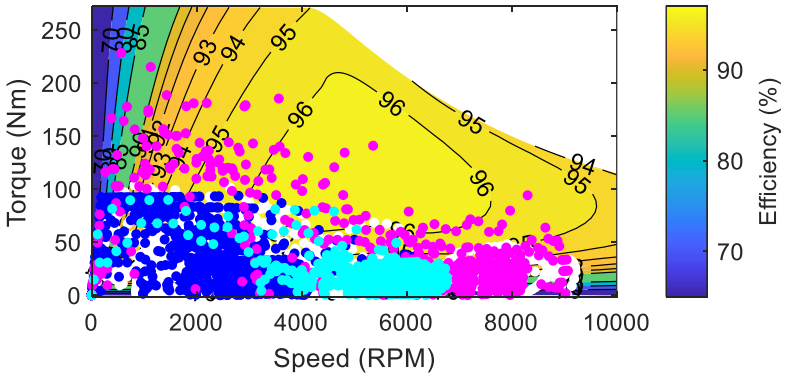

(a)

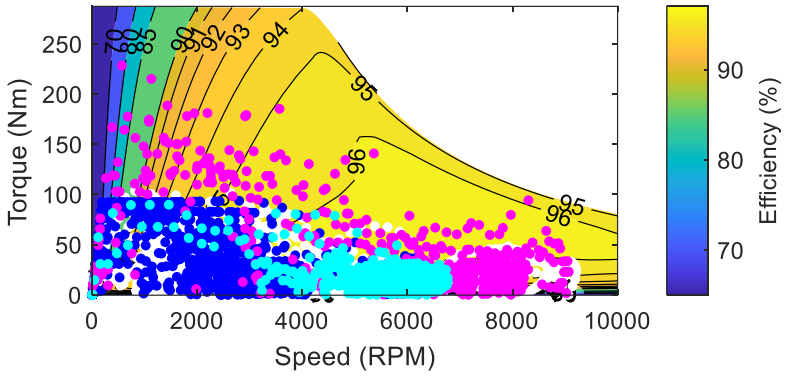

(b)

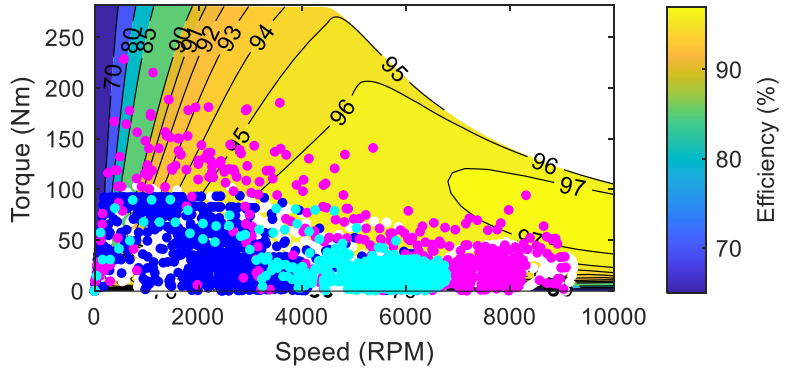

(c)

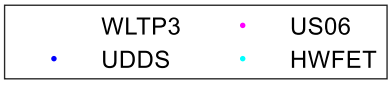

Figure 39: Comparing efficiency maps of the (a) Leaf NdFeB IPMSM reference, (b) the initial MnBi IPMSM1, and (c) the MnBi PMASynRM3 Design #9424

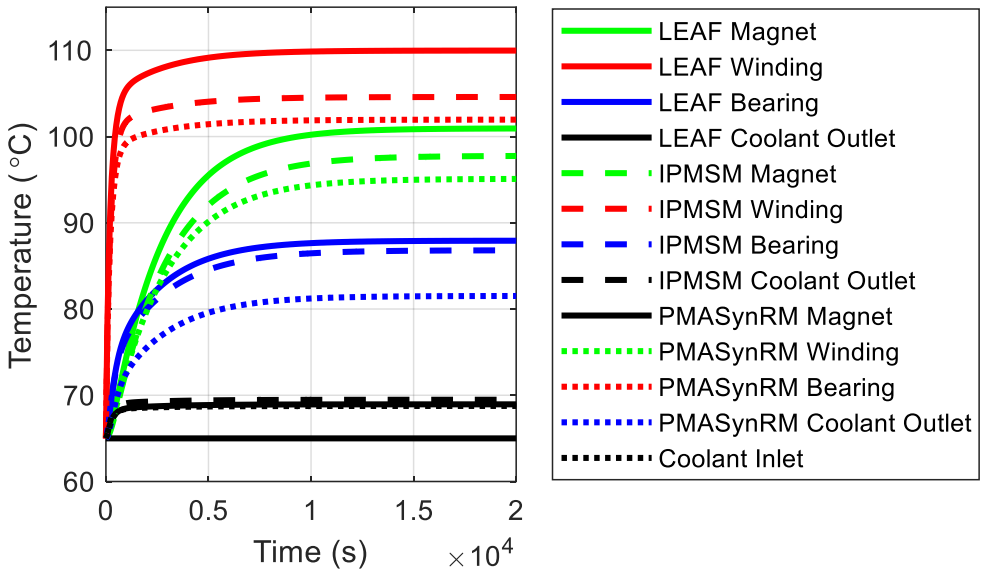

Figure 40: Steady state temperature rise of the (a) Leaf NdFeB IPMSM, (b) MnBi IPMSM1, and (c) MnBi PMASynRM3 at 150 Nm and 1000 RPM

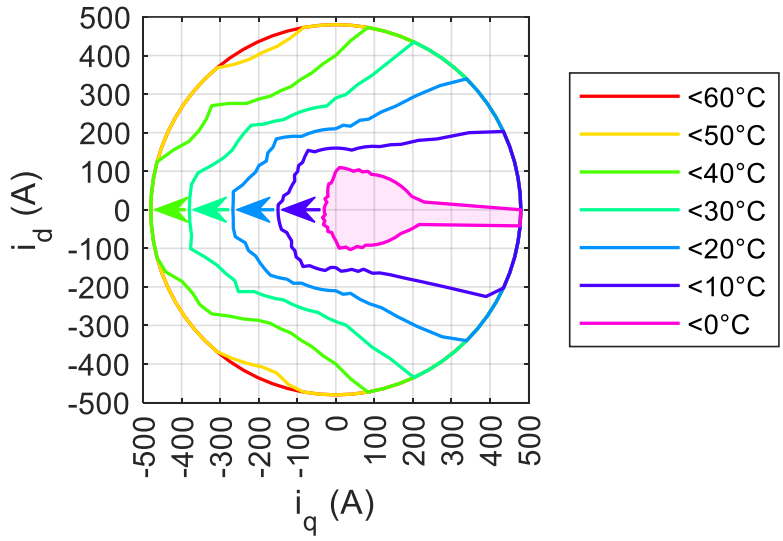

Figure 41: Contour plot enclosing operating regions with no risk of irreversible demagnetization as magnet temperature changes in the PMASynRM3s

4.4 Trends Among MnBi PMASynRM and MnBi IPMSM and Pareto Fronts

This subsection compares all validated, Pareto optimal MnBi PMSMs for both the IPMSM and PMASynRM. Results in this section are calculated for a motor temperature of 100°C. Figure 42 and Figure 43 compares the Pareto optimal front and σ_{MAX}, respectively, for the subset of 20 Pareto optimal designs validated in FEA. Here, torque density represents the objectives to maximize weight and minimize rated torque simultaneously. Figure 43 plots a normalized σ_{MAX}, where a normalized value equal to 1 correspond to the yield stress of the rotor laminations (305 MPa). Post thickness (black arrows in Figure 15) differentiates IPMSM1 (no posts, post thickness = 0, unconstrained σ_{MAX}) and IPMSM2 (min post thickness = 0.6 mm, σ_{MAX} constrained). The Leaf uses the IPMSM1 topology but has sufficiently low σ_{MAX} without posts because it uses less PM material and more complex rotor ducts. As shown in [61], a more detailed mechanical design procedure can substantially lower σ_{MAX} to below the rotor laminations yield stress (i.e., 305 MPa for M19 steel [23]). Furthermore, this can achieve lower σ_{MAX} without substantially degrading torque density if the amount of leakage flux through the rotor bridges does not change substantially [61].

In lieu of a more detailed mechanical design for the PMASynRM (i.e., as done in [61] for the IPMSM), the authors present two different PMASynRM designs here. In particular, PMASynRM2 has thinner posts, yielding similar σ_{MAX} as IPMSM2, while PMASynRM3 has thicker posts, thereby achieving σ_{MAX} less than the rotor lamination yield stress. More specifically, the authors use post thicknesses closer to the lower bounds in Table III for PMASynRM2 yet closer to the upper bounds for PMASynRM3.

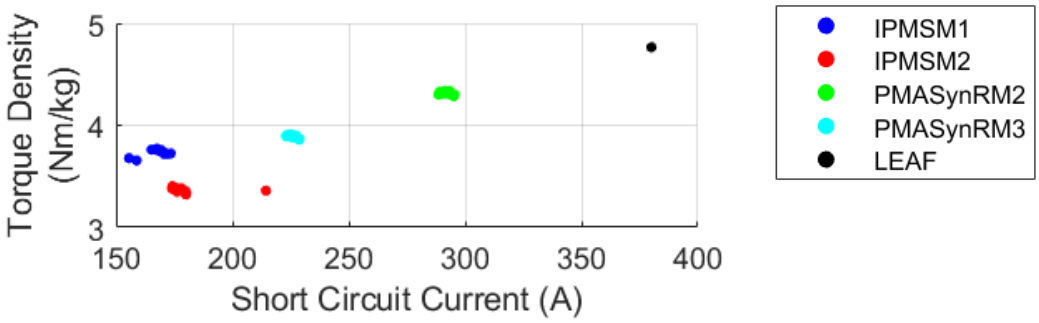

Figure 42: Comparing the Pareto optimal designs validated in FEA as a function of short circuit current and torque density (calculated using the rated torque and weight excluding housing, cooling, shaft, and bearings).

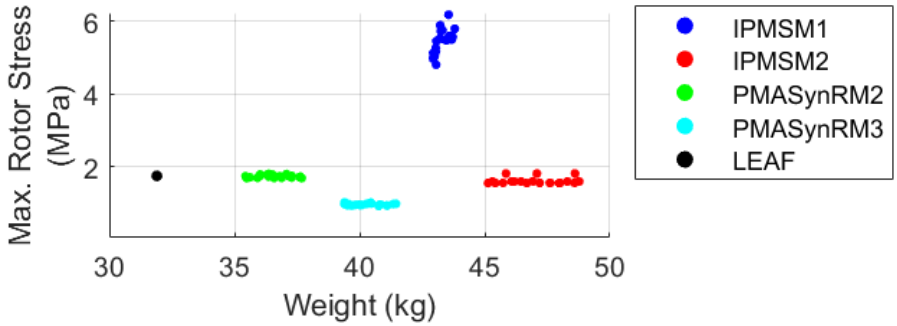

Figure 43: Comparing the maximum rotor stress (σ_{MAX}) for all validated Pareto optimal designs

4.4.1 Capability Curves

Figure 44 shows the rated and peak power vs. speed and torque vs. speed curves for the lightest Pareto optimal designs among each topology. As shown in Figure 43 and mentioned previously, the Leaf and IPMSM2 designs have excessive σ_{MAX}, due to the simplified rotor duct designs used in FEA modeling, but previous work from Nissan [61] suggests that carefully optimizing rotor duct shapes can sufficiently lower σ_{MAX} without significantly impacting electromagnetic performance if the amount of leakage flux in the rotor bridges does not

significantly change. Even so, results in Figure 44 are for a Pareto optimal IPMSM2 with T_{pk} near the maximum allowable value (300 Nm) to account for slight degradation in electromagnetic performance when adjusting rotor duct structure to lower σ_{MAX}.

Therefore, the authors assume the speed range of the Leaf, IPMSM2, and PMASynRm3 do not need to decrease due to excessive σ_{MAX} if considering more advanced duct structures. However, the authors do assume the speed range of IPMSM1 and PMASynRM2 would need to decrease compared to the Leaf, IPMSM2, and PMASynRM3. In particular, the IPMSM1 speed range must decrease because σ_{MAX} is likely too high to remedy by using advanced duct designs as in [61], while the speed range of the PMASynRM2 must decrease because no detailed mechanical designs exist for the PMASynRM as for the IPMSM in [61].

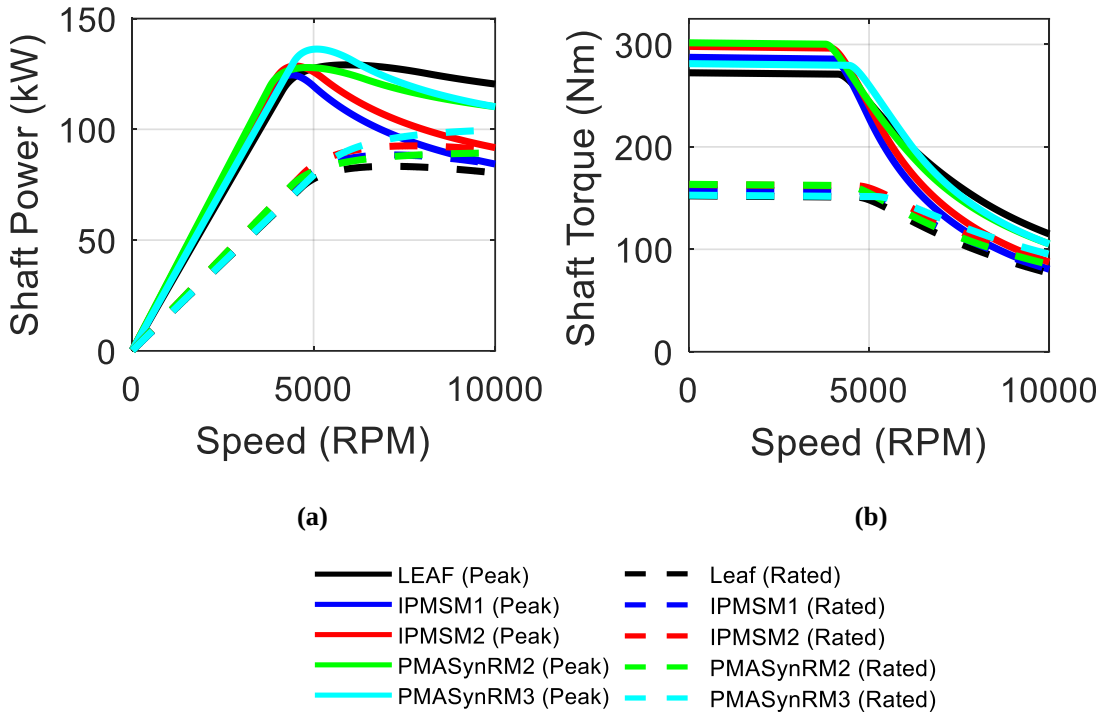

Figure 44: Comparing power (a) and torque (b) capability curves for the lightest Pareto optimal designs.

Figure 45 shows the active material cost for all designs in Figure 42. In Figure 45(a), the "total" cost is normalized according to the cost of active materials reported for the Leaf motor in

Table 18, with a price of \$70/kg for NdFeB, \$11/kg for MnBi, \$2.2/kg for steel, and \$9.5/kg. Likewise, the cost of copper and steel ("Cu+Fe") and cost of the PMs ("PM") is normalized according to the costs reported in Table 18 for the Leaf. Figure 45(b) shows the same costs as Figure 45(a) but divided by the rotor length. The IPMSM2 is the most expensive design overall in Figure 45(a), but Figure 45(b) suggests this is because this design is longer. In fact, the PM cost per unit length is approximately the same for all IPMSM2 and PMASynRM designs, but it is actually slightly *higher* in the PMASynRM2 than PMASynRM3, and slightly *higher* in the PMASynRM3 than in the IPMSM2. The cost of the copper and steel per unit length increases more noticeably in lighter designs, likely because end windings are a larger percentage of the copper mass in lighter designs. The IPMSM1 and PMASynRM3 have comparable cost, but the high σ_{MAX} of IPMSM1 is impractical.

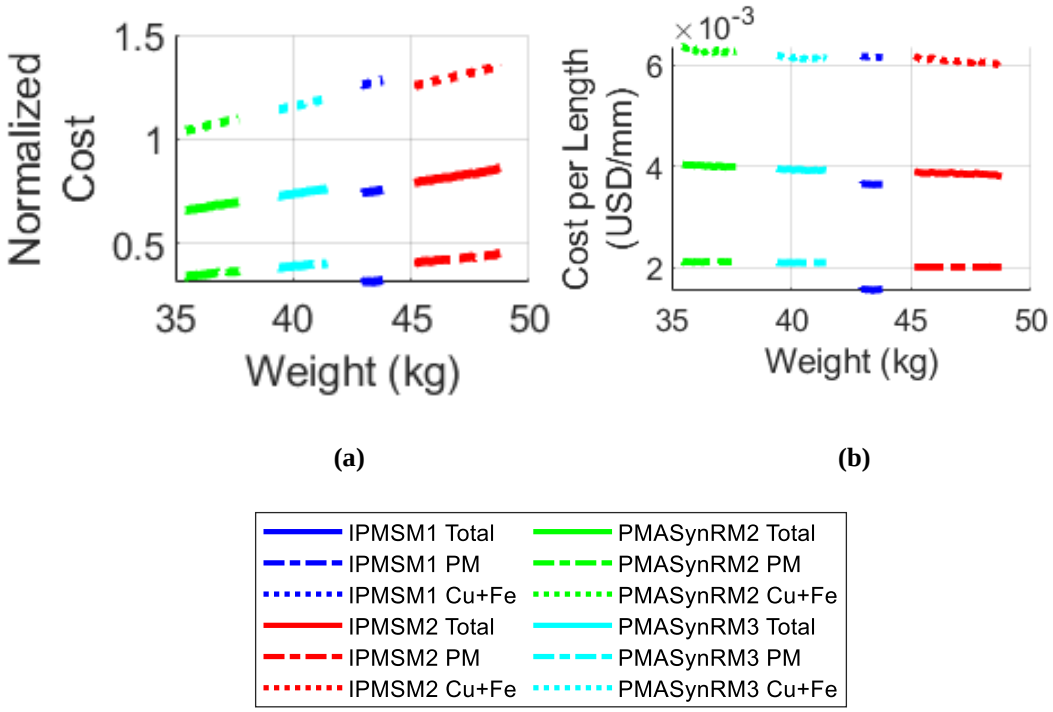

Figure 45: Comparing cost of active materials for the motor overall (a) and per unit length of the rotor (b) for all validated Pareto optimal designs.

Figure 46 compares the power production at peak current (i.e., P_{pk} and P_{MAX}) for the validated Pareto optimal designs in Figure 42. All MnBi designs here fail to achieve $P_{MAX} \geq 120\ kW$. However, all Pareto optimal PMASynRM2 and PMASynRM3 designs have $P_{MAX} \geq 110\ kW$, an 8.33% decrease compared to $120\ kW$ for the Leaf motor. On the other hand, all IPMSM1 and IPMSM2 designs have $P_{MAX} \leq 97\ kW$, a decrease of at least 19% from the Leaf motor. The maximum power at rated current (P_{rt}) increases in the MnBi designs compared to the Leaf motor, but because the maximum rated power of the MnBi designs occurs near the maximum motor speed, the MnBi motors can still only effectively achieve 80 kW of constant power at rated current. This equals the Leaf motor's rated power. PMASynRM3 results are included for two different DC link voltages: 1) a DC link voltage of about 485 V that results in the same P_{MAX} as the PMASynRM2, and 2) a 450 V DC link that yields a P_{pk} similar to that of all other designs Figure 46. Even at 450 V, the PMASynRM3 outperforms the IPMSM2, which uses a 500 V DC link.

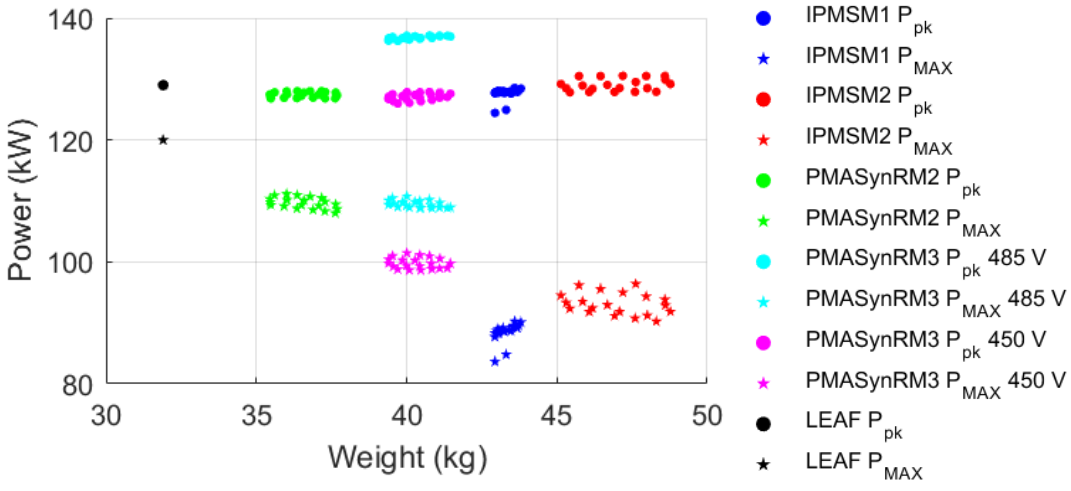

Figure 46: Comparing peak power production in the flux weakening regime for the validated Pareto optimal designs

The improvement in P_{MAX} in terms of kW/kg and $kW/\$$ is the most notable advantage of the MnBi PMASynRM compared to the MnBi IPMSM. The subsequent sizing equation and

equivalent circuit analyses suggest the improvement occurs due to improved flux focusing and saturated saliency ratio in the PMASynRM compared to the IPMSM, resulting in lighter designs with higher short circuit current and thus lower DC link voltages. However, this improvement comes at the expense of increased demagnetization risk at low temperatures, as shown by comparing Figure 23 and Figure 41.

4.4.2 Sizing Equation Parameters and Torque Density

Figure 47 shows the most signficiant sizing equations variables for the Pareto optimal designs in Figure 42. The author predicted a 40% weight increase in Section 3.0 and achieved a weight increase of 34.6-37.3% with a 24-25.5% estimated cost reduction for MnBi IPMSM1 compared to the Leaf. Addressing IPMSM1 design flaws with posts in IPMSM2 now requires a 37 – 43.5% weight increase and only a 14 – 21% cost reduction. While magnet posts in IPMSM2 increases leakage permeance which degrades B_{g1}, it also allows the IPMSM2 to increase permanent magnet weight relative to IPMSM1 (see Figure 45) due to the relationships between post thicknesses and other constraints (e.g., stress, demagnetization, torque ripple, etc.). Expanding the ranges of of r_{tw} and r_{sd} in the IPMSM2 compared to IPMSM1 may have also helped limit performance degradation.

On the other hand, the PMASynRM2 are only about 10.3-18.1% heavier than the Leaf while PMASynRM3s are about 23.4 – 29.2% heavier (lighter than all MnBi IPMSM designs). PMASynRM2 achieves the same B_{g1} as IPMSM1 (about 7-10.5% lower than the Leaf, shown in Figure 47(a)) while also slightly *decreasing* K_s by about 2.1%, as shown in Figure 47(b), due to a slight increase in λ compared to the IPMSM topologies. B_{g1} decreases slightly when increasing

post thickness in the PMASynRM3 compared to the PMASynRM2, leading to similar magnetic shear stress for the PMASynRM2 and PMASynRM3 in Figure 47(c). The PMASynRM3 still achieves higher B_{g1} than the IPMSM2 with lower weight and similar rotor bridge mechanical stress as the IPMSM2 designs (see Figure 43), suggesting that the PMASynRM leverages the flux focusing effect better than the IPMSM. IPMSM1 achieves higher B_{g1} than PMASynRM3, but with excessive mechanical stress.

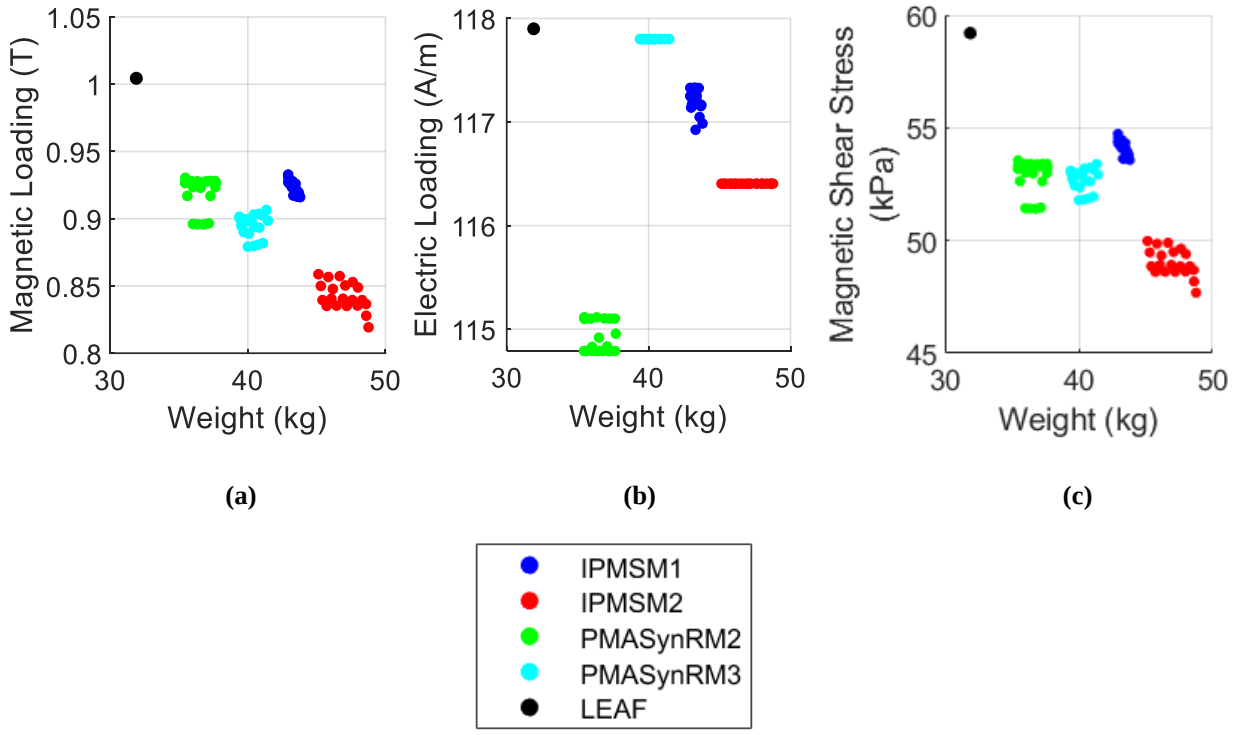

Figure 47: Comparing (a) magnetic loading (B_{g1}), (b) electric loading (K_s), and (c) magnetic shear stress (σ) for all validated Pareto optimal designs.

4.4.3 Equivalent Circuit Parameters and CPSR

Figure 48 – Figure 50 compare various elements of the equivalent circuit analysis related to CPSR explained in Section 2.5. Figure 48 compares ψ_{mn}, L_d, and L_q to ξ. All values used for

L_d and L_q are the minimum (i.e., fully saturated) values calculated at low speeds and peak current because performance during saturation determines the shape of the peak power curve [17]. Both IPMSM1 and IPMSM2 have lower ψ_{mn} and ξ than the Leaf, hence the poor flux weakening performance in Figure 44. While the IPMSM2 has higher ψ_{mn} than IPMSM1, it also has lower ξ, leading to approximately the same flux weakening performance, as in Figure 44. PMASynRM2 can achieve a higher ξ but slightly lower ψ_{mn} than the Leaf motor, thus yielding the best flux weakening performance out of all the MnBi designs presented here. While PMASynRM3 can achieve the same ξ as the Leaf motor, ψ_{mn} is significantly lower, closer the ψ_{mn} of the IPMSM2 than to the PMASynRM2 or Leaf designs. As predicted in Section 2.5, this significant decrease in ψ_{mn} for PMASynRM3 leads to worse flux weakening performance compared to the PMASynRM2.

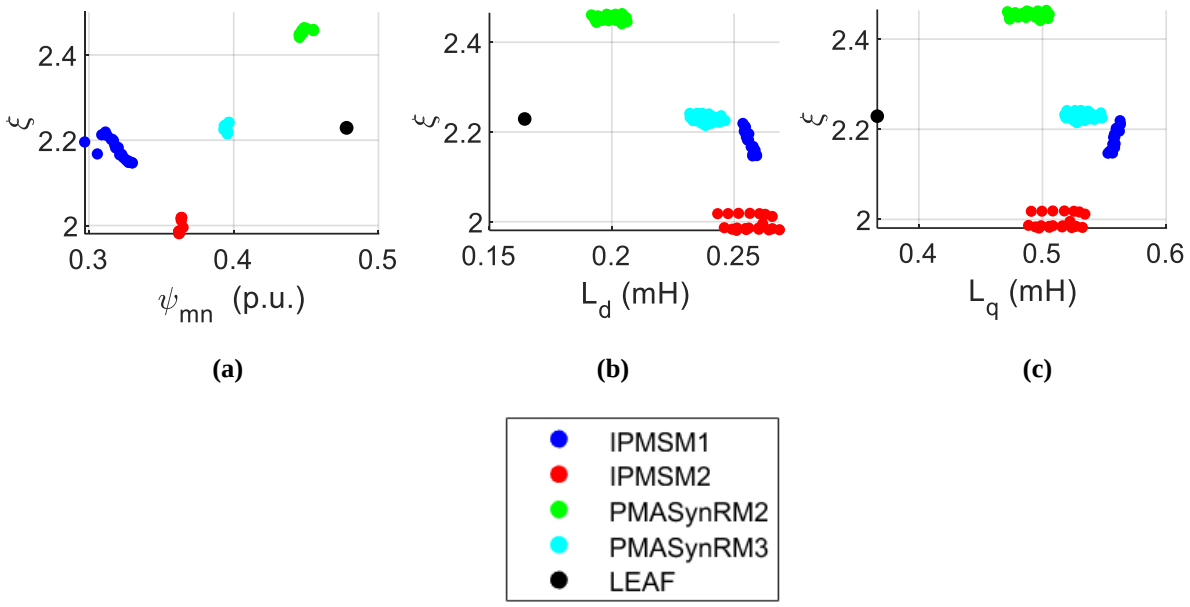

Figure 48: Comparing saliency ratio (ξ) to (a) pu PM flux linkage (ψ_{mn}), (b) d-axis inductance (L_d), and (c) q-axis inductance (L_q) of validated designs.

Similarly, Figure 49 shows the distribution of I_{SC} for Pareto optimal designs plotted with respect to L_d and ψ_m. While (2-24) predicts that these two variables solely determine I_{SC}, this

work uses the value for I_{SC} caluclated by Motor-CAD's Lab module, not (2-24) above, to take nonideal behavior into account. Because no designs achieve a $I_{SC} \geq I_{pk}$, designs with the highest I_{SC} yield the best flux weakening performance. In agreement with Figure 48, this leads to the expectation that the PMASynRM2 has the best flux weakening performance out of all MnBi designs, followed by PMASynRM3, then by IPMSM1 and IPMSM2 with similar performance. Observing Figure 48 and Figure 49 together suggests that the change in L_d primarily drives the change in ξ, I_{SC}, and hence flux weakening performance.

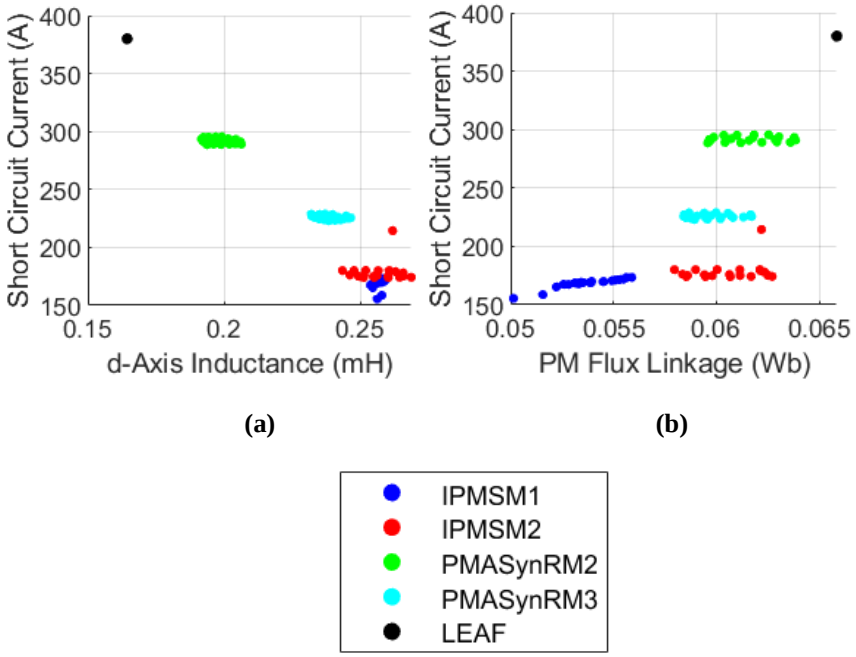

Figure 49: Comparing short circuit current to (a) the d-axis inductance, and (b) the PM flux linkage of validated Pareto optimal designs.

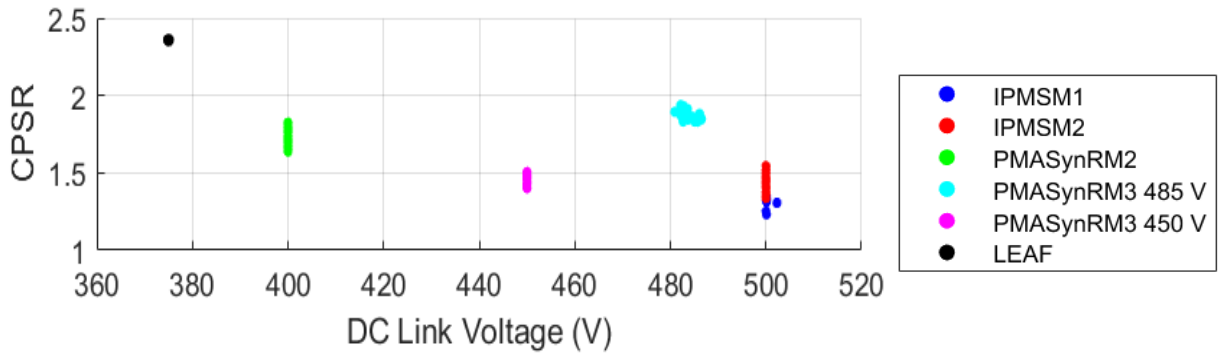

Figure 50: Comparing constant power speed ratio (CPSR) and DC link voltage of validated Pareto optimal designs

Figure 50 then summarize the flux weakening performance of all designs to compare against Figure 48 and Figure 49. Figure 50 compares the CPSR and DC link voltages for the Pareto optimal designs. Here, CPSR is calculated as the ratio between the maximum speed at which the motor can achieve $\geq 120\ kW$ and the base speed of 4000 RPM in Table 3. CPSR with respect to producing 120 kW of constant power is one useful metric for assessing flux weakening performance, but so is the peak power produced at maximum speed (P_{MAX}), shown in Figure 46. While CPSR here represents the speed range at which a motor can achieve 120 kW, P_{MAX} represents the maximum amount of constant power a motor could produce at all speeds in the flux weakening regime. Figure 46 also shows the peak power (P_{pk}) calculated as the maximum power the motor achieve (i.e., occuring at only one speed) for reference.

Considering Figure 46 together with Figure 48 – Figure 50 reveals the following. As a result of lower L_d in MnBi PMASynRMs compared to MnBi IPMSMs, the former achieves higher I_{SC}, lower V_{DC}, higher CPSR and higher P_{MAX} than the latter, although still failing to match the performance of the Leaf. PMASynRM2 achieves a much higher I_{SC} than the other MnBi designs, where $I_{SC} = I_{pk}$ would yield theoretically infinite CPSR if neglecting losses. This leads to a V_{DC} of 400 V, only 25 V higher than the Leaf thereby limiting the need to redesign

power supplies. However, the thicker posts in PMASymRM3 require a notable increase of V_{DC} to achieve the same P_{MAX} as PMASynRM2. To more fairly compare to the MnBi IPMSMs, Figure 46 and Figure 50 also lists P_{MAX} and the CPSR, respectively, for the PMASynRM3 designs with a V_{DC} (i.e., "450 V") that lowers P_{pk} (and P_{rt}) to a similar value as the MnBi IPMSM2. In this case, PMASynRM3 achieves similar CPSR but slightly higher P_{MAX} than the MnBi IPMSM2 with a 50 V decrease in DC link voltage compared to the IPMSM2.

4.5 Impact of Low Temperature Irreversible Demagnetization Risk on Motor Size

This section analyzes the impact of low temperature irreversible demagnetization risk on torque density by altering T_{PM1} in Table 14 for PMASynRM3, thereby impacting Constraint 14 in Table 16. Figure 51 and Figure 52 shows that temperature-dependent demagnetization risk impacts torque and power density for the MnBi PMASynRM. Figure 51 focuses only on designs from this study whereas Figure 52 compares the designs in Figure 51 to the Pareto fronts for the MnBi IPMSM2 and MnBi PMASynRM designs presented previously. Figure 51 shows the Pareto optimal fronts within variation (i.e., variation due only to changes in T_{PM1}), demonstrating that decreasing low temperature demagnetization risk degrades torque density and short circuit current. However, Figure 52 shows the Pareto optimal fronts between variation (i.e., including Pareto fronts for different topologies and mechanical constraints), which suggests demagnetization risk (i.e., Constraints 14 and 15) has less of an impact on MnBi PMSM performance than the topology (i.e., black IPMSM2) or mechanical limitations (i.e., green PMASynRM2, Constraint 18). Note that Figure 51 and Figure 52 use "PMASynRM2" and "PMASynRM Hi σ_{MAX}" interchangeably.

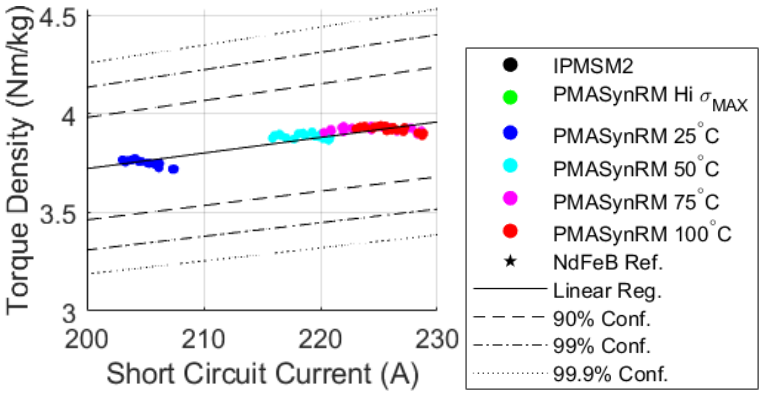

Figure 51: Distribution of Pareto Optimal PMASynRM3 with Different Low Temperature Irreverisble Demagnetization Risk

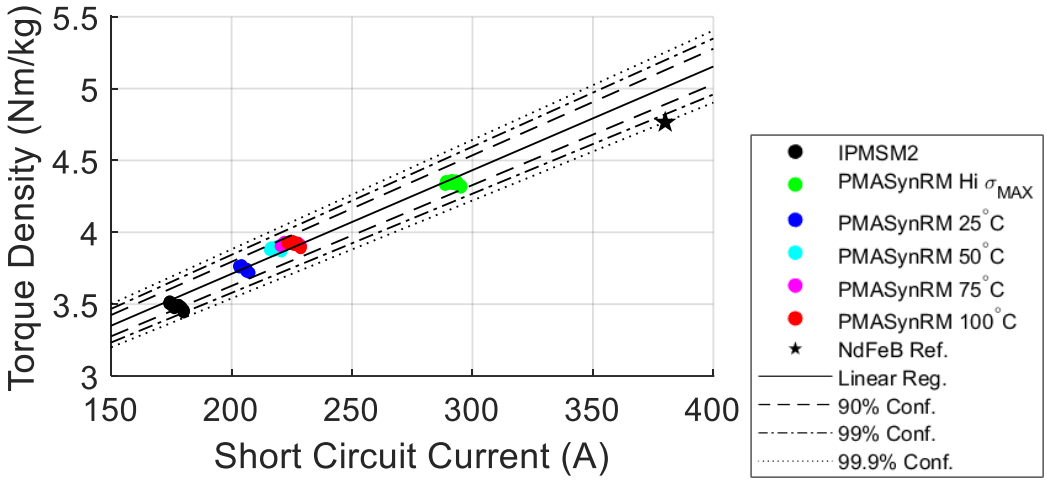

Figure 52: Distribution of Pareto Optimal PMASynRM3 Compared to MnBi IPMSM2 Designs from Section 3.5 and MnBi PMASynRM2 Designs from Section 4.3

Figure 51 and Figure 52 also shows that the Pareto optimal fronts are similar for $T_{PM1} = 50°C$, $T_{PM1} = 75°C$, and $T_{PM1} = 100°C$, with notably worse performance degradation for $T_{PM1} = 25°C$. Figure 53 explains why this occurs by showing how demagnetization risk changes with temperature for the lightest designs in the Pareto optimal fronts calculated at $T_{PM1} = 25°C$ in Figure 53(a), $T_{PM1} = 50°C$ in Figure 53(b), $T_{PM1} = 75°C$ in Figure 53(c), and $T_{PM1} = 100°C$ in Figure 53(d). When $T_{PM1} = 100°C$, almost all operating points are already free of demagnetization risk for PM temperatures as low as $50°C$ except for areas between the yellow

and the red curves in the second and third quadrants of Figure 53(d). All operating points are safe for $T_{PM_1} \geq 60°_C$. This occurs because demagnetization at T_{PM2} (Constraint 15) and rotor mechanical stress (Constraint 18) have greater impact on the Pareto front than demagnetization at T_{PM1} (Constraint 14), and design choices that mitigate the first two, more dominant constraints also have positive impact on the latter. Still, mitigating that small amount of demagnetization risk for $T_{PM1} = 50°C$ requires slight degradation in torque power density shown in Figure 51 and Figure 52.

Despite the similarities in Pareto optimal fronts for $T_{PM1} = 75°C$ and $T_{PM1} = 100°C$, Figure 53(c) shows the demagnetization risk for $T_{PM1} = 75°C$ is not always lower than the demagnetization risk for $T_{PM1} = 100°C$ in Figure 53(d). At lower temperatures, the design for $T_{PM1} = 75°C$ has lower risk of demagnetization than the design for $T_{PM1} = 100°C$ but higher risk of demagnetization than the design for $T_{PM1} = 50°C$, even though Constraint 15, which limits low temperature demagnetization risk, is identical for all three designs. However, at high temperatures, the design for $T_{PM1} = 100°C$ performs slightly worse at $60°C$ than the design for $T_{PM1} = 75°C$, but the design for $T_{PM1} = 75°C$ performs slightly worse than both the design for $T_{PM1} = 50°C$ and the design for $T_{PM1} = 100°C$ for other operating points (i.e., $I_q = -480A, I_d = 0$). This highlights the nonlinear nature of the demagnetization constraints, and the conservative nature of the ROM-based optimization routine used here to control demagnetization risk.

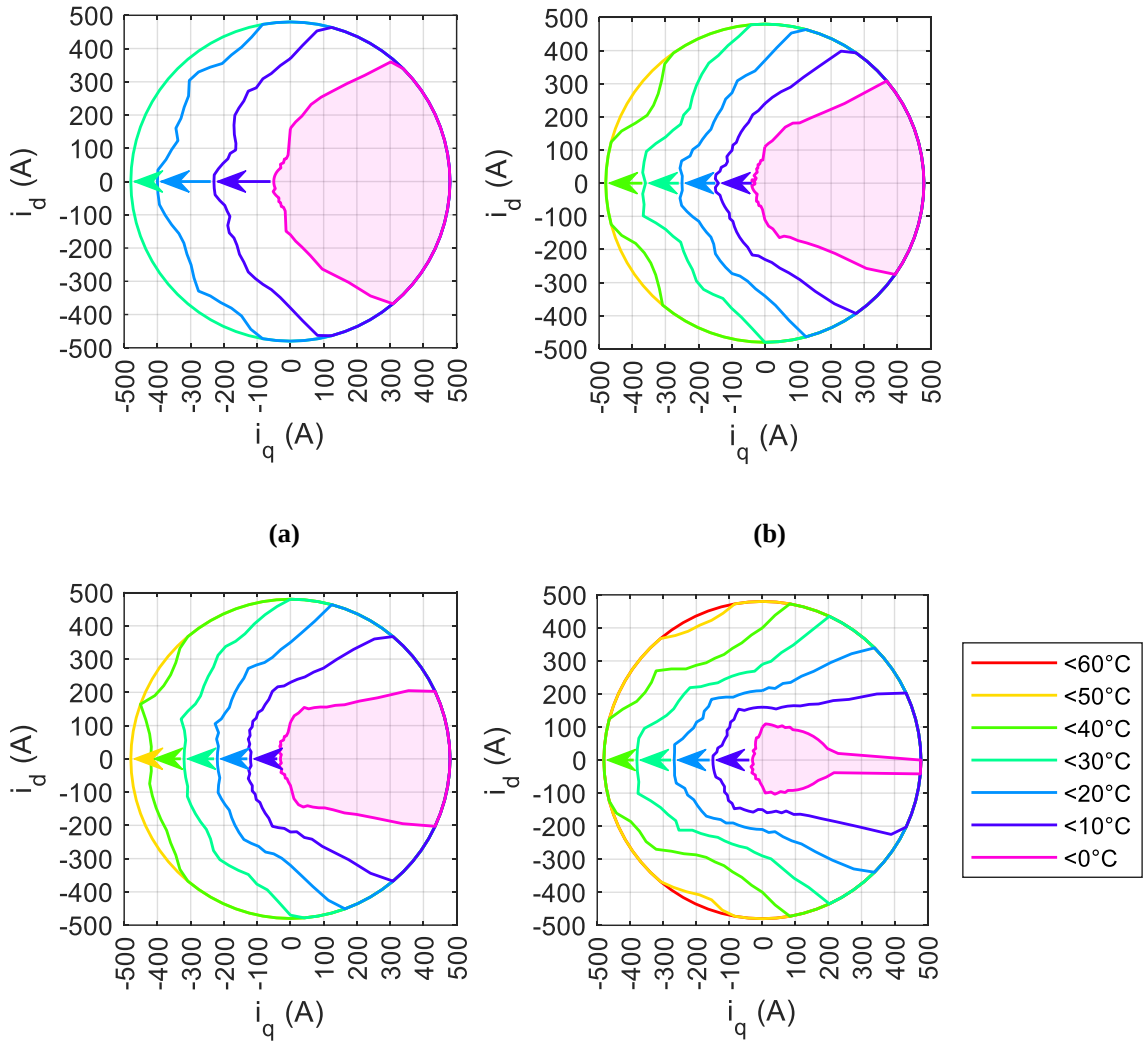

(a) **(b)**

(c) **(d)**

Figure 53: Operating Regions without Demagnetization Risk at Different Temperatures for (a) $T_{PM1} = 25°C$, (b) $T_{PM1} = 50°C$, (c) $T_{PM1} = 75°C$, and (d) $T_{PM1} = 100°C$.

4.6 Impact of Low Temperature Irreversible Demagnetization Risk on EV Drive Cycle Performance

To understand how irreversible demagnetization risk impacts EV drive cycle performance, Figure 54 superimposes the operating points from the EV drive cycles shown in Figure 31 – Figure 34 onto the safe operating regions without irreversible demagnetization risk presented in Figure 28 for the MnBi IPMSM2 and in Figure 53 for various MnBi PMASynRM3 with different T_{PM1}. Similarly, Figure 55 – Figure 59 calculate how many drive cycle operating points lead to irreversible demagnetization for the designs shown in Figure 54. For all, the drive cycle operating points are calculated at a mass equal to the curb weight of the 2011 Nissan Leaf (1521 kg) and a grade of 0%.

The drive cycles primarily operate along the MTPA trajectory, which lies in the second and third quadrants of the plots in Figure 54 for forward and reverse motion, respectively. As a result, even though the shapes and size of the safe operating regions in the first and fourth quadrants of Figure 54 differ significantly between the various designs, Figure 55 – Figure 59 show that all designs can safely operate at roughly the same number of drive cycle operating points at most temperatures. Because most drive cycle operating points require far less than the motor rated current, shown in Figure 33, all designs can safely operate at >90% of all drive cycle operating points for PM temperature >10°C.

Still, due to the changes in the minimum allowable q-axis current, I_{PM2}, at $T_{PM2} = 0°$, the IPMSM2 ($I_{PM2} = 267\ A$) experiences significantly less risk of irreversible demagnetization compared to the PMASynRM3 ($I_{PM2} = 100\ A$). For example, Figure 55 shows that the IPMSM2 can safely operate at 90.9% of all drive cycle operating points, whereas the PMASynRM3 can only safely operate at about 57-61% of all drive cycle operating points, depending on the design.

Compared to the difference between the IPMSM2 and the PMASynRM3 designs, there is relatively little variation in the number of safe operating points among the various PMASynRM3 designs, suggesting that limiting demagnetization at the minimum temperature, T_{PM2} has a greater impact on EV drive cycle performance than limiting demagnetization at T_{PM1} (the temperature above which all motor operating points safely avoid irreversible demagnetization). This is true because most EV drive cycle operating points only require low current, and constraining demagnetization at T_{PM2} appears to have a greater impact on demagnetization risk at low current operating points, while constraining demagnetization at T_{PM1} appears to have a greater impact on demagnetization risk at high current, at least when only considering the second and third quadrants in Figure 54.

Despite relatively little variation in demagnetization risk among the PMASynRM3 designs compared to the IPMSM2, interesting trends can be observed, nonetheless. Due to changes in the PMASynRM3 designs to the minimum safe PM temperature, T_{PM1}, the PMASynRM3 design with the lowest T_{PM1} (25°C) has the highest percentage of operating points free of irreversible demagnetization among the PMASynRM3 designs at all temperatures, except at 0°C for the US06 drive cycle in Figure 57. On the other hand, the PMASynRM3 design with the second lowest T_{PM1} (50°C) unexpectedly has the lowest number of safe operating points across all drive cycles and temperatures. Comparing the demagnetization risk along the MTPA trajectories in Figure 54 suggests that this occurs because the PMASynRM3 designed with T_{PM1} = 50°C has higher demagnetization risk along the MTPA trajectory specifically. This observation and those previously mentioned in this subsection could be leveraged to improve demagnetization risk during EV drive cycles. However, Figure 52 suggest these changes will not significantly impact torque density or short circuit current compared to topology or rotor stress.

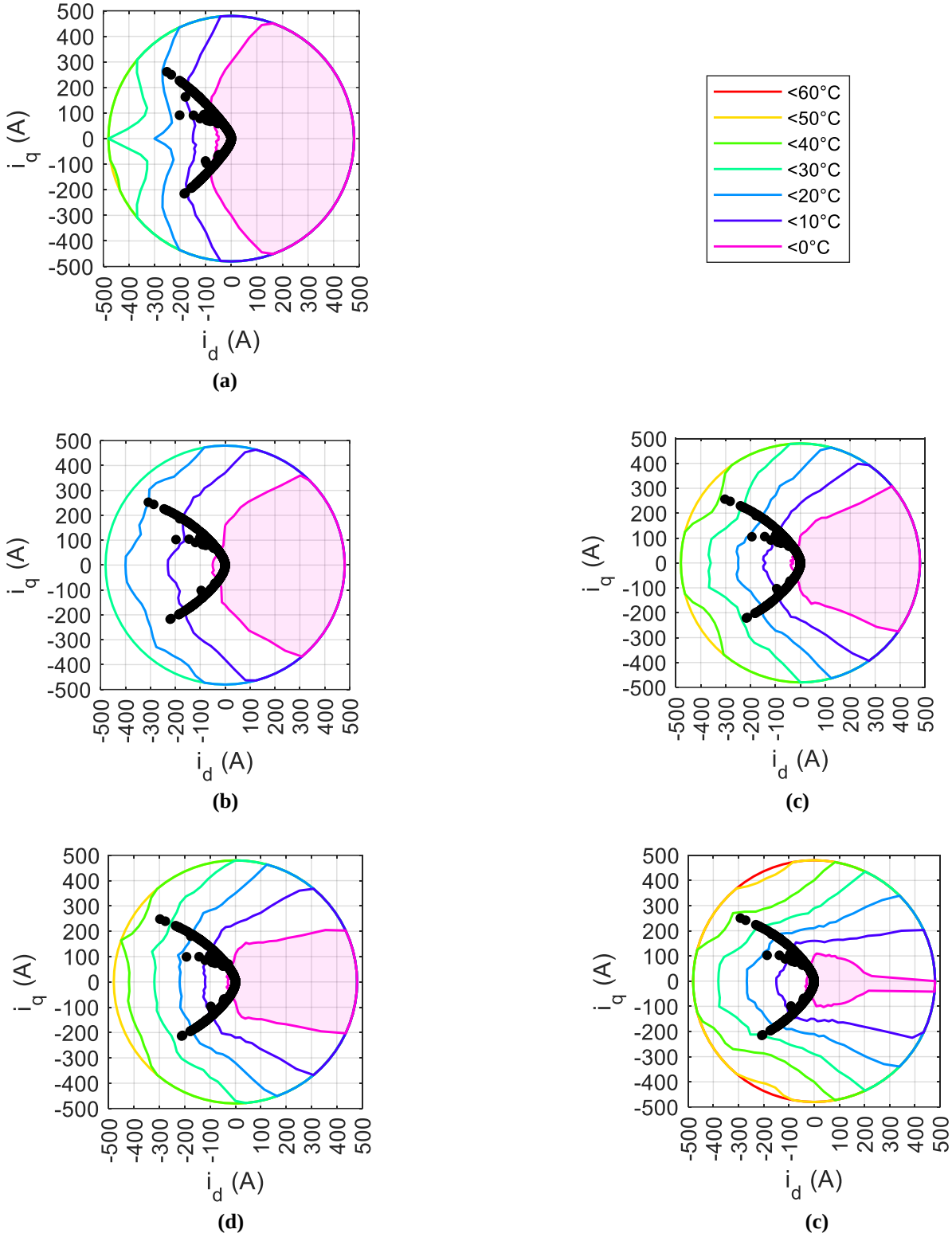

Figure 54: Demagnetization Risk of EV Drive Cycle Operating Points for (a) the IPMSM2 and the PMASynRM3 with (b) $T_{PM1} = 25°C$, (c) $T_{PM1} = 50°C$, (d) $T_{PM1} = 75°C$, and (e) $T_{PM1} = 100°C$

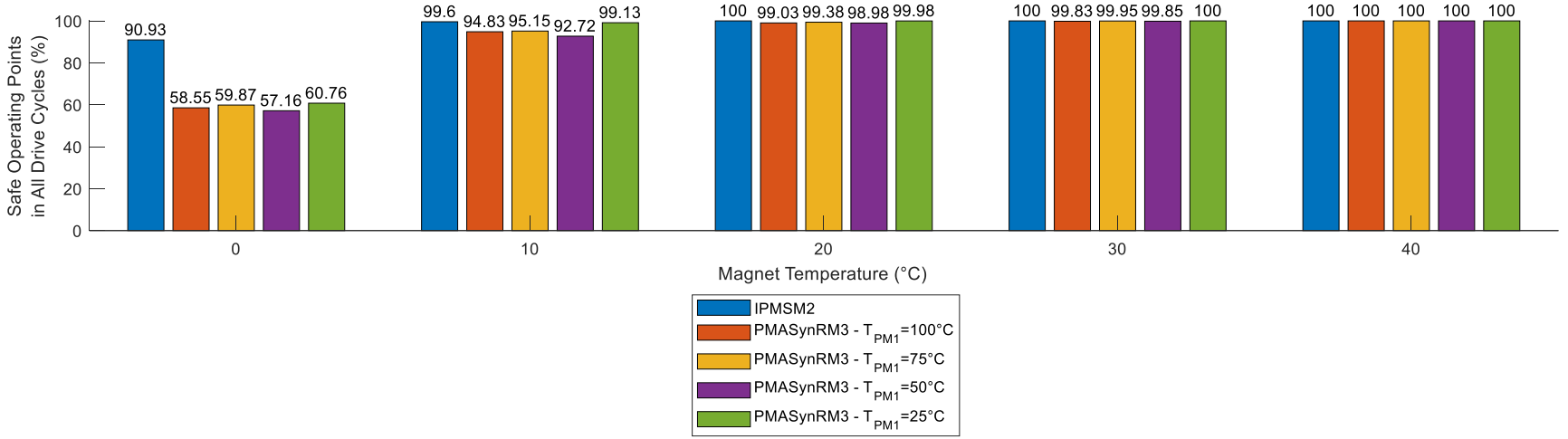

Figure 55: Percentage of EV Drive Cycle Operating Points that Cause Irreversible Demagnetization in MnBi PMSM Designs

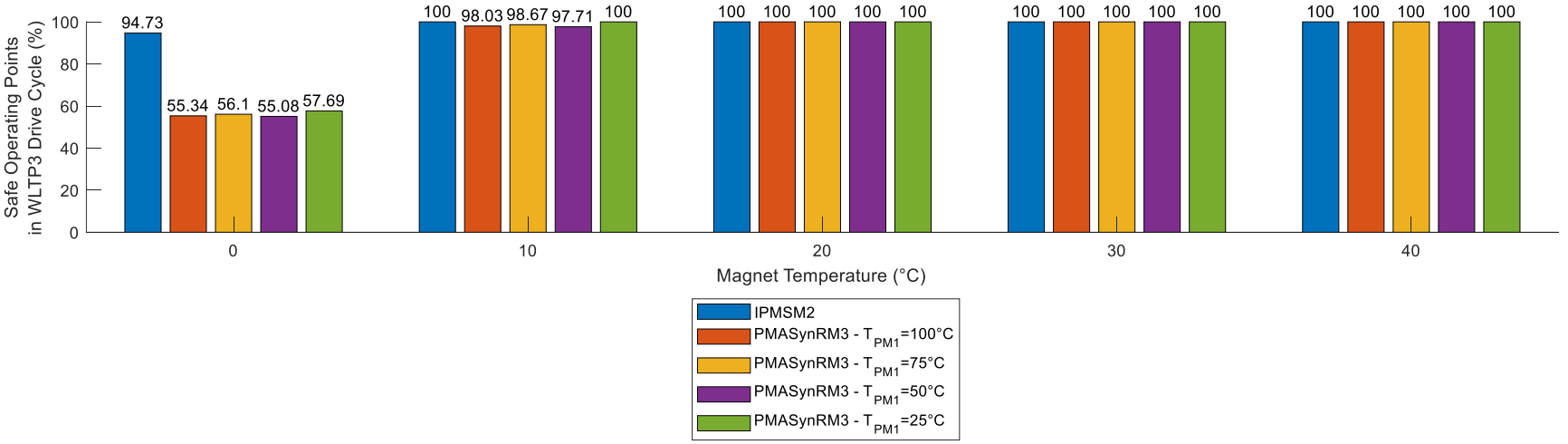

Figure 56: Percentage of WLTP3 Drive Cycle Operating Points that Cause Irreversible Demagnetization in MnBi PMSM Designs

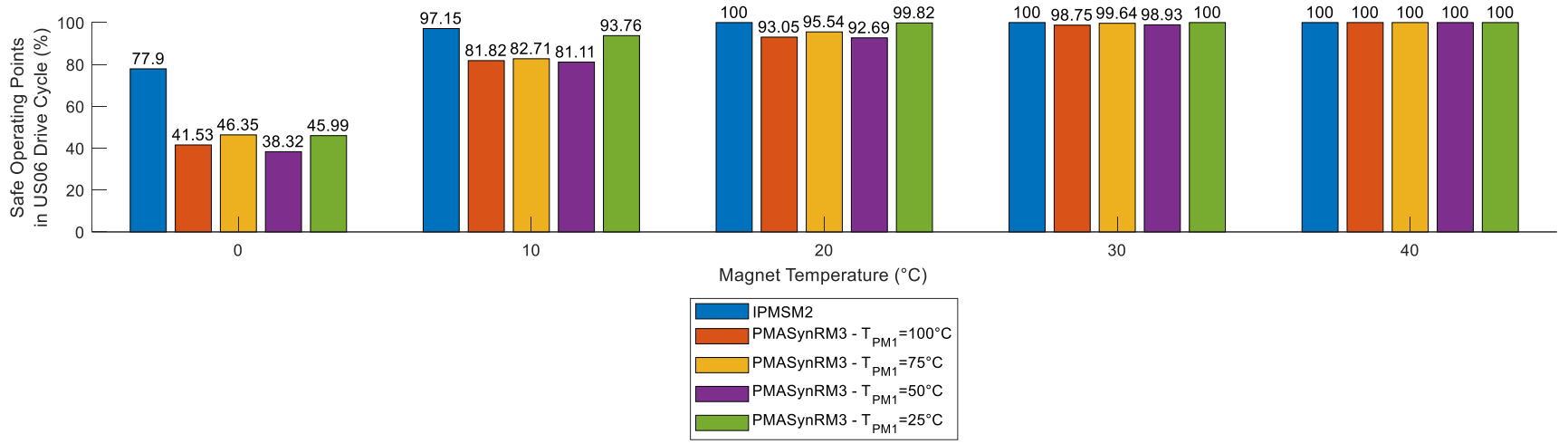

Figure 57: Percentage of US06 Drive Cycle Operating Points that Cause Irreversible Demagnetization in MnBi PMSM Designs

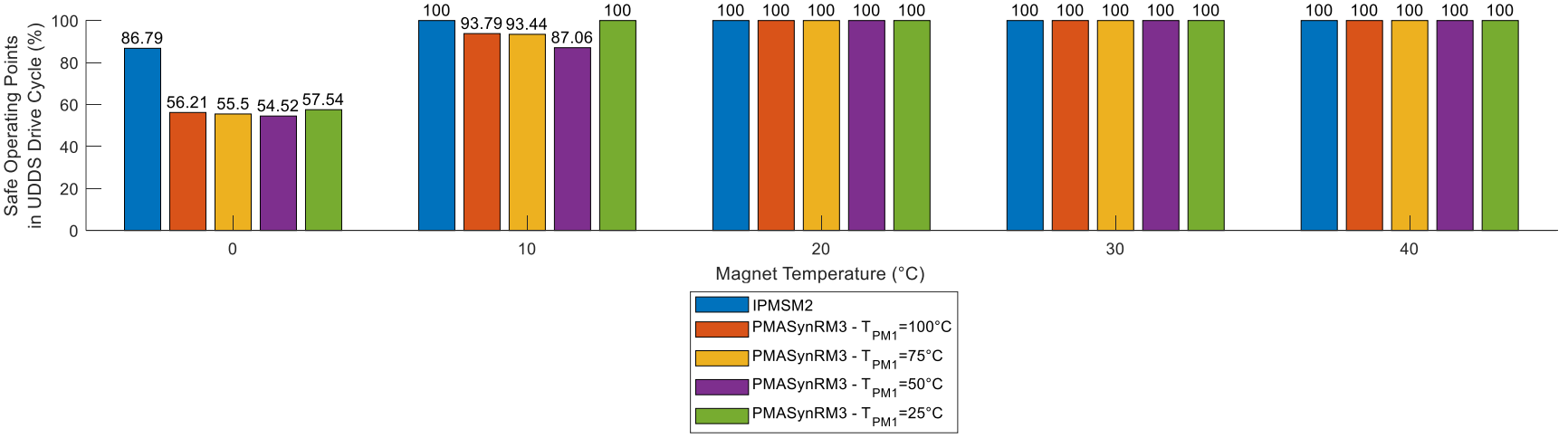

Figure 58: Percentage of UDDS Drive Cycle Operating Points that Cause Irreversible Demagnetization in MnBi PMSM Designs

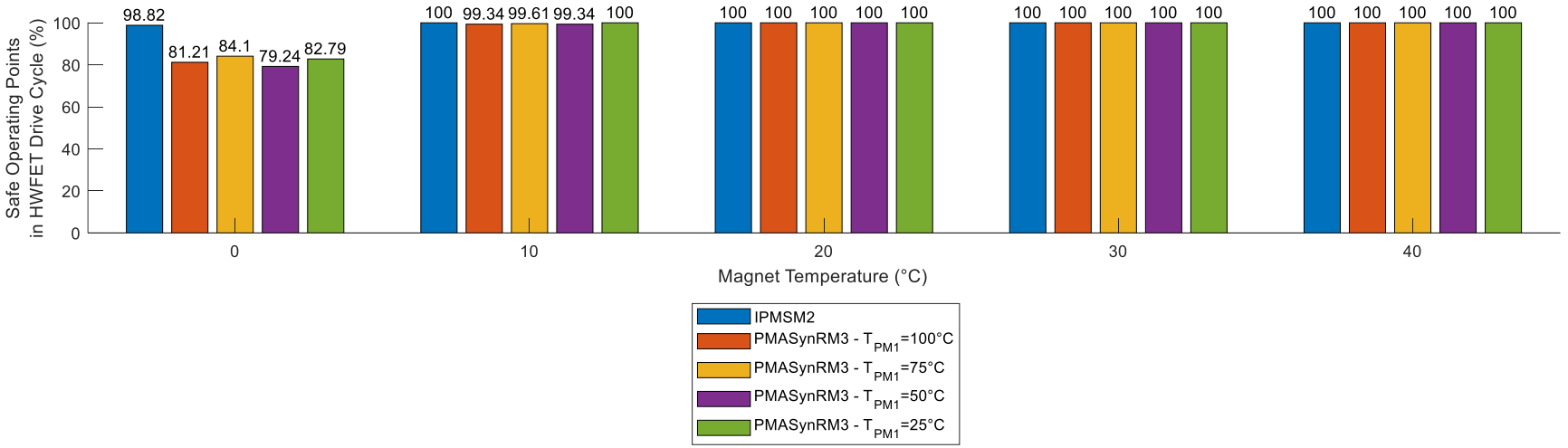

Figure 59: Percentage of HWFET Drive Cycle Operating Points that Cause Irreversible Demagnetization in MnBi PMSM Designs

5.0 Objective 3: Controller Design Tolerant of Demagnetization Risk in PMSMs

This objective proposes a method for limiting motor operating points at low temperatures to prevent irreversible demagnetization during normal operating conditions (i.e., without faults occurring). PM temperature determines irreversible demagnetization risk. Several methods have been introduced in literature for estimating PM temperature without directly measuring, with varying levels of accuracy. This objective explores using the robust integral of sign of error (RISE) observer [82], [83], [84] to estimate PM temperature by estimating the PM flux linkage (λ_{pm}) first, and then correlating the PM flux linkage with the PM temperature. This correlation exists because PM remanent flux density (B_r) impacts λ_{PM}, which can be estimated using PMSM flux observers.

The RISE observer has yet to be applied to observer PM flux linkage or estimate PM temperature for three-phase PMSMs. In literature [82], [83], [84], the RISE observer tends to converge quickly while remaining robust to system uncertainty. Both merits would prove useful in when operating MnBi PMSMs at low temperatures. The RISE observer is evaluated using electrical equivalent circuit parameters estimated with FEA and using an adaptive least-squares (ALS) parameter estimator.

5.1 Literature Review

Others have investigated methods for preventing irreversible demagnetization [48], [85], [86], [87] and estimating PM temperature [88], [89], [90], [91], [92] during closed loop control.

This section reviews these previous approaches. Then it reviews the mathematical background for approach used here based on the RISE observer and ALS parameter estimator.

5.1.1 Robust Motor Drive Control to Prevent Irreversible Demagnetization in PMSMs

Various methods have been introduced to tolerate irreversible demagnetization risk in PMSMs during normal operation, with varying levels of complexity [48], [85], [87]. First, [85] proposes a method based on the magnetic equivalent circuit of a PMSM. However, this has important weaknesses. First, some required elements of the magnetic equivalent circuit, such as the leakage permeances of the rotor and stator, are difficult to quantify. Second, this method ignores the effect of temperature on the magnetic equivalent circuit analysis. Third, it assumes that the PM flux density is uniform across the magnet, ignoring partial irreversible demagnetization, where only portion of the PM demagnetizes.

To put this in terms presented previously, recall that the demagnetization ratio used in Section 3.0 and Section 4.0 is the ratio of PM volume that has been demagnetized to the total volume of the PM. By assuming PM flux density is uniform across the PM, [85] assumes the demagnetization ratio is always either 0 or 1. On the other hand, partial irreversible demagnetization corresponds to a demagnetization ratio greater than 0 but less than 1. In the designs presented in Section 3.0 and Section 4.0, the demagnetization ratio is always less than 1 for the range of currents studied. As an example, the maximum demagnetization ratio in Table 12 throughout all optimization iterations for MnBi IPMSM2 is about 0.15. Hence, considering partial irreversible demagnetization is important in this study.

Accordingly, [48], [87] present more precise methods that can account for partial irreversible demagnetization and temperature effects, but each also have their own weaknesses.

Specifically, [48] requires complicated calculations and unconventional machine simulation and design. To calculate the PM flux density, this method places a coil with one turn around the PMs to estimate the mutual inductance between each phase winding and the PMs. These inductances and the measured phase currents can then estimate the PM flux, and dividing by the magnet area yields a PM flux density. Similarly, [87] uses an artificial neural network to predict the maximum PMSM current that does not lead to irreversible demagnetization. However, training an artificial neural network can be challenging and time consuming, optimization of the neural network parameters and model validation clearly presented, and ultimately, the artificial neural network is a probabilistic approach that cannot predict demagnetization risk deterministically.

This study simplifies determining the boundary of operating points that lead to irreversible demagnetization from those that do not by using FEA. Results presented in [20], [21], [34], [93] suggest FEA can accurately predict when irreversible demagnetization occurs. However, control schemes should include safety margins because there is some discrepancy between FEA and experimental results presented in [20], [34], [93].

5.1.2 PM Temperature Observers for PMSMs

Limiting current operating points to prevent irreversible demagnetization relies on accurately estimating PM temperature. As in [88], [89], thermocouples can be embedded in the rotor to measure temperature with data transmitted to the controller using telemetry. Unfortunately, including openings in the rotor for the thermocouples may locally change the electromagnetic characteristics of the rotor, impacting the boundary between irreversible and reversible demagnetization, and the telemetry equipment adds mass and volume to the system, which are significantly constrained in EV applications and elsewhere.

Observers have therefore become a popular method for estimating rotor PM temperature without directly measuring [90], [91], [92]. Methods for observing PM temperature can be broadly separated into one of five categories: flux observers [91], thermal modeling [91], invasive methods [91], machine learning [92], and fusion methods that combine methods from the any of the previous four categories [90], [91].

Flux observers estimate the PM flux linkage, λ_{pm} from the equivalent circuit model from (2-10) – (2-17) presented in Section 2.5.1, using only the measured current, terminal voltages, ands speed. Because λ_{pm} varies primarily due to temperature in PMSMs, accurate estimates of λ_{pm} can be used to estimate PM temperature, using lookup tables (LUTs) for example. These methods require accurately PMSM model parameterization and measurements to accurately estimate λ_{pm}, as estimation inaccuracy due to inaccurate motor parameters will directly translate to inaccuracies in temperature estimation. Additionally, while valid over the entire torque range, these methods often cannot accurately estimate temperature at low speeds or standstill.

Thermal modeling uses lumped parameter thermal networks (LPTNs) to estimate PM temperature based on motor losses. When used on its own, this approach may require large, complicated thermal networks and loss calculations to accurately predict PM temperature. However, if modeled with sufficient fidelity, these methods can accurately estimate permanent magnet temperature over the entire torque and speed range of the motor.

Invasive methods inject high-frequency signals into the current references to induce high-frequency flux variation in the motor. The flux variations can then be related to the PM temperature by, for example, analyzing the saturation characteristics or high-frequency impedance of the motor. To be accurate, these methods require accurate motor models, like the LPTN and flux observers, and precise voltage and current measurements, like the flux observer.

Additionally, these methods are only accurate at thermal and electrical steady state and require periodically disrupting closed-loop operation.

Machine learning approaches have also been used to estimate temperature but with relatively poor accuracy. Furthermore, these methods require extensive benchmarking data for model training and optimization, with no clear consensus of which machine learning models are the most accurate nor which PMSM model features to use in the machine learning models.

Finally, combinations of these methods can be used to improve performance. For example, flux observer and invasive signal injection techniques can be combined to estimate PM temperature over the entire speed range of the motor, with signal injection used at low speeds and flux observers used at high speeds [91]. Similarly, LTPNs can be combined with flux observers and stator temperature measurements using a Kalman filter [90]. While more complicated to implement, these methods can predict PM temperature more accurately than using one method at a time.

5.1.3 The Adaptive Least-Squares Parameter Estimator

As mentioned in the previous section, temperature observers often require accurate model parameters. The adaptive least-squares (ALS) method, described in Chapter 2 of [94] and applied in [83], [84], [95] and elsewhere, is a popular choice for parameter estimation in time-varying systems. This section explains the essential mathematical background for this algorithm according to [83], [84], [94], [95]. The algorithm requires the system dynamics (Φ) be arranged as in (5-1), where $W \in \mathbb{R}^{1xn}$ is composed of known (e.g., measured) values, and $\theta \in \mathbb{R}^{nx1}$ are the parameters to be estimated for $n \geq 1$. Similarly, $\widehat{\Phi}$ is the estimated system dynamics using W and the estimated parameters $\hat{\theta}$, shown in (5-2). An *a priori* estimate can be used for $\hat{\theta}$

initially. Then, $\hat{\theta}$ is updated as follows. The error, $\tilde{\Phi}$, is calculated as in (5-3), and the covariance matrix is updated according to (5-4) and (5-5). Here, $P(t_0) = \rho I_n$, where $I_n \in \mathbb{R}^{nxn}$ is the identity matrix and k, γ, and ρ are constant gains determining convergence rate and noise sensitivity. Finally, the parameter estimates $\hat{\theta}$ are updated using (5-6) and (5-7), substituted back into (5-3), and the process is repeated as desired.

$$\Phi = W\theta \tag{5-1}$$

$$\hat{\Phi} = W\hat{\theta} \tag{5-2}$$

$$e = \tilde{\Phi} = \hat{\Phi} - \Phi \tag{5-3}$$

$$\dot{P} = -k\frac{PW^TWP}{1 + \gamma WW^T} \tag{5-4}$$

$$P = \int \dot{P}dt + P(t_0) \tag{5-5}$$

$$\dot{\hat{\theta}} = -k\frac{PW^T\tilde{\Phi}}{1 + \gamma WPW^T} \tag{5-6}$$

$$\hat{\theta} = \int \dot{\hat{\theta}}dt \tag{5-7}$$

Properties and a stability analysis of the ALS squares method are found in Chapter 2 found [94]. Notably, this algorithm requires that $\dot{\theta} \cong 0$. However, in systems where this condition does not hold, the algorithm can be restarted periodically, using the previous estimate until the algorithm converges to an updated estimate. Furthermore, the algorithm is stable for bounded W, but global exponential stability (i.e., globally exponentially convergent) is only guaranteed under certain conditions. Of particular concern here is the condition for persistent excitation. This requires that W rotates sufficiently in space such that $W(t)W^T(t)$ is uniformly positive definite for any length of time Δt (i.e., $\int_{t_0}^{t_0+\Delta t} W(t)W^T(t)dt$ is greater than zero and finite).

5.1.4 The RISE Observer

The RISE observer was first introduced in [82] and applied to a variety of nonlinear systems in [83], [84], [95] and elsewhere. This observer boasts fast convergence while robust to model uncertainty. However, it has yet to be applied to three-phase PMSMs. The observer is defined as follows, according to [82], [83], [84], [95]. Consider the state space representation of a nonlinear system shown in (5-8) composed of known dynamics (u) and unknown dynamics ($f(t)$). To apply the RISE observer, define the error signal in terms of the systems states, x, and the estimate of those states, $\hat{x}$, as in (5-9). Finally, update $\hat{f}(t)$ using (5-10), and solve $\hat{f}(t)$ for the estimate of the unknown parameters using $\hat{x}$. The stability analysis in [82], [83], [84], [95] ensures that $e \to 0$ as $t \to \infty$, thus ensuring that $\hat{x} \to x$ as $t \to \infty$.

$$\begin{cases} \dot{x} = & f(t) + u(x) \\ y = & x \end{cases} \tag{5-8}$$

$$e = \hat{x} - x \tag{5-9}$$

$$\hat{f}(t) \coloneqq (k_1 + 1)e + \int [(k_1 + 1)e + k_2 sgn(e)]dt - (k_1 + 1)e(t_0) \tag{5-10}$$

5.2 Applying RISE Observer to Estimate Permanent Magnet Flux Linkage

This section explains how to apply to the RISE observer and ALS parameter estimator to the three-phase PMSM model from (2-10) – (2-17) presented in Section 2.5.1. To date, no group has applied the RISE observer to estimate PM flux linkage or PM temperature in three-phase PMSMs. Similarly, the author proposes a unique approach to applying the ALS parameter

estimator in such a system. The fast convergence time of RISE observer method is useful for MnBi PMSM in EV applications quickly estimate PM temperature at vehicle startup.

The relevant equations from this model are reproduced in (5-11) – (5-14) below. This work assumes that the d-axis and q-axis voltages (V_d and V_q, respectively) and current (I_d and I_q, respectively are measured along with the motor electrical frequency (ω_e). The terminal voltage V_d and V_q are made equal to their reference voltages, but this may not be sufficiently accurate at low speeds due to inverter deadtime. To apply the RISE observer and ALS parameter estimator, (5-11) – (5-14) are reformulated to solve for the current dynamics assuming $\frac{dL_d}{dt} \cong 0$, $\frac{dL_q}{dt} \cong 0$, and $\frac{d\lambda_{pm}}{dt} \cong 0$. As a result, (5-15) and (5-16) give the expressions for $\frac{d\lambda_d}{dt}$ and $\frac{d\lambda_q}{dt}$ from (5-11) and (5-12), respectively. Substituting (5-13) and (5-15) into (5-11) solving for $\frac{di_d}{dt}$ yields (5-17). Similarly, substituting (5-14) and (5-16) into (5-12) and solving for $\frac{di_q}{dt}$ yields (5-18). To keep notation concise, $\dot{I}_d = \frac{dI_d}{dt}$ and $\dot{I}_q = \frac{dI_q}{dt}$ in (5-17) and (5-18), respectively.

$$V_d = R_s I_d + \frac{d\lambda_d}{dt} - \omega_e \lambda_q \tag{5-11}$$

$$V_q = R_s I_q + \frac{d\lambda_q}{dt} + \omega_e \lambda_d \tag{5-12}$$

$$\lambda_d = L_d I_d + \lambda_{pm} \tag{5-13}$$

$$\lambda_q = L_q I_q \tag{5-14}$$

$$\frac{d\lambda_d}{dt} = L_d \frac{dI_d}{dt} \tag{5-15}$$

$$\frac{d\lambda_q}{dt} = L_q \frac{dI_q}{dt} \tag{5-16}$$

$$\dot{I}_d = \frac{1}{L_d}\left(v_d - R_s I_d - \omega_e L_q I_q\right) \tag{5-17}$$

$$\dot{I}_q = \frac{1}{L_q}\left(v_q - R_s I_q - \omega_e L_d I_d - \omega_e \lambda_{pm}\right) \tag{5-18}$$

5.2.1 RISE Observer Implementation for Estimating PM Flux Linkage in Three-Phase PMSMs

To estimate PM flux linkage, λ_{pm}, using the RISE observer, assume L_d, L_q, and R_s are known *a priori* from either LUTs based on FEA, empirical model characterization, or a parameter estimator, such as the adaptive least-squares estimator subsequently derived in Section 5.2.2. Because λ_{pm} only appears in the dynamics for I_q, shown in (5-18), the RISE observer requires only (5-18) to estimate λ_{pm}. To rewrite (5-18) in the form required by (5-8), separate (5-18) into known, measured inputs, u, and an unknown function, $f(t)$, as shown in (5-19). Accordingly, (5-20) defines the error signal using the known, measured I_q and an estimated $\hat{I}_q$. Then, (5-21) defines the update law for the estimate for the unknown function, $\hat{f}(t)$. The left half of (5-21) provides an expression for $\hat{f}(t)$ analogous to the formulation of $f(t)$ in (5-19), and the right half of (5-21) shows the update law the RISE observer uses to calculate $\hat{f}(t)$ from (5-10) if assuming $e(t_0) = 0$. Note the estimated PM flux linkage, $\hat{\lambda}_{pm}$, is the only unknown parameter because ω_e is measured and L_q is provided *a priori*. Equations (5-22) and (5-23) show the update laws for calculating $\hat{I}_q$ based on $\hat{f}\ (t)$. As mentioned previously, the stability analysis in [82], [83] ensures that $e \to 0$ as $t \to \infty$, thus ensuring that $\hat{x} \to x$ as $t \to \infty$, thereby ensuring $\hat{f}(t) \to f(t)$ as $t \to \infty$. Finally, (5-24) solves (5-21) for $\hat{\lambda}_{pm}$.

$$x = I_q$$

$$\dot{x} = \dot{I}_q$$

$$u = \frac{1}{L_q}\left(V_q - R_s I_q - \omega_e L_d I_d\right)$$

$$f(t) = \frac{\omega_e \lambda_{pm}(t)}{L_q}$$

$$\rightarrow \dot{I}_q = \frac{1}{L_q}\left(V_q - R_s I_q - \omega_e L_d I_d\right) + f(t) \tag{5-19}$$

$$e = \hat{I}_q - I_q \tag{5-20}$$

$$\hat{f}(t) = \frac{\omega_e \hat{\lambda}_{pm}(t)}{L_q} = (k_1 + 1)e + \int [(k_1 + 1)e + k_2 sgn(e)]dt \tag{5-21}$$

$$\hat{\dot{I}}_q = \frac{1}{L_q} v_q - \frac{R_s}{L_q} I_q - \frac{\omega_e L_d}{L_q} I_d - \hat{f}(t) \tag{5-22}$$

$$\hat{I}_q = \int \hat{\dot{I}}_q dt \tag{5-23}$$

$$\hat{\lambda}_{pm}(t) = \frac{L_q \hat{f}(t)}{\omega_e} = \frac{L_q}{\omega_e}\left[(k_1 + 1)e + \int [(k_1 + 1)e + k_2 sgn(e)]dt\right] \tag{5-24}$$

5.2.2 Adaptive Least Squares Parameter Estimator for Estimating Resistance and Inductance in Three-Phase PMSMs

To estimate L_d, L_q, and R_s without knowledge of λ_{pm} *a priori*, consider the d-axis current dynamics in (5-18), which does not depend on λ_{pm}. To use the adaptive least-squares algorithm to estimate L_d, L_q, and R_s, rearrange (5-18) into the form shown in (5-1) required for the adaptive least-squares algorithm. If $\dot{I}_d$ could be measured directly, then (5-25) could be substituted directly into (5-3) above, and the adaptive least-squares algorithm could be used exactly as formulated in (5-1) – (5-7) in Section 5.1.3 above. However, $\dot{I}_d$ cannot be measured

directly, and using numerical differentiation to estimate $\dot{I}_d$ based on samples of I_d would introduce inaccuracy.

$$\Phi = \dot{I}_d$$

$$W = [v_d \quad -I_d \quad \omega_e I_q]$$

$$\theta = \begin{bmatrix} \theta_1 \\ \theta_2 \\ \theta_3 \end{bmatrix} = \begin{bmatrix} \frac{1}{L_d} \\ \frac{R_s}{L_d} \\ \frac{L_q}{L_d} \end{bmatrix}$$

$$\dot{I}_d = [v_d \quad -I_d \quad \omega_e I_q] \begin{bmatrix} \frac{1}{L_d} \\ \frac{R_s}{L_d} \\ \frac{L_q}{L_d} \end{bmatrix} \tag{5-25}$$

Thus, the filtering technique explained in [83], [84], [95] is used here to estimate $\dot{I}_d$ with sufficient accuracy to be used in the adaptive least-squares algorithm. Equations (5-26) – (5-35) explain this filtering technique. First, (5-26) defines the update law for the filtered value for $\dot{I}_d$, $\dot{I}_{df}$, based on the actual value of $\dot{I}_d$ and a filter gain, β_0. However, (5-26) still cannot be implemented because it still depends on $\dot{I}_d$. Therefore, consider the additional filter, P_f. The update law for this second filter is defined in (5-27) based only on $\dot{I}_{df}$ and the same filter gain β_0 used in (5-26). Substituting (5-27) into (5-26) then yields (5-28), and integrating both sides of (5-28) yields an expression for $\dot{I}_{df}$ in (5-29) based only on the filtered value P_f, the filter gain β_0, and the measured value of I_d. Substituting (5-29) into (5-27) then yields (5-30), and finally, substituting (5-30) into (5-31) yields (5-32), the numerical implementation of update law for $\dot{I}_{df}$ in (5-29).

$$\ddot{I}_{df} = -\beta_0 \dot{I}_{df} + \beta_0 \dot{I}_d \tag{5-26}$$

$$\dot{P}_f = -\beta_0 \dot{I}_{df} \tag{5-27}$$

$$\rightarrow \ddot{I}_{df} = \dot{P}_f + \beta_0 \dot{I}_d \tag{5-28}$$

$$\rightarrow \dot{I}_{df} = P_f + \beta_0 I_d \tag{5-29}$$

$$\dot{P}_f = -\beta_0 \left(P_f + \beta_0 I_d\right) \tag{5-30}$$

$$\dot{I}_{df} = \int \dot{P}_f dt + \beta_0 I_d \tag{5-31}$$

$$\rightarrow \Phi = \dot{I}_{df} = \int \left(-\beta_0 \left(P_f + \beta_0 I_d\right)\right) dt + \beta_0 I_d \tag{5-32}$$

$$\dot{W}_f = -\beta_0 W_f + \beta_0 W \tag{5-33}$$

$$\rightarrow \widehat{\Phi} = \dot{\hat{I}}_{df} = W_f \hat{\theta} \tag{5-34}$$

$$e = \widetilde{\Phi} = \dot{I}_{df} - \dot{\hat{I}}_{df} \tag{5-35}$$

A similar approach can be used to obtain a filtered W, W_f, with the updated law given by (5-33). The update laws in (5-4) – (5-7) are evaluated using at $W = W_f$ to obtain $\hat{\theta}$, which is used to calculate $\widehat{\Phi}$ at $W = W_f$ as in (5-34). Finally, (5-35) defines the parameter estimator error introduced in (5-3), and the adaptive least-squares algorithm in (5-1) – (5-7) can now be used to estimate θ. The stability analysis in [83], [84], [95] shows that $\hat{\theta} \rightarrow \theta$ as $t \rightarrow \infty$ using this method, provided the persistent excitation condition described in Section 5.1.3 is satisfied. Then, (5-36) – (5-38) estimate the motor parameters L_d, L_q, and R_s as $\hat{L}_d$, $\hat{L}_q$, and $\hat{R}_s$ based on the definition of θ in (5-25), assuming the estimator has converged such that $\theta = \hat{\theta}$.

$$\hat{L}_d = \frac{1}{\hat{\theta}_1} \tag{5-36}$$

$$\hat{R}_s = \frac{\hat{\theta}_2}{\hat{\theta}_1} \tag{5-37}$$

$$\hat{L}_d = \frac{\hat{\theta}_3}{\hat{\theta}_1} \tag{5-38}$$

5.3 Experimental Validation of RISE Observer to Estimate PM Flux Linkage

The RISE observer as described in Section 5.2.1 can readily be implemented in hardware, and this subsection evaluates its performance. Figure 60 shows the testbed used to experimentally validate the RISE observer's ability to estimate PM flux linkage, λ_{pm}. The testbed uses the PLECS RT Box 1 [96], [97] to implement the RISE Observer and interface with the motor drive and motor using power hardware-in-the-loop (P-HIL). In this case, the observer is implanted on the HIL platform and controls physical power hardware (i.e., physical power electronics driving a physical motor). The motor drive is the Texas Instruments BOOSTXL-DRV8305EVM [98], [99] with a DC link voltage of 24 V, and the motor is a prototype designed by the author with a rated current of 15 A, a rated power of 1 kW, a base speed of 2000 RPM, and a maximum speed of 8000 RPM. The prototype motor uses NdFeB PMs because MnBi is not yet commercially available, nor are prototype bulk magnets able to be manufactured at the sizes required for a 1 kW motor.

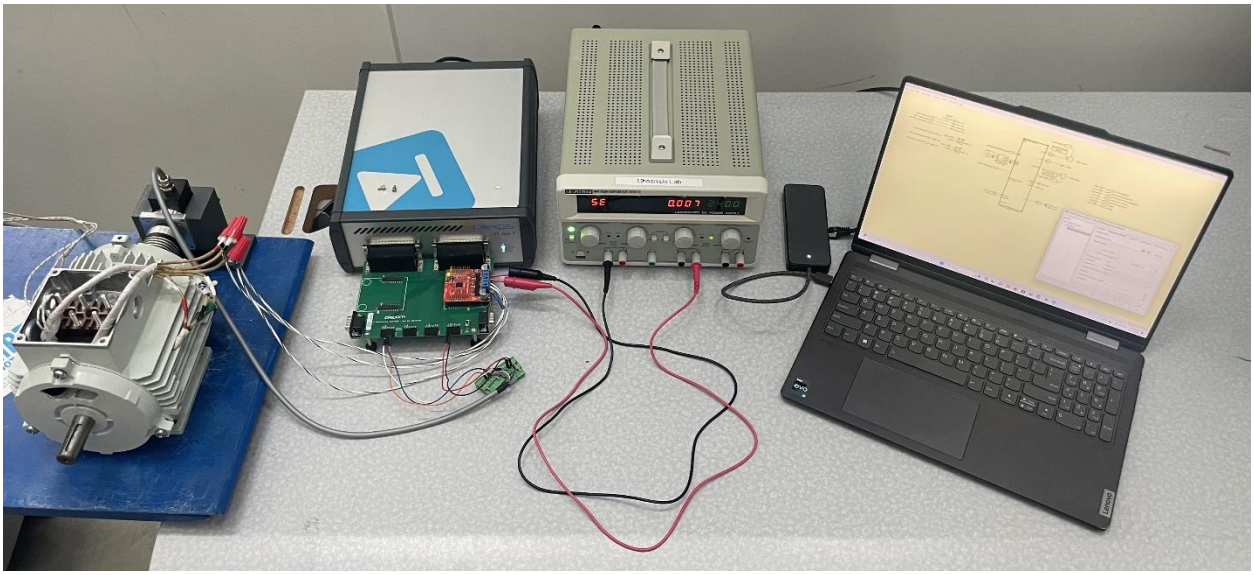

Figure 60: Experimental Test Bed for Validating RISE Observer Using P-HIL

Figure 61 shows the block diagram of the implementation of the RISE observer on the PLECS RT Box. The portion enclosed in the blue box represents (5-22) calculating $\hat{I}_q$, the portion enclosed in the green box represents (5-23) calculating $\hat{I}_q$, the portion enclosed in the grey box represents (5-20) calculating e, the portion enclosed in the orange box represents (5-21) calculating $\hat{f}(x)$, and the portion enclosed in the black box represents (5-24) calculating $\hat{\lambda}_{pm}$. The enable ("En") and reset ("Rst") are binary signals that are the inverse of each other. These signals ensure $e(t_0) = 0$ in (5-10), so this term is ignored in (5-21) and (5-24). Also, these terms ensure stability conditions for the observer are satisfied. In this subsection, FEA data, not the adaptive least-squares method presented previously, is used to estimate L_d, L_q, and R_s to evaluate the performance of the RISE observer specifically. The observer gains, k_1 and k_2, are manually tuned to 1 and 500, respectively, in this subsection.

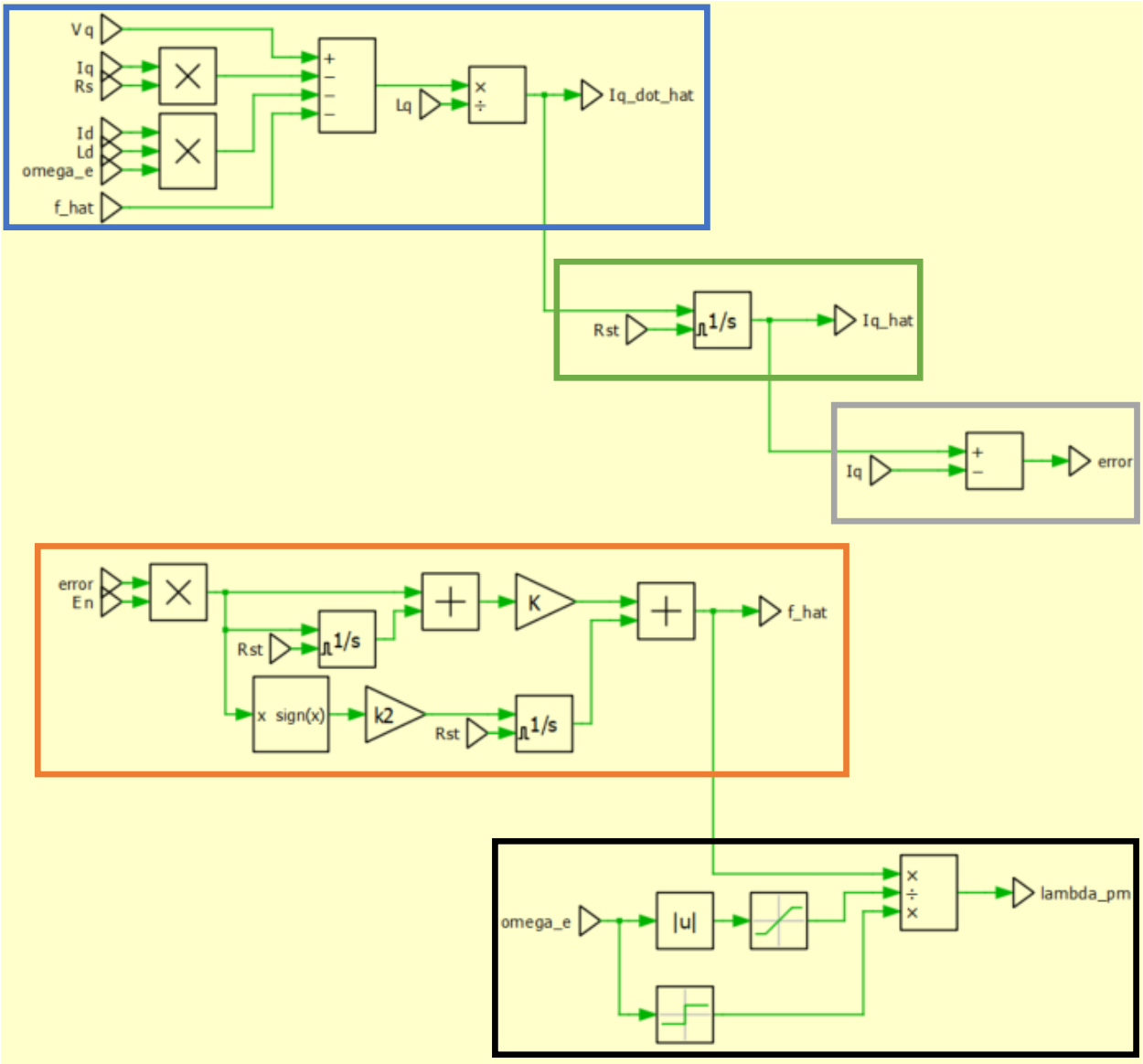

Figure 61: Implementation of RISE Observer on PLECS RT Box for P-HIL Validation

The estimate PM flux linkage, $\hat{\lambda}_{pm}$, is used to estimate the PM temperature using a LUT populated with data from FEA. Table 19 shows the data used in the LUT, and Figure 62 shows a scatter plot of the data in Table 19 with a linear trendline. The coefficient of determination, R^2, is $0.9998 \cong 1$, so a linear fit is sufficient for the LUT here. Unless stated otherwise, the plots shown throughout the remainder of Objective 3 use a discrete moving average filter to filter out the noise in the signals for $\hat{\lambda}_{pm}$ and estimated PM temperature $\hat{T}_{pm}$, but $\hat{T}_{pm}$ is calculated using

the unfiltered $\hat{\lambda}_{pm}$ as calculated by the block diagram in Figure 61. The discrete moving average filter samples the most recent 1000 samples at a sample time of 50μs, which is equivalent to the sampling time used here for the RT Box during P-HIL testing.

Table 19: LUT for Estimating PM Temperature from PM Flux Linkage

PM Temperature, T_{PM}	PM Flux Linkage, λ_{pm}
20°C	13.94 mVs
60°C	13.38 mVs
100°C	12.79 mVs

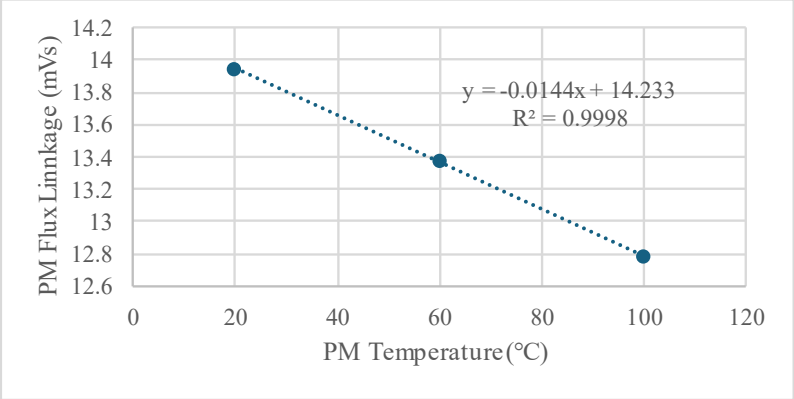

Figure 62: Scatter Plot with Linear Trendline for LUT Used for Estimating PM Temperature

Figure 63 shows the performance of the RISE observer for a motor temperature of 25°C ± 1°C according to thermocouples embedded in the stator, monitored during testing, and thermal imaging of the rotor before and after the test. The top Figure 63(a) and Figure 63(b) show the various combinations of current operating points (I_d and I_q, respectively) tested, while Figure 63(c) and Figure 63(d) show the resultant $\hat{\lambda}_{pm}$ and $\hat{T}_{pm}$, respectively. The observer is initialized such that $\hat{\lambda}_{pm} = 0$ before the observer is enabled, and it is enabled (i.e., "En" changes from 0 to 1 in Figure 61) when $\hat{\lambda}_{pm}$ no longer equals 0 at about 0.138 seconds).

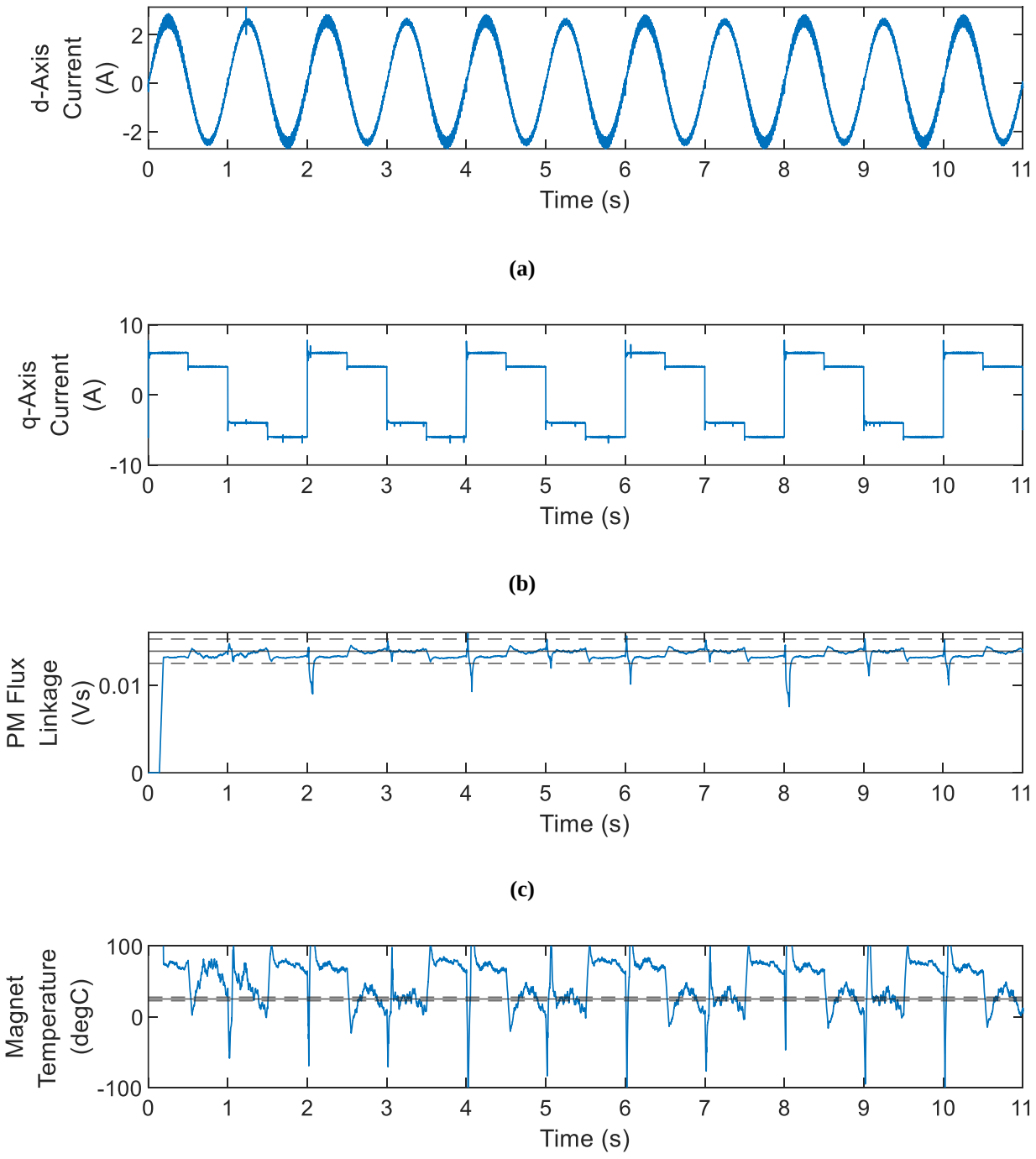

Figure 63: P-HIL Results for RISE Observer Perofmrance with Inductances and Resistance Calculated in FEA

In Figure 63(c), the solid black line shows the actual λ_{pm} calculated in FEA while the dotted black lines represent $\pm$10% of the λ_{pm} calculated in FEA. Similarly, in Figure 63(d), the

solid black line represents the rotor temperature of approximately 25°C measured using thermal imaging after the test sequence in Figure 63, and the dotted black lines represented ±10% of that measured value. The RISE observe quickly converges to a steady-state value after about 0.054 seconds, after which $\hat{\lambda}_{pm}$ remains between ±10% of the value predicted by FEA for the duration of the test, except when transitioning from positive to negative I_q and vice versa. Compared to flux observers found in literature [100], [101], [102], the RISE observer produces comparable estimation error but converges significantly faster. For example, the RISE observer converges in an amount of time approximately an order of magnitude lower than the observer presented in [101] (converging in about a second) and multiple orders of magnitude lower than the observer presented in [102] (converges on the order of minutes).

On the other hand, while ±10% error is a relatively small margin for a flux observer, that translates to an impractical error margin for estimating magnet temperature, $\hat{T}_{pm}$, as shown in Figure 63(d). Here, the solid line once again represents the actual magnet temperature measured using thermal imaging before and after testing (i.e., 25°C ± 1°C), and the dotted lines represent ±10% of 25°C. The mean λ_{pm} of the LUT used to calculate $\hat{T}_{pm}$ based on $\hat{\lambda}_{pm}$ in Table 19 is 13.37 mVs while the maximum and minimum λ_{pm} at 20°C and 100°C, respectively, deviate from the mean by only 4.24% and -4.3%, respectively. Therefore, when using the linear fit described in Figure 62, ±10% error margin for $\hat{\lambda}_{pm}$ imposes a much larger, possibly unacceptable, error margin when estimating $\hat{T}_{pm}$ using the rise observer as described (i.e., with FEA data to estimate L_d, L_q, and R_s).

5.4 Estimating Permanent Magnet Temperature with RISE Observer and Adaptive Least Squares Parameter Estimator

Due to inaccurate PM temperature estimate using solely the RISE observer in Section 5.3, this section explores using the ALS method, introduced in Section 5.2.2, to estimate L_d, L_q, and R_s for the RISE observer rather than using FEA data. The goal is to improve the accuracy of the RISE observer when estimating λ_{pm} and T_{pm}. Figure 64 shows the implementation in PLECS Version 4.7 [100] of the adaptive least-squares parameter estimator proposed in (5-25) – (5-38). Gains k, b, and γ are tuned manually to 100, 100, and 10^{-4}, respectively. Initial conditions for θ are calculated using the values predicted in FEA for L_d, L_q, and R_s. However, initial conditions for P are a diagonal matrix, and the magnitude of each diagonal element is manually tuned based on the desired convergence speed. In this case, larger diagonal elements cause the corresponding element of θ to converge quicker. Initial testing showed that estimates for L_q converged quickly, estimates for L_d converged slowly, and estimates for R_s had a convergence time somewhere between those of L_q and L_d. Therefore, the first diagonal element of P (corresponding to the first element of θ) is set to 10^6, the second diagonal element of P (corresponding to the second element of θ) is set to 10^3, and the third diagonal element of P (corresponding to the third element of θ) is set to 1.

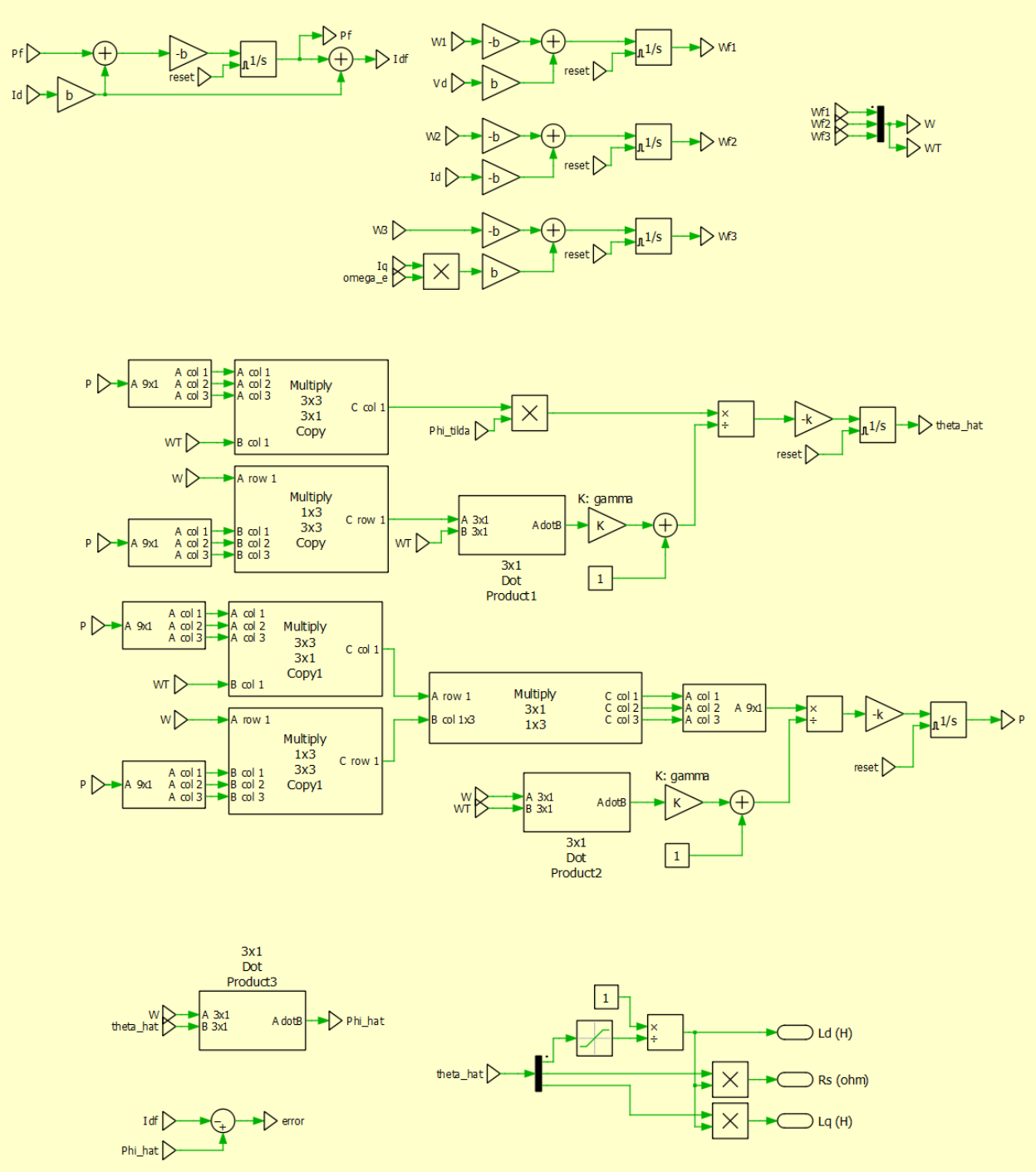

Figure 64: Implementation of the Adaptive Least-Squares Parameter Estimator in Simulation

This simulation uses a model of the 1 kW NdFeB SPMSM used in Section 5.3 for P-HIL testing. The model is constructed using the method from [101], [102] based on FEA modeling. This method considers saturation, cross-saturation between the d- and q-axis, slotting, and

temperature effects. However, despite the relatively high accuracy compared to other modeling methods, this method does not perfectly match FEA results, as reported in [102]. Furthermore, the motor model is driven using a model of a two-level voltage source inverter, and the switch resistance adds resistance not considered by FEA and difficult to measure [103]. Hence, results presented in this section will show that the FEA data used to build this motor model are not accurate enough to use in the RISE observer from Section 5.3, leading to similar temperature error margins as in Figure 63 from Section 5.3.

Three practical details must be explained before presenting the results. First, the adaptive least-squares estimator assumes constant θ, but in this system, θ changes due to saturation and temperature. Therefore, to improve estimator stability and reduce noise in the estimate λ_{pm} from the RISE observer, a zero-order hold (ZOH) is applied to the estimated L_d, L_q, and R_s, and the parameter estimator is reset after the ZOH samples the parameters. A sampling frequency of 2 Hz is used here. The rise observer is not enabled until after the ZOH samples for the first time.

Second, the exponential stability of the adaptive least-squares requires persistent excitation such that WW^T is uniformly positive definite, as described in Section 5.1.3, and noise in the system can impact this condition. For the adaptive least-squares estimator defined in (5-25) – (5-34), a sinusoidal signal is injected into the d-axis current reference to induce dynamics that guarantee persistent excitation. Third, the model used to derive the parameter estimator in (5-25) – (5-34) ignores slotting effects, impacting the accuracy and stability of the parameter estimator. Thus, measurements used to calculate W_f (i.e., V_d, I_d, I_q, and ω_e) are first passed through a low-pass filter to filter out the unmodeled slotting effects. However, the low-pass filter must attenuate the unmodeled slotting effects without significantly attenuating the injected d-axis current signal. As a result, the cutoff frequency of the low-pass filter and the

magnitude and frequency of the injected d-axis current must be chosen carefully to ensure accurate parameter estimation while minimizing the impact on motor performance. Here, the signal injection uses a 1 Hz sinusoid with an amplitude of 2, and the low-pass filter uses a cutoff frequency of 7 Hz.

Figure 65 shows the current excitation used in the simulation to evaluate the parameter estimator. The d-axis current is as described in the previous paragraph, and the magnitude of q-axis current changes between 8 A and 10 A. This magnitude of current is chosen to produce enough torque such that the motor electrical frequency is sufficiently higher than the cutoff frequency of the low-pass filter described in the previous paragraph, and the magnitude changes to demonstrate stability and estimation accuracy during load changes.

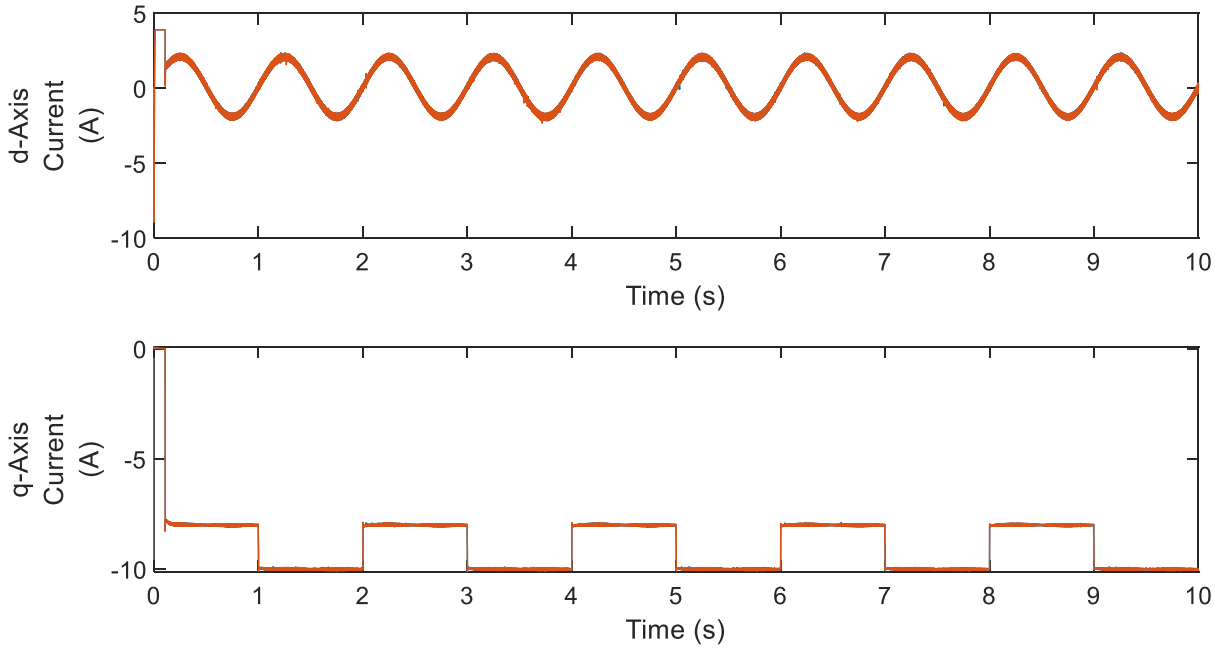

Figure 65: Current Excitation Used to Evaluate the Adaptive Least-Squares Parameter Estimator

Figure 66 compares the estimated $\hat{L}_d$, $\hat{L}_q$, and $\hat{R}_s$ from the ALS parameter estimator, calculated according to (5-36) – (5-38), to the L_d, L_q, and R_s predicted by FEA. In this simulation, motor temperature is controlled as an independent variable to sweep the range of

temperatures used in the LUT from Table 19 (20°C – 100°C). Similarly, Figure 67 shows the parameter estimator error according to (5-35). Each time the parameter estimator resets (i.e., every 0.5 seconds), the estimator error is relatively high then decreases significantly, nearly to zero, as the parameter estimator converges. However, error then increases again until the next time the parameter estimator is reset, though remaining stable. This may be due to the assumption that θ remains approximately constant in the adaptive-least squares algorithm, but R_s changes with temperature while L_d and L_q change due to saturation, thereby changing θ.

Figure 66 also shows the result of applying the ZOH to the to the parameter estimator output. These yellow curves are then used by the RISE observer to estimate $\hat{\lambda}_{pm}$ and $\hat{T}_{pm}$. Figure 68 compares $\hat{\lambda}_{pm}$ and $\hat{T}_{pm}$ calculated using L_d, L_q, and R_s from FEA and $\hat{L}_d$, $\hat{L}_q$, and $\hat{R}_s$ from the parameter estimator. Here, the RISE observer using the ALS parameters is enabled 0.5 seconds after the RISE observer using the FEA parameters because the former waits until the ZOH first samples the ALS parameters.

Once again, the solid black lines indicate values predicted by FEA for λ_{pm} and the exact value used in simulation for T_{pm}, while the dotted black lines represent $\pm$10% of the solid black lines. Both approaches estimate $\hat{\lambda}_{pm}$ within $\pm$10% of the value predicted by FEA, the same error margins produced during P-HIL testing of the RISE observer in Section 5.3. However, using $\hat{L}_d$, $\hat{L}_q$, and $\hat{R}_s$ from the Adaptive Least-Squares parameter estimator reduces $\hat{\lambda}_{pm}$ estimation error significantly, with a maximum error of about 4.09%. This leads to a significantly improved $\hat{T}_{pm}$ estimation when using the parameter estimator error, but the $\hat{T}_{pm}$ error is still appreciable, with a maximum error of 140.4%, because 4.09% error in $\hat{\lambda}_{pm}$ is still significant compared to the range of λ_{pm} shown in Table 19.

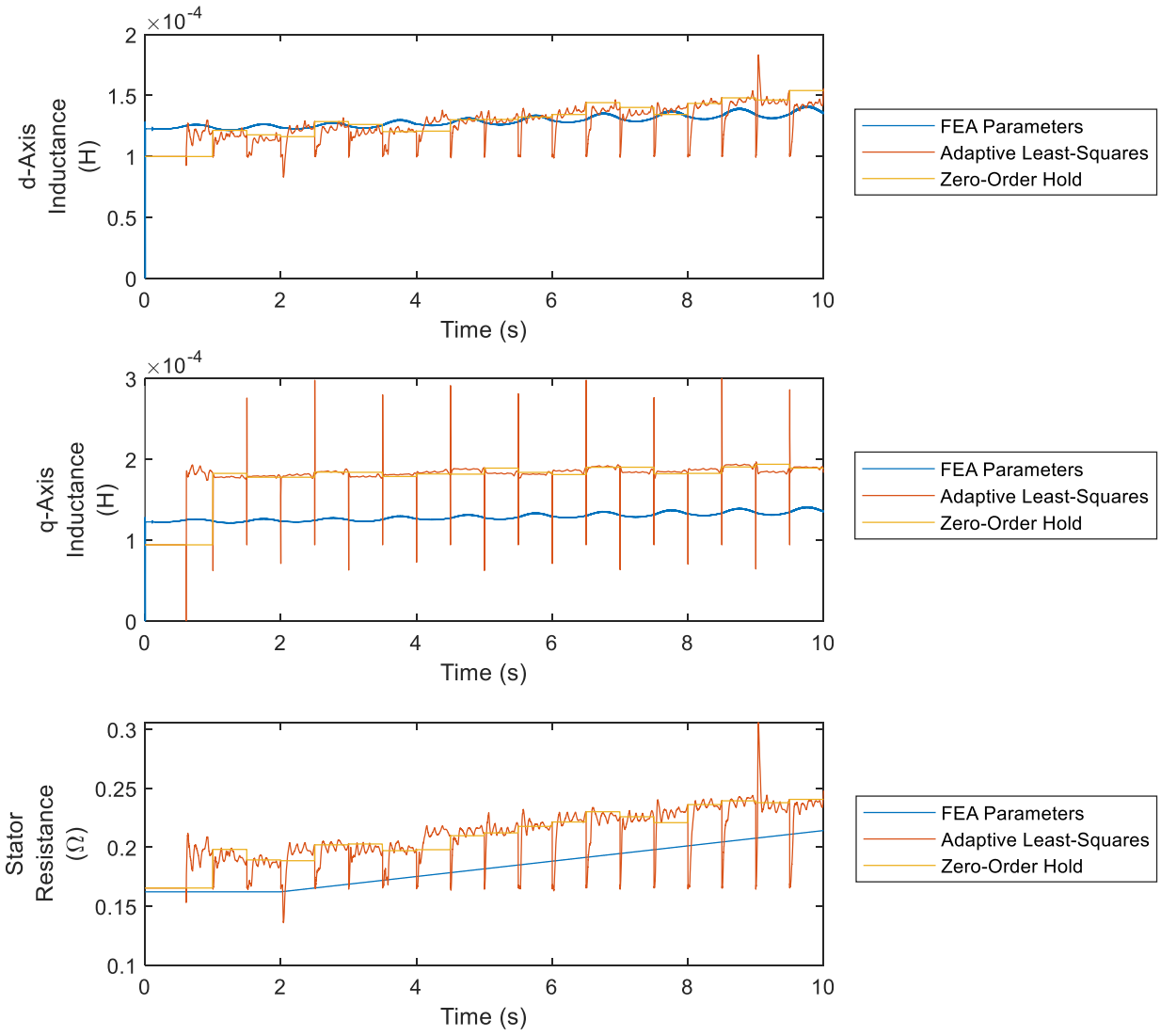

Figure 66: Simulation of the Motor Paramters from the Adaptive Least-Squares Parameter Estimator

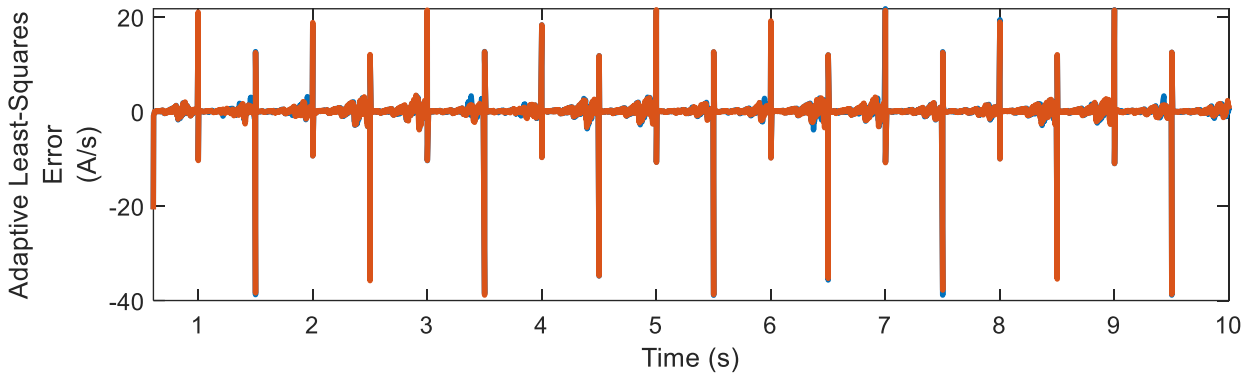

Figure 67: Adaptive Least-Squares Paramter Estimator Error

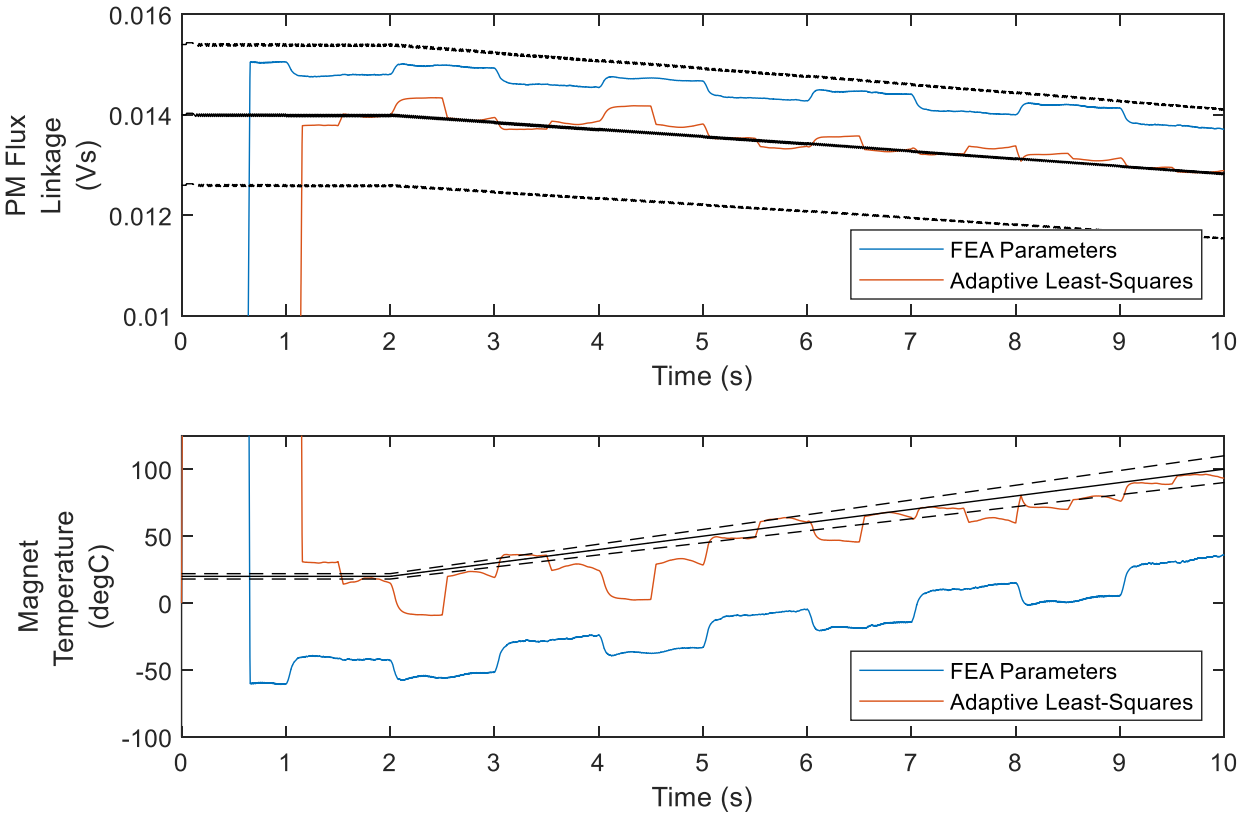

Figure 68: Simulation Results for using Adative Least-Square Parameter Estimator and RISE Observer Together to Esimtate Magnet Temperature

5.5 Limiting PMSM Operating Region Using Estimated Permanent Magnet Temperature

This subsection explains how to limit stator current during closed loop control to prevent irreversible demagnetization. Here and elsewhere in this dissertation, $I_d = i_d$ and $I_q = i_q$, where context dictates format. Recall the example electric vehicle drivetrain in Figure 1, including a battery, power electronic converters, EMI filters, a PMSM, a speed controller, a gearbox, and axles. Figure 69 shows a simplified diagram of a basic speed controller based on proportional integral (PI) control. A desired speed reference, ω_m^*, is used to generate a normalized torque reference, T_{en}^*. When using the normalization procedure described in Section 2.5.2, the normalized torque equals the normalized current, so the normalized torque reference in Figure 69 equals the normalized current reference, i_{sn}^*, for the drivetrain. This determines the magnitude of current required to achieve the desired speed, but the optimum ratio of reference d-axis current, i_d^*, and reference q-axis current, i_q^*, still must be determined based on current and voltage limitations the drive, as described in 2.5.1. Maximum torque per ampere (MTPA) control and flux weakening (FW) control are popular choices, also described in 2.5.1. When speed is less than the base speed (ω_b below), MTPA is used, but when speed is greater than ω_b, FW control is used. The reference i_d^* and i_q^* are then passed to PI controllers to determine reference d-axis voltage, v_d^*, and reference q-axis voltage, v_q^*. Pulse width modulation (PWM) can then use v_d^* and v_q^* to induce the desired current in the motor windings.

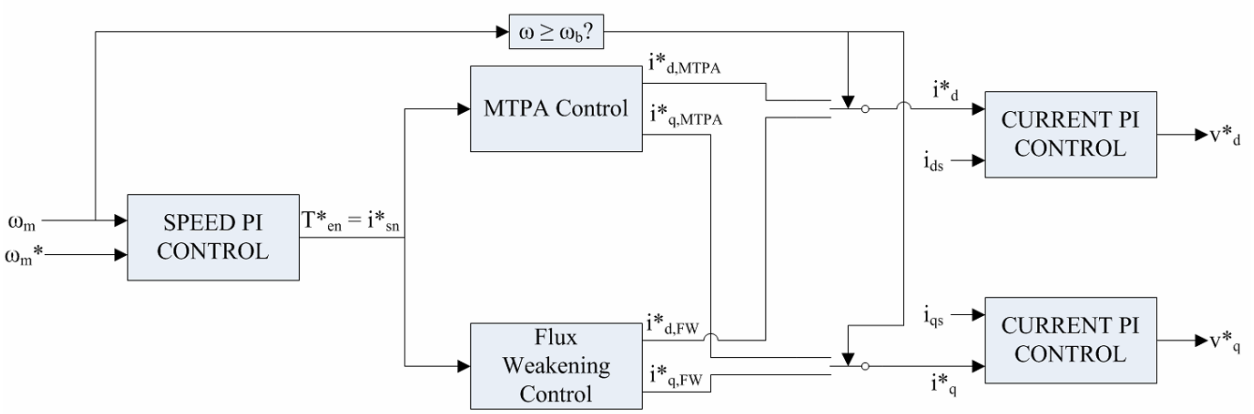

Figure 69: Control Block Diagram for Basic PMSM Speed Contoller

To prevent irreversible demagnetization is MnBi motors, limit i_d^* and i_q^* in Figure 69 to values that do not lead to irreversible demagnetization according to FEA. The contour plots in Figure 28 and Figure 41 show examples of the required FEA data for the IPMSM2 and PMASynRM3, respectively. Results presented in [20], [21], [34], [93] suggest FEA can accurately predict when irreversible demagnetization occurs. However, control schemes should include safety margins because there is some discrepancy between FEA and experimental results presented in [20], [34], [93].

Therefore, these contours based on FEA data can be used to estimate the maximum allowable current magnitude for a desired current angle (i.e., the angle corresponding to the i_d^* and i_q^* in Figure 69) and the permanent magnet temperature using a LUT. The magnet temperature can be estimated using observe techniques, as described in Section 5.1 – Section 0, or by measuring the PM temperature directly using thermocouples, as described in Section 5.1. Figure 70 shows the PLECS implementation of such a current limiter used here. Here, if the reference current operating point lies in an unsafe operating region, the magnitude of the reference current decreases to the maximum safe value while keeping angle of the current reference (i.e., in the dq-plane) constant.

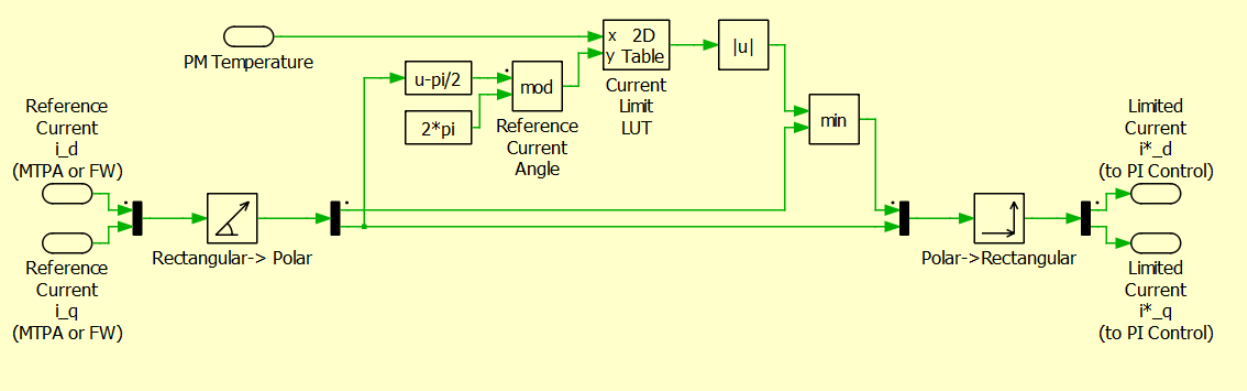

Figure 70: PLECS Implementation of Current Limiter Capable of Preventing Irrevereisble Demagnetization

To demonstrate the efficacy of this procedure, a 1 kW MnBi SPMSM is designed with the same ratings as the 1 kW NdFeB NdFeB SPMSM from the P-HIL test bed in Section 5.3. Safe operating regions free of irreversible demagnetization are then calculated as a function of temperature, as done for the MnBi IPMSMs and MnBi PMASynRMs presented in Section 3.0 and Section 4.0 (e.g., Figure 28 and Figure 41). Figure 71 shows these safe operating regions. Because MnBi PMs are not yet commercially available, the author could not build a prototype MnBi SPMSM. Instead, the safe operating regions in Figure 71 for the 1 kW MnBi SPMSM are applied to the 1kW NdFeB SPMSM prototype designed for the P-HIL testbed in Section 3.0 (i.e., in Figure 60). In other words, the color-coded contours in Figure 71 are used as the LUT in Figure 70, with inputs of PM temperature and the desired current angle. Then, the current limiter in Figure 70 is applied to the NdFeB SPMSM in Figure 60 using P-HIL. Additionally, to evaluate the controller precisely, a change in PM temperature is emulated in the controller manually rather than observer or measuring the PM temperature, as done in Section 5.4. Here, the emulated motor temperature changes between -4°C and -5°C periodically using a square wave with a frequency of 0.5 Hz. Due to this approach, there is no danger of irreversible demagnetization in the NdFeB SPMSM, but the ability of the controller to limit motor operating regions defined by Figure 71 can be evaluated.

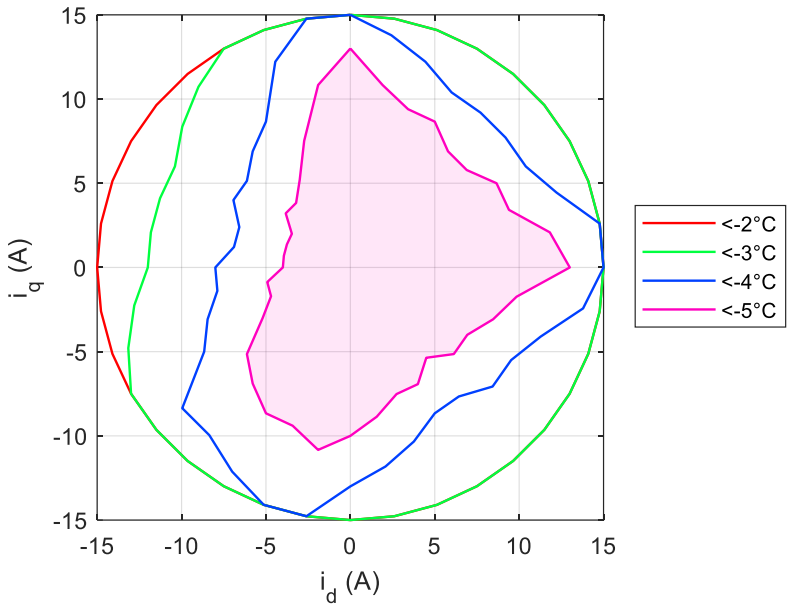

Figure 71: Contour plot enclosing operating regions with no risk of irreversible demagnetization as magnet temperature changes in the prototype 1 kW SPMSM

Figure 72 shows both simulation and P-HIL. Here, current control is used to command the reference current directly, rather than using speed control together with MTPA and FW control, shown in Figure 69. The magnitude of the current reference remains constant and equal to the rated current of 15 A. The current angle (i.e., on the dq-plane) increases with a frequency of 100 rad/s. In Figure 69, this corresponds to $i_d^* = 15\cos(100t)$ and $i_q^* = 15\sin(100t)$, represented by the black circle in Figure 72. The blue and magenta contours represent the safe operating boundaries at -4°C and -5°C from Figure 71. The green and cyan dots represent the resultant motor operating points after applying the current limiter in Figure 70 during P-HIL testing and simulation, respectively. Trails of dots between the two boundaries represent when the emulated PM temperature changes between -4°C and -5°C. Otherwise, the current trajectory approximately traces the boundaries of the safe operating regions as desired. However, some overshoot is observed where the current trajectory exceeds the safe operating boundaries defined in Figure 71 by a small margin. Such behavior is typical of PI control when i_d^* and i_q^* vary

continuously and experiencing sharp changes. Considering this overshoot and the possible inaccuracy of FEA results, the operating boundaries should be designed carefully with sufficient safety margin to safely avoid irreversible demagnetization.

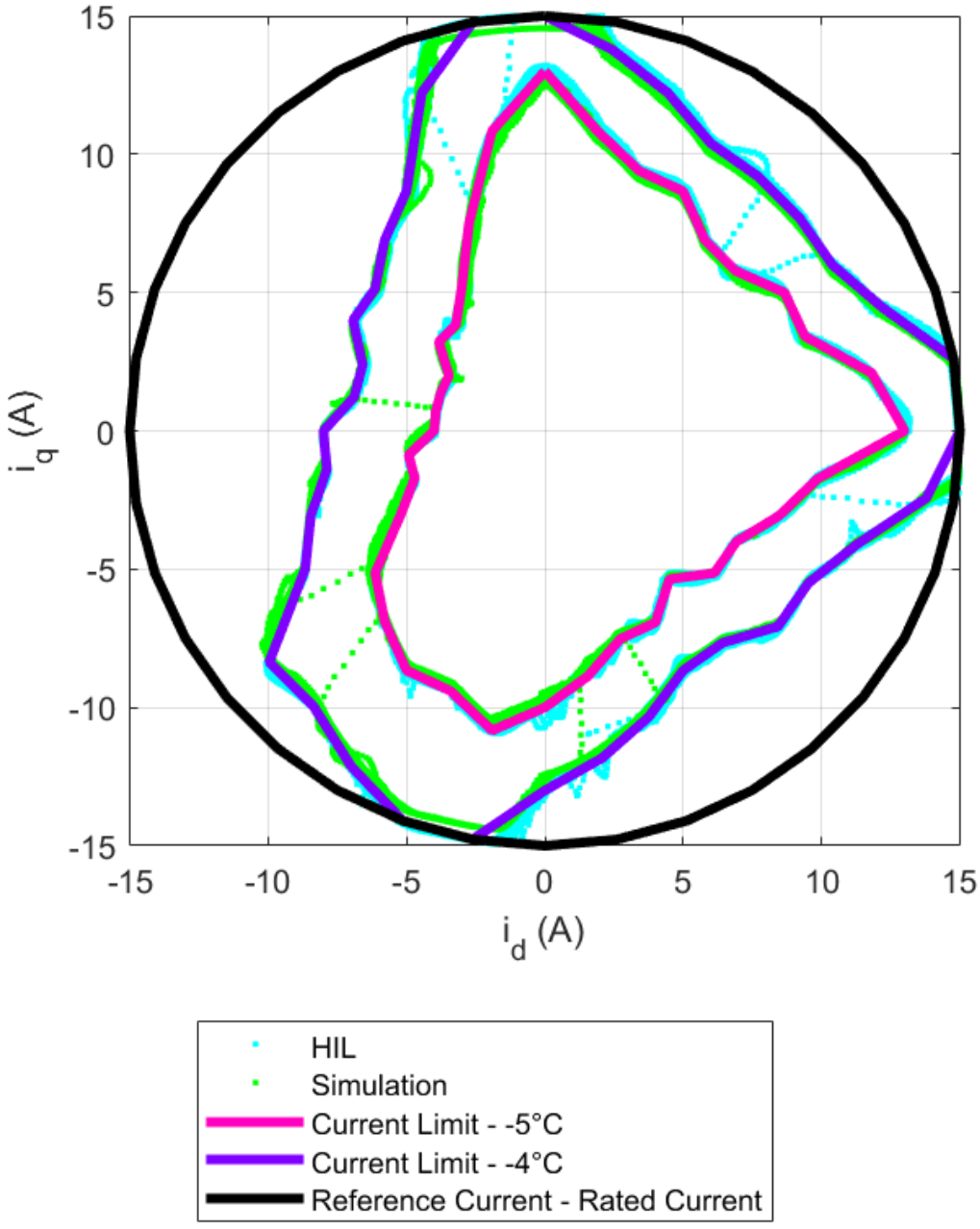

Figure 72: Comparing P-HIL and Simulation Results in the dq-Plane When Using Current Limiter to Prevent Irreversible Demagnetization

Such a current limiter could be directly applied to a current-controlled motor as described. To apply to a speed-controlled motor as in Figure 1 and Figure 69, a trajectory must be defined to convert a desired torque reference (i.e., T_{en}^* in Figure 69) to d-axis and q-axis current references (i.e., i_d^* and i_q^* in Figure 69), similar to MTPA or FW control in Figure 69. To do so, the author defines the "Maximum Torque Without Demagnetizing" (MTWD) trajectory, similar to the MTPA, FW, and MTPV trajectories defined in Section 2.5.1. This can also be calculated as a LUT using FEA data, as is commonly done for FW and MTPV control [25]. Figure 73 shows an example MTWD trajectory over the range of temperatures shown in the figure's legend for the 1 kW MnBi SPMSM. This trajectory includes operating points up to the peak current (i.e., maximum current for thermally limited operation) of 30 A. For this motor, and SPMSMs in general, the MTPA trajectory is simply the q-axis, as shown in Figure 73, because these motors have negligible saliency and thus negligible reluctance torque.

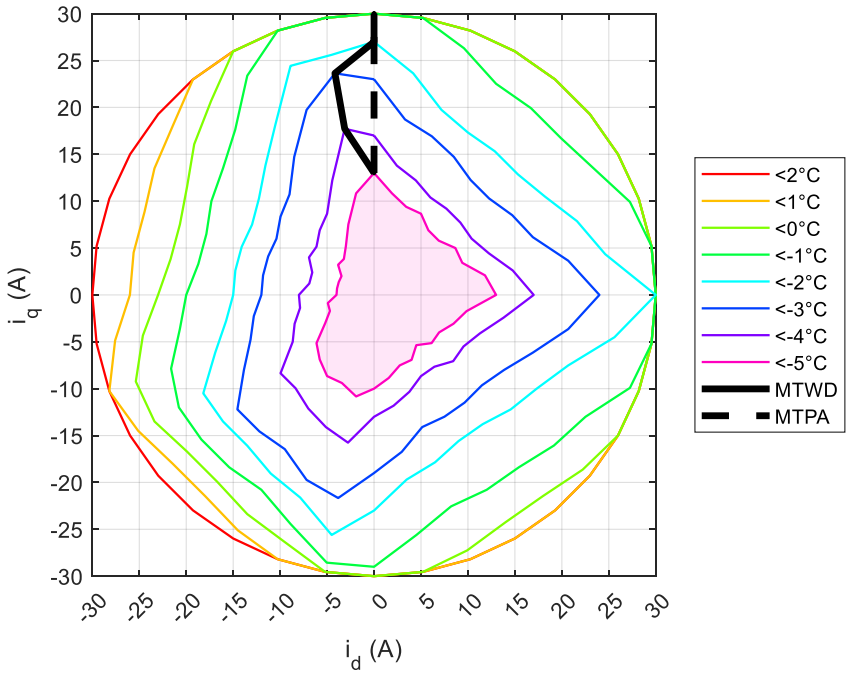

Figure 73: Comparing the MTPD Trajectory to the MTWD Trajectory, Which Maximizes Torque Production while Considering Temperature-Dependent Irreversible Demagnetizatio

6.0 Summary

This dissertation explores the potential of MnBi PMs in PMSMs rated for EV applications. MnBi is a novel RE-free PM material, not yet commercially available, with material properties superior to ferrite PMs at all temperatures yet inferior to NdFeB PMs at low temperatures. In particular, MnBi PMs have the unique PM material property of significantly increasing coercivity with increasing temperature, where the coercivity is relatively close to ferrite PM coercivity at room temperature and below but relatively close to NdFeB PM coercivity at higher temperatures. Because MnBi PMs are not yet commercially available, no group has presented a detailed study of their potential in PMSM applications, with only one group presenting a preliminary trade study evaluating PMSM MnBi PMs in SPMSMs rated for up to 10 kWs. This design is impractical for EV applications, which is projected to rapidly increase demand for RE PMs and thus requiring innovative motor design to stabilize cost.

Therefore, this work presents a trade study for MnBi in a popular IPMSM topology from the EV industry. This reveals that MnBi IPMSMs can notably reduce motor cost but suffer from poor power factor and CPSR due to the low B_r of MnBi relative to NdFeB PMs that dominate in EV applications. Consequently, a second trade study is conducted for MnBi in a PMASynRM topology popular among RE-free designs. This topology remains cost effective compared to the MnBi IPMSM while improving power factor and CPSR. However, this topology experiences significantly increased risk of irreversible demagnetization at low temperatures. As a result, a control method is introduced that prevents irreversible demagnetization when magnet temperature is low, and a nonlinear observer is proposed that estimates magnet temperature with faster convergence than other methods in literature without thermocouples.

Bibliography

[1] R. Reisinger and A. Emadi, "Sensible Transportation Electrification: Get rid of inefficient powertrain designs," *IEEE Electrification Magazine*, vol. 1, no. 2, pp. 6–12, 2013. doi: 10.1109/MELE.2013.2293838.

[2] A. Adib *et al.*, "E-Mobility — Advancements and Challenges," *IEEE Access*, vol. 7, pp. 165226–165240, 2019, doi: 10.1109/ACCESS.2019.2953021.

[3] J.-R. Riba, C. López-Torres, L. Romeral, and A. Garcia, "Rare-earth-free propulsion motors for electric vehicles: A technology review," *Renewable and Sustainable Energy Reviews*, vol. 57, pp. 367–379, 2016.

[4] US DRIVE, "Electrical and electronics technical team roadmap," *Partnership Plan, Roadmaps, and Other Documents*, 2017.

[5] H. Chen, H. Kim, R. Erickson, and D. Maksimovic, "Electrified Automotive Powertrain Architecture Using Composite DC–DC Converters," *IEEE Trans Power Electron*, vol. 32, no. 1, pp. 98–116, Jan. 2017, doi: 10.1109/TPEL.2016.2533347.

[6] I. Husain *et al.*, "Electric Drive Technology Trends, Challenges, and Opportunities for Future Electric Vehicles," *Proceedings of the IEEE*, vol. 109, no. 6, pp. 1039–1059, 2021, doi: 10.1109/JPROC.2020.3046112.

[7] A. Hughes and B. Drury, *Electric motors and drives: fundamentals, types and applications*. Newnes, 2019.

[8] C. Liu, K. T. Chau, C. H. T. Lee, and Z. Song, "A Critical Review of Advanced Electric Machines and Control Strategies for Electric Vehicles," *Proceedings of the IEEE*, vol. 109, no. 6, pp. 1004–1028, 2021, doi: 10.1109/JPROC.2020.3041417.

[9] G. Pellegrino, T. M. Jahns, N. Bianchi, W. L. Soong, and F. Cupertino, *The Rediscovery of Synchronous Reluctance and Ferrite Permanent Magnet Motors: Tutorial Course Notes*. SpringerBriefs in Electrical and Computer Engineering, 2016. doi: DOI 10.1007/978-3-319-32202-5_1.

[10] T. A. Lipo, *Introduction to AC Machine Design*. Hoboken: John Wiley & Sons, Inc., 2017.

[11] J. Pyrhonen, T. Jokinen, and V. Hrabovcova, *Design of Rotating Electrical Machines*, 2nd Editio. Chichester, United Kingdom: John Wiley & Sons, Inc., 2014.

[12] Z. S. Du and J. Tangudu, "Performance comparison between Rare earth and Non-Rare Earth based SPM machines using High Silicon Steel," in *2019 IEEE Energy Conversion Congress and Exposition (ECCE)*, 2019, pp. 3952–3959. doi: 10.1109/ECCE.2019.8912531.

[13] Z. Stephen Du, J. Tangudu, A. Sur, and S. Soni, "Multiphysics Design and Optimization for a SPM Machine with MnBi Magnet and 6.5% Silicon Steel Materials for Traction Applications," in *2019 IEEE International Electric Machines & Drives Conference (IEMDC)*, 2019, pp. 1001–1008. doi: 10.1109/IEMDC.2019.8785312.

[14] J. Tangudu, G. Ouyang, and J. Cui, "Trade Studies for a Manganese Bismuth based Surface Permanent Magnet Machine," in *2018 IEEE Transportation Electrification Conference and Expo (ITEC)*, 2018, pp. 600–605. doi: 10.1109/ITEC.2018.8450233.

[15] J. Cui, G. Hadjipanayi, and J. Tangudu, “Cost Effective 6.5% Silicon Steel Laminate for Electric Machines,” *2020 Annual Merit Review and Peer Evaluation Meeting*. U.S. Department of Energy Vehicle Technologies Office, Washington, D.C., 2020. [Online]. Available: https://www.energy.gov/eere/vehicles/downloads/cost-effective-65-silicon-steel-laminate-electric-machines-0

[16] B. Poudel, E. Amiri, P. Rastgoufard, and B. Mirafzal, “Toward Less Rare-Earth Permanent Magnet in Electric Machines: A Review,” *IEEE Trans Magn*, vol. 57, no. 9, pp. 1–19, Sep. 2021, doi: 10.1109/TMAG.2021.3095615.

[17] W. L. Soong and T. J. E. Miller, “Field-weakening performance of brushless synchronous AC motor drives,” *IEE Proceedings-Electric Power Applications*, vol. 141, no. 6, pp. 331–340, 1994.

[18] W. L. Soong and N. Ertugrul, “Field-weakening performance of interior permanent-magnet motors,” *IEEE Trans Ind Appl*, vol. 38, no. 5, pp. 1251–1258, Sep. 2002, doi: 10.1109/TIA.2002.803013.

[19] Y. Zhang, *Investigation of approaches for improving the performance and fault tolerance of permanent magnet synchronous machine drives using current-source inverters*. The University of Wisconsin-Madison, 2016.

[20] K.-T. Kim, Y.-S. Lee, and J. Hur, “Transient Analysis of Irreversible Demagnetization of Permanent-Magnet Brushless DC Motor With Interturn Fault Under the Operating State,” *IEEE Trans Ind Appl*, vol. 50, no. 5, pp. 3357–3364, 2014, doi: 10.1109/TIA.2014.2311494.

[21] Md. Z. Islam, A. K. M. Arafat, and S. Choi, “Determining the operating region for demagnetization-free fault tolerant control of multiphase PMa-SynRM,” in *2018 IEEE Applied Power Electronics Conference and Exposition (APEC)*, 2018, pp. 198–204. doi: 10.1109/APEC.2018.8341009.

[22] J. D. McFarland and T. M. Jahns, “Investigation of the Rotor Demagnetization Characteristics of Interior PM Synchronous Machines During Fault Conditions,” *IEEE Trans Ind Appl*, vol. 50, no. 4, pp. 2768–2775, 2014, doi: 10.1109/TIA.2013.2294997.

[23] ANSYS, “Motor-CAD.” 2021.

[24] “U.S. Department of Energy - Critical Materials Strategy,” Washington, D.C., 2011. [Online]. Available: https://www.osti.gov/biblio/1219038

[25] S.-H. Kim, *Electric Motor Control*. Cambridge, MA: Elsevier Science, 2017.

[26] V. B. Honsinger, “Sizing Equations for Electrical Machinery,” *IEEE Transactions on Energy Conversion*, vol. EC-2, no. 1, pp. 116–121, 1987, doi: 10.1109/TEC.1987.4765812.

[27] R. Yang, N. Schofield, and A. Emadi, “Comparative study between interior and surface permanent magnet traction machine designs,” in *2016 IEEE Transportation Electrification Conference and Expo (ITEC)*, 2016, pp. 1–6. doi: 10.1109/ITEC.2016.7520249.

[28] G. Pellegrino, A. Vagati, P. Guglielmi, and B. Boazzo, “Performance Comparison Between Surface-Mounted and Interior PM Motor Drives for Electric Vehicle Application,” *IEEE Transactions on Industrial Electronics*, vol. 59, no. 2, pp. 803–811, 2012, doi: 10.1109/TIE.2011.2151825.

[29] N. Zhao and W. Liu, “Loss Calculation and Thermal Analysis of Surface-Mounted PM Motor and Interior PM Motor,” *IEEE Trans Magn*, vol. 51, no. 11, pp. 1–4, 2015, doi: 10.1109/TMAG.2015.2445940.

[30] H. Murakami, Y. Honda, H. Kiriyama, S. Morimoto, and Y. Takeda, “The performance comparison of SPMSM, IPMSM and SynRM in use as air-conditioning compressor,” in *Conference Record of the 1999 IEEE Industry Applications Conference. Thirty-Forth IAS Annual Meeting (Cat. No.99CH36370)*, 1999, pp. 840–845 vol.2. doi: 10.1109/IAS.1999.801607.

[31] J. Ou, Y. Liu, and M. Doppelbauer, “Comparison Study of a Surface-Mounted PM Rotor and an Interior PM Rotor Made From Amorphous Metal of High-Speed Motors,” *IEEE Transactions on Industrial Electronics*, vol. 68, no. 10, pp. 9148–9159, 2021, doi: 10.1109/TIE.2020.3026305.

[32] J. D. McFarland and T. M. Jahns, “Influence of d- and q-axis currents on demagnetization in PM synchronous machines,” in *2013 IEEE Energy Conversion Congress and Exposition*, 2013, pp. 4380–4387. doi: 10.1109/ECCE.2013.6647286.

[33] W. Chlebosz and G. Ombach, “Demagnetization properties of IPM and SPM motors used in the high demanding automotive application,” *COMPEL-The international journal for computation and mathematics in electrical and electronic engineering*, 2013.

[34] H. K. Kim and J. Hur, “Dynamic Characteristic Analysis of Irreversible Demagnetization in SPM-and IPM-Type BLDC Motors,” *IEEE Trans Ind Appl*, vol. 53, no. 2, pp. 982–990, 2017, doi: 10.1109/TIA.2016.2619323.

[35] G. Ombach and J. Junak, “Two rotors designs’ comparison of permanent magnet brushless synchronous motor for an electric power steering application,” in *2007 European Conference on Power Electronics and Applications*, 2007, pp. 1–9. doi: 10.1109/EPE.2007.4417327.

[36] C. Zhou, X. Huang, Y. Fang, and L. Wu, “Comparison of PMSMs with Different Rotor Structures for EV Application,” in *2018 XIII International Conference on Electrical Machines (ICEM)*, 2018, pp. 609–614. doi: 10.1109/ICELMACH.2018.8507258.

[37] A. Fasolo, L. Alberti, and N. Bianchi, “Performance Comparison Between Switching-Flux and IPM Machines With Rare-Earth and Ferrite PMs,” *IEEE Trans Ind Appl*, vol. 50, no. 6, pp. 3708–3716, 2014, doi: 10.1109/TIA.2014.2319592.

[38] T. M. Jahns, “Component rating requirements for wide constant power operation of interior PM synchronous machine drives,” in *Conference Record of the 2000 IEEE Industry Applications Conference. Thirty-Fifth IAS Annual Meeting and World Conference on Industrial Applications of Electrical Energy (Cat. No.00CH37129)*, 2000, pp. 1697–1704 vol.3. doi: 10.1109/IAS.2000.882109.

[39] S. Ferrari, G. Pellegrino, M. J. Mohamed Zubair, and I. Husain, “Computationally Efficient Design Procedure for Single-Layer IPM Machines,” in *2019 IEEE International Electric Machines Drives Conference (IEMDC)*, 2019, pp. 1288–1295. doi: 10.1109/IEMDC.2019.8785394.

[40] R. F. Schiferl and T. A. Lipo, “Power capability of salient pole permanent magnet synchronous motors in variable speed drive applications,” *IEEE Trans Ind Appl*, vol. 26, no. 1, pp. 115–123, 1990, doi: 10.1109/28.52682.

[41] S. E. Rauch and L. J. Johnson, “Design Principles of Flux-Switch Alternators,” *Transactions of the American Institute of Electrical Engineers. Part III: Power Apparatus and Systems*, vol. 74, no. 3, pp. 1261–1268, 1955, doi: 10.1109/AIEEPAS.1955.4499226.

[42] R. Cao, C. Mi, and M. Cheng, “Quantitative Comparison of Flux-Switching Permanent-Magnet Motors With Interior Permanent Magnet Motor for EV, HEV, and PHEV Applications,” *IEEE Trans Magn*, vol. 48, no. 8, pp. 2374–2384, 2012, doi: 10.1109/TMAG.2012.2190614.

[43] J. D. McFarland, T. M. Jahns, and A. M. El-Refaie, “Demagnetization performance characteristics of flux switching permanent magnet machines,” in *2014 International Conference on Electrical Machines (ICEM)*, 2014, pp. 2001–2007. doi: 10.1109/ICELMACH.2014.6960459.

[44] F. Marignetti, M. A. Darmani, and S. M. Mirimani, “Electromagnetic sizing of axial-field flux switching permanent magnet machine,” in *IECON 2016 - 42nd Annual Conference of the IEEE Industrial Electronics Society*, 2016, pp. 1624–1628. doi: 10.1109/IECON.2016.7793175.

[45] S. D. Sudhoff, *Power magnetic devices: a multi-objective design approach*. John Wiley \& Sons, 2021.

[46] R. Krishnan, *Permanent Magnent Synchronous and Brushless DC Motor Drives*, 1st ed. Boca Raton, FL: CRC Press, 2009.

[47] G. Choi and T. M. Jahns, “Demagnetization characteristics of permanent magnet synchronous machines,” in *IECON 2014 - 40th Annual Conference of the IEEE*

Industrial Electronics Society, 2014, pp. 469–475. doi: 10.1109/IECON.2014.7048542.

[48] A. Sarikhani and O. A. Mohammed, "Demagnetization Control for Reliable Flux Weakening Control in PM Synchronous Machine," *IEEE Transactions on Energy Conversion*, vol. 27, no. 4, pp. 1046–1055, 2012, doi: 10.1109/TEC.2012.2217968.

[49] X. Jiang *et al.*, "Mechanical and electrical properties of low temperature phase MnBi," *J Appl Phys*, vol. 119, no. 3, p. 33903, 2016.

[50] R. Brody *et al.*, "Trade Study for Rare-Earth-Free Interior Permanent Magnet Synchronous Machine Using MnBi Permanent Magnets," in *2022 IEEE Energy Conversion Congress and Exposition (ECCE)*, Detroit, MI, USA: IEEE, Oct. 2022, pp. 1–8. doi: 10.1109/ECCE50734.2022.9948166.

[51] J. Cui, "Cost Effective 6.5% Silicon Steel Laminate for Electric Machines," United States, 2020. doi: 10.2172/1749947.

[52] R. K. Gupta and N. Mohan, "A Three-Phase Permanent Magnet Brushless DC Motor for Low-Power Low-Speed Fan Applications - Optimizing Cost and Efficiency," in *2007 IEEE Industry Applications Annual Meeting*, 2007, pp. 846–852. doi: 10.1109/07IAS.2007.133.

[53] "China Magnets Source." Accessed: May 24, 2022. [Online]. Available: https://sourcemagnets.com/magnet-price/

[54] Ryan Brody, Paul Ohodnicki, Mohendro Ghosh, and Brandon Grainger, "Improving Constant Power Flux Weakening in MnBi Interior Permanent Magnet Traction Motors," in *2023 IEEE Energy Conversion Congress and Exposition (ECCE)*, Nashville, TN: IEEE, 2023, pp. 1–8.

[55] R. Brody, P. Ohodnicki, and B. Grainger, “Irreversible Demagnetization Reduced Order Modeling in MnBi Interior Permanent Magnet Synchronous Motor Multi-Objective Optimization,” in *2023 IEEE Transportation Electrification Conference & Expo (ITEC)*, 2023, pp. 1–8. doi: 10.1109/ITEC55900.2023.10187044.

[56] G. Choi and T. M. Jahns, “Analysis and design guidelines to mitigate demagnetization vulnerability in PM synchronous machines,” in *2016 IEEE Energy Conversion Congress and Exposition (ECCE)*, IEEE, Sep. 2016, pp. 1–8. doi: 10.1109/ECCE.2016.7854866.

[57] R. W. De Doncker, D. W. J. Pulle, and A. Veltman, *Advanced electrical drives: analysis, modeling, control*. Springer Nature, 2020.

[58] A. Yazdani and R. Iravani, *Voltage-Sourced Converters in Power Systems: Modeling, Control and Applications*, 1st ed. Hoboken, NJ: Wiley-IEEE Press, 2010.

[59] A. K. Adnanes and T. M. Undeland, “Optimum torque performance in PMSM drives above rated speed,” in *Conference Record of the 1991 IEEE Industry Applications Society Annual Meeting*, 1991, pp. 169–175 vol.1. doi: 10.1109/IAS.1991.178150.

[60] K. Bennion, “Electric motor thermal management R&D. Annual report,” 2016. Accessed: Jan. 30, 2024. [Online]. Available: https://www.nrel.gov/docs/fy16osti/64944.pdf

[61] S. Oki, S. Ishikawa, and T. Ikemi, “Development of High-Power and High-Efficiency Motor for a Newly Developed Electric Vehicle,” *SAE International*

Journal of Alternative Powertrains, vol. 1, no. 1, pp. 2012-01–0342, Apr. 2012, doi: 10.4271/2012-01-0342.

[62] T. Burress, "Benchmarking state-of-the-art technologies," in *Oak Ridge National Laboratory (ORNL), 2013 US DOE Hydrogen and Fuel Cells Program and Vehicle Technologies Program Annual Merit Review and Peer Evaluation Meeting*, 2013.

[63] Y. Sato, S. Ishikawa, T. Okubo, M. Abe, and K. Tamai, "Development of high response motor and inverter system for the Nissan LEAF electric vehicle," SAE Technical Paper, 2011.

[64] S. Li, Y. Li, W. Choi, and B. Sarlioglu, "High-Speed Electric Machines: Challenges and Design Considerations," *IEEE Transactions on Transportation Electrification*, vol. 2, no. 1, pp. 2–13, Mar. 2016, doi: 10.1109/TTE.2016.2523879.

[65] T. M. Jahns and B. Sarlioglu, "The Incredible Shrinking Motor Drive: Accelerating the Transition to Integrated Motor Drives," *IEEE Power Electronics Magazine*, vol. 7, no. 3, pp. 18–27, 2020, doi: 10.1109/MPEL.2020.3011275.

[66] T. Most and J. Will, "Sensitivity analysis using the Metamodel of Optimal Prognosis," in *Weimar Optimization and Stochastic Days*, 2011, pp. 1–17. [Online]. Available: https://www.dynardo.de/fileadmin/Material_Dynardo/bibliothek/WOST_8.0/Paper_Most.pdf

[67] ANSYS, "OptiSLang." 2021.

[68] M. Z. M. Jaffar and I. Husain, "Path permeance based analytical inductance model for IPMSM considering saturation and slot leakage," in *2017 IEEE International*

Electric Machines and Drives Conference (IEMDC), 2017, pp. 1–7. doi: 10.1109/IEMDC.2017.8002132.

[69] "Global Registry Addendum 15: Worldwide harmonized Light vehicles Test Procedure," 2014. [Online]. Available: https://unece.org/fileadmin/DAM/trans/main/wp29/wp29r-1998agr-rules/ECE-TRANS-180a15e.pdf

[70] "Copper Prices." [Online]. Available: https://www.dailymetalprice.com/metalpricecharts.php

[71] E. P. Agency, "Dynamometer Drive Schedules." [Online]. Available: https://www.epa.gov/vehicle-and-fuel-emissions-testing/dynamometer-drive-schedules

[72] Silong Li, Yingjie Li, and B. Sarlioglu, "Partial Irreversible Demagnetization Assessment of Flux-Switching Permanent Magnet Machine Using Ferrite Permanent Magnet Material," *IEEE Trans Magn*, vol. 51, no. 7, pp. 1–9, Jul. 2015, doi: 10.1109/TMAG.2015.2405898.

[73] G. Pellegrino, F. Cupertino, and C. Gerada, "Automatic Design of Synchronous Reluctance Motors Focusing on Barrier Shape Optimization," *IEEE Trans Ind Appl*, vol. 51, no. 2, pp. 1465–1474, 2015, doi: 10.1109/TIA.2014.2345953.

[74] D. A. Staton, T. J. E. Miller, and S. E. Wood, "Maximising the saliency ratio of the synchronous reluctance motor," in *IEE Proceedings B (Electric Power Applications)*, 1993, pp. 249–259. [Online]. Available: https://digital-library.theiet.org/content/journals/10.1049/ip-b.1993.0031

[75] E. C. Lovelace, T. M. Jahns, and J. H. Lang, “A saturating lumped-parameter model for an interior PM synchronous machine,” *IEEE Trans Ind Appl*, vol. 38, no. 3, pp. 645–650, 2002, doi: 10.1109/TIA.2002.1003413.

[76] J. Wang, W. Geng, Q. Li, L. Li, and Z. Zhang, “A New Flux-Concentrating Rotor of Permanent Magnet Motor for Electric Vehicle Application,” *IEEE Transactions on Industrial Electronics*, vol. 69, no. 11, pp. 10882–10892, 2022, doi: 10.1109/TIE.2021.3116558.

[77] J. Li, K. Wang, and H. Zhang, “Flux-Focusing Permanent Magnet Machines With Modular Consequent-Pole Rotor,” *IEEE Transactions on Industrial Electronics*, vol. 67, no. 5, pp. 3374–3385, 2020, doi: 10.1109/TIE.2019.2922922.

[78] A. Shoaei and Q. Wang, “A High Torque Density Flux-Focusing Halbach Magnetic Gear for Electric Vehicle Applications,” in *2022 IEEE 1st Industrial Electronics Society Annual On-Line Conference (ONCON)*, 2022, pp. 1–6. doi: 10.1109/ONCON56984.2022.10126858.

[79] V. M. Acharya, J. Z. Bird, and M. Calvin, “A Flux Focusing Axial Magnetic Gear,” *IEEE Trans Magn*, vol. 49, no. 7, pp. 4092–4095, 2013, doi: 10.1109/TMAG.2013.2248703.

[80] V. Rallabandi, N. Taran, D. M. Ionel, and I. G. Boldea, “MAGNUS — An ultra-high specific torque PM axial flux type motor with flux focusing and modulation,” in *2017 IEEE Energy Conversion Congress and Exposition (ECCE)*, 2017, pp. 1234–1239. doi: 10.1109/ECCE.2017.8095930.

[81] J. S. Smith, R. Pillsbury, and B. J. Sullivan, “Flux focusing arrangement for permanent magnets, methods of fabricating such arrangements, and machines including such arrangements ,” 9269483 B2, Feb. 23, 2016

[82] B. Xian, D. M. Dawson, M. S. de Queiroz, and J. Chen, “A continuous asymptotic tracking control strategy for uncertain nonlinear systems,” *IEEE Trans Automat Contr*, vol. 49, no. 7, pp. 1206–1211, 2004, doi: 10.1109/TAC.2004.831148.

[83] J. Latham, M. L. McIntyre, and M. Mohebbi, “Parameter Estimation and a Series of Nonlinear Observers for the System Dynamics of a Linear Vapor Compressor,” *IEEE Transactions on Industrial Electronics*, vol. 63, no. 11, pp. 6736–6744, 2016, doi: 10.1109/TIE.2016.2582728.

[84] M. L. McIntyre, T. J. Ghotikar, A. Vahidi, X. Song, and D. M. Dawson, “A Two-Stage Lyapunov-Based Estimator for Estimation of Vehicle Mass and Road Grade,” *IEEE Trans Veh Technol*, vol. 58, no. 7, pp. 3177–3185, 2009, doi: 10.1109/TVT.2009.2014385.

[85] S. Morimoto, Y. Takeda, T. Hirasa, and K. Taniguchi, “Expansion of operating limits for permanent magnet motor by current vector control considering inverter capacity,” *IEEE Trans Ind Appl*, vol. 26, no. 5, pp. 866–871, 1990, doi: 10.1109/28.60058.

[86] V. Ghorbanian, S. Hussain, S. Hamidizadeh, R. Chromik, and D. Lowther, “Demagnetization proximity considerations of inverter-fed permanent magnet motors,” in *2017 IEEE International Electric Machines and Drives Conference (IEMDC)*, 2017, pp. 1–7. doi: 10.1109/IEMDC.2017.8002176.

[87] Q. Zhang, Z. Ma, G. Li, Z. Qian, and X. Guo, “Temperature-dependent demagnetization nonlinear Wiener model with neural network for PM synchronous machines in electric vehicle,” in *2016 19th International Conference on Electrical Machines and Systems (ICEMS)*, 2016, pp. 1–4.

[88] M. Ganchev, B. Kubicek, and H. Kappeler, “Rotor temperature monitoring system,” in *The XIX International Conference on Electrical Machines - ICEM 2010*, 2010, pp. 1–5. doi: 10.1109/ICELMACH.2010.5608051.

[89] E. C. Quispe, X. M. López-Fernández, A. M. S. Mendes, A. J. Marques Cardoso, and J. A. Palacios, “Experimental study of the effect of positive sequence voltage on the derating of induction motors under voltage unbalance,” in *2011 IEEE International Electric Machines & Drives Conference (IEMDC)*, 2011, pp. 908–912. doi: 10.1109/IEMDC.2011.5994936.

[90] O. Wallscheid and J. Böcker, “Fusion of direct and indirect temperature estimation techniques for permanent magnet synchronous motors,” in *2017 IEEE International Electric Machines and Drives Conference (IEMDC)*, 2017, pp. 1–8. doi: 10.1109/IEMDC.2017.8002038.

[91] O. Wallscheid, T. Huber, W. Peters, and J. Böcker, “Real-time capable methods to determine the magnet temperature of permanent magnet synchronous motors — A review,” in *IECON 2014 - 40th Annual Conference of the IEEE Industrial Electronics Society*, 2014, pp. 811–818. doi: 10.1109/IECON.2014.7048594.

[92] O. Wallscheid, W. Kirchgässner, and J. Böcker, “Investigation of long short-term memory networks to temperature prediction for permanent magnet synchronous

motors," in *2017 International Joint Conference on Neural Networks (IJCNN)*, 2017, pp. 1940–1947. doi: 10.1109/IJCNN.2017.7966088.

[93] Y.-S. Lee, K.-T. Kim, and J. Hur, "Transient analysis of irreversible demagnetization of permenent magnet brushless DC motor with stator turn fault under the operating state," in *2013 IEEE Energy Conversion Congress and Exposition*, 2013, pp. 4396–4402. doi: 10.1109/ECCE.2013.6647288.

[94] S. Sastry, M. Bodson, and J. F. Bartram, "Adaptive control: stability, convergence, and robustness." Acoustical Society of America, 1990.

[95] M. McIntyre, T. Burg, D. Dawson, and B. Xian, "Adaptive state of charge (SOC) estimator for a battery," in *2006 American Control Conference*, 2006, pp. 5 pp.-. doi: 10.1109/ACC.2006.1657640.

[96] Plexim GmbH, "RT Box User Manual," www.plexim.com. Accessed: Feb. 13, 2024. [Online]. Available: https://www.plexim.com/sites/default/files/rtboxmanual.pdf

[97] "RT Box 1," www.plexim.com. Accessed: Feb. 13, 2024. [Online]. Available: https://www.plexim.com/products/rt_box/rt_box_1

[98] Texas Instruments, "BOOSTXL-DRV8305EVM User's Guide," www.ti.com. Accessed: Feb. 13, 2024. [Online]. Available: https://www.ti.com/lit/ug/slvuai8a/slvuai8a.pdf?ts=1707841127431&ref_url=https%253A%252F%252Fwww.ti.com%252Ftool%252FBOOSTXL-DRV8305EVM%253Futm_source%253Dgoogle%2526utm_medium%253Dcpc%2526utm_campaign%253Dasc-mdbu-null-44700045336317515_prodfolderdynamic-cpc-pf-google-

eu_int%2526utm_content%253Dprodfolddynamic%2526ds_k%253DDYNAMIC%2BSEARCH%2BADS%2526gad_source%253D1%2526gclid%253DEAIaIQobChMIhLqk-duohAMVEadoCR0k2Q51EAAYBCAAEgKvBfD_BwE%2526gclsrc%253Daw.ds

[99] "BOOSTXL-DRV8305EVM," Texas Instruments. Accessed: Feb. 13, 2024. [Online]. Available: https://www.ti.com/tool/BOOSTXL-DRV8305EVM

[100] S. J. Underwood and I. Husain, "Online Parameter Estimation and Adaptive Control of Permanent-Magnet Synchronous Machines," *IEEE Transactions on Industrial Electronics*, vol. 57, no. 7, pp. 2435–2443, 2010, doi: 10.1109/TIE.2009.2036029.

[101] T. Wang *et al.*, "An EMF Observer for PMSM Sensorless Drives Adaptive to Stator Resistance and Rotor Flux Linkage," *IEEE J Emerg Sel Top Power Electron*, vol. 7, no. 3, pp. 1899–1913, 2019, doi: 10.1109/JESTPE.2018.2865862.

[102] D. F. Laborda, D. Díaz Reigosa, D. Fernández, K. Sasaki, T. Kato, and F. Briz, "Magnet Temperature Estimation in Variable Leakage Flux Permanent Magnet Synchronous Machines Using the Magnet Flux Linkage," in *2020 IEEE Energy Conversion Congress and Exposition (ECCE)*, 2020, pp. 6111–6117. doi: 10.1109/ECCE44975.2020.9236059.

[103] Plexim GmbH, "PLECS 4.7." 2023.

[104] X. Chen, J. Wang, and A. Griffo, "A High-Fidelity and Computationally Efficient Electrothermally Coupled Model for Interior Permanent-Magnet Machines in Electric Vehicle Traction Applications," *IEEE Transactions on Transportation Electrification*, vol. 1, no. 4, pp. 336–347, 2015, doi: 10.1109/TTE.2015.2478257.

[105] X. Chen, J. Wang, B. Sen, P. Lazari, and T. Sun, “A High-Fidelity and Computationally Efficient Model for Interior Permanent-Magnet Machines Considering the Magnetic Saturation, Spatial Harmonics, and Iron Loss Effect,” *IEEE Transactions on Industrial Electronics*, vol. 62, no. 7, pp. 4044–4055, Jul. 2015, doi: 10.1109/TIE.2014.2388200.

[106] A. Varatharajan, G. Pellegrino, and E. Armando, “Kinetic-Rotor Self-Commissioning of Synchronous Machines for Magnetic Model Identification with Online Adaptation,” *IEEE Trans Ind Appl*, p. 1, 2022, doi: 10.1109/TIA.2022.3151039.